Università degli Studi di Palermo

AREA RICERCA E TRASFERIMENTO TECNOLOGICO
SETTORE DOTTORATI E CONTRATTI PER LA RICERCA
U. O. DOTTORATI DI RICERCA

Mechanical, Manufacturing, Management and Aerospace Innovation
Dipartimento di Ingegneria
ING-IND/04 Costruzioni e strutture aerospaziali

HIGH-ORDER METHODS FOR THE MECHANICAL CHARACTERIZATION OF LAMINATED SHELL STRUCTURES

IL DOTTORE
ING. GIULIANO GUARINO

IL COORDINATORE
PROF. GIOVANNA LO NIGRO

IL TUTOR
PROF. ALBERTO MILAZZO

IL CO TUTOR
PROF. PABLO ANTOLIN

CICLO XXXVI
ANNO CONSEGUIMENTO TITOLO 2023

UNIVERSITÀ
DEGLI STUDI
DI PALERMO

High-order methods for the mechanical characterization of laminated shell structures

Giuliano Guarino

Thesis for the PhD course in Mechanical, Manufacturing, Management and Aerospace Innovation at the Università degli Studi di Palermo.

Under the supervision of

Tutor
Prof. Alberto Milazzo, Università degli Studi di Palermo

Co-tutor
Prof. Pablo Antolin, École Polytechnique Fédérale de Lausanne

---

XXXVI cycle 2023

Abstract

Two-dimensional theories are crucial in commercial software for industrial applications, serving as the standard for conducting mechanical analyses of thin-walled components. Despite the ongoing advancement of computational resources, which aids in making full three-dimensional analyses less time consuming, the necessity of shell elements persists. This is especially true when it becomes necessary to explore a vast number of drafts with low accuracy, such as in early stages of design, or when analyzing complex large structures typical of transport industry. Notably, the integration of high-order theories augments the precision of 2D analyses, producing results comparable to those derived from fully 3D analyses. In this context, the establishment of a unified framework that facilitates the straightforward adjustment of kinematic order becomes paramount, especially when progressing through different project stages, each demanding varying levels of accuracy.

In this thesis, various shell kinematics are employed in conjunction with methods facilitating the construction of shell elements with high in-plane order. Specifically, the discontinuous Galerkin (DG) and Isogeometric Analysis (IGA) methods are adopted. The formulated approaches enable the modeling of generally-curved shells with arbitrary lamination sequences.

Higher-order theories are combined with DG for both linear and non-linear mechanical analyses of shells for the first time. Cut-outs are represented using the implicit mesh technique, employing a level-set function to implicitly define the integration domain on active elements. The discontinuous nature of DG basis functions is also exploited for studying a damaged plate with a through-the-thickness crack.

For structures composed of multiple shells, IGA is applied, enforcing coupling between patches and boundary conditions through a variationally consistent weak formulation along conforming and trimmed boundaries. In this approach, the boundary of the embedded domain is defined explicitly using trimming curves. Local refinement in critical areas is achieved by either adopting auxiliary IGA boundary layers or implementing local refinement with additional DG elements.

The thesis also provides the main implementation details of the proposed methods. Numerical examples are presented to showcase the accuracy and efficiency of the proposed approaches. The results of all tests are systematically compared with reference solutions obtained either analytically or through commercially available FEM software.

Acknowledgements

This work would not have been possible without the invaluable assistance and support of numerous individuals. Foremost, I express my gratitude to my tutor, Prof. Alberto Milazzo, for your exceptional guidance over the past three years. I extend my sincere thanks for your support, our insightful discussions, the lessons I have learned under your mentorship, and your help in organizing every facet of my PhD journey. Your belief in my scientific capabilities and encouragement to explore various directions within the thesis topic have been pivotal to the success of this work.

I extend my heartfelt gratitude to the co-tutor of my thesis, Prof. Pablo Antolin, and the head of the chair of Modelling and Numerical Simulation at EPFL, Prof. Annalisa Buffa. I appreciate your belief in my capabilities and the extraordinary opportunity you provided me by inviting me to join your team for one year. My time in Lausanne was not only a significant period for personal development but also a valuable opportunity for professional growth. I am confident that it marks the commencement of a fruitful collaboration, and I sincerely thank both of you for your support and trust in my potential.

I express my sincere appreciation to Prof. Robert Saye and Prof. Alfonso Pagani for graciously accepting the responsibility of reviewing this thesis. Your insightful suggestions for improvement have been invaluable, contributing significantly to the refinement of the work. Additionally, I extend my gratitude to Prof. Ivano Benedetti, Prof. Andrea Alaimo, and Prof. Maria Cinefra for generously dedicating your time to serve as commissioners for my PhD examination.

I also extend my sincere thanks to Prof. Vincenzo Gulizzi for his constant availability and continuous engagement in scientific discussions. This work has greatly benefited from your insights, support, and invaluable suggestions. I am truly grateful for your guidance and for being a remarkable role model throughout my PhD journey.

A sincere thanks goes out to all the members of the Aerospace group in Palermo for creating such an enjoyable work environment. Your laughter, and shared moments made office life truly enjoyable. I am grateful not only for the good times but also for the support and comfort provided when needed. Special appreciation is extended also to the members of the MNS team in Lausanne for warmly welcoming me from the very first day. Being part of your team was a marvelous experience and a significant opportunity for connecting on a personal and professional level with great individuals. Thank you all for making these collaborative experiences memorable and enriching.

A warm appreciation goes out to all my friends who helped me throughout this journey. Special gratitude to Chicca, you have been the most exceptional emotional support I could have asked for, initially as a partner and later as a friend. To Marta, Francesco, Giulia, Matteo, Mattia, Benni, and Gabriele, thank you for generously offering your time during moments of need and for helping me navigate the challenges of life.

Lastly, I extend my deepest thanks to my family. To my mother, Tanya, thank you for supporting my educational journey, which has led me to where I am today, and for

consistently wanting the best for me. To my brothers, Giuseppe and Graziano, thank you for always being a source of insight and support, providing valuable perspectives on work, family, and life-related challenges.

Contents

Chapter 1

Introduction

1.1 Motivation

In various industrial sectors, the performance of the final product can be influenced by its weight. This effect is particularly evident in the transport industry, with notable examples in aerospace, automotive, train, and naval sectors. A significant portion of the overall weight can be attributed to the structural configuration. Here, "structure" refers to the collective components that work together to transmit external forces throughout the entire vehicle while also withstanding unforeseen stresses. The weight of these structural elements is determined by a combination of factors, including the chosen materials and the shape and arrangement of the structural components. Therefore, it is crucial to optimize of the stiffness-to-weight ratio through meticulous structural and material design for achieving high-performances. Typically, this involves adopting thin-walled structures such as plates or shells.

On the material side, in recent decades composite multilayered laminates have been increasingly becoming the preferred choice over their metallic counterparts in high-performance demanding applications. This shift is attributed to the numerous possibilities for fine-tuning that these materials offer. These include options such as selecting the stacking sequence of the entire laminate, adjusting the lamination angle, choosing the materials for the fibers and the matrix of the individual layers [1, 2].

Unlike plates, shells are distinguished by a non-flat mid-surface and exhibit what is known as the curvature effect. This effect, as discussed in [3], results in structural stiffening due to geometric curvature, leading to an intricate interplay between flexural and membrane behaviors. This unique characteristic allows the shape of the surface to be utilized as a design parameter. Conversely, there are instances where the necessity for a curved surface arises from non-structural considerations, such as in the design of aerodynamic components.

Nonetheless, even though curved laminate structures offer high versatility, the interplay between the curved geometry and the discrete properties of the composite layers leads to a complex distribution of mechanical fields, including strains and stresses. This complexity is particularly pronounced in the out-of-plane components and must be meticulously resolved to ensure the safe utilization of generally curved composite shells as load-bearing structures.

In general, the analysis of composite multilayered shells is a three-dimensional (3D) problem, necessitating the use of computational methods. In fact, analytical solutions are only available for a very limited number of special cases, as demonstrated, for example,

in [4, 5, 6]. Fully 3D models offer high accuracy but can be computationally demanding and inefficient for early design stages. To address this issue, an order reduction approach involving two-dimensional (2D) theories can be applied. These theories are based on reasonable assumptions regarding the mechanical fields' behavior across the thickness of the laminate. They offer a practical strategy for reducing computational complexity compared to 3D models. It is worth noting that more refined assumptions yield more accurate results, but at the cost of increased computational time. Therefore, comprehending the possibilities and limitations of various two-dimensional theories is essential for their safe and effective use as tools in mechanical analysis.

The physical model obtained using two-dimensional theories typically yields a set of partial differential equations. These equations, due to their inherent complexity, require numerical solutions. The computational time needed to attain a specific level of accuracy in the numerical solution can vary significantly depending on the chosen numerical method, the discretization technique, the type and order of elements used. Consequently, investigating the capabilities of various numerical methods is of paramount importance and a subject of significant research interest.

The most simple type of mechanical analysis of structures consists in characterizing their static mechanical response. Generally, thin-walled structures operate within the realm of small displacements, and a linear elastic analysis may suffice to predict their behavior. However, in advanced applications, these structures may experience significant displacements, necessitating non-linear analysis to accurately describe their response. Among various loading scenarios, it is well-established that dynamic loads can induce larger strain and stress fields than those predicted by static analyses, especially when they excite the natural frequencies of the structures in question. Additionally, loads that induce compressive stress states can cause thin and slender structures to undergo sudden geometric changes and fail at loads significantly lower than those predicted by linear static analyses, a phenomenon referred to as buckling. Typically, in thin-walled metallic components, buckling constitutes the main concern for failure. However, when dealing with laminates, the complexity arising from intrinsic anisotropy and non-homogeneity makes issues related to the material, such as fiber debonding, fiber microbuckling, and layer delamination, among others, the primary failure mechanisms. The modeling and analysis of all of these complex behaviors play a crucial role. These analyses must be both accurate and computationally efficient to effectively address the complexities involved.

Shell structures typically consist of multiple patches, each associated with a specific mapping of its mid-surface. Simple surfaces can be defined using analytical expressions, while for more complex and generally curved shells, Computer-Aided Design (CAD) software is a powerful tool. CAD software empowers designers to craft and manipulate intricate surface geometries, spanning from basic planar ones to highly contoured shapes, providing a comprehensive canvas for engineering design. To prevent undue complexity in the surface definition, details like cut-outs can be incorporated into an underlying surface, by properly describing only its boundary. A further challenge emerges when it is necessary to integrate the geometric descriptions of different components to construct the entire structure through the definition of interfaces between different patches. Hence, it is of paramount importance to establish a seamless connection between the geometric representation in the design phase and the discretized geometry in the numerical analysis phase, ensuring that accuracy in the geometry description is preserved throughout the process.

The objective of this thesis is to advance current models and methods relevant to

the realm of shell structures, with the intention of fulfilling the necessities introduced so far. This involves combining various components, extending to shell problems some methods successfully applied to other contexts, and tackling associated challenges using the most effective strategies documented in the literature. The desired outcome of this work is the creation of novel and efficient modeling approaches implemented in algorithms and routines that can serve as a foundation for the development of commercial software tailored for commercial applications.

1.2 State of the art

The first two-dimensional theory proposed in the literature for the mechanical analysis of shells is the Kirchhoff-Love (KL) shell theory. Originally formulated for plates in [7] and later extended to shells in [8], this theory is also known as Classical Laminated Theory (CLT) [9, 10] when applied to laminated structures. The core assumption of this theory is that a unit segment perpendicular to the shell's mid-surface remains straight and perpendicular to the surface even after deformation. The Reissner-Mindlin theory (RM) [11, 12], also referred to as the First-order Shear Deformation Theory (FSDT), relaxes the assumption of perpendicularity, allowing for the modeling of out-of-plane strain and stress components. As a result, it becomes more suitable for analyzing moderately thick shells. Focusing on geometrically-nonlinear quasi-static behavior, the first model was developed by von Kármán [13], who augmented the definition of the strain in classical KL theory with nonlinear terms. Subsequently, various theories based on different geometrically-nonlinear definition of the strain tensor have been explored, and a comprehensive review of these can be found in the work by Chia [14].

The extensive use of multilayered composite plates and shells has highlighted the need for a more detailed resolution of displacement, strain, and stress distributions at the level of individual layers. To enhance modeling accuracy, researchers have enriched the through-the-thickness assumptions and introduced what are known as higher-order theories. These theories can be categorized into two main groups: Equivalent-Single-Layer (ESL) theories [15, 16, 17], and Layer-Wise (LW) theories [18, 19, 20]. In the ESL approach, the functions used to expand the displacement field along the thickness are defined uniformly for the entire laminate. Consequently, the individual layers are replaced by a single layer with equivalent mechanical properties. On the other hand, Layer-Wise (LW) theories are based on a layer-by-layer expansion. This means that the displacement field is described using piece-wise functions, and at the interfaces between layers, they exhibit only a C^0 continuity.

A unified description of high-order theories for plates and shells has been introduced by Carrera through the Carrera Unified Formulation (CUF) [21, 22, 23]. This framework enables a systematic construction of various structural theories because it allows for flexibility in selecting the order of the approximation and the type of theory, making them free parameters for analysis. However, it is important to note that increasing the through-the-thickness resolution comes at the cost of increasing the number of primary variables, leading to longer computational times. Finding the right balance between computational efficiency and solution accuracy is not always straightforward. In this context, an attempt to determine the most suitable 2D theory in terms of computational efficiency versus solution accuracy for a given structural problem is presented in [24]. The Kirchhoff-Love (KL) shell theory, for instance, requires only the displacement field in the

mid-surface of the shell as the main variable. However, due to the fourth-order nature of the resulting equations, the continuity of the approximation space needs to be C^1. This means that both the displacements and their first derivatives must be continuous across element boundaries. In contrast, most two-dimensional theories lead to second-order problems with standard C^0 continuity requirements.

The governing equations that arise from two-dimensional theories for plates and shells are typically strongly coupled partial differential equations (PDEs). Finding closed-form solutions for these equations is exceptionally challenging and limited to very specific combinations of geometry, materials, and boundary conditions. In most instances, numerical models based on these theories are tackled using Finite Element Methods (FEM) based on continuous Galerkin approximations (CG) [25]. The FEM serves as the foundation for many commercial software libraries, encompassing both 3D and 2D elements [26].

1.2.1 The discontinuous Galerkin method

Amongst the alternatives to CG-based FEM, the discontinuous Galerkin (DG) method is a powerful numerical technique that was initially introduced for hyperbolic partial differential equations [27] and later extended to elliptic PDEs [28], including elasticity problems [29, 30]. Similar to CG-based FEM, DG methods rely on a discretization, or mesh, of the analysed domain. However, unlike most numerical schemes, the DG approach employs an approximation of the solution using discontinuous basis functions over the mesh elements. It also utilizes suitably defined boundary integrals to ensure solution continuity at inter-element interfaces and enforce boundary conditions, including both prescribed displacements and traction fields. This unique feature of the DG method offers several advantages, including the use of nonstandard element and shape functions, the application of non-conformal meshes, the utilization of high-order elements, the implementation of meshing strategies like hierarchical refinement and adaptivity, scalability, and addressing locking phenomena. These features make the DG method a robust approach for handling complex geometries and loads commonly found in advanced lightweight structures.

Indeed, a thorough examination of the relevant literature reveals a growing interest in DG method to the analysis of various thin-walled structures. Specifically, DG formulations and investigations have been proposed for the linear analysis of: i) Plates, where the Kirchhoff [31, 32, 33] and Reissner-Mindlin [34, 35, 36] first-order theories have been employed; ii) Shells, including the Kirchhoff-Love [37], Koiter [38], and Reissner-Mindlin [39] first-order theories; In the realm of non-linear analysis, DG methods have been utilized for: i) Kirchhoff plates [40, 41, 42]; ii) Kirchhoff-Love shells [43, 44, 45]; iii) Shear-flexible shells modeled using the first-order theory [46, 47]. Furthermore, refined shell models have been proposed for both linear [48] and non-linear [49] analyses, based on finite elements developed using a DG approach along the thickness direction. Generally, the reported formulations primarily pertain to isotropic and homogeneous sections, although there are a few works focusing on multilayered structures [48, 49, 40].

For eigenvalue problems, the DG method has found application in various areas: i) It has been used to solve the Laplace eigenproblem [50, 51]; ii) To compute the eigenfrequencies of the Maxwell equations in a cavity [52, 53, 54]; iii) To study the hydrodynamic stability associated with the incompressible Navier–Stokes equations [55, 56]. In the realm of structural analysis for classical plate and shell theories, there have been instances where a mixed continuous-discontinuous Galerkin method was applied. For Kirchhoff plates, this approach has been used for both buckling analysis [57, 58] and

free-vibration analysis [58].

Concerning the application of DG to problems related to damage and fracture mechanics, in [59], singular asymptotic crack tip fields are employed to create extended DG elements weakly connected to the rest of the mesh, addressing two-dimensional elasticity of domains including cracks. A different approach followed by [60] for KL shells and by [47] for RM shells, based on a cohesive zone concept, consists in letting the crack propagate through the elements' boundaries, providing advantages in parallel solution procedures.

In the context of high-order plates and shell theories, the DG method has been effectively utilized for solving the governing equations of multilayered elastic plates modeled by ESL and LW theories [61, 62]. This application extends to multilayered piezoelectric plates modeled by LW theories [63]. Additionally, the DG method has been employed for shells modeled by ESL theories, addressing linear static analysis [64], buckling analysis [65], free-vibration and transient analysis [66], and nonlinear static analysis [67].

1.2.2 The Isogeometric Analysis method

Another particularly promising approach that has gained interest in recent literature is the Isogeometric Analysis (IGA). In IGA, NURBS (Non-Uniform Rational B-Splines) basis functions are used not only to define the surface of the shell but also to construct the approximation space for the primary variables, following an isoparametric concept. This approach facilitates a seamless connection between the design and analysis processes [68], allowing for a geometrically-exact representation of the shell surface and a high-order approximation for the variable of interest, e.g., the displacement field. In this sense, IGA shares some features with the p-version of FEM [69], where, when applied to thin-walled structures, hierarchical refinement of the degree of polynomial shape functions is adopted to describe the geometry of the shell and to construct the trial function space [70, 71, 72, 73]. Nevertheless, p-FEM is limited to C^0 shape functions and does not follow an isoparametric paradigm. Since its introduction [74], IGA has been successfully applied to solve Kirchhoff-Love [75, 76], Reissner-Mindlin [77, 78, 79], and Higher-Order [80] shell theories. One notable advantage of IGA is that NURBS functions can be easily constructed with arbitrary continuity, making it straightforward to satisfy the C^1 continuity requirement for the KL shell equations.

However, when dealing with complex shapes, multiple NURBS-based patches are often required to accurately represent the desired geometry, and efficiently coupling these patches becomes a critical issue. Various approaches have been proposed to enforce coupling in a strong sense by directly merging corresponding degrees of freedom: For example, in [81], IGA regions of the domain are connected in a strong sense with other regions modeled with a mesh-free approach; in [82] patches meeting at G^0 interfaces are both connected in a strong sense to auxiliary bending strips that approximate the kinks; in [83], the approximation functions for the displacement are continuous across the patches with only the coupling of the rotation imposed in a weak sense; in [84], the coupling approach relies on the Reissner-Mindlin theory where also rotation degrees of freedom are directly available; the construction of C^1 multi-patch approximation spaces, as detailed in [85, 86], is used in [87] and [88] for the strong coupling of both displacement and rotation for Kirchhoff-Love IGA patches, but limited to G^1 geometries. However, all of these approaches rely on a conforming requirement, meaning that the parameterization of the common edge is the same for each of the patches to be coupled.

For discretization involving IGA patches meeting at non-conforming interfaces, the continuity of the displacement and rotation must be enforced with a weak method. In fact, the main advantage of such approach is that the coupling condition, as well as the boundary Dirichlet condition, does not need to be intrinsically satisfied by the solution space, allowing more flexibility in its definition. In the literature, various methods have been proposed to weakly enforce coupling between IGA patches for many model problems, including the Kirchhoff-Love equations. Examples of these methods include the morthar type and Lagrange multipliers methods [89, 90, 91, 92, 93, 94, 95], the pure penalty methods [96, 97, 98, 99, 100, 101], the projected super-penalty method [102, 103] and the Nitsche-type methods [104, 105, 106, 107, 108, 109, 110, 111, 112]. Among these, the Nitsche-type methods are particularly appealing as they do not require the introduction of additional degrees of freedom as in the Lagrange multipliers methods and, when properly stabilized, do not suffer from the ill-conditioning issues typically seen in penalty approaches. However, constructing a Nitsche-type method for the Kirchhoff-Love shell equations requires computing the fluxes for the formulation, and the version typically found in the literature [113], that tracks back to Koiter's work [114], has been recently found to be incorrect in [115].

1.2.3 Embedded description of surfaces

NURBS surfaces provide the potential to create any desired curvature profile. However, handling complex structures that involve multiple intersecting surfaces, cut-outs, or local features can be challenging when trying to reconstruct the geometry using only patches that conform to the boundaries or interfaces. To simplify this task, the trimmed approach allows for the definition of complex surfaces while also limiting the number of NURBS patches required. This method involves embedding a trimming curve in the parametric domain of a surface to delimit its outer boundary and identify active and non-active regions. This increased flexibility comes with certain challenges. Specifically, after the discretization of the embedded geometry, the presence of trimmed elements can raise issues related to integration, conditioning of the linear system, and the stability of the method. These same issues arise when coupling between two patches occurs at a trimmed boundary, where one or both of the patches may be trimmed by the interface [108, 102]. Addressing these challenges is crucial to ensure the robustness and accuracy of method.

Regarding the integration over trimmed elements, several techniques have been proposed in the literature, including: i) hierarchical finite cells: where trimmed elements are subdivided into a hierarchy of smaller cells where a standard integration rule is applied [108, 107]; ii) level-set function: that is applicable to domains where the boundary is implicitly represented by the zero level-set of a reference function [116, 117]; iii) blending functions: that are used to approximate the geometry of the trimmed element, enabling efficient integration [118, 106]. In particular, recently, a robust and efficient algorithm based on higher-order reparameterization of trimmed elements has been proposed in [119], which allows dealing with explicitly defined domains. This algorithm has been used in [120] for the Poisson problem with overlapping patches and in [121] for two-dimensional elasticity.

1.2.4 The Immersed Boundary-Conformal Method

Among the drawbacks of adopting a trimming approach for the definition of shell surface, trimmed boundaries and interfaces are intrinsically non-conforming. Therefore, a strong imposition of boundary and coupling conditions is not possible since this should be embedded in the approximation space.

Nonetheless, a recent technique known as the Immersed Boundary-Conformal Method (IBCM) has been introduced in the context of two-dimensional elasticity using IGA [121]. This method offers the capability to strongly enforce essential boundary and coupling conditions by introducing auxiliary boundary-conformal layers. Furthermore, these boundary layers enable the local refinement of the approximation space in regions where local phenomena are more likely to occur.

1.3 Methodology and outline

This thesis includes author's previous work across a number of different projects, encompassing findings from previously published peer-reviewed journal and conference articles [64, 122, 65, 66, 67], as well as articles currently under preparation [123, 124].

This thesis aims to demonstrate the advantages of high-order approaches for the mechanical analysis of shells through the diligent use of DG and IGA methods. In particular, two approaches that have never been investigated in the literature before the author's work in the realm of this thesis are proposed here: the combination of higher-order kinematics and DG for shells and the coupling of IGA KL patches through the proper definition of Interior Penalty integrals. Furthermore, the thesis introduces innovative applications, such as the application of IBCM to shells and the combination between IGA and DG. It is acknowledged, however, that additional development is essential to fully realize the potential of these approaches.

The various components that constitute the methods employed in this thesis, along with the corresponding numerical results, are elaborated in the thesis chapters as described as follows.

- Chapter 2 provides an overview of the general settings for the shell formulations proposed in this work. It introduces the notation used for surface definition and outlines strategies for embedded domain definition and discretization. Within this chapter, two approaches to mitigate ill-conditioning arising from the trimmed approach are discussed: merging and preconditioning. Moreover, the chapter delves into the differential geometry for surfaces and volumes adopted in the formulation. Finally, it covers the fundamental concepts of the theory of elasticity, including the definition of strain tensor, stress tensor, the constitutive relationship, and the weak 3D formulation for various linear and non-linear problems of interest.

- Chapter 3 focuses on the presentation of multiple shell theories. This section provides descriptions of the classical KL theory, the ESL theories, and the LW theories. For each theory, the chapter outlines the kinematic assumptions and elaborates on the corresponding strain tensor. The KL theory is presented specifically for linear static analysis of laminated shells, in accordance with classical literature. The ESL theory, on the other hand, involves obtaining two-dimensional equations through model reduction from the three-dimensional formulation. It covers linear and non-

linear static analysis, linear buckling, transient, and free-vibration analyses. Finally, the extension to LW theory is also presented within this chapter.

- Chapter 4 introduces the first of the two approaches proposed in this work. This approach begins with higher-order kinematic shell formulations and utilizes the DG method for their solution. To prevent ill-conditioning of the linear system, the merging technique is applied. This section covers all types of mechanical problems, addressing various linear analyses using the interior penalty formulation and non-linear static analysis, where the pure penalty method is preferred to reduce computational costs. The chapter also includes the presentation of published results to demonstrate the effectiveness of this approach.

- Chapter 5 delves into the linear elastic static analysis of KL shells using IGA. The chapter commences by providing a description of spline basis functions, which are used for constructing NURBS surfaces and to define approximation functions in IGA. Next, the chapter introduces the interior penalty method for KL shells and its application for connecting patches seamlessly. Additionally, the IBCM is extended to KL shells to create conforming boundaries and interfaces. Finally, a local refinment strategies that leverages the combination of a global IGA model with local DG elements is introduced. Throughout this chapter, several numerical tests are presented, alongside reference solutions, whether they are analytical or obtained using FEM commercial software. These tests help to validate the proposed methodology.

- Finally, Chapter 6 provides a comprehensive conclusion to the thesis that serves as a summary of the findings and a guide for potential developments. It highlights the contributions made by the different methods discussed in the earlier chapters. The chapter also discusses the positive and negative aspects of each of these methods and offers suggestions for further research directions, providing recommendations for future work in this field.

1.4 Software details

The numerical results presented in this thesis have been obtained using various libraries and tools, detailed as follows:

The DG-based approach described in Chapter 4 was implemented in an in-house Python library, which includes some core functions specifically developed in FORTRAN to enhance computational speed. For defining embedded cut-outs, the algorithm proposed in [116, 117] was adopted. Algebraic linear system are solved using the Pardiso solver [125], while algebraic eigenvalue problems are addressed using the SLEPc library [126].

The IGA-based approach in Chapter 5 makes use of the open-source MATLAB library GeoPDEs. GeoPDEs is specifically designed for solving PDEs, including those related to KL shells, using IGA. This library also supports the study of multi-patch scenarios. It is used in conjunction with an in-house tool that implements the algorithms presented in [119]. This tool facilitates the geometric description and meshing of trimmed domains and relies on the open-source geometric modeling environment IRIT and the geometric kernel OpenCASCADE. The linear systems arising from this method are solved using MATLAB internal solver for sparse matrices.

Many results obtained with the proposed approaches are compared with reference FEM solutions. These reference solutions were obtained using Abaqus® commercial software [26], which can construct reference solutions for both higher-order and lower-order kinematic approaches, as it implements both 3D and 2D elements.

Chapter 2

Problem description

2.1 Parametric description of a surface

The formulation adopted in this work starts form the characterization of the shell mid-surface. The description of the geometry of a generally-curved surface can be provided in several ways. One method involves expressing one of the coordinates as a function of the other two, while another approach consists in approximating the surface as a collection of planar shapes. However, to achieve a comprehensive, geometrically exact description that still harnesses the advantages of a function-based characterization, it is opted for the parametric approach in this work. Let $\Omega \in \mathbb{E}^3$ be a generic oriented surface with $\mathbb{E}^3$ representing the three-dimensional Euclidean space. Let Ω be the image of the parametric domain $\hat{\Omega} \in \mathbb{R}^2$, accordingly to the map

$$\boldsymbol{x}_0 = \boldsymbol{x}_0(\xi_1, \xi_2) = \begin{bmatrix} x_{01}(\xi_1, \xi_2) \\ x_{02}(\xi_1, \xi_2) \\ x_{03}(\xi_1, \xi_2) \end{bmatrix} , \tag{2.1}$$

where ξ_1, ξ_2 denotes the set of curvilinear coordinates spamming $\hat{\Omega}$. The components of the vector $\boldsymbol{x}_0$ refer to the standard basis $\boldsymbol{e}_1\boldsymbol{e}_2\boldsymbol{e}_3$ of the Euclidean space. Additionally, let $\partial\hat{\Omega}$ and $\partial\Omega$ be the boundary of $\hat{\Omega}$ and Ω, respectively.

It is important to highlight that no specific assumption is made about the nature of the function $\boldsymbol{x}_0(\xi_1, \xi_2)$. In this work, it is generally preferred employing analytical expressions for simple geometries that permit such descriptions. Nevertheless, for more intricate surfaces, it is leveraged the flexibility of NURBS functions.

In the reminder of the thesis, Greek letter indices take values in the set $\{1, 2\}$, Latin letter indices take values in the set $\{1, 2, 3\}$, and repeated subscripts imply summation unless explicitly stated otherwise.

2.2 Embedded parametric domain and respective discretization

No assumptions have been made regarding the shape of the parametric domain in the geometry description. In fact, the formulation presented in this thesis is applicable to shells of arbitrary mid-surface. The flexibility in shell geometry arises from our ability to handle generally-curved surfaces using a generic mapping in curvilinear coordinates,

combined with the freedom in defining the parametric domain. However, the commonly employed approach to construct $\hat{\Omega}$ typically begins with a rectangular domain defined as

$$\hat{\Pi}_0 = [\xi_{1b}, \xi_{1t}] \times [\xi_{2b}, \xi_{2t}] \,, \tag{2.2}$$

where $\xi_{\alpha b}$ and $\xi_{\alpha t}$ denote the bottom and top limits, respectively, defining the interval over which the curvilinear variable ξ_α ranges. The boundary of $\hat{\Pi}_0$ is denoted as $\partial\hat{\Pi}_0$. For instance, when describing a shell surface using NURBS functions, $\hat{\Pi}_0$ is often defined as the rectangular domain $[0, 1] \times [0, 1]$, [127, 128].

The parametric domain is derived from the reference rectangle by removing regions that do not belong to the desired shape. This process divides the initial rectangular domain into active and non-active regions, with the union of the active regions coinciding with $\hat{\Omega}$. This approach offers the advantage of defining complex shapes using a single geometric patch, comprising a parametric domain and a map. Figure (2.1a) shows an example of a parametric domain (in grey) obtained starting from a reference rectangular domain and trimming away the non-active regions (in white). In Fig.(2.1b) the parametric domain is mapped into the final shape in the Euclidean space.

There are several alternative methods to address the generality of the parametric domain. For instance, one could partition the parametric domain into multiple patches, each with a different geometric description, and then integrate them appropriately. However, such an approach would add extra complexity to the geometry description.

To properly define the parametric domain, it is essential to employ a strategy for delineating the boundary of the trimmed region and establishing criteria for distinguishing between active and non-active regions. In this work, two distinct approaches are considered. The first approach employs an implicit definition of the domain using a level-set function, while the second approach utilizes a Boundary Representation (B-Rep) of the domain, involving the definition of a curve.

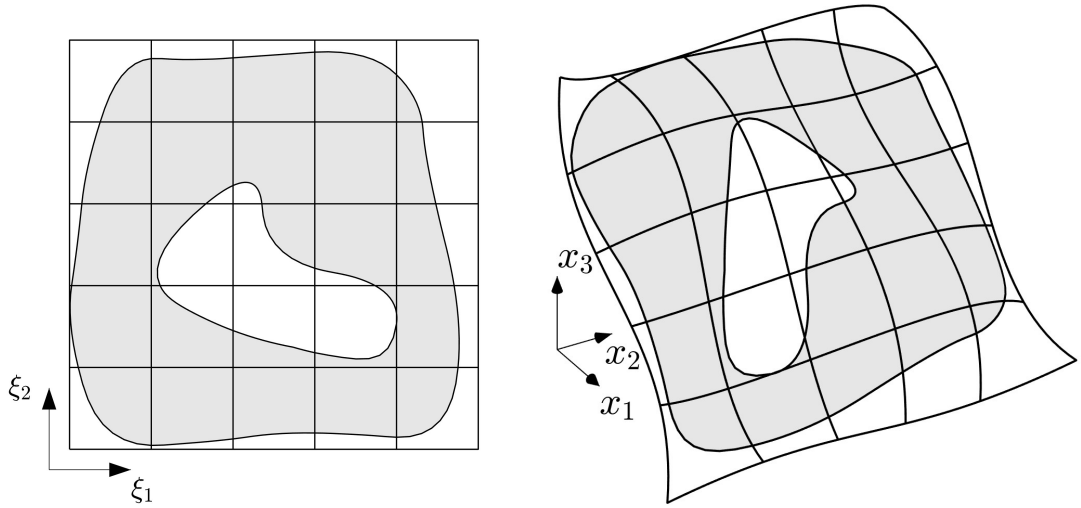

(a) (b)

Figure 2.1: Active (in grey) and non-active (in white) regions of the parametric (a) and physical (b) domains.

2.2.1 Implicitly-defined cut-outs

In this work, the level-set technique is exclusively employed in numerical applications to model cut-outs on the shell surface. However, the definitions presented in this section

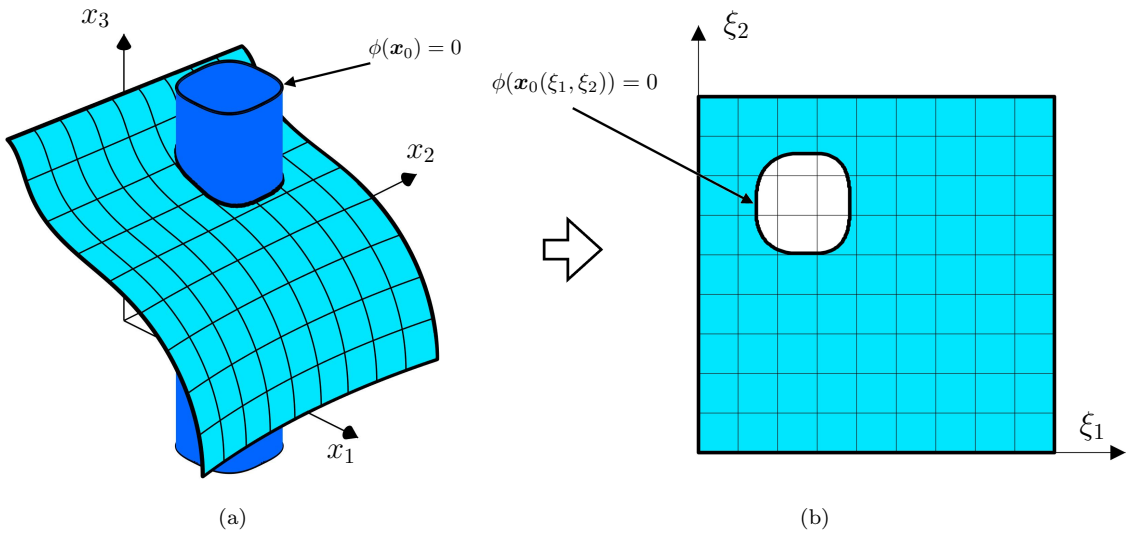

Figure 2.2: (a) Intersection between the zero-contour of the level-set function and the shell mid-surface in R3. (b) Shell reference domain $\hat{\Omega}$ implicitly defined by the level-set function of figure (a).

are also applicable to cases involving trimmed external boundaries. This approach begins with a level-set function, denoted as $\phi(\xi_1, \xi_2)$, whose sign determines whether a point with given curvilinear coordinates belongs to the active region of the surface. Typically, this level-set function is defined using an analytical formula, along with its partial derivatives with respect to the curvilinear coordinates. Consequently, the parametric domain $\hat{\Omega}$ for the shell with cut-outs is defined as

$$\hat{\Omega} = \left\{ (\xi_1, \xi_2) \in \hat{\Pi}_0 \mid \phi(\xi_1, \xi_2) < 0 \right\}, \tag{2.3}$$

while its boundary $\partial\hat{\Omega}$ is defined as

$$\partial\hat{\Omega} = \left\{ (\xi_1, \xi_2) \in \partial\hat{\Pi}_0 \mid \phi(\xi_1, \xi_2) < 0 \right\} \cup \partial\hat{\Omega}, \tag{2.4}$$

where $\partial\hat{\Omega} = \left\{ (\xi_1, \xi_2) \in \hat{\Pi}_0 |\ \phi(\xi_1, \xi_2) = 0 \right\}$ denotes the boundary of the cut-out. It is clear that, for a shell without cut-outs, $\hat{\Omega}$ and $\partial\hat{\Omega}$ coincide with $\hat{\Pi}_0$ and $\partial\hat{\Pi}_0$, respectively. Moreover, it is worth noting that the level-set function can also be defined in the Euclidean space as $\phi = \phi(\boldsymbol{x}_0)$ and then expressed in terms of the curvilinear coordinates using Eq.(2.1), i.e. $\phi = \phi(\boldsymbol{x}_0(\xi_1, \xi_2)) = \phi(\xi_1, \xi_2)$. Figure (2.2a) shows an example of a case where a cut-out is defined by intersecting a generally-curved surface with a level-set function $\phi = \phi(\boldsymbol{x}_0)$. The corresponding implicitly-defined reference domain $\hat{\Omega}$ is displayed in Fig.(2.2b).

The implicit mesh technique

The discretization of $\hat{\Omega}$ is obtained by intersecting a structured background grid and the level-set function $\phi = \phi(\xi_1, \xi_2)$. Let $\hat{\Pi}^e$ denote a generic cell of the background grid generated for the reference rectangle $\hat{\Pi}_0$ and $\partial\hat{\Pi}^e$ denote its boundary. Then, the domain $\hat{\Omega}^e$ and the boundary $\partial\hat{\Omega}^e$ of the corresponding implicitly-defined mesh element are defined as

$$\hat{\Omega}^e = \hat{\Pi}^e \cap \hat{\Omega}\ , \tag{2.5}$$

$$\partial\hat{\Omega}^e = (\partial\hat{\Pi}^e \cap \hat{\Omega}) \cup (\hat{\Pi}^e \cap \partial\hat{\Omega})\ . \tag{2.6}$$

It follows that the implicitly-defined elements are classified into the following groups:

i) the group of entire elements, which fall completely inside $\hat{\Omega}$;

ii) the group of empty elements, that fall completely outside $\hat{\Omega}$;

iii) the group of partial elements, which are cut by $\partial\hat{\Omega}$.

The domain and the boundary integrals appearing in the formulation presented here require suitable quadrature rules. For entire elements, which comprise the majority of the mesh elements, these integrals are evaluated using high-order tensor-product Gauss-Legendre quadrature rules. On the other hand, integration in the the domain and the boundary integrals over partial elements and element boundaries is not trivial. In this work, for domain defined using the level-set technique integrals are evaluated using the high-order quadrature rules obtained using the algorithm developed by Saye [116].

In brief, this algorithm determines a primary integration direction between ξ_1 and ξ_2 and generates integration points along this direction using the Gauss-Legendre scheme. For each of these integration points, it identifies the segment oriented in the orthogonal direction, intersecting the element's boundary (whether cut or not), through an iterative process relying on the level-set function. Integration points are then located along this segment. The algorithm outputs all integration points obtained in this manner, along with their weights calculated using a technique based on Gauss-Legendre quadrature rules. This approach, combined with a hierarchical decomposition of the element, ensures the application of high-order integration rules, even for complex cut geometries. Ultimately, as the algorithm identifies integration points and weights within the parametric domain, it is essential to consider the appropriate transformation of volume, surface, and line elements when performing integrations.

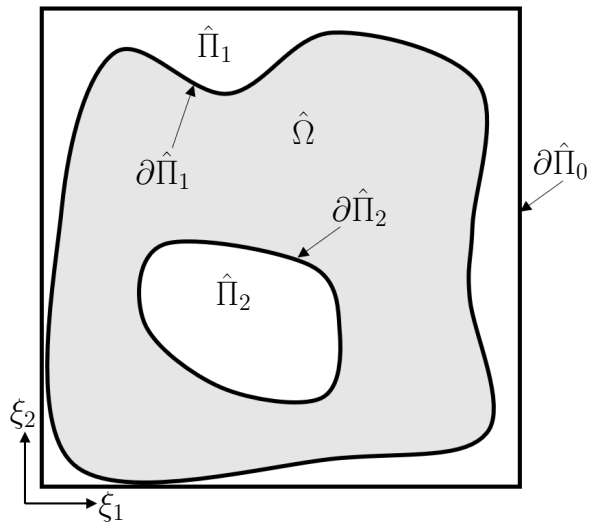

Figure 2.3: Example of a parametric domain defined through the Brep approach. The active region $\hat{\Pi}$ (in grey) is obtained through the trimming operation by removing $\hat{\Pi}_1$ and $\hat{\Pi}_2$ from the original uncut square domain.

2.2.2 Boundary representation of the domain

While the level-set technique is a powerful tool, its applicability is limited to cases where the domain can be expressed through a relatively simple level-set function. Describing the

generality of geometries of typical shell structures encountered in industrial applications using the level-set method would be a challenging task.

In CAD software, the standard approach for describing cut surfaces is the Boundary Representation technique (B-Rep). In this approach, the parametric domain is defined by specifying one or multiple closed trimming curves, typically splines, that explicitly identify its boundary. This approach is adopted for both external trimmed boundaries and internal cut-outs. Each of these curves is associated with a region of the domain to be trimmed, denoted as $\hat{\Pi}_i$, with its boundary $\partial\hat{\Pi}_i$ coinciding with the trimming curve itself. Given a set of trimming curves, the domain is defined as

$$\hat{\Omega} = \hat{\Pi}_0 \setminus \bigcup_{i=1}^{N_\Pi} \hat{\Pi}_i \ , \tag{2.7}$$

where N_Π is the number of regions of the domain to be cut. The boundary of the domain is defined as

$$\partial\hat{\Omega} = \bigcup_{i=0}^{N_\Pi} \partial\hat{\Pi}_i \setminus \bigcup_{i=1}^{N_\Pi} \hat{\Pi}_i \ . \tag{2.8}$$

Figure (2.3) shows a parametric domain defined using the Brep approach. The domain $\hat{\Omega}$ (in grey) is obtained trimming the regions $\hat{\Pi}_1$ and $\hat{\Pi}_2$ from the reference rectangular domain $\hat{\Pi}_0$.

One drawback of this approach is that trimming curves are typically defined in Euclidean space. Since, in general, the inverse of Eq.(2.1) does not have a closed-form solution, the trimming curves in the parametric domain are usually approximations, accurate up to a specific geometric tolerance. When dealing with the coupling of multiple surfaces defined by B-Rep, this can lead to non-watertight interfaces, meaning that the common edge between the two patches does not coincide perfectly.

Discretization and integration over partial elements

The discretization of $\hat{\Omega}$ is achieved in a similar manner as described in the context of the implicit mesh, starting with a background grid. The resulting elements are still categorized as entire, partial, or empty, following the same rules.

However, when dealing with a B-Rep defined domain, integrating over partial elements requires a different technique compared to the level-set approach. A robust and efficient algorithm based on higher-order reparameterization of trimmed elements as B-spline surfaces has recently been proposed in [129, 119]. In essence, this algorithm reparameterizes each partial element as a set of tiles, allowing standard Gauss-Lagrange quadrature to be applied in the parametric space of each tile.

This reparameterization process begins with the boundary of the partial element, using this information to determine its topology. Depending on the topology, various decomposition strategies can be applied, resulting in an appropriate number of tiles that best approximate the shape of the partial element. It is essential to note that the decomposition of partial elements into tiles is solely used to obtain the coordinates and weights for the integration points. From an analysis perspective, no new elements are created through this decomposition.

2.2.3 Strategies to address the ill-conditioning issue

Regardless of the strategy employed for defining the parametric domain, the presence of arbitrary cutting lines can lead to partial elements, some of which have very small areas, referred to as small elements. When the size difference between small elements and entire elements spans several orders of magnitude, it can result in the ill-conditioning of the final linear system, affecting the numerical stability of the solver.

To address this issue, as is customary in embedded approaches, strategies are needed to mitigate these effects. In this work, two different approaches are utilized:

i) Merging: small elements are merged with nearby entire elements or partial elements with a sufficiently large areas. Entire and partial elements used in the merging strategy are then referred to as extended elements. Figure (2.4a) shows the element classification when a 9×9 background grid is employed to initially subdivide the reference rectangle $\hat{\Pi}_0$, whereas Fig.(2.4b) shows the corresponding implicitly-defined mesh after the small elements have been merged with their neighbors. However, it is important to note that this approach can alter the number and shape of elements and requires additional implementation effort.

ii) Preconditioning: Small elements are kept unchanged, but a diagonal Jacobi preconditioner [130] is applied to the final stiffness matrix. This approach is particularly easy to implement and has demonstrated remarkable effectiveness despite its simplicity.

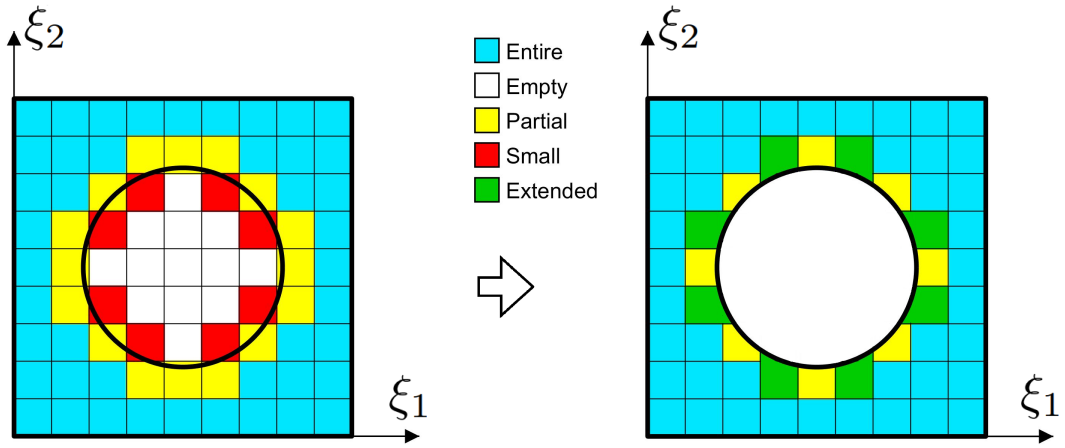

(a) (b)

Figure 2.4: (a) Cell classification according to their area. (b) Resulting implicitly defined mesh after the cell-merging strategy.

2.3 Differential geometry

Starting from the map in Eq.(2.1), the local covariant basis on the shell mid-surface is defined as

$$\boldsymbol{a}_\alpha = \boldsymbol{x}_{0,\alpha}(\xi_1, \xi_2) \ . \tag{2.9}$$

Here, the comma preceding one or more Greek indices indicates a series of coordinate derivatives in the specified sequence of curvilinear directions. It is important to note

that the vectors of the covariant basis are tangential to the lines of constant curvilinear coordinates and, therefore, lie on the plane that is locally tangent to the surface. The unit normal vector $\boldsymbol{a}_3$, orthogonal to the shell mid-surface is computed as

$$\boldsymbol{a}_3(\xi_1, \xi_2) = \frac{\boldsymbol{a}_1 \times \boldsymbol{a}_2}{|\boldsymbol{a}_1 \times \boldsymbol{a}_2|}, \tag{2.10}$$

where $|\bullet|$ is the standard Euclidean norm. It is worth noting that this definition ensures the local orthogonality between vector $\boldsymbol{a}_3$ and the surface Ω through the cross product in the numerator, while the presence of $|\boldsymbol{a}_1 \times \boldsymbol{a}_2|$ in the denominator ensures that the resulting vector has a unit length.

Together with Eq.(2.1) and the additional curvilinear variable ξ_3, Eq.(2.10) is used to define the map of the shell volume as

$$\boldsymbol{x}(\xi_1, \xi_2, \xi_3) = \boldsymbol{x}_0(\xi_1, \xi_2) + \xi_3 \boldsymbol{a}_3(\xi_1, \xi_2), \quad \text{for } (\xi_1, \xi_2, \xi_3) \in \hat{V}, \tag{2.11}$$

where $\hat{V} = \hat{\Omega} \times \hat{I}_3$ is the parametric volume of the shell, $\hat{I}_3 = [-\tau/2, \tau/2]$ is the interval spanned by ξ_3, and τ denotes the thickness of the shell assumed uniform over the whole mid-surface. The volume of the shell is therefore the image of the map in Eq.(2.11) and is denoted as V, while its boundary is ∂V

2.3.1 Differential geometry of the shell mid-surface

The covariant components of the surface metric tensor are defined as $a_{\alpha\beta} = \boldsymbol{a}_\alpha \cdot \boldsymbol{a}_\beta$, where $\cdot$ denotes the dot product. The determinant of the surface metric tensor is denoted as a. The contravariant components of the surface metric tensor are obtained from the covariant components as

$$[a^{\alpha\beta}] = [a_{\alpha\beta}]^{-1} \tag{2.12}$$

and allow us to compute the contravariant basis vectors as

$$\boldsymbol{a}^\alpha = a^{\alpha\beta} \boldsymbol{a}_\beta \ , \tag{2.13}$$

that satisfy the property $\boldsymbol{a}_\alpha \cdot \boldsymbol{a}^\beta = \delta_\alpha^\beta$, where δ_α^β represents the Kronecker delta. Additionally, it is introduces the covariant components and the mixed components of the surface curvature tensor, defined respectively as

$$b_{\alpha\beta} = \boldsymbol{a}_3 \cdot \boldsymbol{a}_{\alpha,\beta} \ , \tag{2.14a}$$

$$b_\beta^\alpha = a^{\alpha\gamma} b_{\gamma\beta} \ . \tag{2.14b}$$

Finally, $\Gamma_{\alpha\beta}^\gamma$ represents the Christoffel symbols of the second kind which are defined as

$$\Gamma_{\alpha\beta}^\gamma = \boldsymbol{a}^\gamma \cdot \boldsymbol{a}_{\alpha,\beta} \ . \tag{2.15}$$

In this thesis, it is adopted the convention of indicating covariant coordinates referring to the contravariant basis with upper indices, as in v^α, and contravariant coordinates referring to the covariant basis with lower indices, as in v_α. However, the use of subscripts and superscripts strictly follows the lower and upper indices notation only when differentiation between covariant and contravariant coordinates is necessary; in all other cases, standard subscripts are used.

Furthermore, the notation $v_{\alpha|\beta}$ denotes the covariant derivative of the α-th component of the generic vector $\boldsymbol{v}$ along the direction β. This notation is extended to tensors as well, where $\tau_{\alpha\beta|\gamma}$ represents the covariant derivative of the $\alpha\beta$ component of the generic tensor $\boldsymbol{\tau}$ with respect to the γ direction.

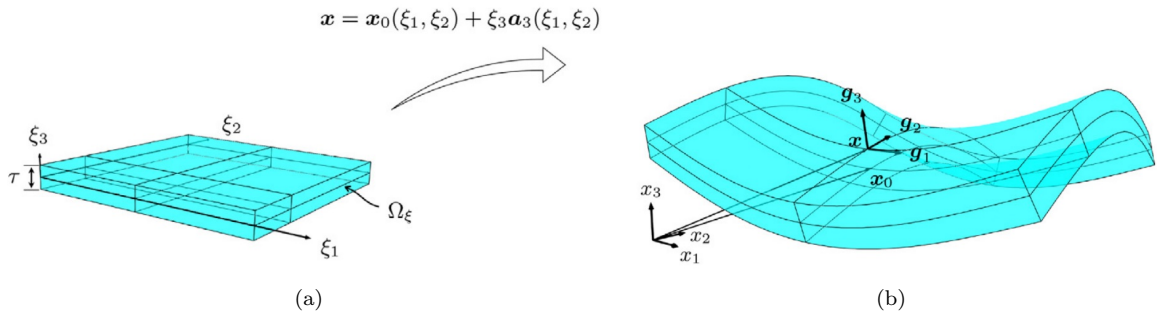

Figure 2.5: (a) Parametric volume space spanned by the curvilinear coordinates $\{\xi_1, \xi_2, \xi_3\}$. (b) Sample mapped geometry showing the covariant basis at the generic point in the shell volume.

2.3.2 Differential geometry of the shell volume

By differentiating the map given in Eq.(2.11) with respect to the curvilinear coordinates, it is possible to introduce:

i) The associated covariant basis, whose vectors are

$$\boldsymbol{g}_i = \boldsymbol{x}_{,i} \ , \tag{2.16}$$

ii) the corresponding covariant and contravariant components of the metric tensor, which are computed as

$$g_{ij} = \boldsymbol{g}_i \cdot \boldsymbol{g}_j \ , \tag{2.17}$$
$$[g^{ij}] = [g_{ij}]^{-1} \ , \tag{2.18}$$

iii) the contravariant basis, whose vectors $\boldsymbol{g}^i$ are defined by

$$\boldsymbol{g}_i = g^{ij} \boldsymbol{g}_j \tag{2.19}$$

and satisfy the property $\boldsymbol{g}^i \cdot \boldsymbol{g}_j = \delta^i_j$.

Here, it is adopted the notation that a subscript with a comma followed by a Latin index indicates the derivative of the vector with respect to the correspondent Cartesian coordinate.

A schematic representation of the parametric volume space spanned by the coordinates $\{\xi_1, \xi_2, \xi_3\}$ is shown in Fig.(2.5a), whereas a sample mapped geometry and the vectors of the associated covariant basis at a point $\boldsymbol{x} \in V$ are shown in Fig.(2.5b). Eventually, given the map (2.11), the following relations hold [113]

$$\mathrm{d}V = \sqrt{g} \ \mathrm{d}\hat{V} \ , \tag{2.20}$$
$$\mathrm{d}\Omega = \sqrt{g}\sqrt{n_i g^{ij} n_j} \ \mathrm{d}\hat{\Omega} \ , \tag{2.21}$$

where $\mathrm{d}V$ is the Cartesian volume element, $\mathrm{d}\Omega$ is the Cartesian surface element, $\mathrm{d}\hat{V}$ is the parametric volume element, $\mathrm{d}\hat{\Omega}$ is the parametric surface element, $g = \det(g_{ij})$ and n_i is the i-th Cartesian components of the outer unit normal at $\boldsymbol{x} \in \partial V$. Moreover, the relationship between the Cartesian components of a generic vector and its covariant components collected in the 3×1 vectors $\boldsymbol{v}$ and $\boldsymbol{v}_\xi$, respectively, can be written using the following matrix notation

$$\boldsymbol{v} = \boldsymbol{R}\boldsymbol{v}_\xi, \tag{2.22}$$

where $\boldsymbol{R}$ is a 3×3 transformation matrix whose i-th column coincides with $\boldsymbol{g}^i$.

2.4 Fundamentals of the theory of elasticity

Let's consider that when external loads are applied to the structure, whether on its volume or external surfaces, the initially undeformed geometry, referred to as the reference configuration, undergoes a transformation into the deformed geometry known as the actual configuration. Each material point within the volume V changes its position in accordance with the displacement map $\boldsymbol{u}(\xi_1, \xi_2)$, and this relationship is expressed as

$$\boldsymbol{X}(\xi_1, \xi_2) = \boldsymbol{x}(\xi_1, \xi_2) + \boldsymbol{u}(\xi_1, \xi_2) \ , \tag{2.23}$$

where $\boldsymbol{X}(\xi_1, \xi_2)$ maps from the parametric volume to the actual shell configuration. The convention employed here uses uppercase letters to denote quantities associated with the actual configuration and lowercase letters for quantities related to the reference configuration.

2.4.1 Strain measures

In the context of structural mechanics, a generic differential line $\mathrm{d}\boldsymbol{x}$ in the reference configuration undergoes deformation and becomes the differential line $\mathrm{d}\boldsymbol{X}$ in the actual configuration. This transformation is established through the use of the deformation gradient $\boldsymbol{F}$, represented as

$$\mathrm{d}\boldsymbol{X} = \boldsymbol{F} \ \mathrm{d}\boldsymbol{x} \ . \tag{2.24}$$

The deformation gradient is expressed as

$$\boldsymbol{F} = \nabla_x \boldsymbol{X} = \boldsymbol{I} + \nabla_x \boldsymbol{u} \ , \tag{2.25}$$

where $\boldsymbol{I}$ represents the identity tensor, and ∇_x is the standard gradient operator in Cartesian coordinates. An alternative expression for the deformation gradient, which is based on the covariant basis in the actual configuration and the contravariant basis in the reference configuration, is given as

$$\boldsymbol{F} = \boldsymbol{G}_i \otimes \boldsymbol{g}^i \ , \tag{2.26}$$

where $\boldsymbol{G}_i = \boldsymbol{X}_{,i}$ represents the i-th covariant base vector in the actual configuration, and the $\otimes$ operator denotes the tensor product.

In the context of finite displacement elasticity, various measures of strain can be employed to formulate the non-linear governing equations. In this work, the Green-Lagrange strain tensor is adopted and defined as

$$\boldsymbol{\gamma} = \frac{1}{2}(\boldsymbol{F}^\intercal \boldsymbol{F} - \boldsymbol{I}) \ , \tag{2.27}$$

where the definition of $\boldsymbol{F}$ to express the strain tensor depends on the chosen approach.

Strain tensor in Cartesian components and Voigt notation

For higher-order shell theories derived from fundamental three-dimensional principles, it has been found advantageous to begin with Eq.(2.25) for defining the Green-Lagrange strain. The Green-Lagrange strain tensor, rearranged in accordance with Voigt notation, is expressed as follows

$$\boldsymbol{\gamma} = \{\gamma_{11} \ \gamma_{22} \ \gamma_{33} \ \gamma_{23} \ \gamma_{13} \ \gamma_{12} \ \}^\intercal \ , \tag{2.28}$$

where the mixed components of the strain tensor in Voigt notation are twice the corresponding ones in tensor notation. In Voigt notation, Eq.(2.27) is equivalent to

$$\boldsymbol{\gamma} = \left(\boldsymbol{I}_i + \frac{1}{2} \boldsymbol{W}_i \right) \boldsymbol{u}_{,i} \tag{2.29}$$

where auxiliary matrices are introduced as follows

$$\boldsymbol{I}_1 = \begin{bmatrix} 1 & 0 & 0 \\ 0 & 0 & 0 \\ 0 & 0 & 0 \\ 0 & 0 & 0 \\ 0 & 0 & 1 \\ 0 & 1 & 0 \end{bmatrix}, \quad \boldsymbol{I}_2 = \begin{bmatrix} 0 & 0 & 0 \\ 0 & 1 & 0 \\ 0 & 0 & 0 \\ 0 & 0 & 1 \\ 0 & 0 & 0 \\ 1 & 0 & 0 \end{bmatrix}, \quad \boldsymbol{I}_3 = \begin{bmatrix} 0 & 0 & 0 \\ 0 & 0 & 0 \\ 0 & 0 & 1 \\ 0 & 1 & 0 \\ 1 & 0 & 0 \\ 0 & 0 & 0 \end{bmatrix}, \tag{2.30a}$$

$$\boldsymbol{W}_1 = \begin{bmatrix} u_{1,1} & u_{2,1} & u_{3,1} \\ 0 & 0 & 0 \\ 0 & 0 & 0 \\ 0 & 0 & 0 \\ u_{1,3} & u_{2,3} & u_{3,3} \\ u_{1,2} & u_{2,2} & u_{3,2} \end{bmatrix}, \quad \boldsymbol{W}_2 = \begin{bmatrix} 0 & 0 & 0 \\ u_{1,2} & u_{2,2} & u_{3,2} \\ 0 & 0 & 0 \\ u_{1,3} & u_{2,3} & u_{3,3} \\ 0 & 0 & 0 \\ u_{1,1} & u_{2,1} & u_{3,1} \end{bmatrix}, \quad \boldsymbol{W}_3 = \begin{bmatrix} 0 & 0 & 0 \\ 0 & 0 & 0 \\ u_{1,3} & u_{2,3} & u_{3,3} \\ u_{1,2} & u_{2,2} & u_{3,2} \\ u_{1,1} & u_{2,1} & u_{3,1} \\ 0 & 0 & 0 \end{bmatrix}, \tag{2.30b}$$

where the derivatives expressed using comma notation refer to Cartesian coordinates. The matrix definitions in Eq.(2.30) account for all the nonlinear terms arising in the strain tensor definition, extending the notation introduced in [61] to the finite displacement regime. It is important to note that additional assumptions in the definition of nonlinear strain, such as the von Kármán approximation for plates, can be incorporated by suitably modifying the matrices $\boldsymbol{W}_i$. A discussion regarding the effect of different definitions of the strain tensor, along with recommendations regarding which definition to use and when, can be found in [131].

Furthermore, to obtain the linear strain in the small displacements regime, linearizing around the condition $\boldsymbol{u} = \boldsymbol{0}$ in Eq.(2.29) involves neglecting the terms $\boldsymbol{W}_i$. In this case, the definition is modified as

$$\boldsymbol{\gamma} = \boldsymbol{I}_i \boldsymbol{u}_{,i} \, , \tag{2.31}$$

which coincides with the expression proposed in [61].

Strain tensor in covariant components

In the context of the Kirchhoff-Love shell theory, the conventional approach involves utilizing Eq.(2.26) to describe the strain tensor. This choice, when substituted into Eq.(2.27), yields the following expression

$$\boldsymbol{\gamma} = \frac{1}{2}((\boldsymbol{g}^i \otimes \boldsymbol{G}_i) \times (\boldsymbol{G}_j \otimes \boldsymbol{g}^j) - g_{ij} \boldsymbol{G}^i \otimes \boldsymbol{G}^j) = \frac{1}{2}(G_{ij} - g_{ij}) \boldsymbol{G}^i \otimes \boldsymbol{G}^j \, . \tag{2.32}$$

This formulation enables the computation of the covariant components of the Green-Lagrange strain tensor as

$$\gamma_{ij} = \frac{1}{2}(G_{ij} - g_{ij}) \, , \tag{2.33}$$

where γ_{ij} represents the ij-th covariant component referred to the contravariant basis tensor $\boldsymbol{G}^i \otimes \boldsymbol{G}^j$, which is entirely expressed in the reference configuration

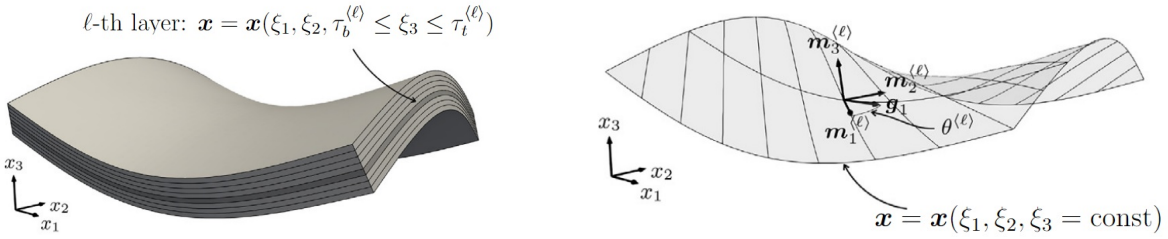

(a) (b)

Figure 2.6: (a) Schematic representation of a multilayered shell where the generic ℓ-th layer is shown in darker color. (b) Fibers orientation at a slice $\boldsymbol{x} = \boldsymbol{x}(\xi_1, \xi_2, \xi_3 = \text{const})$ of the ℓ-th lamina.

2.4.2 Laminate layout and constitutive behaviour

It is assumed here that the shell is a laminate built by stacking N_ℓ fiber-reinforced layers, which are modeled as homogeneous and orthotropic and perfectly bonded at their interfaces. A quantity referring to the ℓ-th layer is denoted by a superscript $\langle\ell\rangle$; as such, the volume occupied by the ℓ-th layer is denoted by $V^{\langle\ell\rangle}$, its boundary by $\partial V^{\langle\ell\rangle}$ and its fiber deposition angle by $\theta^{\langle\ell\rangle}$. Each layer has uniform thickness $\tau^{\langle\ell\rangle}$ and thus the thickness of the whole laminate is

$$\tau = \sum_{\ell=1}^{N_\ell} \tau^{\langle\ell\rangle} \ . \tag{2.34}$$

The volume of the shell $V \subset \mathbb{R}^3$ is obtained as $V = \cup_{\ell=1}^{N_\ell} V^{\langle\ell\rangle}$. The layers are stacked in such a way that they follow the curvature of the shell surface as shown in Fig.(2.6a). More specifically, given the coordinates $\tau_b^{\langle\ell\rangle}$ and $\tau_t^{\langle\ell\rangle} = \tau_b^{\langle\ell\rangle} + \tau^{\langle\ell\rangle}$ of the ℓ-th layer's bottom and top reference surfaces, respectively, the volume $V^{\langle\ell\rangle}$ of the layer is assumed to coincide with the points $\boldsymbol{x} = \boldsymbol{x}(\xi_1, \xi_2, \xi_3 \in \hat{I}_3^{\langle\ell\rangle})$, being $\hat{I}_3^{\langle\ell\rangle} = [\tau_b^{\langle\ell\rangle}, \tau_t^{\langle\ell\rangle}]$.

At each point $\boldsymbol{x}$ of the layer's volume $V^{\langle\ell\rangle}$, it is possible to introduce the material local reference system identified by the unit vectors $\boldsymbol{m}_1^{\langle\ell\rangle}$, $\boldsymbol{m}_2^{\langle\ell\rangle}$ and $\boldsymbol{m}_3^{\langle\ell\rangle}$, which are defined as

$$\boldsymbol{m}_3^{\langle\ell\rangle} = \boldsymbol{a}_3 \ , \tag{2.35}$$

$$\boldsymbol{m}_1^{\langle\ell\rangle} = \boldsymbol{R}_{\boldsymbol{a}_3}\left(\theta^{\langle\ell\rangle}\right) \frac{\boldsymbol{g}_1}{|\boldsymbol{g}_1|} \ , \tag{2.36}$$

$$\boldsymbol{m}_2^{\langle\ell\rangle} = \boldsymbol{m}_3^{\langle\ell\rangle} \times \boldsymbol{m}_1^{\langle\ell\rangle} \ , \tag{2.37}$$

where $\boldsymbol{R}_{\boldsymbol{a}_3}$ is a matrix that performs a rotation of the angle $\theta^{\langle\ell\rangle}$ around the axis $\boldsymbol{a}_3$, being $\theta^{\langle\ell\rangle}$ the orientation associated to the fibers of ℓ-th lamina. It is worth noting that for general curvilinear coordinates, the vectors $\boldsymbol{m}_1^{\langle\ell\rangle}$, $\boldsymbol{m}_2^{\langle\ell\rangle}$ and $\boldsymbol{m}_3^{\langle\ell\rangle}$ not only are different from layer to layer but they continuously vary within each layer according to the definition given in Eq.(2.35). Additionally, the superscript $\langle\ell\rangle$ might be superfluous for the vector $\boldsymbol{m}_3^{\langle\ell\rangle}$ because $\boldsymbol{m}_3^{\langle\ell\rangle}$ does not explicitly depend on $\theta^{\langle\ell\rangle}$; however, the present notation has been used for the sake of consistency. As an example, Fig.(2.6b) shows the material reference system and the angle between the vector $\boldsymbol{g}_1$ and the unit vector $\boldsymbol{m}_1^{\langle\ell\rangle}$ that describes the fibers orientation for a slice $\boldsymbol{x} = \boldsymbol{x}(\xi_1, \xi_2, \xi_3 = \text{const})$ of the ℓ-th lamina.

It is assumed that each layer obeys a generalized Hooke's law, meaning that a linear relationship between the second Piola–Kirchhoff stress tensor and the Green–Lagrange strain tensor holds. In the reference system identified by $\boldsymbol{m}_1^{\langle\ell\rangle}$, $\boldsymbol{m}_2^{\langle\ell\rangle}$ and $\boldsymbol{m}_3^{\langle\ell\rangle}$, the material is governed by the constitutive relationship

$$\tilde{\boldsymbol{\sigma}}^{\langle\ell\rangle} = \tilde{\boldsymbol{c}}^{\langle\ell\rangle} \tilde{\boldsymbol{\gamma}}^{\langle\ell\rangle}, \tag{2.38}$$

where $\tilde{\boldsymbol{\gamma}}^{\langle\ell\rangle}$ and $\tilde{\boldsymbol{\sigma}}^{\langle\ell\rangle}$ collects the strain and stress components in the local material reference system according to the Voigt notation and $\tilde{\boldsymbol{c}}^{\langle\ell\rangle}$ is the 6×6 stiffness matrix of the corresponding elastic coefficients, which are typically given in terms of Young's moduli $E_1^{\langle\ell\rangle}$, $E_2^{\langle\ell\rangle}$ and $E_3^{\langle\ell\rangle}$, shear moduli $G_{12}^{\langle\ell\rangle}$, $G_{13}^{\langle\ell\rangle}$ and $G_{23}^{\langle\ell\rangle}$ and Poisson's ratios $\nu_{12}^{\langle\ell\rangle}$, $\nu_{13}^{\langle\ell\rangle}$ and $\nu_{23}^{\langle\ell\rangle}$ [1]. Provided this quantities, the stiffness matrix is constructed as

$$\tilde{\boldsymbol{c}}^{\langle\ell\rangle} = \begin{bmatrix} 1/E_1^{\langle\ell\rangle} & -\nu_{21}^{\langle\ell\rangle}/E_2^{\langle\ell\rangle} & -\nu_{31}^{\langle\ell\rangle}/E_3^{\langle\ell\rangle} & 0 & 0 & 0 \\ -\nu_{12}^{\langle\ell\rangle}/E_1^{\langle\ell\rangle} & 1/E_2^{\langle\ell\rangle} & -\nu_{32}^{\langle\ell\rangle}/E_3^{\langle\ell\rangle} & 0 & 0 & 0 \\ -\nu_{13}^{\langle\ell\rangle}/E_1^{\langle\ell\rangle} & -\nu_{23}^{\langle\ell\rangle}/E_2^{\langle\ell\rangle} & 1/E_3^{\langle\ell\rangle} & 0 & 0 & 0 \\ 0 & 0 & 0 & 1/G_{23}^{\langle\ell\rangle} & 0 & 0 \\ 0 & 0 & 0 & 0 & 1/G_{31}^{\langle\ell\rangle} & 0 \\ 0 & 0 & 0 & 0 & 0 & 1/G_{12}^{\langle\ell\rangle} \end{bmatrix}^{-1} . \tag{2.39}$$

Constitutive matrix in Cartesian reference system

The constitutive matrix $\boldsymbol{c}^{\langle\ell\rangle}$ expressed in the Cartesian reference system is deduced applying the 4-th rank tensor transformation of axes formulas [132] to $\tilde{\boldsymbol{c}}^{\langle\ell\rangle}$ obtaining

$$\boldsymbol{\sigma}^{\langle\ell\rangle} = \boldsymbol{T}\ \tilde{\boldsymbol{c}}^{\langle\ell\rangle}\boldsymbol{T}^{\intercal}\boldsymbol{\gamma}^{\langle\ell\rangle} = \boldsymbol{c}^{\langle\ell\rangle}\boldsymbol{\gamma}^{\langle\ell\rangle} , \tag{2.40}$$

where $\boldsymbol{\sigma}^{\langle\ell\rangle} = \{\sigma_{11}^{\langle\ell\rangle}\ \sigma_{22}^{\langle\ell\rangle}\ \sigma_{33}^{\langle\ell\rangle}\ \sigma_{23}^{\langle\ell\rangle}\ \ \sigma_{13}^{\langle\ell\rangle}\ \sigma_{12}^{\langle\ell\rangle}\}^{\intercal}$ and $\boldsymbol{\gamma}^{\langle\ell\rangle} = \{\gamma_{11}^{\langle\ell\rangle}\ \gamma_{22}^{\langle\ell\rangle}\ \gamma_{33}^{\langle\ell\rangle}\ \gamma_{23}^{\langle\ell\rangle}\ \ \gamma_{13}^{\langle\ell\rangle}\ \gamma_{12}^{\langle\ell\rangle}\}^{\intercal}$ are the vectors of the stress and strain components, respectively, in the Cartesian reference system and the transformation matrix $\boldsymbol{T}$ is defined as

$$\boldsymbol{T} = \begin{bmatrix} \lambda_{11}^2 & \lambda_{12}^2 & \lambda_{13}^2 & 2\lambda_{12}\lambda_{13} & 2\lambda_{11}\lambda_{13} & 2\lambda_{11}\lambda_{12} \\ \lambda_{21}^2 & \lambda_{22}^2 & \lambda_{23}^2 & 2\lambda_{22}\lambda_{23} & 2\lambda_{21}\lambda_{23} & 2\lambda_{21}\lambda_{22} \\ \lambda_{31}^2 & \lambda_{32}^2 & \lambda_{33}^2 & 2\lambda_{32}\lambda_{33} & 2\lambda_{31}\lambda_{33} & 2\lambda_{31}\lambda_{32} \\ \lambda_{21}\lambda_{31} & \lambda_{22}\lambda_{32} & \lambda_{23}\lambda_{33} & \lambda_{22}\lambda_{33}+\lambda_{23}\lambda_{32} & \lambda_{21}\lambda_{33}+\lambda_{23}\lambda_{31} & \lambda_{21}\lambda_{32}+\lambda_{22}\lambda_{31} \\ \lambda_{11}\lambda_{31} & \lambda_{12}\lambda_{32} & \lambda_{13}\lambda_{33} & \lambda_{12}\lambda_{33}+\lambda_{13}\lambda_{32} & \lambda_{11}\lambda_{33}+\lambda_{13}\lambda_{31} & \lambda_{11}\lambda_{32}+\lambda_{12}\lambda_{31} \\ \lambda_{11}\lambda_{21} & \lambda_{12}\lambda_{22} & \lambda_{13}\lambda_{23} & \lambda_{12}\lambda_{23}+\lambda_{13}\lambda_{22} & \lambda_{11}\lambda_{23}+\lambda_{13}\lambda_{21} & \lambda_{11}\lambda_{22}+\lambda_{12}\lambda_{21} \end{bmatrix} , \tag{2.41}$$

where λ_{ij} is the directional cosine of $\boldsymbol{m}_i$ on $\boldsymbol{e}_j$.

Reduced constitutive matrix in an auxiliary local orthonormal reference system

For the Kirchhoff-Love shell theory, the out-of-plane stress components are neglected, leading to the consideration of a reduced stiffness matrix. This matrix is obtained by eliminating the rows and columns corresponding to the out-of-plane components, resulting in the following form

$$\tilde{\boldsymbol{c}}_R^{\langle\ell\rangle} = \begin{bmatrix} 1/E_1^{\langle\ell\rangle} & -\nu_{12}^{\langle\ell\rangle}/E_1^{\langle\ell\rangle} & 0 \\ -\nu_{21}^{\langle\ell\rangle}/E_2^{\langle\ell\rangle} & 1/E_2^{\langle\ell\rangle} & 0 \\ 0 & 0 & 1/G_{12}^{\langle\ell\rangle} \end{bmatrix}^{-1} . \tag{2.42}$$

This reduced stiffness matrix is then transformed into an auxiliary local orthonormal reference system $\boldsymbol{n}_1$ and $\boldsymbol{n}_2$, which are common for each layer and constructed from the

local curvilinear bases of the shell mid-surface

$$\boldsymbol{n}_1 = \frac{\boldsymbol{a}_1}{|\boldsymbol{a}_1|} \,, \tag{2.43a}$$

$$\boldsymbol{n}_2 = \frac{\boldsymbol{a}^2}{|\boldsymbol{a}^2|} \,. \tag{2.43b}$$

The rotation is carried out using the equation

$$\overline{\boldsymbol{c}}_R^{\langle \ell \rangle} = \boldsymbol{T}_R \tilde{\boldsymbol{c}}_R^{\langle \ell \rangle} \boldsymbol{T}_R^{\mathsf{T}} \,, \tag{2.44}$$

where the rotation matrix $\boldsymbol{T}_R$ is defined as

$$\boldsymbol{T}_R = \begin{bmatrix} \cos^2\theta^{\langle \ell \rangle} & \sin^2\theta^{\langle \ell \rangle} & -2\sin\theta^{\langle \ell \rangle}\cos\theta \\ \sin^2\theta^{\langle \ell \rangle} & \cos^2\theta^{\langle \ell \rangle} & 2\sin\theta^{\langle \ell \rangle}\cos\theta^{\langle \ell \rangle} \\ \sin\theta^{\langle \ell \rangle}\cos\theta^{\langle \ell \rangle} & -\sin\theta^{\langle \ell \rangle}\cos\theta^{\langle \ell \rangle} & \cos^2\theta^{\langle \ell \rangle} - \sin^2\theta^{\langle \ell \rangle} \end{bmatrix} \,. \tag{2.45}$$

2.4.3 Three-dimensional formulations for mechanical problems

To develop two-dimensional formulations that accurately model the typical mechanical behaviors of shell structures, the approach pursued in this thesis for higher-order theories begins with a three-dimensional formulation. The two-dimensional version can then be derived by introducing the kinematic hypothesis specific to the theory in question. The three-dimensional theories are expressed in their weak form, which is represented by the principle of virtual displacements (PVD) that expresses an energy balance between the virtual work of the internal forces and the external forces.

In this section, it is specified the weak form of the three-dimensional governing equations for a multi-layered solid for various types of analyses, including nonlinear and linear static analyses, buckling analyses, transient analyses, and free vibration analyses. These variational statements are briefly discussed in the reminder of this section and summarized in Tab.(2.1).

Static analysis

The static analysis aims to determine the equilibrium configuration of a structure subjected to external loads and constrained by specific boundary conditions. In the context of this problem, the PVD is formulated as follows

$$\sum_{\ell=1}^{N_\ell} \int_{V^{\langle \ell \rangle}} \delta\boldsymbol{\gamma}^{\langle \ell \rangle \mathsf{T}} \boldsymbol{\sigma}^{\langle \ell \rangle} \mathrm{d}V = \sum_{\ell=1}^{N_\ell} \int_{V^{\langle \ell \rangle}} \delta\boldsymbol{u}^{\langle \ell \rangle \mathsf{T}} \overline{\boldsymbol{b}}^{\langle \ell \rangle} \, \mathrm{d}V + \sum_{\ell=1}^{N_\ell} \int_{\partial V^{\langle \ell \rangle}} \delta\boldsymbol{u}^{\langle \ell \rangle \mathsf{T}} \overline{\boldsymbol{t}}^{\langle \ell \rangle} \, \mathrm{d}\partial V \,, \tag{2.46}$$

where, $\overline{\boldsymbol{b}}^{\langle \ell \rangle}$ represents a vector containing the Cartesian components of the prescribed volume forces acting within the volume of the ℓ-th layer, and $\overline{\boldsymbol{t}}^{\langle \ell \rangle}$ is a vector containing the Cartesian components of the prescribed tractions applied to the surface of the ℓ-th layer

It is important to note that Eq.(2.46) remains the same whether a linear or nonlinear expression for the strain is considered. However, the nonlinear formulation results in a nonlinear algebraic system that requires an iterative scheme for solving.

Linear buckling analysis

A similar derivation to the one presented in the preceding section can be followed to derive the variational statement for the linear buckling problem. The formulation for the linear buckling analysis begins with a distribution of internal stresses, referred to as pre-stress, typically obtained from a previous linear static analysis. Since the static analysis is linear, the pre-stress scales linearly with a loading factor, denoted as λ. The linear buckling problem seeks to find adjacent configurations, existing for some certain values of λ, that are very close to the initial equilibrium state, allowing the quantities involved to be linearized with respect to the adjacent displacement.

The adjacent configuration must satisfy the condition where the virtual work of the adjacent stress with the adjacent strain is equal and opposite to the virtual work of the pre-stress with the adjacent strain. When this condition is met, the critical buckling instability occurs, and the structure may undergo sudden changes in shape without the need for an increase in external forces.

The three-dimensional variational statement of Eulerian buckling, specified for a multi-layered solid, is expressed as follows

$$\sum_{\ell=1}^{N_\ell} \int_{V^{\langle\ell\rangle}} \delta\boldsymbol{\gamma}^{\langle\ell\rangle\intercal}\boldsymbol{\sigma}^{\langle\ell\rangle}\mathrm{d}V = -\lambda \sum_{\ell=1}^{N_\ell} \int_{V^{\langle\ell\rangle}} \overline{\sigma}_{ij}^{\langle\ell\rangle}\delta\boldsymbol{u}_{,i}^{\langle\ell\rangle\intercal}\boldsymbol{u}_{,j}^{\langle\ell\rangle}\mathrm{d}V \ , \tag{2.47}$$

where the derivatives with the comma notation refer to the Cartesian coordinates, $\overline{\sigma}_{ij}^{\langle\ell\rangle}$ is the ij-th component of the initial stress field, the vectors $\boldsymbol{u}^{\langle\ell\rangle}$, $\boldsymbol{\gamma}^{\langle\ell\rangle}$ and $\boldsymbol{\sigma}^{\langle\ell\rangle}$ are the displacement, strain and stress fields, respectively, of the additional adjacent equilibrium configuration, and λ is the eigenvalue of the buckling problem. Note that the vectors $\boldsymbol{u}^{\langle\ell\rangle}$, $\boldsymbol{\gamma}^{\langle\ell\rangle}$ and $\boldsymbol{\sigma}^{\langle\ell\rangle}$ represent the eigenfunction associated with the eigenvector λ and have a different meaning than the vectors appearing in Eq.(2.46). Eventually, the smallest value of λ represents the critical multiplicative factor to be applied to the external loads in order for the structure to buckle.

Linear transient analysis

The governing equations for the transient analysis of a multilayered shell are derived from the weak form of the elasto-dynamic problem for a three-dimensional structure consisting of N_ℓ layers. The three-dimensional weak form is expressed as

$$\sum_{\ell=1}^{N_\ell} \int_{V^{\langle\ell\rangle}} \left(\delta\boldsymbol{u}^{\langle\ell\rangle\intercal}\rho^{\langle\ell\rangle}\ddot{\boldsymbol{u}}^{\langle\ell\rangle} + \delta\boldsymbol{\gamma}^{\langle\ell\rangle\intercal}\boldsymbol{\sigma}^{\langle\ell\rangle}\right)\mathrm{d}V = \sum_{\ell=1}^{N_\ell} \int_{V^{\langle\ell\rangle}} \delta\boldsymbol{u}^{\langle\ell\rangle\intercal}\overline{\boldsymbol{b}}^{\langle\ell\rangle}\mathrm{d}V + \sum_{\ell=1}^{N_\ell} \int_{\partial V^{\langle\ell\rangle}} \delta\boldsymbol{u}^{\langle\ell\rangle\intercal}\overline{\boldsymbol{t}}^{\langle\ell\rangle}\mathrm{d}\partial V \ . \tag{2.48}$$

In this equation, $\rho^{\langle\ell\rangle}$ represents the density of the ℓ-th layer, $\boldsymbol{\gamma}^{\langle\ell\rangle}$ and $\boldsymbol{\sigma}^{\langle\ell\rangle}$ denote the strain and stress fields in Voigt notation, respectively, $\ddot{\boldsymbol{u}}^{\langle\ell\rangle}$ is the second derivative of $\boldsymbol{u}^{\langle\ell\rangle}$ with respect to time, $\overline{\boldsymbol{t}}^{\langle\ell\rangle}$ is the vector of prescribed tractions on the external surface, and $\overline{\boldsymbol{b}}^{\langle\ell\rangle}$ is the vector of prescribed external volume forces.

It is important mentioning that while damping terms are not present in Eq.(2.48), they will be introduced within the formulation using the Rayleigh damping method.

Linear free-vibration analysis

Similarly to the case discussed for transient analysis, the equations governing the free-vibration analysis of a laminated shell are derived from the following weak form of a

three-dimensional multilayered structure

$$\sum_{\ell=1}^{N_\ell}\int_{V^{\langle\ell\rangle}}\delta\boldsymbol{\gamma}^{\langle\ell\rangle\intercal}\boldsymbol{\sigma}^{\langle\ell\rangle}\mathrm{d}V=\omega^2\sum_{\ell=1}^{N_\ell}\int_{V^{\langle\ell\rangle}}\delta\boldsymbol{u}^{\langle\ell\rangle\intercal}\rho^{\langle\ell\rangle}\boldsymbol{u}^{\langle\ell\rangle}\mathrm{d}V\ , \tag{2.49}$$

where ω represents a generic natural frequency. This expression is derived from the weak form of the elasto-dynamic problem, assuming no external forces are applied and the equation of motion takes the form

$$\ddot{\boldsymbol{u}}^{\langle\ell\rangle}=-\omega^2\boldsymbol{u}\ . \tag{2.50}$$

Under these circumstances, Eq.(2.48) reduces to the eigenvalue problem shown in Eq.(2.49).

Table 2.1: Three-dimensional formulation for the mechanical problems investigated in this thesis

Static analysis

$$\sum_{\ell=1}^{N_\ell}\int_{V^{\langle\ell\rangle}}\delta\boldsymbol{\gamma}^{\langle\ell\rangle\intercal}\boldsymbol{\sigma}^{\langle\ell\rangle}\mathrm{d}V=\sum_{\ell=1}^{N_\ell}\int_{V^{\langle\ell\rangle}}\delta\boldsymbol{u}^{\langle\ell\rangle\intercal}\overline{\boldsymbol{b}}^{\langle\ell\rangle}\ \mathrm{d}V+\sum_{\ell=1}^{N_\ell}\int_{\partial V^{\langle\ell\rangle}}\delta\boldsymbol{u}^{\langle\ell\rangle\intercal}\overline{\boldsymbol{t}}^{\langle\ell\rangle}\ \mathrm{d}\partial V$$

Linear buckling analysis

$$\sum_{\ell=1}^{N_\ell}\int_{V^{\langle\ell\rangle}}\delta\boldsymbol{\gamma}^{\langle\ell\rangle\intercal}\boldsymbol{\sigma}^{\langle\ell\rangle}\mathrm{d}V=-\lambda\sum_{\ell=1}^{N_\ell}\int_{V^{\langle\ell\rangle}}\overline{\sigma}_{ij}^{\langle\ell\rangle}\delta\boldsymbol{u}_{,i}^{\langle\ell\rangle\intercal}\boldsymbol{u}_{,j}^{\langle\ell\rangle}\mathrm{d}V$$

Linear transient analysis

$$\sum_{\ell=1}^{N_\ell}\int_{V^{\langle\ell\rangle}}\left(\delta\boldsymbol{u}^{\langle\ell\rangle\intercal}\rho^{\langle\ell\rangle}\ddot{\boldsymbol{u}}^{\langle\ell\rangle}+\delta\boldsymbol{\gamma}^{\langle\ell\rangle\intercal}\boldsymbol{\sigma}^{\langle\ell\rangle}\right)\mathrm{d}V=\sum_{\ell=1}^{N_\ell}\int_{V^{\langle\ell\rangle}}\delta\boldsymbol{u}^{\langle\ell\rangle\intercal}\overline{\boldsymbol{b}}^{\langle\ell\rangle}\mathrm{d}V+\sum_{\ell=1}^{N_\ell}\int_{\partial V^{\langle\ell\rangle}}\delta\boldsymbol{u}^{\langle\ell\rangle\intercal}\overline{\boldsymbol{t}}^{\langle\ell\rangle}\mathrm{d}\partial V$$

Linear free-vibration analysis

$$\sum_{\ell=1}^{N_\ell}\int_{V^{\langle\ell\rangle}}\delta\boldsymbol{\gamma}^{\langle\ell\rangle\intercal}\boldsymbol{\sigma}^{\langle\ell\rangle}\mathrm{d}V=\omega^2\sum_{\ell=1}^{N_\ell}\int_{V^{\langle\ell\rangle}}\delta\boldsymbol{u}^{\langle\ell\rangle\intercal}\rho^{\langle\ell\rangle}\boldsymbol{u}^{\langle\ell\rangle}\mathrm{d}V$$

Chapter 3

Shell theories

3.1 The Kirchhoff-Love shell theory

In the context of the Kirchhoff-Love shell theory, which was originally proposed by Kirchhoff [7] for plates and extended to shells by Love [8], the only variable considered is the displacement of the mid-surface, expressed in Cartesian coordinates. This theory is particularly suitable for thin shells where transverse shear effects are negligible and does not pose a threat to structural integrity. The resulting formulation is a fourth-order problem, necessitating C^1 continuity for its solution. This means that both displacements and their first derivatives must be continuous across element boundaries. In this section, we will present the theory and provide definitions for all the relevant quantities involved.

3.1.1 The Kirchhoff hypothesis

The Kirchhoff-Love assumption is based on the idea that the thickness segment perpendicular to the mid-surface in the reference configuration remains undeformed in length and maintains its perpendicularity to the mid-surface in the actual configuration. This assumption effectively neglects the out-of-plane components of the strain tensor, specifically γ_{13}, γ_{23}, and γ_{33} when expressed in covariant components. It is important to note that this assumption holds true primarily for thin shells, where a shell is considered thin when the radius of curvature is approximately 20 times the thickness of the shell. Given the deformed mean surface defined by the mapping:

$$\boldsymbol{X}_0(\xi_1, \xi_2) = \boldsymbol{x}_0(\xi_1, \xi_2) + \boldsymbol{u}(\xi_1, \xi_2) \ , \tag{3.1}$$

for $(\xi_1, \xi_2) \in \hat{\Omega}$, the correspondent covariant basis vectors for the deformed mid-surface are

$$\boldsymbol{A}_\alpha = \boldsymbol{X}_{0,\alpha} \ . \tag{3.2}$$

Additionally, the unit vector normal to the surface is defined as

$$\boldsymbol{A}_3 = \frac{\boldsymbol{A}_1 \times \boldsymbol{A}_2}{|\boldsymbol{A}_1 \times \boldsymbol{A}_2|} \ . \tag{3.3}$$

3.1.2 Boundary conditions

The boundary of the mid-surface $\partial\Omega$ is divided into two distinct parts as $\partial\Omega = \partial\Omega_{D_1} \cup \partial\Omega_{N_1}$, and as $\partial\Omega = \partial\Omega_{D_2} \cup \partial\Omega_{N_2}$.

- $\partial\Omega_{D_1}$ and $\partial\Omega_{D_2}$ represent the portions of the boundary where Dirichlet displacement and rotation boundary conditions are applied, respectively.

- $\partial\Omega_{N_1}$ and $\partial\Omega_{N_2}$ represent the portions of the boundary where Neumann force and moment boundary conditions are applied, respectively.

It is important to mention that $\partial\Omega_{D_1}$ and $\partial\Omega_{N_1}$ are disjoint sets whose union coincide with $\partial\Omega$, and the same applies to $\partial\Omega_{D_2}$ and $\partial\Omega_{N_2}$. It is also defined the set of corners $\chi \in \partial\Omega$ which is further divided into

- $\chi^D \in \overline{\partial\Omega_{D_1}}$ where Dirichlet displacement boundary conditions are applied.

- $\chi^N \in \partial\Omega_{N_1}$ where Neumann force boundary conditions are applied.

The external force distributed on the shell surface is denoted as $\tilde{\boldsymbol{F}}$. Regarding the surface boundary, the applied force is denoted as $\tilde{\boldsymbol{\tau}}$, while the bending and twisting moments are denoted as $\tilde{M}_{nn}$ and $\tilde{M}_{nt}$, respectively. However, for the Kirchhoff-Love shell theory $\tilde{\boldsymbol{\tau}}$ and $\tilde{M}_{nt}$ cannot be imposed separately and both contribute to the equivalent ersatz force applied on $\partial\Omega_{N_1}$. On the other hand, $\tilde{M}_{nn}$ is the only moment applied on $\partial\Omega_{N_2}$.

3.1.3 Weak form of Kirchhoff-Love shell equation

Focusing on a single patch shell, the weak form of the Kirchhoff-Love equation is stated as: find $\boldsymbol{u} \in \mathcal{V}^u$ such that

$$a(\boldsymbol{u}, \boldsymbol{v}) = f(\boldsymbol{v}) \quad \forall \boldsymbol{v} \in \mathcal{V}^v \,, \tag{3.4}$$

where the choice of the vector spaces $\mathcal{V}^v$ and $\mathcal{V}^u$ depends on the specific boundary conditions of the problem. In the discretized version of Eq.(3.4) the choice of the spaces also takes into account whether the boundary condition are applied in a strong or a weak sense. The bilinear and the linear forms in Eq.(3.4) are defined as

$$a(\boldsymbol{u}, \boldsymbol{v}) = \int_S \boldsymbol{\varepsilon}(\boldsymbol{v}) : \boldsymbol{N}(\boldsymbol{u}) \mathrm{d}\Omega + \int_S \boldsymbol{\kappa}(\boldsymbol{v}) : \boldsymbol{M}(\boldsymbol{u}) \mathrm{d}\Omega \,, \tag{3.5a}$$

$$f(\boldsymbol{v}) = \int_S \boldsymbol{v} \cdot \tilde{\boldsymbol{F}} \mathrm{d}\Omega + \int_{\partial\Omega_{N_1}} \boldsymbol{v} \cdot \tilde{\boldsymbol{T}} \mathrm{d}\partial\Omega + \int_{\partial\Omega_{N_2}} \theta_n(\boldsymbol{v}) \tilde{M}_{nn} \mathrm{d}\partial\Omega + \sum_{C \in \chi^N} \left(v_3 \tilde{R} \right) \Big|_C \,, \tag{3.5b}$$

where $\boldsymbol{\varepsilon}$ and $\boldsymbol{\kappa}$ represent the membrane and bending strains, respectively, while $\boldsymbol{N}$ and $\boldsymbol{M}$ represent the generalized force and moment, respectively. Since the Kirchhoff-Love shell theory discards the out-of-plane components, these quantities are all rank-2 tensors, and the following constitutive equations apply

$$N^{\alpha\beta} = \mathbb{A}^{\alpha\beta\gamma\delta} \varepsilon_{\gamma\delta} + \mathbb{B}^{\alpha\beta\gamma\delta} \kappa_{\gamma\delta} \,, \tag{3.6a}$$

$$M^{\alpha\beta} = \mathbb{C}^{\alpha\beta\gamma\delta} \varepsilon_{\gamma\delta} + \mathbb{D}^{\alpha\beta\gamma\delta} \kappa_{\gamma\delta} \,, \tag{3.6b}$$

where $N^{\alpha\beta}$ and $M^{\alpha\beta}$ represent the contravariant components of $\boldsymbol{N}$ and $\boldsymbol{M}$, respectively, while $\varepsilon_{\gamma\delta}$ and $\kappa_{\gamma\delta}$ are generic covariant components of $\boldsymbol{\varepsilon}$ and $\boldsymbol{\kappa}$. Additionally, the coefficients introduced $\mathbb{A}^{\alpha\beta\gamma\delta}$, $\mathbb{B}^{\alpha\beta\gamma\delta}$, $\mathbb{C}^{\alpha\beta\gamma\delta}$, and $\mathbb{D}^{\alpha\beta\gamma\delta}$ form the components of the generalized stiffness tensors for a Kirchhoff-Love shell. Their values depend on both the material and the geometry of the shell. A comprehensive description of how these coefficients are obtained is provided in Sec. 3.1.6 for the sake of completeness. Furthermore, the components of the membrane and bending strains, as well as the normal or bending rotation

θ_n, are derived as linear combinations of the first and second coordinate derivatives of the displacement vector. Detailed expressions for these quantities can be found in Sec. 3.1.5.

Regarding the terms related to the applied forces in Eq.(3.4), in addition to the bending moment $\tilde{M}_{nn}$ and the surface force $\tilde{\boldsymbol{F}}$ that were already described in Sec. 3.1.2, two additional forces are introduced: the ersatz force $\tilde{\boldsymbol{T}}$ and the corner force $\tilde{R}$. These are defined, respectively, as

$$\tilde{\boldsymbol{T}} = \left(\tilde{\tau}_\alpha - \tilde{M}_{nt} b_{\alpha\beta} t^\beta\right) \boldsymbol{a}^\alpha + \left(\tilde{\tau}_3 + \frac{\partial \tilde{M}_{nt}}{\partial t}\right) \boldsymbol{a}^3 \,, \tag{3.7}$$

$$\tilde{R} = \lim_{\epsilon \to 0} \left(\tilde{M}_{nt}(\boldsymbol{x} + \epsilon \boldsymbol{t}) - \tilde{M}_{nt}(\boldsymbol{x} - \epsilon \boldsymbol{t})\right) \,, \tag{3.8}$$

where t^α represents the α-th contravariant coordinate of the vector $\boldsymbol{t}$, which is the unit vector locally tangent to the counterclockwise-oriented boundary $\partial\Omega$, $\tilde{\tau}_\alpha$ is the α-th covariant component of $\tilde{\boldsymbol{\tau}}$, and $\tilde{\tau}_3$ refers to $\boldsymbol{a}_3$. Additionally, $\boldsymbol{n} = \boldsymbol{t} \times \boldsymbol{a}_3$ is the outer unit vector orthogonal to the boundary and lying in the local plane tangent to Ω. The components of the applied moment $\tilde{M}_{nn}$ and $\tilde{M}_{nt}$ are referred to the basis formed by the vectors $\boldsymbol{n}$ and $\boldsymbol{t}$.

3.1.4 Extension to multi-patch structures

The variational statement in Eq.(3.4)applies to shell structures consisting on a single patch. However, if the structure is composed of N_P patches that intersect at N_I interfaces, the problem becomes finding $\boldsymbol{u} \in \boldsymbol{\mathcal{V}}^u$ such that:

$$\sum_{p=1}^{N_P} a^p(\boldsymbol{u}, \boldsymbol{v}) = \sum_{p=1}^{N_P} f^p(\boldsymbol{v}) \quad \forall \boldsymbol{v} \in \boldsymbol{\mathcal{V}}^v \,, \tag{3.9}$$

where $a^p(\boldsymbol{u}, \boldsymbol{v})$ and $f^p(\boldsymbol{v})$ are defined as in Eq.(3.5)), but a superscript p is added to indicate that they belong to the p-th patch. Additionally, $\boldsymbol{\mathcal{V}}^u$ and $\boldsymbol{\mathcal{V}}^v$ are vector spaces defined over the union of the surfaces of the patches of the structure. These spaces have to be defined in a way that, apart from satisfying the essential boundary conditions, ensures the following conditions over each of the interfaces Γ_i:

$$[\boldsymbol{u}] = \boldsymbol{0} \,, \tag{3.10a}$$

$$[\theta_n] = 0 \,, \tag{3.10b}$$

where $[\bullet]$ represents the jump operator, which calculates the difference between the quantity of interest computed from the different patches at the interface.

In order to enforce this coupling condition in a strong sense, Eq.(3.10)should be embedded in the spaces $\boldsymbol{\mathcal{V}}^v$ and $\boldsymbol{\mathcal{V}}^u$. In practice, after discretization, it is relatively easy to enforce Eq.(3.10a)in the case where the patches are conforming at the interface, but is not straightforward to do the same for Eq.(3.10b)and this is restricted to G^1 surfaces [85, 87, 133]. However, in situations where the interface is generated in a non-conforming manner, such as when two patches meet on a trimmed boundary, the coupling condition can only be enforced in a weak sense. The same applies to essential boundary conditions on the trimmed boundary of each patch.

3.1.5 Membrane and bending strains

In this section the Kirchhoff-Love shell problem is completed by defining $\boldsymbol{\varepsilon}$, $\boldsymbol{\kappa}$ and θ_n. These definitions are derived through linearization of their non-linear expressions under the condition of uniform zero displacement. For a more comprehensive understanding of the fundamental concepts in continuum mechanics introduced in this section, interested readers are encouraged to consult [113].

With reference to the deformed mid-surface mapping in Eq.(3.1), it is introduced the covariant component of the metric tensor and the curvature tensor of the shell mid-surface as follows

$$A_{\alpha\beta} = \boldsymbol{A}_\alpha \cdot \boldsymbol{A}_\beta \ , \tag{3.11}$$

$$B_{\alpha\beta} = \boldsymbol{A}_{\alpha,\beta} \cdot \boldsymbol{A}_3 \ . \tag{3.12}$$

Due to the Kirchhoff hypothesis, the volume of the shell in the deformed configuration can still be expressed using the unit vector orthogonal to the deformed shell mid-surface $\boldsymbol{A}_3$. As such, the following equation holds

$$\boldsymbol{X}(\xi_1, \xi_2, \xi_3) = \boldsymbol{X}_0(\xi_1, \xi_2) + \xi_3 \boldsymbol{A}_3(\xi_1, \xi_2) \ , \tag{3.13}$$

with $(\xi_1, \xi_2, \xi_3) \in \hat{V}$. Therefore, the covariant basis for the shell volume in the actual configuration is introduced as

$$\boldsymbol{G}_\alpha = \boldsymbol{X}_{,\alpha} = \boldsymbol{A}_\alpha + \xi_3 \boldsymbol{A}_{3,\alpha} \ . \tag{3.14}$$

Whereas the covariant components of the metric tensor for the deformed shell volume are computed as

$$\begin{aligned} G_{\alpha\beta} = \boldsymbol{G}_\alpha \cdot \boldsymbol{G}_\beta &= (\boldsymbol{A}_\alpha + \xi_3 \boldsymbol{A}_{3,\alpha}) \cdot (\boldsymbol{A}_\beta + \xi_3 \boldsymbol{A}_{3,\beta}) \\ &= A_{\alpha\beta} - 2\xi_3 B_{\alpha\beta} + \xi_3^2 \boldsymbol{A}_{3,\alpha} \cdot \boldsymbol{A}_{3,\beta} \ . \end{aligned} \tag{3.15}$$

In the thin shell hypothesis the term that multiply ξ_3^2 is neglected, leading to the simplified expression

$$G_{\alpha\beta} \approx A_{\alpha\beta} - 2\xi_3 B_{\alpha\beta} \ . \tag{3.16}$$

With this groundwork, the strain in covariant coordinates, specifically in the Kirchhoff-Love hypothesis, are defined as

$$\gamma_{\alpha\beta} = \frac{1}{2}(A_{\alpha\beta} - a_{\alpha\beta}) + \xi_3 (b_{\alpha\beta} - B_{\alpha\beta}) \ , \tag{3.17}$$

where $\gamma_{\alpha\beta}$ represents the $\alpha\beta$-th covariant component of the Green-Lagrange strain tensor. At this point, two distinct contributions can be discerned. The first contribution pertains to the metric tensor of the shell mid-surface, and it provides a uniform contribution across the thickness of the shell. The second contribution pertains to the curvature tensor of the shell mid-surface, and it yields a contribution that varies linearly along the shell's thickness. These are further distinguished through the introduction of membrane and bending strains, which are defined, respectively, as

$$\varepsilon_{\alpha\beta} = \frac{1}{2}(A_{\alpha\beta} - a_{\alpha\beta}) \ , \tag{3.18a}$$

$$\kappa_{\alpha\beta} = b_{\alpha\beta} - B_{\alpha\beta} \ . \tag{3.18b}$$

In this work, the Kirchhoff-Love shell theory is adopted only for linear static analysis. Given this context, the expression presented in Equation (3.18) necessitates linearization under the condition of uniform zero displacement. This linearization is achieved as follows

$$\varepsilon_{\alpha\beta} = \left.\frac{\partial\left(\frac{1}{2}(A_{\alpha\beta}-a_{\alpha\beta})\right)}{\partial \boldsymbol{u}}\right|_{\mathbf{0}} \cdot \boldsymbol{u} + \left.\frac{\partial\left(\frac{1}{2}(A_{\alpha\beta}-a_{\alpha\beta})\right)}{\partial \boldsymbol{u}_{,\gamma}}\right|_{\mathbf{0}} \cdot \boldsymbol{u}_{,\gamma} \ , \tag{3.19a}$$

$$\kappa_{\alpha\beta} = \left.\frac{\partial(b_{\alpha\beta}-B_{\alpha\beta})}{\partial \boldsymbol{u}}\right|_{\mathbf{0}} \cdot \boldsymbol{u} + \left.\frac{\partial(b_{\alpha\beta}-B_{\alpha\beta})}{\partial \boldsymbol{u}_{,\gamma}}\right|_{\mathbf{0}} \cdot \boldsymbol{u}_{,\gamma} + \left.\frac{\partial(b_{\alpha\beta}-B_{\alpha\beta})}{\partial \boldsymbol{u}_{,\gamma\delta}}\right|_{\mathbf{0}} \cdot \boldsymbol{u}_{,\gamma\delta} \ , \tag{3.19b}$$

where $\bullet|_{\mathbf{0}}$ denotes the evaluation of the generic function $\bullet$ for $\boldsymbol{u} = \boldsymbol{u}_{,\alpha} = \boldsymbol{u}_{,\alpha\beta} = \mathbf{0}$. In the membrane strain the derivatives with respect to $\boldsymbol{u}_{,\gamma\beta}$ are discarded since it easy to show that $\varepsilon_{\alpha\beta}$ does not depend on $\boldsymbol{u}_{,\gamma\delta}$. After some algebra the previous expression are simplified into

$$\varepsilon_{\alpha\beta} = \frac{1}{2}(\boldsymbol{a}_\alpha \cdot \boldsymbol{u}_{,\beta} + \boldsymbol{a}_\beta \cdot \boldsymbol{u}_{,\alpha}) \ , \tag{3.20a}$$

$$\kappa_{\alpha\beta} = -\boldsymbol{a}_3 \cdot \boldsymbol{u}_{,\alpha\beta} - \left(\frac{\boldsymbol{a}_{\alpha,\beta}\times\boldsymbol{a}_1}{\lambda} + \boldsymbol{a}_{\alpha,\beta}^T\boldsymbol{\mathcal{M}}\boldsymbol{\mathcal{M}}_1\right)\cdot\boldsymbol{u}_{,2} + \left(\frac{\boldsymbol{a}_{\alpha,\beta}\times\boldsymbol{a}_2}{\lambda} + \boldsymbol{a}_{\alpha,\beta}^T\boldsymbol{\mathcal{M}}\boldsymbol{\mathcal{M}}_2\right)\cdot\boldsymbol{u}_{,1} \ . \tag{3.20b}$$

In Eq.(3.20) the auxiliary matrices $\boldsymbol{\mathcal{M}}$ and $\boldsymbol{\mathcal{M}}_\alpha$ have been introduced, these are defined as

$$\boldsymbol{\mathcal{M}} = \frac{\boldsymbol{a}_3\boldsymbol{a}_3^T}{\lambda} \ , \tag{3.21a}$$

$$\boldsymbol{\mathcal{M}}_\alpha = [\boldsymbol{e}_1\times\boldsymbol{a}_\alpha \quad \boldsymbol{e}_2\times\boldsymbol{a}_\alpha \quad \boldsymbol{e}_3\times\boldsymbol{a}_\alpha] \ . \tag{3.21b}$$

Likewise, the linear expression for the normal rotation is obtained from the non-linear counterpart [99] as

$$\theta_n = \left.\frac{\partial\left(\boldsymbol{t}\cdot(\boldsymbol{a}_3\times(\boldsymbol{A}_3-\boldsymbol{a}_3))\right)}{\partial \boldsymbol{u}_{,\alpha}}\right|_{\mathbf{0}} \cdot \boldsymbol{u}_{,\alpha} \ , \tag{3.22}$$

that leads to

$$\theta_n = \left(\frac{(\boldsymbol{t}\times\boldsymbol{a}_3)\times\boldsymbol{a}_1}{\lambda} + (\boldsymbol{t}\times\boldsymbol{a}_3)^T\boldsymbol{\mathcal{M}}\boldsymbol{\mathcal{M}}_1\right)\cdot\boldsymbol{u}_{,2} - \left(\frac{(\boldsymbol{t}\times\boldsymbol{a}_3)\times\boldsymbol{a}_2}{\lambda} + (\boldsymbol{t}\times\boldsymbol{a}_3)^T\boldsymbol{\mathcal{M}}\boldsymbol{\mathcal{M}}_2\right)\cdot\boldsymbol{u}_{,1} \ . \tag{3.23}$$

It is remarked that the expressions shown in Eq.(3.20) for the strain are equivalent to those in [81]. However, the proposed notation is more convenient as it allows for the introduction of some terms that are common with the definition of θ_n.

3.1.6 Generalized stiffness matrices in tensor notation

In the plane stress hypothesis, the in-plane contravariant components of the stress tensor are related to the in-plane covariant components of the strain tensor through the constitutive relationship

$$\sigma^{\langle\ell\rangle\,\alpha\beta} = c_R^{\langle\ell\rangle\,\alpha\beta\gamma\delta}\gamma_{\gamma\delta}^{\langle\ell\rangle} = c_R^{\langle\ell\rangle\,\alpha\beta\gamma\delta}\varepsilon_{\gamma\delta} + \xi_3 c_R^{\langle\ell\rangle\,\alpha\beta\gamma\delta}\kappa_{\gamma\delta} \ , \tag{3.24}$$

where $c_R^{\langle\ell\rangle\,\alpha\beta\gamma\delta}$ represents the stiffness coefficients relative to the covariant basis, with the out-of-plane behavior being disregarded. With this definition, the generalized force and moment can be expressed in terms of the membrane and bending strain as follows

$$N^{\alpha\beta} = \sum_{\ell=1}^{N_\ell} \int_{\tau_b^{\langle\ell\rangle}}^{\tau_t^{\langle\ell\rangle}} \sigma^{\langle\ell\rangle\,\alpha\beta} \mathrm{d}\xi_3 = \mathbb{A}^{\alpha\beta\gamma\delta}\varepsilon_{\gamma\delta} + \mathbb{B}^{\alpha\beta\gamma\delta}\kappa_{\gamma\delta} \ , \tag{3.25a}$$

$$M^{\alpha\beta} = \sum_{\ell=1}^{N_\ell} \int_{\tau_b^{\langle\ell\rangle}}^{\tau_t^{\langle\ell\rangle}} \xi_3\sigma^{\langle\ell\rangle\,\alpha\beta} \mathrm{d}\xi_3 = \mathbb{C}^{\alpha\beta\gamma\delta}\varepsilon_{\gamma\delta} + \mathbb{D}^{\alpha\beta\gamma\delta}\kappa_{\gamma\delta} \ . \tag{3.25b}$$

To obtain the generalized stiffness coefficients $\mathbb{A}^{\alpha\beta\gamma\delta}$, $\mathbb{B}^{\alpha\beta\gamma\delta}$, $\mathbb{C}^{\alpha\beta\gamma\delta}$, and $\mathbb{D}^{\alpha\beta\gamma\delta}$, it is performed a through-the-thickness integration on the stiffness matrix $\overline{\boldsymbol{c}}_R^{\langle\ell\rangle}$ expressed in the auxiliary orthonormal basis $\boldsymbol{n}_1, \boldsymbol{n}_2$. The following generalized stiffness matrices are introduced

$$\bar{\boldsymbol{A}} = \sum_{\ell=1}^{N_\ell} \int_{\tau_b^{\langle\ell\rangle}}^{\tau_t^{\langle\ell\rangle}} \overline{\boldsymbol{c}}_R^{\langle\ell\rangle} \mathrm{d}\xi_3 \ , \tag{3.26a}$$

$$\bar{\boldsymbol{B}} = \sum_{\ell=1}^{N_\ell} \int_{\tau_b^{\langle\ell\rangle}}^{\tau_t^{\langle\ell\rangle}} \overline{\boldsymbol{c}}_R^{\langle\ell\rangle} \xi_3 \mathrm{d}\xi_3 \ , \tag{3.26b}$$

$$\bar{\boldsymbol{D}} = \sum_{\ell=1}^{N_\ell} \int_{\tau_b^{\langle\ell\rangle}}^{\tau_t^{\langle\ell\rangle}} \overline{\boldsymbol{c}}_R^{\langle\ell\rangle} \xi_3^2 \mathrm{d}\xi_3 \ , \tag{3.26c}$$

$$\bar{\boldsymbol{C}} = \bar{\boldsymbol{B}}^T \ , \tag{3.26d}$$

These constitutive matrices, in Voigt notation, are employed to derive the constitutive tensors. For instance, taking $\bar{\boldsymbol{A}}$ as an example, the associated stiffness tensor notation is established as $\bar{\mathbb{A}}^{\alpha\beta\gamma\delta} = \bar{A}^{ab}$, using the correspondences $\alpha\beta \longleftrightarrow a$ and $\gamma\delta \longleftrightarrow b$, where the indices 11, 22, 12, and 21 correspond to 1, 2, 3, and 3, respectively. Finally, the constitutive tensors in the local covariant basis are derived through the following transformation law

$$\mathbb{A}^{\alpha_1\beta_1\gamma_1\delta_1} = \bar{\mathbb{A}}^{\alpha_2\beta_2\gamma_2\delta_2} \, (\boldsymbol{n}_{\alpha_2} \cdot \boldsymbol{a}^{\alpha_1})(\boldsymbol{n}_{\beta_2} \cdot \boldsymbol{a}^{\beta_1})(\boldsymbol{n}_{\gamma_2} \cdot \boldsymbol{a}^{\gamma_1})(\boldsymbol{n}_{\delta_2} \cdot \boldsymbol{a}^{\delta_1}) \ . \tag{3.27}$$

3.2 The Equivalent-Single-Layer shell theories

While the Kirchhoff-Love shell theory offers simplicity with the fewest amount of primary variables among shell theories, it exhibits inaccuracies when dealing with thick shells. These inaccuracies arise because out-of-plane strains become significant. Furthermore, the Kirchhoff hypothesis assumes a linear variation of the in-plane components and a uniform out-of-plane component of the displacement vector across the shell thickness. However, this assumption does not hold for thick shells, where the displacement distribution exhibits higher-order behavior. Furthermore, in the context of laminates, accurate prediction of shear stresses becomes critically important. These shear stresses are closely related to delamination, which is a primary cause of failure in multi-layered structures.

In this section, it is introduced the Equivalent-Single-Layer (ESL) approach. In ESL theories, the displacement throughout the entire laminate is approximated as a higher-degree function. This treatment allows to treat the entire laminate as a single layer

with equivalent homogenized properties, hence the name of the approach. The two-dimensional variational statements for various mechanical problems of interest are derived in the reminder of this section and summarized in Tab.(3.1).

3.2.1 Shell kinematics

According to the geometrical description introduced in the previous Chapter, the shell deformation can be described in terms of the displacement vector. This can be expressed either in Cartesian components as $\boldsymbol{u} = \{u_1 \; u_2 \; u_3\}^\intercal$ or in covariant components as $\boldsymbol{u}_\xi = \{u_{\xi_1} \; u_{\xi_2} \; u_{\xi_3}\}^\intercal$. The shell kinematics employed to develop the present formulation is based on the expansion of the displacement components across the shell thickness through known functions of ξ_3. Thus, the covariant components u_{ξ_i} of the displacement vector are expressed as

$$u_{\xi_i}(\xi_1, \xi_2, \xi_3) = \sum_{k=0}^{N_i} Z_{ik}(\xi_3) U_{ik}(\xi_1, \xi_2) \; , \tag{3.28}$$

where N_i is the order of the expansion assumed for u_{ξ_i}, $Z_{ik}(\xi_3)$ is the k-th function of the expansion of u_{ξ_i} and $U_{ik}(\xi_1, \xi_2)$ are the unknown generalized displacements. It is worth noting that, according to the Carrera Unified Formulation underlying principles [21], in Eq.(3.28) N_i can be considered as parameters whose values allow to build different order shell structural theories falling within the ESL approach. The shell theory corresponding to the expansion orders N_1, N_2 and N_3 is denoted as $\mathrm{ED}_{N_1 N_2 N_3}$. Collecting the generalized displacements as elements of the vector $\boldsymbol{U}(\xi_1, \xi_2)$, having size $N_U = N_1 + N_2 + N_3 + 3$, and consistently arranging the functions Z_{ik} as elements of the matrix $\boldsymbol{Z}(\xi_3)$, the Eq.(3.28) is compactly rewritten in matrix form as

$$\boldsymbol{u}_\xi = \boldsymbol{Z}(\xi_3) \boldsymbol{U}(\xi_1, \xi_2) \; . \tag{3.29}$$

and, recalling that $\boldsymbol{u} = \boldsymbol{R}\boldsymbol{u}_\xi$, the displacement $\boldsymbol{u}$ in the Cartesian reference system is obtained in terms of the generalized displacement vector $\boldsymbol{U}$ as

$$\boldsymbol{u} = \boldsymbol{R}\boldsymbol{Z}\boldsymbol{U} \; . \tag{3.30}$$

It is observed that the expansion functions $Z_{ik}(\xi_3)$ can be chosen without particular restrictions (e.g polynomial, exponential, trigonometric). Here, they are taken either as Legendre or Taylor polynomials having order $k \leq N_i$ and scaled in the interval $\hat{I}_3$. As an example, for the ED_{222} theory with Legendre polynomials, the matrix $\boldsymbol{Z}$ is obtained as

$$\boldsymbol{Z} = \begin{bmatrix} 1 & 2\xi_3/\tau & (2\xi_3/\tau)^2 & 0 & 0 & 0 & 0 & 0 & 0 \\ 0 & 0 & 0 & 1 & 2\xi_3/\tau & (2\xi_3/\tau)^2 & 0 & 0 & 0 \\ 0 & 0 & 0 & 0 & 0 & 0 & 1 & 2\xi_3/\tau & (2\xi_3/\tau)^2 \end{bmatrix} \; . \tag{3.31}$$

3.2.2 Green-Lagrange strain for ESL

Recalling that the Green-Lagrange strain components vector, namely $\boldsymbol{\gamma} = \{\gamma_{11} \; \gamma_{22} \; \gamma_{33} \; \gamma_{23} \; \gamma_{13} \; \gamma_{12} \; \}^\intercal$, expressed in the Cartesian reference system is given by

$$\boldsymbol{\gamma} = \left(\boldsymbol{I}_i + \frac{1}{2} \boldsymbol{W}_i \right) \boldsymbol{u}_{,i} \; , \tag{3.32}$$

where the following auxiliary matrices $\boldsymbol{I}_i$ and $\boldsymbol{W}_i$ are defined as

$$\boldsymbol{I}_1 = \begin{bmatrix} 1 & 0 & 0 \\ 0 & 0 & 0 \\ 0 & 0 & 0 \\ 0 & 0 & 0 \\ 0 & 0 & 1 \\ 0 & 1 & 0 \end{bmatrix}, \quad \boldsymbol{I}_2 = \begin{bmatrix} 0 & 0 & 0 \\ 0 & 1 & 0 \\ 0 & 0 & 0 \\ 0 & 0 & 1 \\ 0 & 0 & 0 \\ 1 & 0 & 0 \end{bmatrix}, \quad \boldsymbol{I}_3 = \begin{bmatrix} 0 & 0 & 0 \\ 0 & 0 & 0 \\ 0 & 0 & 1 \\ 0 & 1 & 0 \\ 1 & 0 & 0 \\ 0 & 0 & 0 \end{bmatrix}, \tag{3.33a}$$

$$\boldsymbol{W}_1 = \begin{bmatrix} u_{1,1} & u_{2,1} & u_{3,1} \\ 0 & 0 & 0 \\ 0 & 0 & 0 \\ 0 & 0 & 0 \\ u_{1,3} & u_{2,3} & u_{3,3} \\ u_{1,2} & u_{2,2} & u_{3,2} \end{bmatrix}, \quad \boldsymbol{W}_2 = \begin{bmatrix} 0 & 0 & 0 \\ u_{1,2} & u_{2,2} & u_{3,2} \\ 0 & 0 & 0 \\ u_{1,3} & u_{2,3} & u_{3,3} \\ 0 & 0 & 0 \\ u_{1,1} & u_{2,1} & u_{3,1} \end{bmatrix}, \quad \boldsymbol{W}_3 = \begin{bmatrix} 0 & 0 & 0 \\ 0 & 0 & 0 \\ u_{1,3} & u_{2,3} & u_{3,3} \\ u_{1,2} & u_{2,2} & u_{3,2} \\ u_{1,1} & u_{2,1} & u_{3,1} \\ 0 & 0 & 0 \end{bmatrix}, \tag{3.33b}$$

and $u_{i,j}$ is the derivative of the i-th Cartesian component of the displacement vector with respect to x_j. Using Eq.(3.30) and applying the chain rule to express the derivatives in the Cartesian reference system coordinates through those in the curvilinear coordinates,, one obtains

$$\boldsymbol{u}_{,i} = \frac{\partial(\boldsymbol{R}\boldsymbol{u}_\xi)}{\partial \xi_j}\xi_{j,i} = \boldsymbol{D}_{0i}\boldsymbol{U} + \boldsymbol{D}_{\alpha i}\boldsymbol{U}_{,\alpha} \ , \tag{3.34}$$

where $\boldsymbol{u}_{,i} = \partial \boldsymbol{u}/\partial x_i$, $\xi_{i,j} = \partial \xi_j/\partial x_i$ corresponds to the ij-th component of $\boldsymbol{R}$, and $\boldsymbol{U}_{,\alpha} = \partial \boldsymbol{U}/\partial \xi_\alpha$. Additionally,

$$\boldsymbol{D}_{0i} = \xi_{j,i}\boldsymbol{R}_{,j}\boldsymbol{Z} + \xi_{3,i}\boldsymbol{R}\boldsymbol{Z}_{,3} \ , \tag{3.35a}$$

$$\boldsymbol{D}_{\alpha i} = \xi_{\alpha,i}\boldsymbol{R}\boldsymbol{Z} \ . \tag{3.35b}$$

where $\boldsymbol{R}_{,i} = \partial \boldsymbol{R}/\partial \xi_i$, and $\boldsymbol{Z}_{,3} = \mathrm{d}\boldsymbol{Z}/\mathrm{d}\xi_3$. Finally, upon introducing Eq.(3.34) in Eqs.(3.32), the Green-Lagrange strains are expressed as

$$\boldsymbol{\gamma} = \left(\boldsymbol{I}_i + \frac{1}{2}\boldsymbol{W}_i\right)\left(\boldsymbol{D}_{0i}\boldsymbol{U} + \boldsymbol{D}_{\alpha i}\boldsymbol{U}_{,\alpha}\right) \ . \tag{3.36}$$

To what regards the strain in small displacement hypothesis, recalling the definition of the linear strain Voigt vector

$$\boldsymbol{\gamma} = \boldsymbol{I}_i\boldsymbol{u}_{,i} \ , \tag{3.37}$$

upon substituting Eq.(3.34) the previous equation becomes

$$\boldsymbol{\gamma} = \boldsymbol{I}_i\left(\boldsymbol{D}_{0i}\boldsymbol{U} + \boldsymbol{D}_{\alpha i}\boldsymbol{U}_{,\alpha}\right) \ . \tag{3.38}$$

To conclude this section, it is worth noting that Eqs.(3.30) and (3.36) have been introduced without using the superscript $\langle \ell \rangle$ or mentioning the stacking sequence of the shell. In fact, these equations are valid throughout the shell thickness and for each layer of the shell. This is typical of ESL formulations and has the advantage that the continuity of the displacement field at the interface between consecutive layers is automatically satisfied.

Derivatives of the transformation matrix

The present formulation relies on the knowledge of the matrix $\boldsymbol{R}$, whose columns are the vectors $\boldsymbol{g}^i$ of the contravariant basis, as well as its derivatives with respect to the curvilinear variables ξ_1 and ξ_2. These quantities play a crucial role, as they enter the definitions of the matrices $\boldsymbol{D}_{0i}$ and $\boldsymbol{D}_{\alpha i}$ as given in Eq.(3.35a). However, despite seemingly complex expressions, obtaining $\boldsymbol{R}$ and $\boldsymbol{R}_{,i}$, requires knowledge of just the derivatives of the shell mid-surface map with respect to ξ_1 and ξ_2 up to the third order. A set of easy-to-use formulas to compute the quantities of interest for the present formulation are provided here.

Let us introduce the derivatives of the map of the mid-surface with respect to ξ_1 and ξ_2. Besides $\boldsymbol{a}_1$ and $\boldsymbol{a}_2$ already defined, ones has

$$\boldsymbol{a}_{1,1} = \boldsymbol{x}_{0,11} \ , \tag{3.39a}$$
$$\boldsymbol{a}_{1,2} = \boldsymbol{x}_{0,12} \ , \tag{3.39b}$$
$$\boldsymbol{a}_{2,2} = \boldsymbol{x}_{0,22} \ , \tag{3.39c}$$

and

$$\boldsymbol{a}_{1,11} = \boldsymbol{x}_{0,111} \ , \tag{3.40a}$$
$$\boldsymbol{a}_{1,12} = \boldsymbol{x}_{0,112} \ , \tag{3.40b}$$
$$\boldsymbol{a}_{1,22} = \boldsymbol{x}_{0,122} \ , \tag{3.40c}$$
$$\boldsymbol{a}_{2,22} = \boldsymbol{x}_{0,222} \ . \tag{3.40d}$$

It is important to note that additional mixed derivatives are not explicitly defined, as they satisfy the equality dictated by the Schwarz theorem. For instance, $\boldsymbol{a}_{2,1} = \boldsymbol{x}_{0,21} = \boldsymbol{x}_{0,12} = \boldsymbol{a}_{1,2}$, and $\boldsymbol{a}_{2,11} = \boldsymbol{x}_{0,211} = \boldsymbol{x}_{0,121} = \boldsymbol{a}_{1,21}$.

To simplify our calculations, it is introduced an auxiliary vector $\boldsymbol{p} = \boldsymbol{a}_1 \times \boldsymbol{a}_2$. Computing its first and second-order derivatives with respect to the curvilinear coordinates can be achieved using the derivative rule for the product of functions

$$\boldsymbol{p}_{,1} = \boldsymbol{a}_{1,1} \times \boldsymbol{a}_2 + \boldsymbol{a}_1 \times \boldsymbol{a}_{1,2}, \tag{3.41a}$$
$$\boldsymbol{p}_{,2} = \boldsymbol{a}_{1,2} \times \boldsymbol{a}_2 + \boldsymbol{a}_1 \times \boldsymbol{a}_{2,2}, \tag{3.41b}$$
$$\boldsymbol{p}_{,11} = \boldsymbol{a}_{1,11} \times \boldsymbol{a}_2 + 2\boldsymbol{a}_{1,1} \times \boldsymbol{a}_{1,2} + \boldsymbol{a}_1 \times \boldsymbol{a}_{1,12}, \tag{3.41c}$$
$$\boldsymbol{p}_{,12} = \boldsymbol{a}_{1,12} \times \boldsymbol{a}_2 + \boldsymbol{a}_{1,1} \times \boldsymbol{a}_{2,2} + \boldsymbol{a}_{1,2} \times \boldsymbol{a}_{1,2} + \boldsymbol{a}_1 \times \boldsymbol{a}_{1,22}, \tag{3.41d}$$
$$\boldsymbol{p}_{,22} = \boldsymbol{a}_{1,22} \times \boldsymbol{a}_2 + 2\boldsymbol{a}_{1,2} \times \boldsymbol{a}_{2,2} + \boldsymbol{a}_1 \times \boldsymbol{a}_{2,22}. \tag{3.41e}$$

Let us now introduce the scalar λ and the auxiliary matrix $\boldsymbol{\mathcal{N}}$ as

$$\lambda = |\boldsymbol{p}| \ , \tag{3.42}$$
$$\boldsymbol{\mathcal{N}} = \frac{1}{\lambda}(\boldsymbol{I} - \boldsymbol{a}_3\boldsymbol{a}_3^\intercal) \ , \tag{3.43}$$

where it is recalled that $\boldsymbol{a}_3 = \boldsymbol{p}/\lambda$ is the mid-surface unit normal and $\boldsymbol{I}$ is the 3×3 identity matrix. The derivatives of $\boldsymbol{a}_3$ are then computed in terms of the derivatives of $\boldsymbol{p}$ as

$$\boldsymbol{a}_{3,\alpha} = \boldsymbol{\mathcal{N}}\boldsymbol{p}_{,\alpha} \ , \tag{3.44a}$$
$$\boldsymbol{a}_{3,\alpha\beta} = \boldsymbol{\mathcal{N}}\boldsymbol{p}_{,\alpha\beta} - \frac{1}{\lambda}\left(\boldsymbol{\mathcal{N}}\left(\boldsymbol{a}_3^\intercal\boldsymbol{p}_{,\beta}\right) + \boldsymbol{\mathcal{N}}\boldsymbol{p}_{,\beta}\boldsymbol{a}_3^\intercal + \boldsymbol{a}_3\boldsymbol{p}_{,\beta}^\intercal\boldsymbol{\mathcal{N}}\right)\boldsymbol{p}_{,\alpha} \ . \tag{3.44b}$$

Finally, upon introducing the matrix $\boldsymbol{P}$, whose columns are the vectors $\boldsymbol{g}_i$ of the covariant basis, i.e.

$$\boldsymbol{P} = [\ \boldsymbol{g}_1\ \boldsymbol{g}_2\ \boldsymbol{g}_3\ ] = [\ \boldsymbol{a}_1 + \xi_3\boldsymbol{a}_{3,1} \quad \boldsymbol{a}_2 + \xi_3\boldsymbol{a}_{3,2} \quad \boldsymbol{a}_3\ ]\ , \tag{3.45}$$

one has

$$\boldsymbol{P}_{,1} = [\ \boldsymbol{a}_{1,1} + \xi_3\boldsymbol{a}_{3,11} \quad \boldsymbol{a}_{1,2} + \xi_3\boldsymbol{a}_{3,12} \quad \boldsymbol{a}_{3,1}\ ]\ , \tag{3.46a}$$

$$\boldsymbol{P}_{,2} = [\ \boldsymbol{a}_{1,2} + \xi_3\boldsymbol{a}_{3,12} \quad \boldsymbol{a}_{2,2} + \xi_3\boldsymbol{a}_{3,22} \quad \boldsymbol{a}_{3,2}\ ]\ , \tag{3.46b}$$

$$\boldsymbol{P}_{,3} = [\ \boldsymbol{a}_{3,1} \quad \boldsymbol{a}_{3,2} \quad \boldsymbol{0}\ ]\ , \tag{3.46c}$$

where the derivatives refer to the curvilinear coordinates. The derivatives of the transformation matrix $\boldsymbol{R}$ are finally obtained as

$$\boldsymbol{R}_{,i} = -\boldsymbol{R}\boldsymbol{P}_{,i}^{\intercal}\boldsymbol{R}, \tag{3.47}$$

where Eq.(3.47)is obtained by using $\boldsymbol{R} = \boldsymbol{P}^{-\intercal}$ [113].

3.2.3 Boundary conditions

Since the formulation for ESL theories is derived from the fully 3D principle of virtual work, the boundary conditions are determined based on the applied traction and restraints on the shell volume. The Neumann boundary conditions, applied to the part of the boundary denoted as $\partial\hat{\Omega}_N$, are obtained through a through-the-thickness integration of the traction on the external surface, which is detailed in the following section.

On the other hand, Dirichlet boundary conditions, applied on $\partial\hat{\Omega}_D$, must inherently satisfy the assumptions of shell kinematics at the 3D level. If they do not, an L^2 projection of the displacement field onto the space of shell kinematics is necessary.

It is important to note that different components of the generalized displacement may have different types of boundary conditions applied to the same edge. In other words, the partition of $\partial\hat{\Omega}$ into $\partial\hat{\Omega}_N \cup \partial\hat{\Omega}_D$ may not be uniform for each component of the generalized displacement vector. This situation arises, for instance, when modeling mixed boundary conditions, as is the case in simply-supported edges.

3.2.4 Static analysis

The governing equations for the introduced shell models are inferred from the principle of virtual works that reads as

$$\delta L_{int} = \delta L_{ext}\ , \tag{3.48}$$

where δL_{int} and δL_{ext} are the virtual work of the internal and external forces, respectively. For a multilayered structure they are expressed as

$$\delta L_{int} = \sum_{\ell=1}^{N_\ell} \int_{V^{\langle\ell\rangle}} \delta\boldsymbol{\gamma}^{\langle\ell\rangle\intercal}\boldsymbol{\sigma}^{\langle\ell\rangle}\mathrm{d}V\ , \tag{3.49a}$$

$$\delta L_{ext} = \sum_{\ell=1}^{N_\ell} \int_{V^{\langle\ell\rangle}} \delta\boldsymbol{u}^{\langle\ell\rangle\intercal}\overline{\boldsymbol{b}}^{\langle\ell\rangle}\mathrm{d}V + \sum_{\ell=1}^{N_\ell} \int_{\partial V^{\langle\ell\rangle}} \delta\boldsymbol{u}^{\langle\ell\rangle\intercal}\overline{\boldsymbol{t}}^{\langle\ell\rangle}\mathrm{d}\partial V\ , \tag{3.49b}$$

where $\overline{\boldsymbol{b}}^{\langle\ell\rangle}$ and $\overline{\boldsymbol{t}}^{\langle\ell\rangle}$ are the volume forces acting on $V^{\langle\ell\rangle}$ and the applied tractions acting on $\partial V^{\langle\ell\rangle}$, respectively. It is straightforward to demonstrate from Eq.(3.32) that the virtual strains are given by

$$\delta\boldsymbol{\gamma}^{\langle\ell\rangle} = (\boldsymbol{I}_i + \boldsymbol{W}_i^{\langle\ell\rangle})\delta\boldsymbol{u}_{,i}^{\langle\ell\rangle}\ , \tag{3.50}$$

where the i-th derivative is in Cartesian coordinates. Inserting Eqs.(3.50), (3.32) into Eq.(3.49), and considering the constitutive relationship

$$\boldsymbol{\sigma}^{\langle\ell\rangle} = \boldsymbol{c}^{\langle\ell\rangle}\boldsymbol{\gamma}^{\langle\ell\rangle} \,, \tag{3.51}$$

the virtual internal work is written as

$$\delta L_{int} = \sum_{\ell=1}^{N_\ell} \int_{V^{\langle\ell\rangle}} \delta \boldsymbol{u}_{,i}^{\langle\ell\rangle\intercal} \boldsymbol{C}_{ij}^{\langle\ell\rangle} \boldsymbol{u}_{,j}^{\langle\ell\rangle} \mathrm{d}V, \tag{3.52}$$

where

$$\boldsymbol{C}_{ij}^{\langle\ell\rangle} = \left(\boldsymbol{I}_i^{\intercal} + \boldsymbol{W}_i^{\langle\ell\rangle\intercal}\right) \boldsymbol{c}^{\langle\ell\rangle} \left(\boldsymbol{I}_i + \frac{1}{2}\boldsymbol{W}_i^{\langle\ell\rangle}\right). \tag{3.53}$$

Furthermore, introducing Eq.(3.34) into Eq.(3.52) and integrating along the thickness, one obtains

$$\delta L_{int} = \int_{\hat{\Omega}} \left[\delta \boldsymbol{U}_{,\alpha}^{\intercal} \left(\boldsymbol{Q}_{\alpha\beta}\boldsymbol{U}_{,\beta} + \boldsymbol{R}_{\alpha 3}\boldsymbol{U}\right) + \delta \boldsymbol{U}^{\intercal} \left(\boldsymbol{R}_{3\alpha}\boldsymbol{U}_{,\alpha} + \boldsymbol{S}_{33}\boldsymbol{U}\right)\right] \mathrm{d}\hat{\Omega} \,, \tag{3.54}$$

where the generalized stiffness matrices are introduced as

$$\boldsymbol{Q}_{\alpha\beta} = \sum_{\ell=1}^{N_\ell} \int_{\tau_b^{\langle\ell\rangle}}^{\tau_t^{\langle\ell\rangle}} \boldsymbol{D}_{\alpha i}^{\langle\ell\rangle\intercal} \boldsymbol{C}_{ij}^{\langle\ell\rangle} \boldsymbol{D}_{\beta j}^{\langle\ell\rangle} \sqrt{g} \, \mathrm{d}\xi_3 \,, \tag{3.55a}$$

$$\boldsymbol{R}_{\alpha 3} = \sum_{\ell=1}^{N_\ell} \int_{\tau_b^{\langle\ell\rangle}}^{\tau_t^{\langle\ell\rangle}} \boldsymbol{D}_{\alpha i}^{\langle\ell\rangle\intercal} \boldsymbol{C}_{ij}^{\langle\ell\rangle} \boldsymbol{D}_{0 j}^{\langle\ell\rangle} \sqrt{g} \, \mathrm{d}\xi_3 \,, \tag{3.55b}$$

$$\boldsymbol{R}_{3\alpha} = \sum_{\ell=1}^{N_\ell} \int_{\tau_b^{\langle\ell\rangle}}^{\tau_t^{\langle\ell\rangle}} \boldsymbol{D}_{0 i}^{\langle\ell\rangle\intercal} \boldsymbol{C}_{ij}^{\langle\ell\rangle} \boldsymbol{D}_{\alpha j}^{\langle\ell\rangle} \sqrt{g} \, \mathrm{d}\xi_3 \,, \tag{3.55c}$$

$$\boldsymbol{S}_{33} = \sum_{\ell=1}^{N_\ell} \int_{\tau_b^{\langle\ell\rangle}}^{\tau_t^{\langle\ell\rangle}} \boldsymbol{D}_{0 i}^{\langle\ell\rangle\intercal} \boldsymbol{C}_{ij}^{\langle\ell\rangle} \boldsymbol{D}_{0 j}^{\langle\ell\rangle} \sqrt{g} \, \mathrm{d}\xi_3 \,, \tag{3.55d}$$

being g the determinant of the metric tensor. Similarly, introducing Eq.(3.30) into Eq.(3.49) and integrating along the thickness, for the virtual work of the external forces one writes

$$\delta L_{ext} = \int_{\hat{\Omega}} \delta \boldsymbol{U}^{\intercal} \overline{\boldsymbol{B}} \, \mathrm{d}\hat{\Omega} + \int_{\partial\hat{\Omega}} \delta \boldsymbol{U}^{\intercal} \overline{\boldsymbol{T}} \, \mathrm{d}\partial\hat{\Omega} \,, \tag{3.56}$$

where $\overline{\boldsymbol{B}}$ and $\overline{\boldsymbol{T}}$ are the generalized domain forces and the generalized boundary forces, respectively. They are defined, as

$$\overline{\boldsymbol{B}} = \boldsymbol{Z}^{\langle\ell\rangle\intercal} \boldsymbol{R}^{\intercal} \bar{\boldsymbol{t}}^{\langle\ell\rangle} \sqrt{g} \sqrt{n_i g^{ij} n_j} \, \Big|_{\xi_3 = \pm\tau/2} + \sum_{\ell=1}^{N_\ell} \int_{\tau_b^{\langle\ell\rangle}}^{\tau_t^{\langle\ell\rangle}} \boldsymbol{Z}^{\langle\ell\rangle\intercal} \boldsymbol{R}^{\intercal} \bar{\boldsymbol{b}}^{\langle\ell\rangle} \sqrt{g} \, \mathrm{d}\xi_3 \,, \tag{3.57a}$$

$$\overline{\boldsymbol{T}} = \sum_{\ell=1}^{N_\ell} \int_{\tau_b^{\langle\ell\rangle}}^{\tau_t^{\langle\ell\rangle}} \boldsymbol{Z}^{\langle\ell\rangle\intercal} \boldsymbol{R}^{\intercal} \bar{\boldsymbol{t}}^{\langle\ell\rangle} \sqrt{g} \sqrt{n_i g^{ij} n_j} \, \mathrm{d}\xi_3 \,. \tag{3.57b}$$

where the notation $f|_{\xi_3=\bar{\xi}_3}$ indicates evaluation of f at $\xi_3 = \bar{\xi}_3$. Finally, the following expression of the principle of virtual works for the non-linear static analysis of multilayered shells is obtained, which represents the weak form of the problem governing equations

$$\int_{\hat{\Omega}} \left[\delta \boldsymbol{U}_{,\alpha}^{\intercal} \left(\boldsymbol{Q}_{\alpha\beta}\boldsymbol{U}_{,\beta} + \boldsymbol{R}_{\alpha 3}\boldsymbol{U}\right) + \delta \boldsymbol{U}^{\intercal} \left(\boldsymbol{R}_{3\alpha}\boldsymbol{U}_{,\alpha} + \boldsymbol{S}_{33}\boldsymbol{U}\right)\right] \mathrm{d}\hat{\Omega} = \int_{\hat{\Omega}} \delta \boldsymbol{U}^{\intercal} \overline{\boldsymbol{B}} \, \mathrm{d}\hat{\Omega} + \int_{\partial\hat{\Omega}} \delta \boldsymbol{U}^{\intercal} \overline{\boldsymbol{T}} \, \mathrm{d}\partial\hat{\Omega} \,. \tag{3.58}$$

As a final remark, it should be noted that Eq.(3.58) corresponds to a non-linear static analysis. In cases where small displacements are expected, the linearized equation for strain can be adopted. This simplification corresponds to neglecting the terms $\boldsymbol{W}_i$ in the all the equations of this section. Additionally, it is straightforward to prove that under the small displacement assumption assumption, $\boldsymbol{R}_{3\alpha} = \boldsymbol{R}_{\alpha 3}^{\mathrm{T}}$.

Variation of the virtual work of the internal forces

Since the formulation proposed for statics relies on the geometrically non-linear expression of the strain, the solving strategy must use an iterative scheme that requires the Jacobian of the virtual work. Therefore, the variation in the virtual work of the internal forces is written as

$$\delta(\delta L_{int}) = \sum_{\ell=1}^{N_\ell} \int_{V^{\langle \ell \rangle}} \delta(\delta \boldsymbol{\gamma}^{\langle \ell \rangle \intercal} \boldsymbol{\sigma}^{\langle \ell \rangle}) \mathrm{d}V \ . \tag{3.59}$$

After some manipulations, accounting for Eqs.(3.32) and (3.51), Eq.(3.59) is written as

$$\delta(\delta L_{int}) = \sum_{\ell=1}^{N_\ell} \int_{V^{\langle \ell \rangle}} \delta \boldsymbol{u}_{,i}^{\langle \ell \rangle \intercal} \boldsymbol{C}_{ij}^{\langle \ell \rangle J} \delta \boldsymbol{u}_{,j}^{\langle \ell \rangle} \mathrm{d}V \ . \tag{3.60}$$

where the derivatives with the comma notation refer to the Cartesian coordinates. The matrices $\boldsymbol{C}_{ij}^{\langle \ell \rangle J}$ are defined as

$$\boldsymbol{C}_{ij}^{\langle \ell \rangle J} = \left(\boldsymbol{I}_i + \boldsymbol{W}_i^{\langle \ell \rangle} \right)^{\intercal} \boldsymbol{c}^{\langle \ell \rangle} \left(\boldsymbol{I}_j + \boldsymbol{W}_j^{\langle \ell \rangle} \right) + \sigma_{ij}^{\langle \ell \rangle} \boldsymbol{I} \ , \tag{3.61}$$

being $\boldsymbol{I}$ the 3×3 identity matrix. Using Eq.(3.34) and integrating over the thickness, Eq.(3.60) becomes

$$\delta(\delta L_{int}) = \int_{\hat{\Omega}} \left[\delta \boldsymbol{U}^{\intercal}{}_{,\alpha} \left(\boldsymbol{Q}_{\alpha\beta}^{J} \delta \boldsymbol{U}_{,\beta} + \boldsymbol{R}_{\alpha 3}^{J} \delta \boldsymbol{U} \right) + \delta \boldsymbol{U}^{\intercal} \left(\boldsymbol{R}_{3\alpha}^{J} \delta \boldsymbol{U}_{,\alpha} + \boldsymbol{S}_{33}^{J} \delta \boldsymbol{U} \right) \right] \mathrm{d}\hat{\Omega} \ , \tag{3.62}$$

where the generalized tangent stiffness matrices are introduced as

$$\boldsymbol{Q}_{\alpha\beta}^{J} = \sum_{\ell=1}^{N_\ell} \int_{\tau_b^{\langle \ell \rangle}}^{\tau_t^{\langle \ell \rangle}} \boldsymbol{D}_{\alpha i}^{\langle \ell \rangle \intercal} \boldsymbol{C}_{ij}^{\langle \ell \rangle J} \boldsymbol{D}_{\beta j}^{\langle \ell \rangle} \sqrt{g} \ \mathrm{d}\xi_3 \ , \tag{3.63a}$$

$$\boldsymbol{R}_{\alpha 3}^{J} = \sum_{\ell=1}^{N_\ell} \int_{\tau_b^{\langle \ell \rangle}}^{\tau_t^{\langle \ell \rangle}} \boldsymbol{D}_{\alpha i}^{\langle \ell \rangle \intercal} \boldsymbol{C}_{ij}^{\langle \ell \rangle J} \boldsymbol{D}_{0 j}^{\langle \ell \rangle} \sqrt{g} \ \mathrm{d}\xi_3 \ , \tag{3.63b}$$

$$\boldsymbol{R}_{3\alpha}^{J} = \sum_{\ell=1}^{N_\ell} \int_{\tau_b^{\langle \ell \rangle}}^{\tau_t^{\langle \ell \rangle}} \boldsymbol{D}_{0 i}^{\langle \ell \rangle \intercal} \boldsymbol{C}_{ij}^{\langle \ell \rangle J} \boldsymbol{D}_{\alpha j}^{\langle \ell \rangle} \sqrt{g} \ \mathrm{d}\xi_3 \ , \tag{3.63c}$$

$$\boldsymbol{S}_{33}^{J} = \sum_{\ell=1}^{N_\ell} \int_{\tau_b^{\langle \ell \rangle}}^{\tau_t^{\langle \ell \rangle}} \boldsymbol{D}_{0 i}^{\langle \ell \rangle \intercal} \boldsymbol{C}_{ij}^{\langle \ell \rangle J} \boldsymbol{D}_{0 j}^{\langle \ell \rangle} \sqrt{g} \ \mathrm{d}\xi_3 \ . \tag{3.63d}$$

To conclude, it is worth mentioning that it is easy to demonstrate that $\boldsymbol{R}_{3\alpha}^{J} = \boldsymbol{R}_{3\alpha}^{J \intercal}$.

Strong form of the equations for statics

After integration by parts of the Eq.(3.58), ensuring that the resulting relation holds for any virtual variation of the primary variables provides the following shell governing equations and the associated natural boundary conditions

$$-\frac{\partial}{\partial\xi_\alpha}\left(\boldsymbol{Q}_{\alpha\beta}\boldsymbol{U}_{,\beta}+\boldsymbol{R}_{\alpha3}\boldsymbol{U}\right)+\boldsymbol{R}_{3\alpha}\boldsymbol{U}_{,\alpha}+\boldsymbol{S}_{33}\boldsymbol{U}=\overline{\boldsymbol{B}} \qquad \text{in } \hat{\Omega}\ , \tag{3.64a}$$

$$\nu_\alpha\left(\boldsymbol{Q}_{\alpha\beta}\boldsymbol{U}_{,\beta}+\boldsymbol{R}_{\alpha3}\boldsymbol{U}\right)=\overline{\boldsymbol{T}} \qquad \text{on } \partial\hat{\Omega}_N\ , \tag{3.64b}$$

where ν_α are the direction cosines of the outer unit normal defined over the part $\partial\hat{\Omega}_N$ of the $\hat{\Omega}$ domain where natural boundary conditions are prescribed.

3.2.5 Buckling analysis

To obtain the two-dimensional formulation for linear buckling, the starting point is the three-dimensional variational statement of the Eulerian buckling [134] introduced in Chapter 2, and recalled here as

$$\sum_{\ell=1}^{N_\ell}\int_{V^{\langle\ell\rangle}}\delta\boldsymbol{\gamma}^{\langle\ell\rangle\intercal}\boldsymbol{\sigma}^{\langle\ell\rangle}\mathrm{d}V=-\lambda\sum_{\ell=1}^{N_\ell}\int_{V^{\langle\ell\rangle}}\overline{\sigma}_{ij}^{\langle\ell\rangle}\delta\boldsymbol{u}_{,i}^{\langle\ell\rangle\intercal}\boldsymbol{u}_{,j}^{\langle\ell\rangle}\mathrm{d}V\ . \tag{3.65}$$

The buckling problem is then expressed only in terms of the adjacent configuration of the generalized displacement vector $\boldsymbol{U}$ by substituting Eqs.(3.34), (3.38), and (3.51) into Eq.(3.65) to obtain

$$\begin{aligned}\int_{\hat{\Omega}}\left[\delta\boldsymbol{U}_{,\alpha}^{\intercal}\left(\boldsymbol{Q}_{\alpha\beta}\boldsymbol{U}_{,\beta}+\boldsymbol{R}_{\alpha3}\boldsymbol{U}\right)+\delta\boldsymbol{U}^{\intercal}\left(\boldsymbol{R}_{\alpha3}^{\intercal}\boldsymbol{U}_{,\alpha}+\boldsymbol{S}_{33}\boldsymbol{U}\right)\right]\mathrm{d}\hat{\Omega}=\\ -\lambda\int_{\hat{\Omega}}\left[\delta\boldsymbol{U}_{,\alpha}^{\intercal}\left(\boldsymbol{Q}_{\alpha\beta}^{G}\boldsymbol{U}_{,\beta}+\boldsymbol{R}_{\alpha3}^{G}\boldsymbol{U}\right)+\delta\boldsymbol{U}^{\intercal}\left(\boldsymbol{R}_{\alpha3}^{G\intercal}\boldsymbol{U}_{,\alpha}+\boldsymbol{S}_{33}^{G}\boldsymbol{U}\right)\right]\mathrm{d}\hat{\Omega}\ ,\end{aligned} \tag{3.66}$$

where the matrices $\boldsymbol{Q}_{\alpha\beta}$, $\boldsymbol{R}_{\alpha3}$, and $\boldsymbol{S}_{33}$ have the same meaning of those appearing in Eq.(3.58) and are given in Eq.(3.55), while the matrices $\boldsymbol{Q}_{\alpha\beta}^{G}$, $\boldsymbol{R}_{\alpha3}^{G}$, and $\boldsymbol{S}_{33}^{G}$ represent the generalized geometric stiffness matrices and are defined as follows

$$\boldsymbol{Q}_{\alpha\beta}^{G}=\sum_{\ell=1}^{N_\ell}\int_{\tau_b^{\langle\ell\rangle}}^{\tau_t^{\langle\ell\rangle}}\boldsymbol{D}_{\alpha i}^{\intercal}\overline{\sigma}_{ij}^{\langle\ell\rangle}\boldsymbol{D}_{\beta j}\sqrt{g}\ \mathrm{d}\xi_3\ , \tag{3.67a}$$

$$\boldsymbol{R}_{\alpha3}^{G}=\sum_{\ell=1}^{N_\ell}\int_{\tau_b^{\langle\ell\rangle}}^{\tau_t^{\langle\ell\rangle}}\boldsymbol{D}_{\alpha i}^{\intercal}\overline{\sigma}_{ij}^{\langle\ell\rangle}\boldsymbol{D}_{0j}\sqrt{g}\ \mathrm{d}\xi_3\ , \tag{3.67b}$$

$$\boldsymbol{S}_{33}^{G}=\sum_{\ell=1}^{N_\ell}\int_{\xi_{3b}^{\langle\ell\rangle}}^{\xi_{3t}^{\langle\ell\rangle}}\boldsymbol{D}_{0i}^{\intercal}\overline{\sigma}_{ij}^{\langle\ell\rangle}\boldsymbol{D}_{0j}\sqrt{g}\ \mathrm{d}\xi_3\ . \tag{3.67c}$$

The problem stated in Eq.(3.66) aims at finding the smallest eigenvalue that would represent the first multiplicative factor to the external loads in order for the structure to buckle. The associated eigenfunction $\boldsymbol{U}$ represent the shape of the deformed buckled configuration.

At this point, it is wort mentioning that the formulation presented does not pose limitation on the definition of the mid-surface and the laminate employed. However, the utility of a buckling analysis for shells with generic curvature and lamination sequences is questionable. This is due to the coupling that appears in the general case between membrane and flexural behaviours of the structure considered that make the buckling phenomena not clearly identified, unless the loading condition does not excite this coupling, which is a rather academic situation for a general laminated shell. However, when the aforementioned coupling exists but is small, the buckling analysis would still be useful to give indications regarding the values of the load for which the response of the structure can drastically change. Keeping this in mind, it was decided not to impose limitation on the shell geometry and the lamination sequence.

3.2.6 Transient analysis

The two-dimensional governing equations of transient analysis for shells are derived from the weak form of the elasto-dynamic problem for a multi-layered solid, which reads

$$\sum_{\ell=1}^{N_\ell} \int_{V^{\langle\ell\rangle}} \left(\delta \boldsymbol{u}^{\langle\ell\rangle\intercal} \rho^{\langle\ell\rangle} \ddot{\boldsymbol{u}}^{\langle\ell\rangle} + \delta \boldsymbol{\gamma}^{\langle\ell\rangle\intercal} \boldsymbol{\sigma}^{\langle\ell\rangle}\right) \mathrm{d}V = \sum_{\ell=1}^{N_\ell} \int_{V^{\langle\ell\rangle}} \delta \boldsymbol{u}^{\langle\ell\rangle\intercal} \overline{\boldsymbol{b}}^{\langle\ell\rangle} \mathrm{d}V + \sum_{\ell=1}^{N_\ell} \int_{\partial V^{\langle\ell\rangle}} \delta \boldsymbol{u}^{\langle\ell\rangle\intercal} \overline{\boldsymbol{t}}^{\langle\ell\rangle} \mathrm{d}\partial V \ , \tag{3.68}$$

where $\rho^{\langle\ell\rangle}$ is the density of the ℓ-th layer, $\ddot{\boldsymbol{u}}^{\langle\ell\rangle}$ is the second derivative of $\boldsymbol{u}^{\langle\ell\rangle}$ with respect to time. It is worth noting that the damping will be modeled through the Rayleigh method directly on the final solving system. Using Eqs.(3.51), (3.38), (3.30) and (3.34), it is possible to obtain the following weak formulation for the transient analysis of laminated shells in terms of the vector of the generalized displacements $\boldsymbol{U}$

$$\int_{\hat{\Omega}} \delta \boldsymbol{U}^\intercal \boldsymbol{M} \ddot{\boldsymbol{U}} \mathrm{d}\hat{\Omega} + \int_{\hat{\Omega}} \left[\delta \boldsymbol{U}^\intercal_{,\alpha} \left(\boldsymbol{Q}_{\alpha\beta} \boldsymbol{U}_{,\beta} + \boldsymbol{R}_{\alpha 3} \boldsymbol{U}\right) + \delta \boldsymbol{U}^\intercal \left(\boldsymbol{R}^\intercal_{\alpha 3} \boldsymbol{U}_{,\alpha} + \boldsymbol{S}_{33} \boldsymbol{U}\right)\right] \mathrm{d}\hat{\Omega} = \\ + \int_{\hat{\Omega}} \delta \boldsymbol{U}^\intercal \overline{\boldsymbol{B}} \ \mathrm{d}\hat{\Omega} + \int_{\partial\hat{\Omega}} \delta \boldsymbol{U}^\intercal \overline{\boldsymbol{T}} \ \mathrm{d}\partial\hat{\Omega} \ , \tag{3.69}$$

where the matrices $\boldsymbol{Q}_{\alpha\beta}$, $\boldsymbol{R}_{\alpha 3}$, are the same as those introduced for the static analysis and $\ddot{\boldsymbol{U}}$ is the second time derivative of $\boldsymbol{U}$. The matrix $\boldsymbol{M}$ is referred to as generalized mass matrix and is defined as

$$\boldsymbol{M} = \sum_{\ell=1}^{N_\ell} \int_{\tau_b^{\langle\ell\rangle}}^{\tau_t^{\langle\ell\rangle}} \boldsymbol{Z}^{\langle\ell\rangle\intercal} \boldsymbol{R}^\intercal \boldsymbol{R} \boldsymbol{Z}^{\langle\ell\rangle} \rho^{\langle\ell\rangle} \sqrt{g} \ \mathrm{d}\xi_3 \ . \tag{3.70}$$

3.2.7 Free-vibration

Similarly to the preceding sections, the equations governing the free-vibration analysis of a laminated shell are derived from the following variational statement that refers to three-dimensional multilayered solid

$$\sum_{\ell=1}^{N_\ell} \int_{V^{\langle\ell\rangle}} \delta \boldsymbol{\gamma}^{\langle\ell\rangle\intercal} \boldsymbol{\sigma}^{\langle\ell\rangle} \mathrm{d}V = \omega^2 \sum_{\ell=1}^{N_\ell} \int_{V^{\langle\ell\rangle}} \delta \boldsymbol{u}^{\langle\ell\rangle\intercal} \rho^{\langle\ell\rangle} \boldsymbol{u}^{\langle\ell\rangle} \mathrm{d}V \ , \tag{3.71}$$

where ω is a generic natural frequency. Upon applying the same substitutions as in the previous sections, the corresponding two-dimensional shell formulation is obtained

$$\int_{\hat{\Omega}} \left[\delta \boldsymbol{U}_{,\alpha}^{\intercal} \left(\boldsymbol{Q}_{\alpha\beta}\boldsymbol{U}_{,\beta} + \boldsymbol{R}_{\alpha 3}\boldsymbol{U}\right) + \delta \boldsymbol{U}^{\intercal} \left(\boldsymbol{R}_{\alpha 3}^{\intercal}\boldsymbol{U}_{,\alpha} + \boldsymbol{S}_{33}\boldsymbol{U}\right)\right] \mathrm{d}\hat{\Omega} = \omega^2 \int_{\hat{\Omega}} \delta \boldsymbol{U}^{\intercal}\boldsymbol{M}\boldsymbol{U}\mathrm{d}\hat{\Omega}\,. \tag{3.72}$$

Table 3.1: Two-dimensional formulation for the mechanical problems investigated in this thesis using higher-order theories.

Static analysis

$$\int_{\hat{\Omega}} \left[\delta \boldsymbol{U}_{,\alpha}^{\intercal} \left(\boldsymbol{Q}_{\alpha\beta}\boldsymbol{U}_{,\beta} + \boldsymbol{R}_{\alpha 3}\boldsymbol{U}\right) + \delta \boldsymbol{U}^{\intercal} \left(\boldsymbol{R}_{3\alpha}\boldsymbol{U}_{,\alpha} + \boldsymbol{S}_{33}\boldsymbol{U}\right)\right] \mathrm{d}\hat{\Omega} = + \int_{\hat{\Omega}} \delta \boldsymbol{U}^{\intercal}\overline{\boldsymbol{B}}\ \mathrm{d}\hat{\Omega} + \int_{\partial\hat{\Omega}} \delta \boldsymbol{U}^{\intercal}\overline{\boldsymbol{T}}\ \mathrm{d}\partial\hat{\Omega}\,.$$

Linear buckling analysis

$$\int_{\hat{\Omega}} \left[\delta \boldsymbol{U}_{,\alpha}^{\intercal} \left(\boldsymbol{Q}_{\alpha\beta}\boldsymbol{U}_{,\beta} + \boldsymbol{R}_{\alpha 3}\boldsymbol{U}\right) + \delta \boldsymbol{U}^{\intercal} \left(\boldsymbol{R}_{\alpha 3}^{\intercal}\boldsymbol{U}_{,\alpha} + \boldsymbol{S}_{33}\boldsymbol{U}\right)\right] \mathrm{d}\hat{\Omega} = - \lambda \int_{\hat{\Omega}} \left[\delta \boldsymbol{U}_{,\alpha}^{\intercal} \left(\boldsymbol{Q}_{\alpha\beta}^{G}\boldsymbol{U}_{,\beta} + \boldsymbol{R}_{\alpha 3}^{G}\boldsymbol{U}\right) + \delta \boldsymbol{U}^{\intercal} \left(\boldsymbol{R}_{\alpha 3}^{G\intercal}\boldsymbol{U}_{,\alpha} + \boldsymbol{S}_{33}^{G}\boldsymbol{U}\right)\right] \mathrm{d}\hat{\Omega},$$

Linear transient analysis

$$\int_{\hat{\Omega}} \delta \boldsymbol{U}^{\intercal}\boldsymbol{M}\ddot{\boldsymbol{U}}\mathrm{d}\hat{\Omega} + \int_{\hat{\Omega}} \left[\delta \boldsymbol{U}_{,\alpha}^{\intercal} \left(\boldsymbol{Q}_{\alpha\beta}\boldsymbol{U}_{,\beta} + \boldsymbol{R}_{\alpha 3}\boldsymbol{U}\right) + \delta \boldsymbol{U}^{\intercal} \left(\boldsymbol{R}_{\alpha 3}^{\intercal}\boldsymbol{U}_{,\alpha} + \boldsymbol{S}_{33}\boldsymbol{U}\right)\right] \mathrm{d}\hat{\Omega} = + \int_{\hat{\Omega}} \delta \boldsymbol{U}^{\intercal}\overline{\boldsymbol{B}}\ \mathrm{d}\hat{\Omega} + \int_{\partial\hat{\Omega}} \delta \boldsymbol{U}^{\intercal}\overline{\boldsymbol{T}}\ \mathrm{d}\partial\hat{\Omega},$$

Linear free-vibration analysis

$$\int_{\hat{\Omega}} \left[\delta \boldsymbol{U}_{,\alpha}^{\intercal} \left(\boldsymbol{Q}_{\alpha\beta}\boldsymbol{U}_{,\beta} + \boldsymbol{R}_{\alpha 3}\boldsymbol{U}\right) + \delta \boldsymbol{U}^{\intercal} \left(\boldsymbol{R}_{\alpha 3}^{\intercal}\boldsymbol{U}_{,\alpha} + \boldsymbol{S}_{33}\boldsymbol{U}\right)\right] \mathrm{d}\hat{\Omega} = \omega^2 \int_{\hat{\Omega}} \delta \boldsymbol{U}^{\intercal}\boldsymbol{M}\boldsymbol{U}\mathrm{d}\hat{\Omega}\,.$$

3.3 Layer-Wise shell theories

The ESL approach excels at accurately capturing higher-order through-the-thickness behaviors in moderately thick shells. However, when dealing with laminates, the level of accuracy might not suffices in certain applications. In fact, to ensure accurate analysis, two critical condition must be met at the interfaces of adjacent layers:

i. The displacement vector field should be continuous in order to prevent voids or interpenetration in the deformed configuration.

ii. Equilibrium conditions must be met, particularly the continuous variation of out-of-plane stress components across the thickness. This necessitates discontinuity in the ξ_3 derivative of the displacement field at the layers' interfaces. In fact, the material properties exhibit a discontinuity at these interfaces, and to maintain continuous out-of-plane stress components, the strain, that is a linear combination of derivatives of the displacement, must exhibit discontinuity.

In the ESL approach, the thickness functions are assumed to be C^∞ (infinitely differentiable). Consequently, while the first condition is automatically met, the second condition is not guaranteed. This limitation can impact the accuracy in predicting the out-of-plane stress components.

In this section, the Layer-Wise (LW) approach is introduced, which is designed to tackle this issue by modifying the space for the thickness function in the kinematic hypothesis. In the LW approach, C^0 thickness functions are employed, which are continuous but not necessarily differentiable. These thickness functions are designed such that the points of non-differentiability coincide with the layers' interfaces [135].

3.3.1 Shell kinematics

In the Layer-Wise LW approach, the shell kinematics relies on a per-layer expansion of the displacement field throughout the shell thickness. This means that the covariant components of the displacement vector can be expressed as follows

$$u_{\xi_i}^{\langle\ell\rangle}(\xi_1,\xi_2,\xi_3) = \sum_{k=0}^{N_i\langle\ell\rangle} Z_{ik}^{\langle\ell\rangle i}(\xi_3) U_{ik}^{\langle\ell\rangle}(\xi_1,\xi_2) \ , \tag{3.73}$$

where $N_i^{\langle\ell\rangle}$ represents the order of the expansion assumed for u_{ξ_i}, $Z_{ik}^{\langle\ell\rangle}(\xi_3)$ are the thickness function and $U_{ik}(\xi_1,\xi_2)$ are the unknown generalized displacements for the ℓ-th layer. It is worth noting that, when comparing Eq.(3.73) with Eq.(3.28) the generalized displacements $U_{ik}^{\langle\ell\rangle}$ as well as the thickness functions $Z_{ik}^{\langle\ell\rangle}$ have been enriched with a superscript $\langle\ell\rangle$. This superscript signifies their dependence on the laminate layer.

In the LW approach, the functions $Z_{ik}^{\langle\ell\rangle}(\xi_3)$ must be carefully chosen to ensure that $u_{\xi_i}^{\langle\ell\rangle}$ remains C^0 continuous, with points of non-differentiability positioned at the interfaces between layers. Various options are available for making this choice, with examples including Lagrange functions [136] or spline functions [137]. In this work, a linear combination of Legendre polynomials scaled to the layers' interval is employed. The functions $Z_{ik}^{\langle\ell\rangle}(\xi_3)$ are thus expressed as

$$Z_{ik}^{\langle\ell\rangle}(\xi_3) = \begin{cases} (\mathcal{L}_0(\zeta^{\langle\ell\rangle}) - \mathcal{L}_1(\zeta^{\langle\ell\rangle}))/2 & \text{when } k = 0 \ , \\ \mathcal{L}_{k+1}(\zeta^{\langle\ell\rangle}) - \mathcal{L}_{k-1}(\zeta^{\langle\ell\rangle}) & \text{when } k = 1, ..., N_i^{\langle\ell\rangle} - 1 \ , \\ (\mathcal{L}_0(\zeta^{\langle\ell\rangle}) + \mathcal{L}_1(\zeta^{\langle\ell\rangle}))/2 & \text{when } k = N_i^{\langle\ell\rangle} \ , \end{cases} \tag{3.74}$$

where $\mathcal{L}_i$ is the i-th Legendre polynomial scaled in the interval $\hat{I}_3^{\langle\ell\rangle}$ and $\zeta^{\langle\ell\rangle}$ spans from -1 to $+1$ within each interval $\hat{I}_3^{\langle\ell\rangle}$ where ξ_3 spans. Specifically, $\zeta^{\langle\ell\rangle}$ is defined as

$$\zeta^{\langle\ell\rangle} = \frac{2\xi_3 - \tau_b^{\langle\ell\rangle} - \tau_t^{\langle\ell\rangle}}{\tau_t^{\langle\ell\rangle} - \tau_b^{\langle\ell\rangle}} \ . \tag{3.75}$$

This choice ensures that

$$Z_{i0}^{\langle\ell\rangle}(\zeta^{\langle\ell\rangle}=0)=1\ , \tag{3.76}$$
$$Z_{ik}^{\langle\ell\rangle}(\zeta^{\langle\ell\rangle}=0)=0\quad\text{for}\quad k\neq 0\ , \tag{3.77}$$
$$Z_{iN_i^{\langle\ell\rangle}}^{\langle\ell\rangle}(\zeta^{\langle\ell\rangle}=1)=1\ , \tag{3.78}$$
$$Z_{ik}^{\langle\ell\rangle}(\zeta^{\langle\ell\rangle}=1)=0\quad\text{for}\quad k\neq N_i^{\langle\ell\rangle}\ . \tag{3.79}$$

Hence, for each covariant component, the first and last generalized displacements directly correspond to that component at $\tau_b^{\langle\ell\rangle}$ and $\tau_t^{\langle\ell\rangle}$ respectively. More specifically,

$$u_{\xi_i}(\zeta^{\langle\ell\rangle}=0)=u_{\xi_i}(\xi_3=\tau_b^{\langle\ell\rangle})=U_{i0}^{\langle\ell\rangle}\ , \tag{3.80a}$$
$$u_{\xi_i}(\zeta^{\langle\ell\rangle}=1)=u_{\xi_i}(\xi_3=\tau_t^{\langle\ell\rangle})=U_{iN_i^{\langle\ell\rangle}}^{\langle\ell\rangle}\ . \tag{3.80b}$$

The continuity of the displacement between nearby layers is therefore enforced by simply imposing that $U_{iN_i^{\langle\ell\rangle}}^{\langle\ell\rangle}=U_{i0}^{\langle\ell+1\rangle}$. This means that for each interface, there are three conditions (one for each covariant component of the displacement) that reduce the number of independent generalized displacements. Collecting the generalized displacements of the ℓ-th layer in the vector $\boldsymbol{U}^{\langle\ell\rangle}$ in such a way that

$$\boldsymbol{u}_\xi^{\langle\ell\rangle}=\boldsymbol{Z}^{\langle\ell\rangle}\boldsymbol{U}^{\langle\ell\rangle}\ , \tag{3.81}$$

where $\boldsymbol{Z}^{\langle\ell\rangle}$ consistently collects the thickness function for the ℓ-th layer, one may write

$$\begin{bmatrix}\boldsymbol{U}^{\langle 1\rangle}\\ \boldsymbol{U}^{\langle 2\rangle}\\ \vdots\\ \boldsymbol{U}^{\langle N_\ell\rangle}\end{bmatrix}\boldsymbol{\mathcal{H}}=\boldsymbol{U}\ , \tag{3.82}$$

where the matrix $\boldsymbol{\mathcal{H}}$ contains only zeros and ones is such a way to link the generalized displacements for each layer with the correspondent independent generalized displacement at the laminate level.

In the LW approach, the orders for the expansion of the displacement are typically taken the same for each component and for each layer. A generic LW theory is therefore denoted as LD_{N_p} where N_p is the common order of expansion. To exemplify, for a first order LW theory L_1, where $N_i^{\langle\ell\rangle}=1$ for each component and for each layer, Eq.(3.82) is

expressed with extended matrices as

$$\begin{bmatrix} U_{10}^{\langle 1\rangle} \\ U_{20}^{\langle 1\rangle} \\ U_{30}^{\langle 1\rangle} \\ U_{11}^{\langle 1\rangle} \\ U_{21}^{\langle 1\rangle} \\ U_{31}^{\langle 1\rangle} \\ U_{10}^{\langle 2\rangle} \\ U_{20}^{\langle 2\rangle} \\ U_{30}^{\langle 2\rangle} \\ U_{11}^{\langle 2\rangle} \\ U_{21}^{\langle 2\rangle} \\ U_{31}^{\langle 2\rangle} \\ U_{10}^{\langle 3\rangle} \\ U_{20}^{\langle 3\rangle} \\ U_{30}^{\langle 3\rangle} \\ U_{11}^{\langle 3\rangle} \\ U_{21}^{\langle 3\rangle} \\ U_{31}^{\langle 3\rangle} \end{bmatrix} = \begin{bmatrix} 1 & 0 & 0 & 0 & 0 & 0 & 0 & 0 & 0 & 0 & 0 & 0 \\ 0 & 1 & 0 & 0 & 0 & 0 & 0 & 0 & 0 & 0 & 0 & 0 \\ 0 & 0 & 1 & 0 & 0 & 0 & 0 & 0 & 0 & 0 & 0 & 0 \\ 0 & 0 & 0 & 1 & 0 & 0 & 0 & 0 & 0 & 0 & 0 & 0 \\ 0 & 0 & 0 & 0 & 1 & 0 & 0 & 0 & 0 & 0 & 0 & 0 \\ 0 & 0 & 0 & 0 & 0 & 1 & 0 & 0 & 0 & 0 & 0 & 0 \\ 0 & 0 & 0 & 1 & 0 & 0 & 0 & 0 & 0 & 0 & 0 & 0 \\ 0 & 0 & 0 & 0 & 1 & 0 & 0 & 0 & 0 & 0 & 0 & 0 \\ 0 & 0 & 0 & 0 & 0 & 1 & 0 & 0 & 0 & 0 & 0 & 0 \\ 0 & 0 & 0 & 0 & 0 & 0 & 1 & 0 & 0 & 0 & 0 & 0 \\ 0 & 0 & 0 & 0 & 0 & 0 & 0 & 1 & 0 & 0 & 0 & 0 \\ 0 & 0 & 0 & 0 & 0 & 0 & 0 & 0 & 1 & 0 & 0 & 0 \\ 0 & 0 & 0 & 0 & 0 & 0 & 1 & 0 & 0 & 0 & 0 & 0 \\ 0 & 0 & 0 & 0 & 0 & 0 & 0 & 1 & 0 & 0 & 0 & 0 \\ 0 & 0 & 0 & 0 & 0 & 0 & 0 & 0 & 1 & 0 & 0 & 0 \\ 0 & 0 & 0 & 0 & 0 & 0 & 0 & 0 & 0 & 1 & 0 & 0 \\ 0 & 0 & 0 & 0 & 0 & 0 & 0 & 0 & 0 & 0 & 1 & 0 \\ 0 & 0 & 0 & 0 & 0 & 0 & 0 & 0 & 0 & 0 & 0 & 1 \end{bmatrix} \begin{bmatrix} U_1 \\ U_2 \\ U_3 \\ U_4 \\ U_5 \\ U_6 \\ U_7 \\ U_8 \\ U_9 \\ U_{10} \\ U_{11} \\ U_{12} \end{bmatrix} .$$

3.3.2 Shell mechanics

In order to obtain a two-dimensional formulation for the mechanical problems discussed in the previous section using the LW approximation, the approach followed here consists of building the generalized matrices as described in Sec.3.2 using the polynomial expansion presented in Eq.(3.74) for each layer and assembling them consistently with the continuity condition enforced through Eq.(3.82).

For the sake of conciseness, this process is presented only for definition of the generalized stiffness matrix $\boldsymbol{Q}_{\alpha\beta}$ and the generalized external forces $\overline{\boldsymbol{T}}$ and $\overline{\boldsymbol{B}}$. At a layer level, the contribution to the generalized stiffness matrix is computed as

$$\boldsymbol{Q}_{\alpha\beta}^{\langle\ell\rangle} = \int_{\tau_b^{\langle\ell\rangle}}^{\tau_t^{\langle\ell\rangle}} \boldsymbol{D}_{\alpha i}^{\langle\ell\rangle\intercal} \boldsymbol{C}_{ij}^{\langle\ell\rangle} \boldsymbol{D}_{\beta j}^{\langle\ell\rangle} \sqrt{g}\, \mathrm{d}\xi_3 \,. \tag{3.83}$$

The contribute to the virtual work of the internal forces associated with $\delta\boldsymbol{U}_{,\alpha}^{\langle\ell\rangle}$ and $\boldsymbol{U}_{,\beta}^{\langle\ell\rangle}$ is written as

$$\delta L_{int}^{\alpha\beta} = \sum_{\ell=1}^{N_\ell} \delta\boldsymbol{U}_{,\alpha}^{\langle\ell\rangle} \boldsymbol{Q}_{\alpha\beta}^{\langle\ell\rangle} \boldsymbol{U}_{,\beta}^{\langle\ell\rangle} \,, \tag{3.84}$$

or equivalently

$$\delta L_{int}^{\alpha\beta} = \begin{bmatrix} \delta\boldsymbol{U}^{\langle 1\rangle\intercal} \\ \delta\boldsymbol{U}^{\langle 2\rangle\intercal} \\ \vdots \\ \delta\boldsymbol{U}^{\langle N_\ell\rangle\intercal} \end{bmatrix} \begin{bmatrix} \boldsymbol{Q}_{\alpha\beta}^{\langle 1\rangle} & \boldsymbol{0} & \dots & \boldsymbol{0} \\ \boldsymbol{0} & \boldsymbol{Q}_{\alpha\beta}^{\langle 2\rangle} & \dots & \boldsymbol{0} \\ \vdots & \vdots & \ddots & \vdots \\ \boldsymbol{0} & \boldsymbol{0} & \dots & \boldsymbol{Q}_{\alpha\beta}^{\langle N_\ell\rangle} \end{bmatrix} \begin{bmatrix} \boldsymbol{U}^{\langle 1\rangle} \\ \boldsymbol{U}^{\langle 2\rangle} \\ \vdots \\ \boldsymbol{U}^{\langle N_\ell\rangle} \end{bmatrix} . \tag{3.85}$$

The previous expression can be further modified through Eq.(3.82) in

$$\delta L_{int}^{\alpha\beta} = \delta \boldsymbol{U}^{\intercal} \boldsymbol{\mathcal{H}}^{\intercal} \boldsymbol{Q}_{\alpha\beta} \boldsymbol{\mathcal{H}} \delta \boldsymbol{U} \ , \tag{3.86}$$

where the the generalized stiffness matrix $\boldsymbol{Q}_{\alpha\beta}$ for the whole laminate is defined as

$$\boldsymbol{Q}_{\alpha\beta} = \boldsymbol{\mathcal{H}}^{\intercal} \begin{bmatrix} \boldsymbol{Q}_{\alpha\beta}^{\langle 1 \rangle} & \boldsymbol{0} & \dots & \boldsymbol{0} \\ \boldsymbol{0} & \boldsymbol{Q}_{\alpha\beta}^{\langle 2 \rangle} & \dots & \boldsymbol{0} \\ \vdots & \vdots & \ddots & \vdots \\ \boldsymbol{0} & \boldsymbol{0} & \dots & \boldsymbol{Q}_{\alpha\beta}^{\langle N_\ell \rangle} \end{bmatrix} \boldsymbol{\mathcal{H}} \ . \tag{3.87}$$

Similarly, the definition for the generalized domain and boundary external forces in the LW case are, respectively,

$$\overline{\boldsymbol{B}} = \boldsymbol{\mathcal{H}}^{\intercal} \left(\begin{bmatrix} \int_{\tau_b^{\langle 1 \rangle}}^{\tau_t^{\langle 1 \rangle}} \boldsymbol{Z}^{\langle 1 \rangle \intercal} \boldsymbol{R}^{\intercal} \overline{\boldsymbol{b}}^{\langle 1 \rangle} \sqrt{g} \ \mathrm{d}\xi_3 \\ \int_{\tau_b^{\langle 2 \rangle}}^{\tau_t^{\langle 2 \rangle}} \boldsymbol{Z}^{\langle 2 \rangle \intercal} \boldsymbol{R}^{\intercal} \overline{\boldsymbol{b}}^{\langle 2 \rangle} \sqrt{g} \ \mathrm{d}\xi_3 \\ \vdots \\ \int_{\tau_b^{\langle N_\ell \rangle}}^{\tau_t^{\langle N_\ell \rangle}} \boldsymbol{Z}^{N_\ell \intercal} \boldsymbol{R}^{\intercal} \overline{\boldsymbol{b}}^{\langle N_\ell \rangle} \sqrt{g} \ \mathrm{d}\xi_3 \end{bmatrix} + \begin{bmatrix} \boldsymbol{Z}^{\langle 1 \rangle \intercal} \boldsymbol{R}^{\intercal} \overline{\boldsymbol{t}}^{\langle 1 \rangle} \sqrt{g} \sqrt{n_i g^{ij} n_j} \ \Big|_{\xi_3 = -\tau/2} \\ \boldsymbol{0} \\ \vdots \\ \boldsymbol{Z}^{\langle N_\ell \rangle \intercal} \boldsymbol{R}^{\intercal} \overline{\boldsymbol{t}}^{\langle N_\ell \rangle} \sqrt{g} \sqrt{n_i g^{ij} n_j} \ \Big|_{\xi_3 = +\tau/2} \end{bmatrix} \right) \tag{3.88a}$$

$$\overline{\boldsymbol{T}} = \boldsymbol{\mathcal{H}}^{\intercal} \begin{bmatrix} \int_{\tau_b^{\langle 1 \rangle}}^{\tau_t^{\langle 1 \rangle}} \boldsymbol{Z}^{\langle 1 \rangle \intercal} \boldsymbol{R}^{\intercal} \overline{\boldsymbol{t}}^{\langle 1 \rangle} \sqrt{g} \sqrt{n_i g^{ij} n_j} \ \mathrm{d}\xi_3 \\ \int_{\tau_b^{\langle 2 \rangle}}^{\tau_t^{\langle 2 \rangle}} \boldsymbol{Z}^{\langle 2 \rangle \intercal} \boldsymbol{R}^{\intercal} \overline{\boldsymbol{t}}^{\langle 2 \rangle} \sqrt{g} \sqrt{n_i g^{ij} n_j} \ \mathrm{d}\xi_3 \\ \vdots \\ \int_{\tau_b^{\langle N_\ell \rangle}}^{\tau_t^{\langle N_\ell \rangle}} \boldsymbol{Z}^{\langle N_\ell \rangle \intercal} \boldsymbol{R}^{\intercal} \overline{\boldsymbol{t}}^{\langle N_\ell \rangle} \sqrt{g} \sqrt{n_i g^{ij} n_j} \ \mathrm{d}\xi_3 \end{bmatrix} \tag{3.88b}$$

In a similar fashion, the definition of the remaining generalized matrices introduced in Sec. 3.2 can be easily extended in the LW case. The variational statements can be built in such a way that they have the same expressions as in Tab.(3.1), and they are not reported here for the sake of conciseness.

Chapter 4

The discontinuous Galerkin method

4.1 Discontinuous Galerkin formulation

In this section the principles of the discontinuous Galerkin method are introduced taking as example the linear static analysis through the ESL approach, whose variational statement was discussed in Chapter 3. The subsequent subsections provide a comprehensive formulation tailored to address remaining the mechanical problems outlined in Chapter 3. In this thesis the DG method is used in combination with high-order shell theories, whereas for the Kirchhoff-Love shell theory the Isogeometric Analysis method will be adopted as discussed in Chapter 5. As customary in DG formulations [28], the governing equations are transformed into a system of first-order partial differential equations. This transformation involves the introduction of an auxiliary variable, which, is defined in Ref. [61] as

$$\boldsymbol{\Sigma}_\alpha = \boldsymbol{Q}_{\alpha\beta}\boldsymbol{U}_{,\beta} + \boldsymbol{R}_{\alpha 3}\boldsymbol{U}\,. \tag{4.1}$$

This auxiliary variable enables the replacement of the governing equation with an equivalent set, expressed as

$$-\boldsymbol{\Sigma}_{\alpha,\alpha} + \boldsymbol{R}_{\alpha 3}^{\intercal}\boldsymbol{U}_{,\alpha} + \boldsymbol{S}_{33}\boldsymbol{U} = \overline{\boldsymbol{B}}\,, \tag{4.2a}$$

$$\boldsymbol{\Sigma}_\alpha = \boldsymbol{Q}_{\alpha\beta}\boldsymbol{U}_{,\beta} + \boldsymbol{R}_{\alpha 3}\boldsymbol{U}\,. \tag{4.2b}$$

Upon discretization of the parametric domain $\hat{\Omega}$, these equations, as presented in Eqs.(4.2), are formulated in a weak sense over each mesh element as

$$\int_{\hat{\Omega}^e} \left[\boldsymbol{V}_{,\alpha}^{\intercal}\boldsymbol{\Sigma}_{h\alpha} + \boldsymbol{V}^{\intercal}\left(\boldsymbol{R}_{\alpha 3}^{\intercal}\boldsymbol{U}_{h,\alpha} + \boldsymbol{S}_{33}\boldsymbol{U}_h\right)\right] \mathrm{d}\hat{\Omega} = \int_{\partial\hat{\Omega}^e} \boldsymbol{V}^{\intercal}\widehat{\boldsymbol{\Sigma}}_\alpha \nu_\alpha \mathrm{d}\partial\hat{\Omega} + \int_{\hat{\Omega}^e} \boldsymbol{V}^{\intercal}\overline{\boldsymbol{B}}\mathrm{d}\hat{\Omega}\,, \tag{4.3a}$$

$$\int_{\hat{\Omega}^e} \boldsymbol{\Gamma}_\alpha^{\intercal}\boldsymbol{\Sigma}_{h\alpha}\mathrm{d}\hat{\Omega} = \int_{\hat{\Omega}^e} \boldsymbol{\Gamma}_\alpha^{\intercal}\left(\boldsymbol{Q}_{\alpha\beta}\boldsymbol{U}_{h,\beta} + \boldsymbol{R}_{\alpha 3}\boldsymbol{U}_h\right)\mathrm{d}\hat{\Omega} + \\ + \int_{\partial\hat{\Omega}^e} (\boldsymbol{\Gamma}_\alpha^{\intercal}\boldsymbol{Q}_{\alpha\beta} + \boldsymbol{V}^{\intercal}\boldsymbol{R}_{\beta 3}^{\intercal})(\widehat{\boldsymbol{U}} - \boldsymbol{U}_h)\nu_\beta \mathrm{d}\partial\hat{\Omega}\,, \tag{4.3b}$$

respectively, where: $\boldsymbol{\Sigma}_\alpha$ and $\boldsymbol{U}$ have been replaced by their respective numerical approximations $\boldsymbol{\Sigma}_{h\alpha}$ and $\boldsymbol{U}_h$; $\widehat{\boldsymbol{\Sigma}}_\alpha$ and $\widehat{\boldsymbol{U}}$ are the so-called numerical fluxes, whose explicit expression will be given in Sec. 4.1.1; $\boldsymbol{V}$ and $\boldsymbol{\Gamma}_\alpha$ are the test functions which are taken from the space $\mathcal{V}_{hp}^{N_U}$ as discussed later in this section.

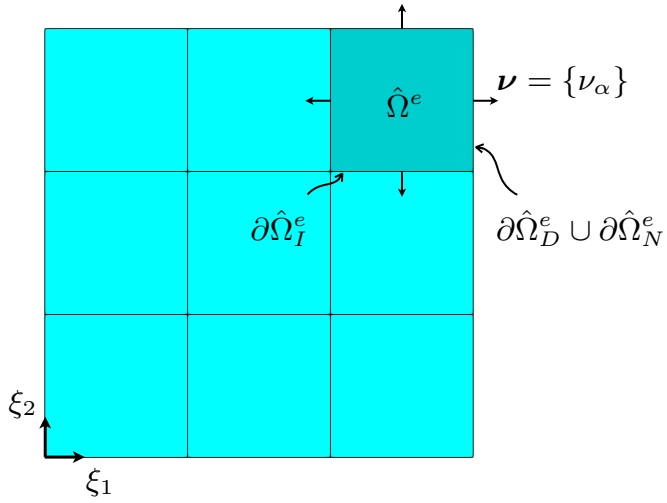

Figure 4.1: Sample 3×3 mesh of a square domain with a generic element in darker color.

Mesh discretization

The domain discretization is carried out using the implicit mesh technique discussed in Chapter 2. The domain $\hat{\Omega}$ is subdivided into N_e non-overlapping elements, such that $\hat{\Omega}^h = \cup_e \hat{\Omega}^e$, where $\hat{\Omega}^e$ denotes the domain of the generic e-th element and $\hat{\Omega}^h$ is an approximation of $\hat{\Omega}$ following discretization. To illustrate, Fig.(4.1) shows a sample 3×3 mesh of a square domain and the generic element $\hat{\Omega}^e$ (in darker color); the figure also shows the element's outer unit normal $\boldsymbol{\nu} = \{\nu_\alpha\}$ and its boundary $\partial\hat{\Omega}^e = \partial\hat{\Omega}^e_I \cup \partial\hat{\Omega}^e_D \cup \partial\hat{\Omega}^e_N$, which consists of the boundary $\partial\hat{\Omega}^e_I$ that the element shares with its neighboring elements, the boundary $\partial\hat{\Omega}^e_D$ where kinematic boundary conditions are prescribed and the boundary $\partial\hat{\Omega}^e_N$ where mechanical boundary conditions are prescribed.

The boundary of $\hat{\Omega}^h$ is denoted as $\partial\hat{\Omega}^h$, which can be partitioned into two parts: $\partial\hat{\Omega}^h_D = \cup_e \partial\hat{\Omega}^e_D$, where Dirichlet boundary conditions are enforced, and $\partial\hat{\Omega}^h_N = \cup_e \partial\hat{\Omega}^e_N$, where Neumann boundary conditions are applied. Additionally, in the meshing process, N_i interfaces $\partial\hat{\Omega}^i_I = \partial\hat{\Omega}^e_I \cap \partial\hat{\Omega}^{e'}_I$ are generated, connecting two neighboring elements e and e', where i denotes the generic i-th interface. The collective set of these interfaces is referred to as $\partial\hat{\Omega}^h_I = \cup_i \partial\hat{\Omega}^i_I$,often referred to as the mesh skeleton.

Average and jump operator

As commonly employed in DG formulations, $\{\bullet\}$ and $[\![\bullet]\!]_\alpha$ are introduced as the so-called average and jump operators, respectively, which are defined at the interface between the elements e and e' as

$$\{\bullet\} = \frac{1}{2}\left(\bullet^e + \bullet^{e'}\right) \quad \text{and} \quad [\![\bullet]\!]_\alpha = \nu^e_\alpha \bullet^e + \nu^{e'}_\alpha \bullet^{e'} \ . \tag{4.4}$$

Here, ν^e_α represents the α-th component of the outer unit normal to the boundary of the e-th element.

Broken integrals

In the reminder of this section, integration over the discretized domain, its boundary, and its skeleton is denoted using the so-called broken integrals, which are defined as

$$\int_{\hat{\Omega}^h} \bullet = \sum_{e=1}^{N_e} \int_{\hat{\Omega}^e} \bullet^e \, \mathrm{d}\hat{\Omega} \,, \tag{4.5a}$$

$$\int_{\partial\hat{\Omega}_D^h} \bullet = \sum_{e=1}^{N_e} \int_{\partial\hat{\Omega}_D^e} \bullet^e \, \mathrm{d}\partial\hat{\Omega} \,, \tag{4.5b}$$

$$\int_{\partial\hat{\Omega}_N^h} \bullet = \sum_{e=1}^{N_e} \int_{\partial\hat{\Omega}_N^e} \bullet^e \, \mathrm{d}\partial\hat{\Omega} \,, \tag{4.5c}$$

$$\int_{\partial\hat{\Omega}^h} \bullet = \sum_{e=1}^{N_e} \int_{\partial\hat{\Omega}_D^e \cup \partial\hat{\Omega}_N^e} \bullet^e \, \mathrm{d}\partial\hat{\Omega} \,, \tag{4.5d}$$

$$\int_{\partial\hat{\Omega}_I^h} \bullet = \sum_{i=1}^{N_i} \int_{\partial\hat{\Omega}_I^i} \bullet^e \, \mathrm{d}\partial\hat{\Omega} \,. \tag{4.5e}$$

Furthermore, the following useful relationship is established

$$\sum_{e=1}^{N_e} \int_{\partial\hat{\Omega}_I^e} \hat{\bullet}^e \tilde{\bullet}^e \nu_\alpha \mathrm{d}\hat{\Omega} = \int_{\partial\hat{\Omega}_I^h} (\{\hat{\bullet}\}[\![\tilde{\bullet}]\!]_\alpha + [\![\hat{\bullet}]\!]_\alpha \{\tilde{\bullet}\}) + \int_{\partial\hat{\Omega}^h} \hat{\bullet}\tilde{\bullet}\nu_\alpha \,, \tag{4.6}$$

where $\hat{\bullet}$ and $\tilde{\bullet}$ are two generic quantities defined over the discretized domain $\hat{\Omega}^h$.

Space of discontinuous vector field

As elaborated in the following sections, the proposed formulation adopts test and trial functions from the space $\mathcal{V}_{hp}^{N_U}$ of discontinuous vector fields defined as

$$\mathcal{V}_{hp}^{N_U} = \left\{ v : \hat{\Omega} \to \mathbb{R} \mid v|_{\hat{\Omega}^e} \in \mathcal{P}_p^e \; \forall e = 1, ..., N_e \right\}^{N_U} , \tag{4.7}$$

where $\mathcal{P}_p^e$ is the space of tensor-product polynomials with degree p defined over the e-th untrimmed mesh element $\hat{\Pi}^e$. Consistently with Chapter 2, it is worth reminding that for entire elements, $\hat{\Pi}^e$ corresponds to $\hat{\Omega}^e$. As the mesh is constructed upon a rectangular background grid, $\hat{\Pi}^e$ is given by $[\xi_{1b}^e, \xi_{1t}^e] \times [\xi_{2b}^e, \xi_{2t}^e]$. On the other hand, when dealing with partial or extended elements, the domain for the definition of $\mathcal{P}_p^e$ is suitably restricted or extended, as appropriate. This operation is always possible when using a polynomial space for the test and trial functions. Additionally, it is worth mentioning that selecting test and trial functions from the same space $\mathcal{V}_{hp}^{N_U}$ results in symmetric algebraic systems for the formulations at hand.

Finally, it is important to note that the specific choice of the function space does not impact the DG formulation significantly. DG formulations offer the advantage of allowing for elements that differ in size, shape, approximation functions' type, and approximation functions' order within the same mesh, as the continuity of the solution is restored in a weak sense through penalty integrals.

4.1.1 Discontinuous Galerkin schemes

The selection of different definitions of $\widehat{\boldsymbol{\Sigma}}_\alpha$ and $\widehat{\boldsymbol{U}}$ results in distinct DG formulations [28]. In this work, it is employed either the interior penalty formulation proposed in [61] or the pure penalty formulation discussed in [62].

Interior penalty method

In the interior penalty formulation was originally proposed by [138] for the Poisson problem and extended to Reissner-Mindlin plates in [139] and to ESL plates in [62]. In particular, following [61] for ESL plates and shells the numerical fluxes are specified as

$$\widehat{\boldsymbol{U}} = \begin{cases} \{\boldsymbol{U}_h\}, & \text{on } \partial\hat{\Omega}_I^e \\ \overline{\boldsymbol{U}}, & \text{on } \partial\hat{\Omega}_D^e \\ \boldsymbol{U}_h, & \text{on } \partial\hat{\Omega}_N^e \end{cases} , \tag{4.8a}$$

$$\begin{cases} \widehat{\boldsymbol{\Sigma}}_\alpha = \{\boldsymbol{\Sigma}_\alpha(\boldsymbol{U}_h)\} - \mu[\![\boldsymbol{U}_h]\!]_\alpha, & \text{on } \partial\hat{\Omega}_I^e \\ \widehat{\boldsymbol{\Sigma}}_\alpha = \boldsymbol{\Sigma}_\alpha(\boldsymbol{U}_h) - \mu(\boldsymbol{U}_h - \overline{\boldsymbol{U}})\nu_\alpha, & \text{on } \partial\hat{\Omega}_D^e \\ \nu_\alpha \widehat{\boldsymbol{\Sigma}}_\alpha = \overline{\boldsymbol{T}}, & \text{on } \partial\hat{\Omega}_N^e \end{cases} , \tag{4.8b}$$

where $\overline{\boldsymbol{U}}$ are the applied displacements over $\partial\Omega_D^e$. Additionally, the following relationship is introduced

$$\boldsymbol{\Sigma}_\alpha(\boldsymbol{U}_h) = \boldsymbol{Q}_{\alpha\beta}\boldsymbol{U}_{h,\beta} + \boldsymbol{R}_{\alpha 3}\boldsymbol{U}_h \, . \tag{4.9}$$

The parameter μ is referred to as the penalty parameter and is a user-defined value that requires careful consideration in its definition, as further elaborated in this section.

Pure penalty method

An alternative approach for solving the governing equations of the problem is the pure penalty discontinuous Galerkin (DG) method. This method was originally introduced by Babuška in [140] for the Poisson problem and in [141] for the Kirchhoff plate problem with homogeneous boundary conditions. It was further extended by Gulizzi et al. in [61, 62] to linear analysis of multilayered plates. In the pure penalty formulation, the fluxes are specified as

$$\widehat{\boldsymbol{U}} = \begin{cases} \{\boldsymbol{U}_h\}, & \text{on } \partial\hat{\Omega}_I^e \\ \overline{\boldsymbol{U}}, & \text{on } \partial\hat{\Omega}_D^e \\ \boldsymbol{U}_h, & \text{on } \partial\hat{\Omega}_N^e \end{cases} , \tag{4.10a}$$

$$\begin{cases} \widehat{\boldsymbol{\Sigma}}_\alpha = -\mu[\![\boldsymbol{U}_h]\!]_\alpha, & \text{on } \partial\hat{\Omega}_I^e \\ \widehat{\boldsymbol{\Sigma}}_\alpha = -\mu(\boldsymbol{U}_h - \overline{\boldsymbol{U}})\nu_\alpha, & \text{on } \partial\hat{\Omega}_D^e \\ \nu_\alpha \widehat{\boldsymbol{\Sigma}}_\alpha = \overline{\boldsymbol{T}}, & \text{on } \partial\hat{\Omega}_N^e \end{cases} . \tag{4.10b}$$

However, it is important to note that the proposed pure penalty method for static analysis cannot be obtained simply by substituting the expressions for the fluxes. It necessitates discarding certain integrals that would otherwise appear in the formulation.

Choice of the penalty parameter

The choice of the penalty parameter μ is crucial for the efficiency of the method. Although the penalty terms in Eqs.(4.8) and (4.10) are the same, their purposes differ in the interior penalty and pure penalty methods:

i) In the interior penalty method, the penalty terms are introduced primarily to ensure the stability of the method. In this case, a common choice for the penalty parameter is $\mu = Q/h$, where Q is typically a sufficiently large constant proportional to the highest Young modulus of the structural materials, and h is a characteristic mesh size.

ii) In the pure penalty method, the penalty terms are the sole components responsible for enforcing the continuity of the solution among nearby elements. In the pure penalty DG formulation, a typical choice for the penalty parameter is $\mu = Q/h^{2p}$, where p is the degree of the polynomial basis used in the method.

A too small penalty value could lead to significant discontinuities of the solution across element interfaces, while a too high penalty can result in an ill-conditioning of the linear system being solved [142]. This ill-conditioning issue is particularly pronounced in the pure penalty formulation, where the penalty parameter needs to be significantly higher to ensure the same level of accuracy as in the interior penalty formulation.

One of the advantages of a pure penalty formulation over an interior penalty one is that it eliminates the need to compute the terms $\boldsymbol{\Sigma}_\alpha(\boldsymbol{U}_h)$ at $\partial\Omega_I^h$ and $\partial\Omega_D^h$. This advantage becomes particularly apparent in nonlinear analysis, where $\boldsymbol{\Sigma}_\alpha$ is not linear with respect to $\boldsymbol{U}_h$. A such, while in a pure penalty formulation, the integrals that enforce continuity and essential boundary conditions are computed only once and can be reused for each step of the nonlinear analysis, in an interior penalty formulation these integrals are not linear with respect to $\boldsymbol{U}_h$ and their Jacobian needs to be recomputed for each iteration.

4.1.2 DG for linear static analysis

In this thesis, for linear static analysis, an interior penalty formulation is utilized. The corresponding DG variational statement is obtained by setting $\boldsymbol{\Gamma}_\alpha = \boldsymbol{V}_{,\alpha}$, combining Eqs. (4.3) and (4.8), summing over all the mesh elements and using Eq.(4.6). This results in the so-called primal form of the proposed method, which is expressed as follows: find $\boldsymbol{U}_h \in \mathcal{V}_{hp}^{N_U}$ such that

$$B^K(\boldsymbol{V},\boldsymbol{U}_h) + B^{IP}(\boldsymbol{V},\boldsymbol{U}_h) = F^B(\boldsymbol{V},\overline{\boldsymbol{B}}) + F^T(\boldsymbol{V},\overline{\boldsymbol{T}}) + F^{IP}(\boldsymbol{V},\overline{\boldsymbol{U}}) \qquad \forall \boldsymbol{V} \in \mathcal{V}_{hp}^{N_U} \,. \tag{4.11}$$

The bilinear forms and the linear forms appearing in the previous equations are expressed as

$$B^K(\boldsymbol{V},\boldsymbol{U}_h) = \int_{\hat{\Omega}^h} \boldsymbol{V}^\intercal_{,\alpha}\boldsymbol{\Sigma}_\alpha(\boldsymbol{U_h}) + \boldsymbol{V}^\intercal\left(\boldsymbol{R}_{3\alpha}\boldsymbol{U}_{h,\alpha} + \boldsymbol{S}_{33}\boldsymbol{U}_h\right) \,, \tag{4.12}$$

$$B^{IP}(\boldsymbol{V},\boldsymbol{U}_h) = -\int_{\partial\hat{\Omega}^h_I} [\![\boldsymbol{V}]\!]^\intercal_\alpha\{\boldsymbol{\Sigma}_\alpha(\boldsymbol{U}_h)\} + \{\boldsymbol{\Sigma}_\alpha(\boldsymbol{V})\}^\intercal[\![\boldsymbol{U}_h]\!]_\alpha + \int_{\partial\hat{\Omega}^h_I}\mu[\![\boldsymbol{V}]\!]^\intercal_\alpha[\![\boldsymbol{U}_h]\!]_\alpha + \\ -\int_{\partial\hat{\Omega}^h_D}\nu_\alpha\boldsymbol{V}^\intercal\boldsymbol{\Sigma}_\alpha(\boldsymbol{U}_h) + \boldsymbol{\Sigma}^\intercal_\alpha(\boldsymbol{V})\boldsymbol{U}_h\nu_\alpha + \int_{\partial\hat{\Omega}^h_D}\mu\boldsymbol{V}^\intercal\boldsymbol{U}_h \,, \tag{4.13}$$

$$F^B(\boldsymbol{V},\overline{\boldsymbol{B}}) = \int_{\hat{\Omega}^h}\boldsymbol{V}^\intercal\overline{\boldsymbol{B}} \,, \tag{4.14}$$

$$F^T(\boldsymbol{V},\overline{\boldsymbol{T}}) = \int_{\partial\hat{\Omega}^h_N}\boldsymbol{V}^\intercal\overline{\boldsymbol{T}} \,, \tag{4.15}$$

$$F^{IP}(\boldsymbol{V},\overline{\boldsymbol{U}}) = -\int_{\partial\hat{\Omega}^h_D}\left(\boldsymbol{V}^\intercal_{,\alpha}\boldsymbol{Q}_{\alpha\beta} + \boldsymbol{V}^\intercal\boldsymbol{R}^\intercal_{\beta3}\right)\overline{\boldsymbol{U}}\nu_\beta + \int_{\partial\hat{\Omega}^h_D}\mu\boldsymbol{V}^\intercal\overline{\boldsymbol{U}} \,, \tag{4.16}$$

where the following relationship is used

$$\boldsymbol{\Sigma}_\alpha(\boldsymbol{V}) = \boldsymbol{Q}_{\alpha\beta}\boldsymbol{V}_{,\beta} + \boldsymbol{R}_{\alpha3}\boldsymbol{V} \,. \tag{4.17}$$

It is important to note that in Eqs.(4.13) and (4.16), the integrals on $\partial\hat{\Omega}^h_D$ are used to enforce the Dirichlet boundary conditions in terms of prescribed displacements $\overline{\boldsymbol{U}}$, the integrals on $\partial\hat{\Omega}^h_N$ are used to enforce the Neumann boundary conditions, and the integrals on $\partial\hat{\Omega}^h_I$ are used to enforce the inter-element continuity.

Following the rules presented in Sec. 4.1.7 the bilinear forms B^K, B^{IP} are assembled in the matrices $\mathcal{K}_K$, $\mathcal{K}_{IP}$ as well as the linear forms F^B, F^T, F^{IP} are assembled in the vectors $\mathcal{F}_B$, $\mathcal{F}_T$, $\mathcal{F}_{IP}$. In such way the problem in Eq.(4.11) is reduced to the algebraic problem

$$\mathcal{K}\boldsymbol{X} = \mathcal{F} \,, \tag{4.18}$$

where $\boldsymbol{X}$ is the vector collecting the problem unknowns, $\mathcal{K} = \mathcal{K}_K + \mathcal{K}_{IP}$ is the stiffness matrix of the system and $\mathcal{F} = \mathcal{F}_B + \mathcal{F}_T + \mathcal{F}_{IP}$ is the vector that constitute the right-hand side of the system.

4.1.3 DG for buckling analysis

The formulation presented in this work for addressing the linear buckling problem in multilayered shells is derived from the corresponding two-dimensional variational statement elucidated in Chapter 3. In particular, it is stated as follow: find the eigenfunction $\boldsymbol{U}_h \in \mathcal{V}^{N_U}_{hp}$ and the eigenvalue λ_h that satisfy

$$B^K(\boldsymbol{V},\boldsymbol{U}_h) + B^{IP}(\boldsymbol{V},\boldsymbol{U}_h) = -\lambda_h B^G(\boldsymbol{V},\boldsymbol{U}_h,\overline{\sigma}_{ij}), \quad \forall\boldsymbol{V}\in\mathcal{V}^{N_U}_{hp}, \tag{4.19}$$

where $B^K(\boldsymbol{V},\boldsymbol{U}_h)$ and $B^{IP}(\boldsymbol{V},\boldsymbol{U}_h)$ are given in Eq.(4.12) and (4.13), respectively, and $B^G(\boldsymbol{V},\boldsymbol{U}_h,\overline{\sigma}_{ij})$ is defined as

$$B^G(\boldsymbol{V},\boldsymbol{U}_h,\overline{\sigma}_{ij}) = \int_{\hat{\Omega}^h}\boldsymbol{V}^\intercal_{,\alpha}\left(\boldsymbol{Q}^G_{\alpha\beta}\boldsymbol{U}_{h,\beta} + \boldsymbol{R}^G_{\alpha3}\boldsymbol{U}_h\right) + \boldsymbol{V}^\intercal\left(\boldsymbol{R}^{G\intercal}_{\alpha3}\boldsymbol{U}_{h,\alpha} + \boldsymbol{S}^G_{33}\boldsymbol{U}_h\right). \tag{4.20}$$

The buckling DG formulation given in Eq.(4.19) employs the same bilinear form $B^{IP}(\boldsymbol{V},\boldsymbol{U}_h)$ introduced for the static DG formulation given in Eq.(4.13) and including the boundary terms defined over $\partial\hat{\Omega}_I^h$ and $\partial\hat{\Omega}_D^h$. While it is clear that the boundary terms defined over $\partial\hat{\Omega}_I^h$ are needed to ensure the continuity of the solution among the mesh elements, it is worth noting that the boundary terms defined over $\partial\hat{\Omega}_D^h$ are also required because the adjacent solution $\boldsymbol{U}$ must verify $\boldsymbol{U}=\boldsymbol{0}$ on $\partial\hat{\Omega}_D^h$. On the other hand, the bilinear form $B^G(\boldsymbol{V},\boldsymbol{U}_h,\overline{\sigma}_{ij})$ consists of the approximate version of the second integral appearing in the two-dimensional ESL buckling formulation introduced in Chapter 3, without additional boundary terms. As demonstrated by the corresponding numerical tests, the DG formulation in Eq.(4.19) effectively yields accurate solutions for the linear buckling problem in multilayered shells.

It is work noting that, in Eq.(4.19), the penalty parameter appears only in the definition of $B^{IP}(\boldsymbol{V},\boldsymbol{U}_h)$ to enforce the inter-element continuity and the homogeneous boundary conditions, while it does not appear in the bilinear form $B^G(\boldsymbol{V},\boldsymbol{U}^h,\overline{\sigma}_{ij})$, which is the one related to the buckling problem. Although not explicitly shown in the results section, the buckling eigenvalues and eigenvectors obtained from Eq.(4.19) were not influenced by the choice of μ when this was selected following the same recommendations specified for linear static analysis.

By assembling the bilinear form B^G into the matrix $\mathcal{G}$ using the principles outlined in Sec. 4.1.7, the problem in Eq.(4.19) can be reformulated as a generalized eigenvalue algebraic problem, expressed as

$$\mathcal{K}\boldsymbol{X}=-\lambda_h\mathcal{G}\boldsymbol{X}\ , \tag{4.21}$$

where $\mathcal{K}$ has the same definition introduced in Sec. 4.1.2. Due to the symmetry of the interior penalty terms and the choice of test and trial functions, both $\mathcal{K}$ and $\mathcal{G}$ are real and symmetric and therefore Hermitian. Additionally, $\mathcal{K}$ is positive defined. As such, Eq.(4.21) can be easily turned into a generalized Hermitian eigenvalue problem by introducing $\mu_h=-1/\lambda_h$ and looking for the highest eigenvalues μ_h. The solution is then obtained through the SLEPc library [126] that implements a Krylov-Schur algorithm.

4.1.4 DG for transient analysis

The DG problem for transient dynamic analysis is derived from the two-dimensional elasto-dynamic problem for a multi-layered solid. It is expressed as follows: find $\boldsymbol{U}_h\in\mathcal{V}_{hp}^{N_U}$ such that

$$B^M(\boldsymbol{V},\ddot{\boldsymbol{U}}_h)+B^K(\boldsymbol{V},\boldsymbol{U}_h)+B^{IP}(\boldsymbol{V},\boldsymbol{U}_h)=F^B(\boldsymbol{V},\overline{\boldsymbol{B}})+F^T(\boldsymbol{V},\overline{\boldsymbol{T}})+F^{IP}(\boldsymbol{V},\overline{\boldsymbol{U}})\quad\forall\boldsymbol{V}\in\mathcal{V}_{hp}^{N_U}\ , \tag{4.22}$$

where the bilinear form $B^M(\boldsymbol{V},\ddot{\boldsymbol{U}}_h)$ is defined as

$$B^M(\boldsymbol{V},\ddot{\boldsymbol{U}}_h)=\int_{\hat{\Omega}^h}\boldsymbol{V}^{\intercal}\boldsymbol{M}\ddot{\boldsymbol{U}}_h\ , \tag{4.23}$$

and $B^K(\boldsymbol{V},\boldsymbol{U}_h)$, $B^{IP}(\boldsymbol{V},\boldsymbol{U}_h)$, $F^B(\boldsymbol{V},\overline{\boldsymbol{B}})$, $F^T(\boldsymbol{V},\overline{\boldsymbol{T}})$, and $F^{IP}(\boldsymbol{V},\overline{\boldsymbol{U}})$ are defined in Sec. 4.1.2. Once the DG-based space discretization is introduced in Eq.(4.22), one obtains the following linear system of second-order differential equations involving only time derivatives

$$\mathcal{M}\ddot{\boldsymbol{X}}+\mathcal{D}\dot{\boldsymbol{X}}+\mathcal{K}\boldsymbol{X}=\mathcal{F}\ , \tag{4.24}$$

where $\mathcal{M}$, $\mathcal{D}$ and $\mathcal{K}$ are the mass matrix, the damping matrix and the stiffness matrix of the system, respectively, $\dot{\boldsymbol{X}}$ and $\ddot{\boldsymbol{X}}$ are the first and second time derivatives of the vector of the unknowns $\boldsymbol{X}$, respectively, and $\mathcal{F}$ is the right-hand side of the linear system. It is worth mentioning that while $\mathcal{K}$ and $\mathcal{F}$ have the same definitions as in Sec. 4.1.2, and $\mathcal{M}$ is obtained assembling the bilinear form B^M, the second term in Eq.(4.24) does not come directly from Eq.(4.22); instead, it is introduced to model the damping in the structure. In this thesis this term is constructed using the Rayleigh damping method, as detailed as follows.

Finally, the temporal time-stepping is solved employing the Newmark integration scheme which, for the sake of conciseness, it is not reported here but may be found in [25]. Unlike other direct integration methods, the Newmark scheme exhibits both unconditional stability and remarkable accuracy when compared to other explicit and implicit time integration schemes. These characteristics contribute to its widespread use in structural analysis.

Rayleigh damping method

Using Rayleigh damping method, see e.g.[143], the matrix $\mathcal{D}$ is constructed as a linear combination of the matrices $\mathcal{M}$ and $\mathcal{K}$ as

$$\mathcal{D} = \alpha\mathcal{M} + \beta\mathcal{K}. \tag{4.25}$$

where the coefficients α and β are obtained by specifying the damping ratios ζ_i and ζ_j for the i-th and j-th mode and solving the system

$$\frac{1}{2}\begin{bmatrix} \frac{1}{\omega_i} & \omega_i \\ \frac{1}{\omega_j} & \omega_j \end{bmatrix}\begin{bmatrix} \alpha \\ \beta \end{bmatrix} = \begin{bmatrix} \zeta_i \\ \zeta_j \end{bmatrix}. \tag{4.26}$$

4.1.5 DG for free-vibration analysis

For free-vibration analysis, the DG statement becomes: find the eigenvalues $\lambda_h = \frac{1}{\omega_h^2}$ and the eigenfunctions $\boldsymbol{U}_h$ such that

$$B^M(\boldsymbol{V}, \boldsymbol{U}_h) = \lambda_h \left(B^K(\boldsymbol{V}, \boldsymbol{U}_h) + B^{IP}(\boldsymbol{V}, \boldsymbol{U}_h) \right), \quad \forall \boldsymbol{V} \in \mathcal{V}_{hp}^{N_U}, \tag{4.27}$$

where ω_h is an approximation of the free-vibration frequencies and $B^M(\boldsymbol{V}, \boldsymbol{U}_h)$, $B^K(\boldsymbol{V}, \boldsymbol{U}_h)$, and $B^{IP}(\boldsymbol{V}, \boldsymbol{U}_h)$ have the same meaning as in the previous section. Assembling the bilinear forms in Eq.4.27, the following eigenvalues algebraic problem is obtained

$$\mathcal{M}\boldsymbol{X} = \lambda_h \mathcal{K}\boldsymbol{X}\ , \tag{4.28}$$

where $\mathcal{M}$, $\mathcal{K}$ and $\boldsymbol{X}$ have already been defined.

4.1.6 DG for non-linear static analysis

For the geometrically non-linear static analysis the pure penalty method is adopted in this work. The primal form is stated as: find $\boldsymbol{U}_h$ such that

$$B^K(\boldsymbol{V}, \boldsymbol{U}_h) + B^{PP}(\boldsymbol{V}, \boldsymbol{U}_h) = F^B(\boldsymbol{V}, \overline{\boldsymbol{B}}) + F^T(\boldsymbol{V}, \overline{\boldsymbol{T}}) + F^{PP}(\boldsymbol{V}, \overline{\boldsymbol{U}}) \quad \forall \boldsymbol{V} \in \mathcal{V}_{hp}^U\ , \tag{4.29}$$

where

$$B^{PP}(\boldsymbol{V},\boldsymbol{U}_h) = \int_{\partial\hat{\Omega}_I^h} \mu[\![\boldsymbol{V}]\!]_\alpha^\intercal [\![\boldsymbol{U}_h]\!]_\alpha + \int_{\partial\hat{\Omega}_D^h} \mu \boldsymbol{V}^\intercal \boldsymbol{U}_h \,, \tag{4.30}$$

$$F^{PP}(\boldsymbol{V},\overline{\boldsymbol{U}}) = \int_{\partial\hat{\Omega}_D^h} \mu \boldsymbol{V}^\intercal \overline{\boldsymbol{U}} \,. \tag{4.31}$$

It is important to note that while the definition for $B^K(\boldsymbol{V},\boldsymbol{U}_h)$ is formally the same as in Eq.(4.12), the generalized stiffness matrices adopted in this case are nonlinear with respect to $\boldsymbol{U}_h$. Following the assembly procedure detailed in Sec. 4.1.7, from Eq.4.29 it is obtained the following nonlinear algebraic system

$$\mathcal{K}(\boldsymbol{X})\boldsymbol{X} = \mathcal{F} \,. \tag{4.32}$$

Here, $\mathcal{K}(\boldsymbol{X}) = \mathcal{K}_K(\boldsymbol{X}) + \mathcal{K}_{PP}$ and $\mathcal{F} = \mathcal{F}_B + \mathcal{F}_T + \mathcal{F}_{PP}$. It is worth noting that $\mathcal{K}_K$, in this case, depends on the unknowns $\boldsymbol{X}$. Additionally, $\mathcal{K}_{PP}$ and $\mathcal{F}_{PP}$ result from the assembly of B^{PP}, and F^{PP}, whereas the remaining quantities have the same definition as introduced before.

The non-linear algebraic system in Eq.(4.32) is solved in this thesis using the Newton-Raphson method with the path-following arc-length iteration scheme proposed by Crisfield [144, 145]. To apply this solution procedure, the tangent stiffness matrix $\mathcal{K}_T$ is required, representing the Jacobian of the left-hand side of Eq.4.32.

The Jacobian of $\mathcal{K}_K(\boldsymbol{X})\boldsymbol{X}$ is assembled following the rules in Sec. 4.1.7, starting from the discretized version of the variation of the virtual work of the internal forces introduced in Chapter 3. The Jacobian of $\mathcal{K}_{PP}\boldsymbol{X}$ is simply $\mathcal{K}_{PP}$ since, differently from the interior penalty case, the contribute to the stiffness matrix arising from the pure penalty terms is not a function of $\boldsymbol{X}$. This property allows for computing the penalty integrals only once, storing the result, and using it for each iteration in the arc-length iterative scheme, making the analysis more efficient in terms of computational time.

4.1.7 Assembly of the algebraic systems

The DG primal forms introduced in previous sections are transformed into algebraic systems by selecting appropriate approximations for the test function $\boldsymbol{V}$ and the primary variable $\boldsymbol{U}_h$ within the space $\mathcal{V}_{hp}^{N_U}$. Specifically, in this thesis the Legendre polynomials are used as the basis for the in-plane expansion and the k-th components V_k^e and U_k^e of the restriction $\boldsymbol{V}^e$ and $\boldsymbol{U}_h^e$ of the fields $\boldsymbol{V}$ and $\boldsymbol{U}_h$ to the e-th element are approximated as

$$U_k^e = \sum_{p_1=0}^{p}\sum_{p_2=0}^{p} \mathcal{L}_{p_1}^e(\xi_1)\mathcal{L}_{p_2}^e(\xi_2) X_{p_1p_2}^{ek} \tag{4.33a}$$

$$V_k^e = \sum_{p_1=0}^{p}\sum_{p_2=0}^{p} \mathcal{L}_{p_1}^e(\xi_1)\mathcal{L}_{p_2}^e(\xi_2) \delta X_{p_1p_2}^{ek} \tag{4.33b}$$

where $\mathcal{L}_{p_\alpha}^e(\xi_\beta)$ represents the Legendre polynomial of order p_α scaled in the interval $[\xi_{\beta b}^e, \xi_{\beta t}^e]$, $X_{p_1p_2}^{ek}$ are the unknown expansion coefficients and $\delta X_{p_1p_2}^{ek}$ are the arbitrary parameters of the test function. Accordingly, in compact matrix form, one writes

$$\boldsymbol{U}_h^e = \boldsymbol{P}^e(\xi_1,\xi_2)\boldsymbol{X}^e, \tag{4.34a}$$

$$\boldsymbol{V}^e = \boldsymbol{P}^e(\xi_1, \xi_2)\delta\boldsymbol{X}^e \tag{4.34b}$$

where the vectors $\boldsymbol{X}^e$ and $\delta\boldsymbol{X}^e$ collect the unknowns $X^{ek}_{p_1p_2}$ and the parameters of the test function $\delta X^{ek}_{p_1p_2}$, respectively, while the matrix $\boldsymbol{P}^e(\xi_1, \xi_2)$ consistently collects the functions used for the expansion of the elements of $\boldsymbol{U}^e_h$ and $\boldsymbol{V}^e$. Using Eqs.(4.34) the terms of the DG primal forms introduced in this section can be assembled in the final matrices that transform the DG problems into algebraic problems. This process is carried out using the following rules

i) The e-th element provides

- A contribution to the problem matrices that sums to the rows and columns associated with the degrees of freedom of the e-th element, generated from integrals over $\hat{\Omega}^e$. E.g.

$$\mathcal{K}^e_K = \int_{\hat{\Omega}^e} \left[\boldsymbol{P}^{e\intercal}_{,\alpha}\left(\boldsymbol{Q}_{\alpha\beta}\boldsymbol{P}^e_{,\beta} + \boldsymbol{R}_{\alpha 3}\boldsymbol{P}^e\right) + \boldsymbol{P}^{e\intercal}\left(\boldsymbol{R}_{3\alpha}\boldsymbol{P}^e_{,\alpha} + \boldsymbol{S}_{33}\boldsymbol{P}^e\right)\right] \mathrm{d}\hat{\Omega} \, .$$

- A contribution to the problem vectors that sums to the rows associated with the degrees of freedom of the e-th element, generated from integrals over $\hat{\Omega}^e$. E.g.

$$\mathcal{F}^e_B = \int_{\hat{\Omega}^e} \boldsymbol{P}^\intercal \overline{\boldsymbol{B}} \, \mathrm{d}\hat{\Omega} \, .$$

- A contribution to the problem vectors that sums to the rows associated with the degrees of freedom of the e-th element, generated from integrals over $\partial\hat{\Omega}^e_N$ or $\partial\hat{\Omega}^e_D$. E.g.

$$\mathcal{F}^e_T = \int_{\partial\hat{\Omega}^e_N} \boldsymbol{V}^\intercal \overline{\boldsymbol{T}} \, \mathrm{d}\partial\hat{\Omega} \, .$$

- A contribution to the stiffness matrices that sums to the rows and columns associated with the degrees of freedom of the e-th element, generated from integrals over $\partial\hat{\Omega}^e_D$. E.g.

$$\mathcal{K}^e_{PP} = \int_{\partial\hat{\Omega}^e_D} \mu \boldsymbol{P}^{e\intercal}\boldsymbol{P}^e \, \mathrm{d}\partial\hat{\Omega} \, .$$

ii) The i-th interface between the elements e and e' provides four contributions to the corresponding stiffness matrix enforcing the inter-element continuity

- A contribution that sums to the rows and columns associated with the degrees of freedom of the e-th element. E.g.

$$\mathcal{K}^{iee}_{PP} = \int_{\partial\hat{\Omega}^i_I} \mu \boldsymbol{P}^{e\intercal}\boldsymbol{P}^e \, \mathrm{d}\partial\hat{\Omega} \, .$$

- A contribution that sums to the rows and columns associated with the degrees of freedom of the e'-th element. E.g.

$$\mathcal{K}^{ie'e'}_{PP} = \int_{\partial\hat{\Omega}^i_I} \mu \boldsymbol{P}^{e'\intercal}\boldsymbol{P}^{e'} \, \mathrm{d}\partial\hat{\Omega} \, .$$

- A contribution that sums to the rows associated with the degrees of freedom of the e-th element and columns associated with the degrees of freedom of the e'-th element.E.g.

$$\mathcal{K}_{PP}^{iee'} = \int_{\partial\hat{\Omega}_I^i} \mu \boldsymbol{P}^{e\intercal} \boldsymbol{P}^{e'} \, \mathrm{d}\partial\hat{\Omega} \, .$$

- A contribution that sums to the rows associated with the degrees of freedom of the e'-th element and columns associated with the degrees of freedom of the e-th element.E.g.

$$\mathcal{K}_{PP}^{ie'e} = \int_{\partial\hat{\Omega}_I^i} \mu \boldsymbol{P}^{e'\intercal} \boldsymbol{P}^{e} \, \mathrm{d}\partial\hat{\Omega} \, .$$

4.2 Numerical results for static analysis

In this section, the capabilities of the proposed DG formulation for the linear static analysis are assessed through several test cases involving isotropic, orthotropic and multilayered shells in various curved geometric configurations. For each test case, different shell theories are considered and the theory corresponding to the choice of a specific order of expansion is denoted, for the ESL approach, by $\mathrm{ED}_{N_1N_2N_3}$, where it is recalled that N_i is the order of thickness expansion for the i-th covariant component of the displacement field, and, for the LW approach, by LD_{N_p}, where N_p is the common order of thickness expansion for each component of the displacement field and each layer of the laminate. The numerical tests are also performed using the FSDT, which is the most commonly employed theory for laminated thin and moderately thick structures and can be considered as a special case of the theory ED_{110} where the stiffness coefficients are modified according to the plane-stress assumption [1, 2].

Several test cases are presented: Secs. 4.2.1, 4.2.2 and 4.2.3 are devoted to the analysis of cylindrical, toroidal and wing-shaped shells, respectively, and refer to geometries that are parametrized via orthogonal curvilinear coordinates; Secs. 4.2.4 and 4.2.5 are devoted to the analysis of a planar shell and a generally-shaped shell, respectively, and show examples of geometries that are parametrized via non-orthogonal curvilinear coordinates; Secs. 4.2.6 and 4.2.7 refer to geometries with internal cut-outs, more specifically, to a fuselage panel and a generally-curved NURBS-based shell, respectively.

The last two tests are devoted to two special cases aimed at demonstrating the versatility of the proposed method. In particular, in Sec. 4.2.8, a LW approach is adopted to demonstrate the accuracy of the through-th-thickness resolution of LW expansion, and in Sec. 4.2.9 the mechanical response of a damaged plate with a circular cut-out is obtained leveraging the flexibility of the DG method when modeling discontinuities in the geometry.

The materials considered for the numerical tests are grouped and reported in Tab.(4.1), the properties of the considered shell sections are reported in Tab.(4.2) and the parameters entering the equations of shell mid-surfaces are given in Tab.(4.3). The geometries of the shell without and with cut-outs are shown in Figs.(4.2) and (4.3), respectively.

Table 4.1: Properties of the considered materials.

Material ID	**Property**	**Component**	**Value**
M_1 (Isotropic)	Young's modulus	E	70 GPa
	Poisson's ratio	ν	0.33
M_2 (Orthotropic)	Young's moduli	E_1	100.0 GPa
		E_2, E_3	4.0 GPa
	Poisson's ratios	ν_{23}, ν_{13}, ν_{12}	0.25
	Shear moduli	G_{23}	0.8 GPa
		G_{13}, G_{12}	2.0 GPa
M_3 (Orthotropic)	Young's moduli	E_1	160.0 GPa
		E_2, E_3	20.0 GPa
	Poisson's ratios	ν_{23}, ν_{13}, ν_{12}	0.25
	Shear moduli	G_{23}	4 GPa
		G_{13}, G_{12}	10.0 GPa
M_4 (Isotropic)	Young's modulus	E/E_r	1
	Poisson's ratio	ν	0.25
M_5 (Orthotropic)	Young's moduli	E_1/E_r	25
		E_2/E_r, E_3/E_r	1
	Poisson's ratios	ν_{23}, ν_{13}, ν_{12}	0.25
	Shear moduli	G_{23}/E_r	0.2
		G_{13}/E_r, G_{12}/E_r	0.5

Table 4.2: Properties of the considered shell sections.

Shell ID	**Material**	**Layup**	**Layer(s) thickness**
C_1 (Single-layer)	M_1	$[0]$	1 cm
C_2 (Single-layer)	M_2	$[0]$	1 cm
C_3 (Multilayered)	M_2	$[0/90]_4$	0.125 cm
T_1 (Single-layer)	M_1	$[0]$	1 cm
T_2 (Single-layer)	M_2	$[0]$	1 cm
T_3 (Multilayered)	M_2	$[0/90]_2$	0.25 cm
W_1 (Single-layer)	M_1	$[0]$	1 cm
W_3 (Multilayered)	M_3	$[0/90]_s$	0.25 cm
P_2 (Single-layer)	M_2	$[0]$	1 cm
P_3 (Multilayered)	M_2	$[0/90/0/90]_s$	0.125 cm
G_1 (Single-layer)	M_1	$[0]$	1 cm
F_1 (Single-layer)	M_4	$[0]$	10 cm
F_2 (Single-layer)	M_5	$[0]$	10 cm
F_3 (Multilayered)	M_5	$[0/90]_s$	0.25 mm
F_4 (Multilayered)	M_5	$[+45/-45]_2$	0.25 mm
N_1 (Single-layer)	M_4	$[0]$	1 mm
N_2 (Multilayered)	M_5	$[0/90]_s$	0.25 mm
L_1 (Multilayered)	M_5	$[-30/0/0/45]$	2.5 cm
D_1 (Multilayered)	M_5	$[90/0]_s$	0.25 cm

Table 4.3: Quantities entering the parametric equation of the considered shell mid-surfaces.

Cylinder		**Torus**		**Wing**		**Planar**		**General**		**Fuselage**		**NURBS**	
R_c	1 m	R_{1t}	2 m	x_w	0.1 m	b_m	0.5 m	a_g	2 m	R_f	3 m	H_n	50 cm
θ_c	$\pi/4$	R_{2t}	0.5 m	y_w	0 m	l_m	0.5 m	b_g	1 m	θ_f	$\pi/12$	D_n	5 cm
L_c	1 m	θ_{1t}	$\pi/8$	L_{wa}	10 m			f_g	0.44	L_f	60 cm	L_n	60 cm
		θ_{2t}	$\pi/2$	L_{wb}	20 m			Δ_g	4.0	a_f	15 cm	a_n	8.5 cm
				R_w	1.1 m			L_g	8 m	b_f	22.5 cm	d_n	3
										d_f	3	x_{1n}	15 cm
												x_{2n}	12 cm

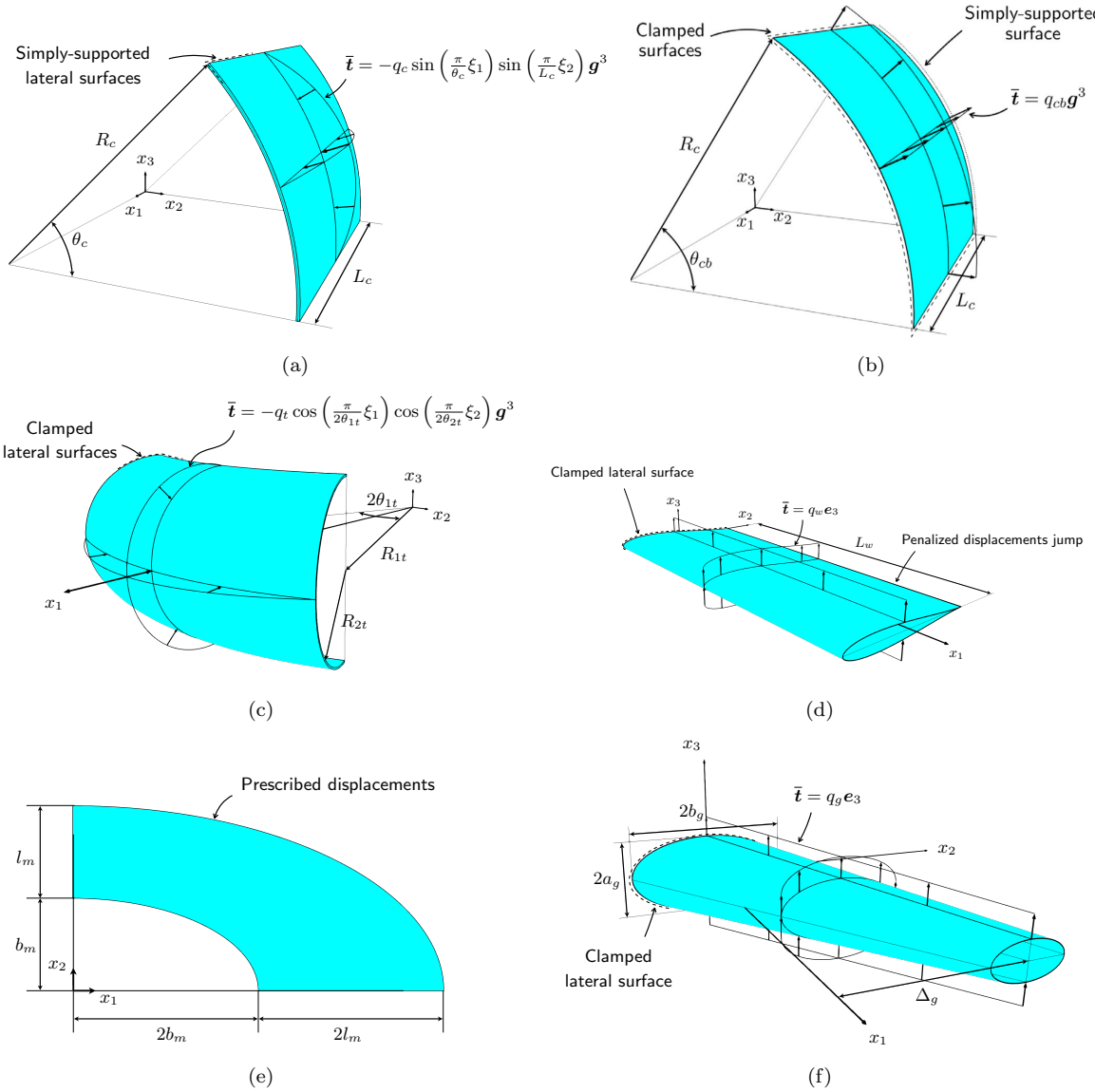

Figure 4.2: Geometry, boundary conditions and load conditions of the considered geometries without internal cut-outs. In particular: the considered cylindrical shells with Navier-type solution (a) and without Navier-type solution (b); the considered toroidal shell (c); the considered wing-shaped shell (d); the considered planar shell parametrized using a system of non-orthogonal curvilinear coordinates (e); the considered generally-curved shell (f).

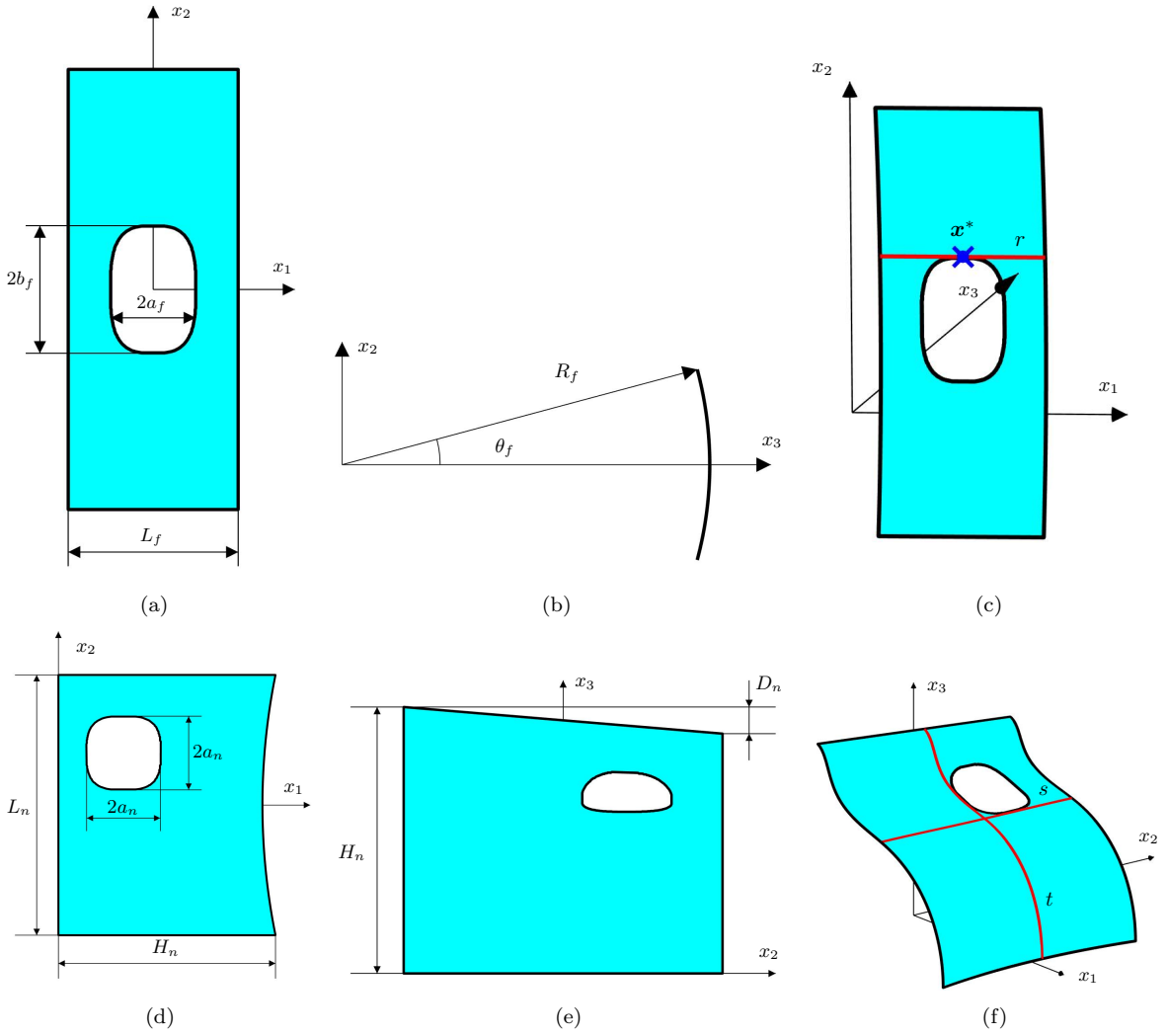

Figure 4.3: Geometry, boundary conditions and load conditions of the considered geometries with internal cut-outs. In particular: the considered fuselage panel with a window in three different views (a), (b), and (c); the NURBS-based shell in three different views (d), (e), and (f).

4.2.1 Cylindrical shell

In the first set of tests, the cylindrical shell shown in Fig.(4.2a) is considered. The mid-surface of the shell is described by the equation

$$\boldsymbol{x}_0 = \begin{bmatrix} \xi_2 \\ R_c \cos(\xi_1) \\ R_c \sin(\xi_1) \end{bmatrix} \tag{4.35}$$

where $\xi_1 \in [0, \theta_c]$, $\xi_2 \in [0, L_c]$ and R_c, θ_c and L_c are reported in the first column of Tab.(4.3). The shell is subjected to simply supported boundary conditions, which are prescribed in terms of generalized displacements as

$$\begin{cases} \overline{U}_{2k} = 0, & \text{for } k = 0, \dots, N_2 \\ \overline{U}_{3k} = 0, & \text{for } k = 0, \dots, N_3 \end{cases}, \text{ at } \xi_1 = 0, \theta_c, \tag{4.36a}$$

$$\begin{cases} \overline{U}_{1k} = 0, & \text{for } k = 0, \dots, N_1 \\ \overline{U}_{3k} = 0, & \text{for } k = 0, \dots, N_3 \end{cases}, \text{ at } \xi_2 = 0, L_c. \tag{4.36b}$$

The contribution to the vector $\overline{\boldsymbol{T}}$ of the generalized boundary loads is zero, whereas the only contribution to the vector $\overline{\boldsymbol{B}}$ of the generalized domain loads is given by the traction applied on the top surface of the shell as

$$\bar{\boldsymbol{t}} = -q_c \sin\left(\frac{\pi}{\theta_c}\xi_1\right) \sin\left(\frac{\pi}{L_c}\xi_2\right) \boldsymbol{g}^3, \quad \text{at } \xi_3 = \tau_c/2, \tag{4.37}$$

where $q_c = 10$ MPa and τ_c is the thickness of the cylindrical shell. As regards the material properties and the stacking sequences, the three shell sections denoted by C_1, C_2 and C_3 in Tab.(4.2) are considered. It is noted that they all have the same thickness. These settings have been chosen because they admit exact two-dimensional Navier solutions [2] and allow to compute the solution of the corresponding three-dimensional elasticity problem [4].

The reference domain $\hat{\Omega}$ of the shell is subdivided into $n \times n$ rectangular elements such that the dimensions of each element is $h\theta_c \times hL_c$, being $h = 1/n$ a measure of the element size. Given the existence of the Navier solutions, the following error measure is introduced

$$e(\boldsymbol{U}_h) = \frac{|\boldsymbol{U}_h - \boldsymbol{U}_{\text{ref}}|_\infty}{|\boldsymbol{U}_{\text{ref}}|_\infty}, \tag{4.38}$$

where $\boldsymbol{U}_h$ is the solution computed using the present interior interior formulation, $\boldsymbol{U}_{\text{ref}}$ is the exact Navier solution and $|\bullet|_\infty$ is the ∞-norm defined over $\hat{\Omega}$. Fig.(4.4) shows the *hp*-convergence analyses in terms of the error given in Eq.(4.38) as a function of the element size h and the polynomial order p. As it is possible to notice, the present formulation allows to obtain optimal convergence for all the tested shell sections and shell theories.

The solution obtained using the present formulation with a 4×4 mesh, $p = 6$ and the theories FSDT, ED_{111}, ED_{222}, ED_{333}, ED_{444} is then compared with the corresponding solution of three-dimensional elasticity [4]. The comparison is reported in Fig.(4.5) in the terms of the non-dimensional through-the-thickness Cartesian displacement component $\overline{u}_1$ and curvilinear covariant component $\overline{u}_{\xi_3}$ defined as

$$\overline{u}_1 = u_1 \cdot \left(\frac{\tau_c^2 E_2}{L_c^3 q_c}\right) \quad \text{and} \quad \overline{u}_{\xi_3} = u_{\xi_3} \cdot \left(\frac{\tau_c^3 E_2}{L_c^4 q_c}\right). \tag{4.39}$$

The top, center and bottom rows of Fig.(4.5) refer to the isotropic shell C_1, the orthotropic shell C_2 and the laminated shell C_3, respectively, and show that the differences between the 3D solution and the ESL theories are more pronounced for the covariant component $\overline{u}_{\xi_3}$ rather than the Cartesian component $\overline{u}_1$. More specifically regarding $\overline{u}_{\xi_3}$, Fig.(4.5b) shows that all the considered ESL theories with the exception of the ED_{111} are able to recover the 3D solution, Fig.(4.5d) shows that the ESL theories ED_{333} and ED_{444} are able to fully recover the 3D solution and, eventually, Fig.(4.5f) shows that, although the theories ED_{333} and ED_{444} provide a converged ESL solution, ESL theories are not able to fully recover the 3D solution. The obtained results are consistent with the findings reported in [61] for multilayered plates and, as expected, show that higher-order theories provide a better response than low-order theories when employed for orthotropic and laminated shells. They also suggest that layer-wise theories are generally required to fully recover the 3D solution in laminated structures.

The accuracy of the present formulation is then tested against different configurations of boundary conditions that lead to non-Navier-type solutions and for which analytical methods have been recently proposed [146, 147]. The analysed shell is shown in Fig.(4.2b) and its mid-surface is given by Eq.(4.35) where $\xi_1 \in [0, \theta_{cb}]$ and θ_{cb} is reported in the first column of Tab.(4.3); the remaining geometrical parameters are the same as those of the cylindrical shell of Fig.4. However, unlike the simulations of the Navier-type solutions, in this case the shell is subjected to clamped boundary conditions, i.e. $\boldsymbol{U} = 0$ at $\xi_1 = 0$, θ_{cb} and $\xi_2 = L_c$, and to simply-supported boundary conditions, as given in Eq.(4.36), at $\xi_2 = 0$. The contribution to the vector $\overline{\boldsymbol{T}}$ is zero, whereas, as illustrated in Fig.(4.2b), the contribution to the vector $\overline{\boldsymbol{B}}$ is given by a uniform traction $\overline{\boldsymbol{t}} = q_{cb}\boldsymbol{g}3$ applied on the top surface of the shell, where $q_{cb} = 1$ kPa. To compare with the analytical results obtained by Zheng et al. [146] via the Symplectic superposition method (SSM) and by An et al. [147] via the Finite integral transform method (FITM), the shell section denoted by C_{1b} in Tab.(4.2) and having thickness $\tau_{cb} = 0.1$ cm is considered. The numerical results are computed in terms of non-dimensional longitudinal displacement u_{ξ_2} , circumferential displacement u_{ξ_1} and radial displacement u_{ξ_3} defined as

$$\overline{u}_{\xi_2} = u_{\xi_2} \cdot \left(\frac{10^7 E \tau_{cb}^3}{q_{cb} L_c^4} \right) \quad , \quad \overline{u}_{\xi_1} = u_{\xi_1} \cdot \left(\frac{10^7 E \tau_{cb}^3}{R q_{cb} L_c^4} \right) \quad \text{and} \quad \overline{u}_{\xi_3} = u_{\xi_3} \cdot \left(\frac{10^7 E \tau_{cb}^3}{q_{cb} L_c^4} \right). \tag{4.40}$$

and evaluated at different locations of the shell mid-surface. The comparison between the results obtained with the present DG formulation using the FSDT, a 8×8 mesh and polynomial order $p = 7$, and the results obtained with FEM [147], with SSM [146] and with FITM [147], is reported in Tab.(4.4) and demonstrates that the present approach accurately reproduces the static response of cylindrical shells in non-Navier-type configurations

4.2.2 Toroidal shell

In the second set of tests, the toroidal shell shown in Fig.(4.2c) is considered. The mid-surface of the shell is described by the equation

$$\boldsymbol{x}_0 = \begin{bmatrix} \cos(\xi_1)(R_{1t} + R_{2t}\cos(\xi_2)) \\ \sin(\xi_1)(R_{1t} + R_{2t}\cos(\xi_2)) \\ R_{2t}\sin(\xi_2) \end{bmatrix} \tag{4.41}$$

where $\xi_1 \in [-\theta_{1t}, \theta_{1t}]$, $\xi_2 \in [-\theta_{2t}, \theta_{2t}]$ and R_{1t}, R_{2t}, θ_{1t} and θ_{2t} are reported in the second column of Tab.(4.3). The shell is subjected to clamped boundary conditions, i.e. $\boldsymbol{U} = \boldsymbol{0}$

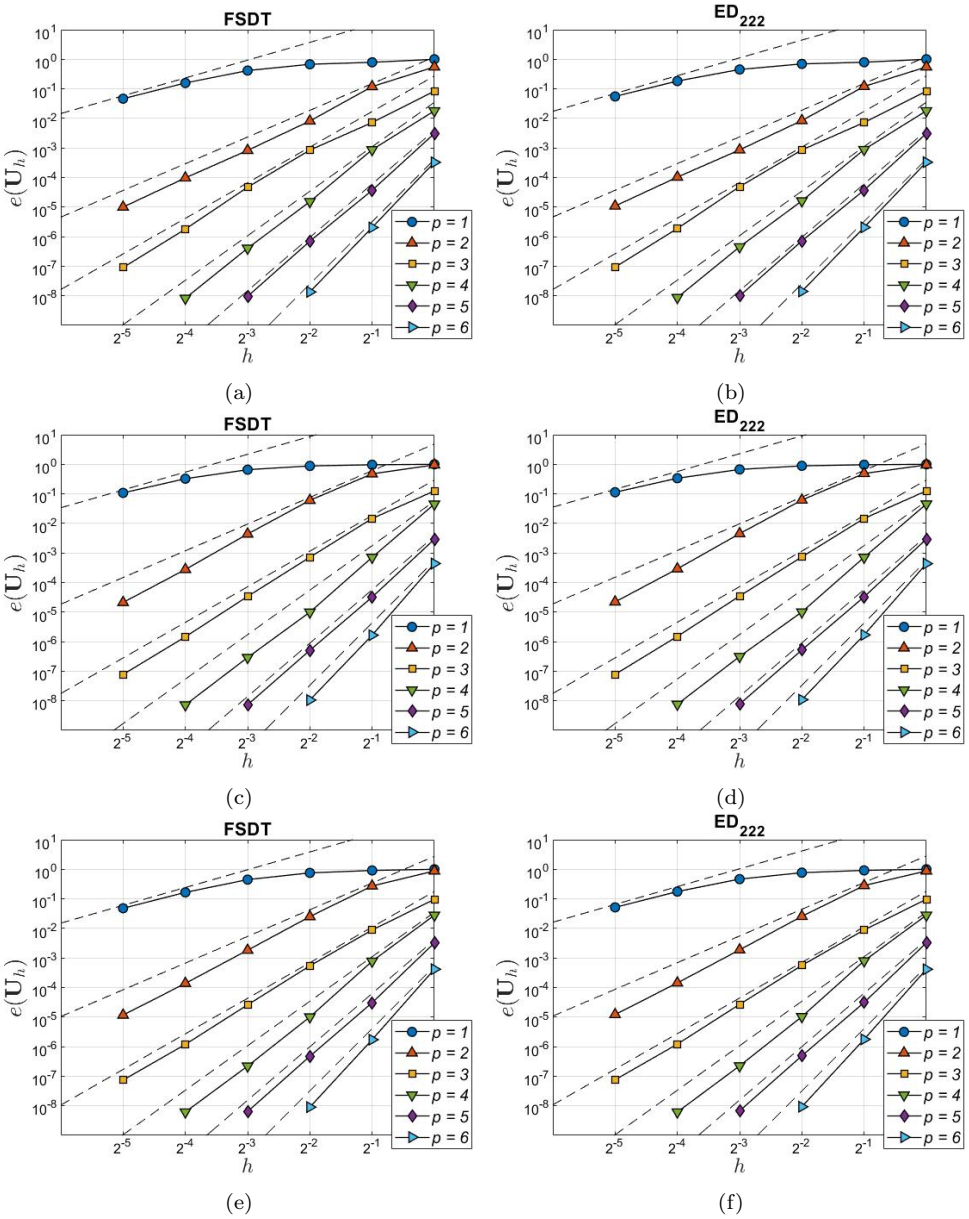

Figure 4.4: *hp*-convergence analysis for the cylindrical shells shown in Fig.(4.2a). The figures in the left and the right columns refer to the FSDT and the ED_{222} theory, respectively, whereas, from top to bottom, the figures refer to the shell sections C_1, C_2 and C_3 reported in Tab.(4.2). The slope of the dashed lines is $p+1$.

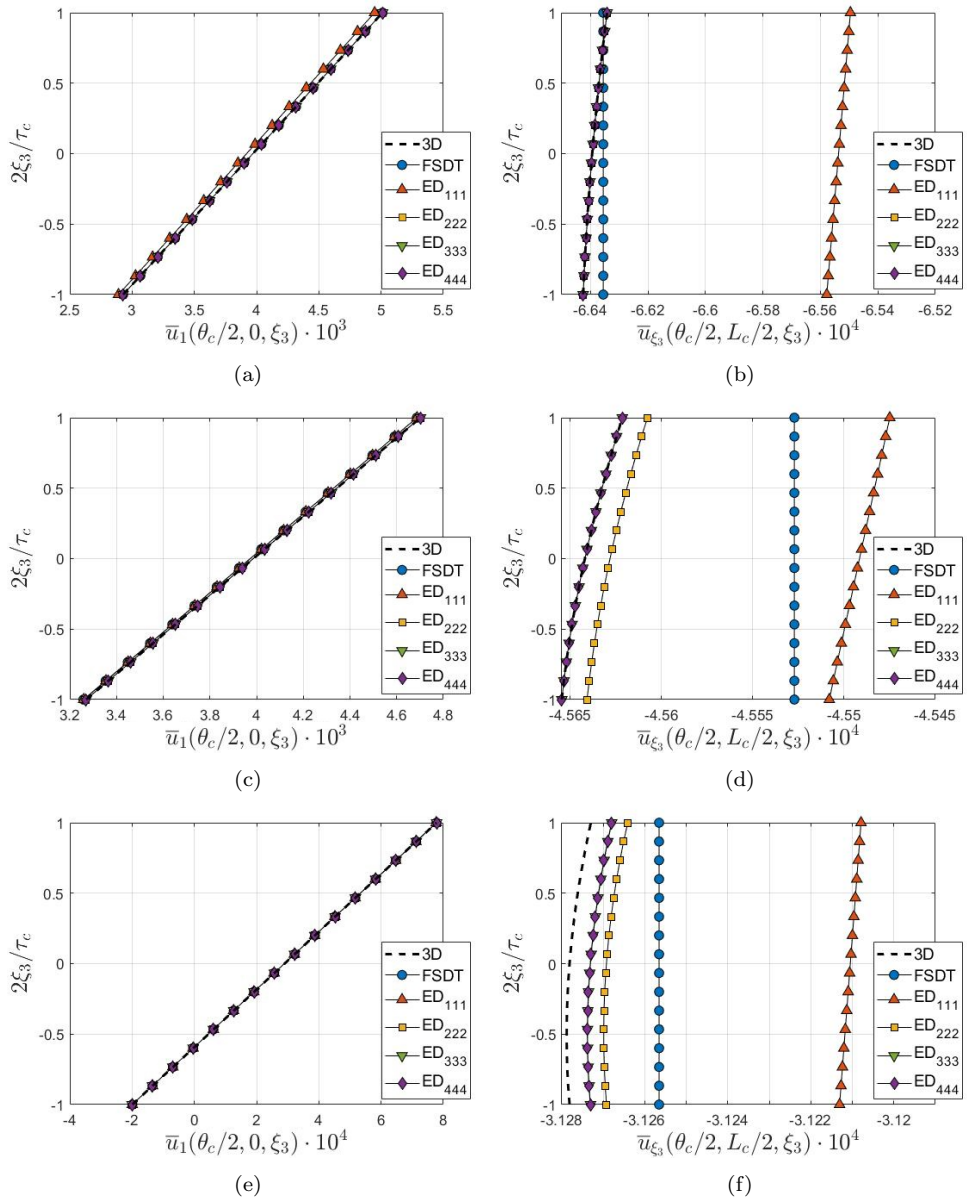

Figure 4.5: Comparison between the 3D solution and the solution obtained with the present formulation and different shell theories for the cylindrical shells shown in Fig.(4.2a).

Table 4.4: Comparison between the results obtained with the present DG formulation and the results obtained with FEM [147], with SSM [146] and with FITM [147] for the cylindrical shell shown in Fig.(4.2b)

		$\overline{u}_{\xi_2}$				$\overline{u}_{\xi_1}$				$\overline{u}_{\xi_3}$			
		$\xi_1 = 1/8$	1/4	3/8	1/2	1/8	1/4	3/8	1/2	1/8	1/4	3/8	1/2
FEM	$\xi_2 = L_c/8$	0.5367	1.055	1.427	1.522	0.004785	−0.3555	−0.1474	0	15.43	9.317	8.141	9.119
SSM		0.5407	1.057	1.429	1.524	0.003268	−0.3552	−0.1475	0	15.43	9.287	8.133	9.110
FITM		0.5343	1.052	1.425	1.520	0.003474	−0.3552	−0.1476	0	15.43	9.288	8.133	9.109
DG		0.5345	1.053	1.426	1.521	0.002996	−0.3556	−0.1474	0	15.44	9.288	8.136	9.118
FEM	$L_c/4$	0.4032	0.7872	1.101	1.188	0.01070	−0.6137	−0.2809	0	16.99	9.775	6.513	8.374
SSM		0.3986	0.7827	1.097	1.184	0.008871	−0.6133	−0.2811	0	17.00	9.746	6.505	8.363
FITM		0.3986	0.7826	1.097	1.184	0.009131	−0.6132	−0.2812	0	16.99	9.749	6.505	8.362
DG		0.3988	0.7832	1.098	1.185	0.008489	−0.6140	−0.2809	0	17.01	9.746	6.505	8.373
FEM	$3L_c/8$	0.3118	0.5837	0.8074	0.8788	0.02697	−0.7422	−0.3749	0	17.44	10.48	5.464	7.769
SSM		0.3086	0.5799	0.8038	0.8753	0.02538	−0.7416	−0.3752	0	17.29	10.85	5.197	7.459
FITM		0.3086	0.5798	0.8037	0.8752	0.02565	−0.7415	−0.3753	0	17.44	10.46	5.456	7.755
DG		0.3087	0.5802	0.8043	0.8758	0.02498	−0.7425	−0.3749	0	17.45	10.46	5.454	7.769
FEM	$L_c/2$	0.2440	0.4256	0.5499	0.5996	0.05502	−0.7533	−0.4038	0	17.31	10.84	5.188	7.465
SSM		0.2457	0.4243	0.5515	0.6011	0.05369	−0.7525	−0.4040	0	17.28	10.84	5.191	7.445
FITM		0.2434	0.4243	0.5484	0.5981	0.05395	−0.7523	−0.4041	0	17.28	10.84	5.191	7.444
DG		0.2436	0.4246	0.5488	0.5985	0.05331	−0.7534	−0.4037	0	17.30	10.84	5.189	7.457
FEM	$5L_c/8$	0.1899	0.2991	0.3327	0.3613	0.08441	−0.6641	−0.3600	0	16.75	10.68	5.683	7.522
SSM		0.1909	0.3003	0.3341	0.3625	0.08324	−0.6631	−0.3599	0	16.73	10.67	5.680	7.510
FITM		0.1895	0.2983	0.3317	0.3601	0.08347	−0.6629	−0.3600	0	16.73	10.67	5.680	7.508
DG		0.1896	0.2984	0.3319	0.3605	0.08291	−0.6639	−0.3597	0	16.74	10.67	5.679	7.520
FEM	$3L_c/4$	0.1368	0.1850	0.1559	0.1700	0.09871	−0.4880	−0.2583	0	15.88	10.01	6.801	7.885
SSM		0.1361	0.1839	0.1544	0.1684	0.09765	−0.4868	−0.2579	0	15.85	10.01	6.801	7.877
FITM		0.1360	0.1839	0.1544	0.1683	0.09785	−0.4867	−0.2580	0	15.85	10.01	6.801	7.876
DG		0.1362	0.1839	0.1545	0.1686	0.09738	−0.4874	−0.2578	0	15.86	10.01	6.802	7.885
FEM	$7L_c/8$	0.07198	0.0626	0.02122	0.02653	0.07049	−0.2426	−0.1297	0	14.27	9.434	8.213	8.496
SSM		0.07182	0.06218	0.02062	0.02579	0.06966	−0.2413	−0.1290	0	14.24	9.427	8.214	8.493
FITM		0.07178	0.06218	0.02061	0.02576	0.06980	−0.2413	−0.1291	0	14.24	9.428	8.214	8.493
DG		0.07193	0.06221	0.02064	0.02589	0.06949	−0.2416	−0.1290	0	14.25	9.430	8.217	8.499

for $(\xi_1, \xi_2) \in \partial\hat{\Omega}$, and to surface tractions over its top surface prescribed as

$$\bar{\boldsymbol{t}} = -q_t \cos\left(\frac{\pi}{2\theta_{1t}}\xi_1\right) \cos\left(\frac{\pi}{2\theta_{2t}}\xi_2\right) \boldsymbol{g}^3, \quad \text{at } \xi_3 = \tau_t/2, \tag{4.42}$$

where $q_t = 100$ MPa and τ_t is the shell thickness. The considered material properties and the stacking sequences are those of the three shell sections denoted by T_1, T_2 and T_3 in Tab.(4.2).

Analytical solutions are not available for these tests. Therefore, the solution obtained using the present formulation is compared with the solution computed using the FEM software Abaqus® [26]. The comparison is performed in terms of the non-dimensional covariant component $\overline{u}_{\xi_3}$, defined as

$$\overline{u}_{\xi_3} = u_{\xi_3} \cdot \left(\frac{\tau_t^3 E_2}{R_{2t}^4 q_t}\right), \tag{4.43}$$

versus the number of total degrees of freedom of the algebraic system to be solved. Figs.(4.6a), (4.6c) and (4.6e) show $\overline{u}_{\xi_3}$ evaluated at $(\xi_1, \xi_2, \xi_3) = (0, 0, \tau_t/2)$ using the present formulation with the FSDT and a polynomial order $p = 3$ and using Abaqus' S4R elements for the shell sections T_1, T_2 and T_3, respectively. Similarly, Figs.(4.6b), (4.6d) and (4.6e) show $\overline{u}_{\xi_3}$ evaluated at $(\xi_1, \xi_2, \xi_3) = (0, 0, \tau_t/2)$ using the present formulation with the ESL theory ED_{222} and a polynomial order $p = 3$ and the results obtained using Abaqus' C3D8R elements for the shell sections T_1, T_2 and T_3, respectively. From the figures, it is possible to note that the present formulation reproduces the FEM results and, when using the ED_{222}, offers a significant saving in terms of total number of degrees of freedom with respect to the 3D model.

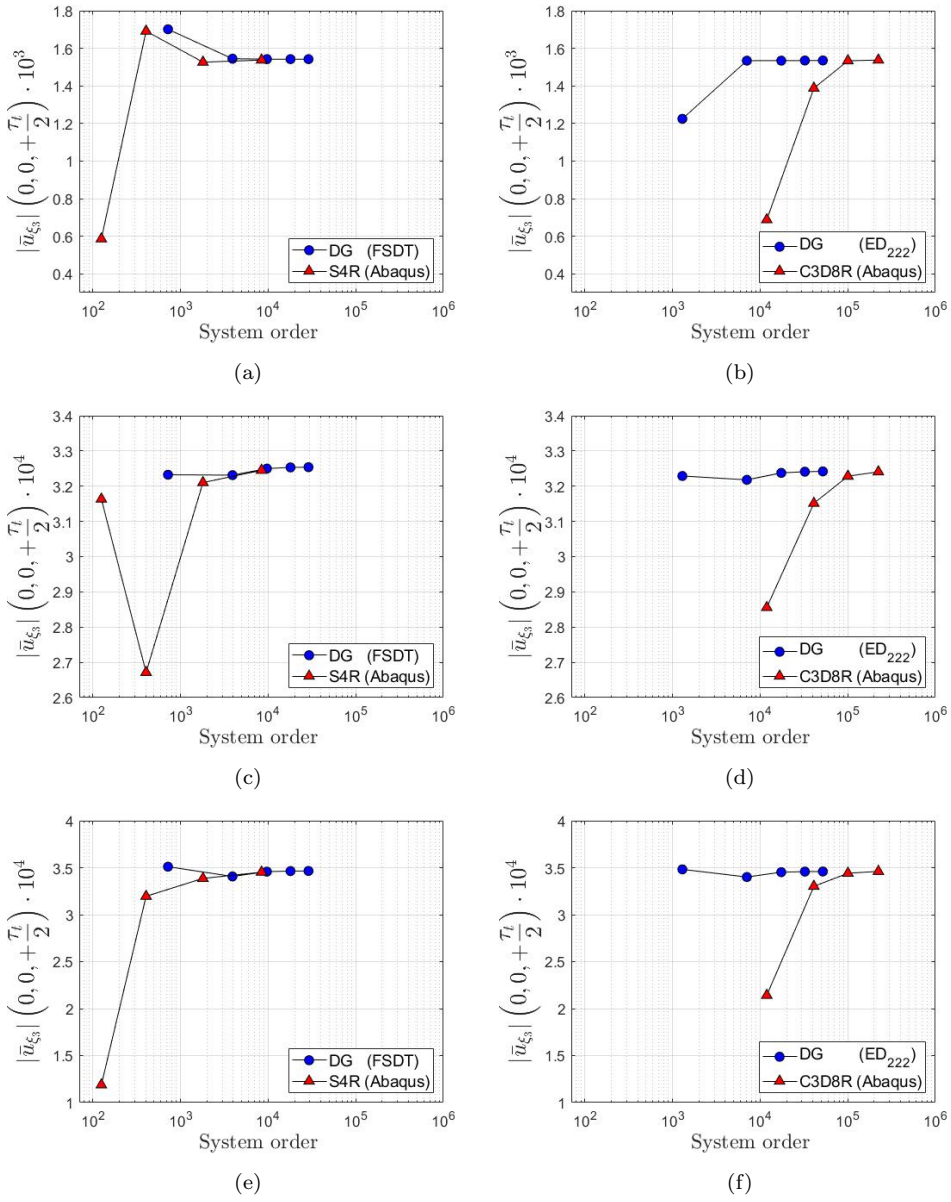

Figure 4.6: Comparison between the results obtained with the present formulation and the results obtained with FEM for the toroidal shell shown in Fig.(4.2c).

Table 4.5: Numerical values at convergence of Fig.(4.6).

Material	**Theory**	**Value**
Isotropic	DG (FSDT)	1.5422
	DG (ED_{222})	1.5352
	S4R (Abaqus)	1.5375
	C3D8R (Abaqus)	1.5375
Orthotropic	DG (FSDT)	3.2539
	DG (ED_{222})	3.2419
	S4R (Abaqus)	3.2451
	C3D8R (Abaqus)	3.2408
Laminated	DG (FSDT)	3.4652
	DG (ED_{222})	3.4595
	S4R (Abaqus)	3.4522
	C3D8R (Abaqus)	3.4607

4.2.3 Wing-shaped shell

In the tests discussed in this section, the wing-shaped shell shown in Fig.(4.2d) is considered. The profile of the wing is generated by means of a Joukowsky transformation [148] and the mid-surface of the shell is described by the equation

$$\boldsymbol{x}_0 = \begin{bmatrix} \xi_2 \\ (R_w \cos(\xi_1) - x_w)(1 + 1/\phi(\xi_1)) \\ (R_w \sin(\xi_1) + y_w)(1 - 1/\phi(\xi_1)) \end{bmatrix}, \tag{4.44}$$

with

$$\phi(\xi_1) = x_w^2 + y_w^2 + 2R_w(-x_w \cos(\xi_1) + y_w \sin(\xi_1)) + R_w^2, \tag{4.45}$$

where $\xi_1 \in [0, 2\pi]$, $\xi_2 \in [0, L_w]$, being L_w equal to L_{wa} or L_{wb} whether a short wing or a slender wing is considered, and x_w, y_w, L_{wa}, L_{wb} and R_w are reported in the third column of Tab.(4.3). As sketched in Fig.(4.2d), the shell is clamped over the lateral surface identified by the points $\boldsymbol{x} = \boldsymbol{x}(\xi_1, \xi_2 = 0, \xi_3)$ and is subjected to prescribed traction $\bar{\boldsymbol{t}} = q_w \boldsymbol{e}_3$ on the outer surface, i.e. the surface identified by $\boldsymbol{x} = \boldsymbol{x}(\xi_1, \xi_2, \xi_3 = \tau_w/2)$, being $\boldsymbol{e}_3 = \{0, 0, 1\}^\intercal$, $q_w = 10$ kPa and τ_w the thickness of the shell. The remaining surfaces are traction-free.

Eventually, the parameterization of the shell given by Eq.(4.44) is such that $\boldsymbol{x}_0(\xi_1, \xi_2 = 0) = \boldsymbol{x}_0(\xi_1, \xi_2 = 2\pi)$, i.e. the mid-surface is a closed surface, albeit non-smooth at $\xi_2 = 0$ and $\xi_2 = 2\pi$. Therefore, to enforce the displacement continuity at the trailing edge of the wing, the interior interior DG scheme is supplemented with an additional term the penalizes the jump between the Cartesian components of the displacement field evaluated at $\boldsymbol{x}_0 = \boldsymbol{x}_0(\xi_1, \xi_2 = 0)$ and the Cartesian components of the displacement field evaluated at $\boldsymbol{x}_0 = \boldsymbol{x}_0(\xi_1, \xi_2 = 2\pi)$. It is worth noting that such an approach has been employed to study assemblies of plates and shells, see e.g. [149, 150, 151] and has been implemented only for this specific test case to show the flexibility of the proposed formulation. A general treatment regarding the assembly of multilayered shells modeled using the ESL approach is not treated in this work.

The two shell sections denoted by W_1 and W_3 in Tab.(4.2) are considered and the results obtained with the present formulation are compared with those obtained using FEM. The comparison is performed in terms of the non-dimensional Cartesian component

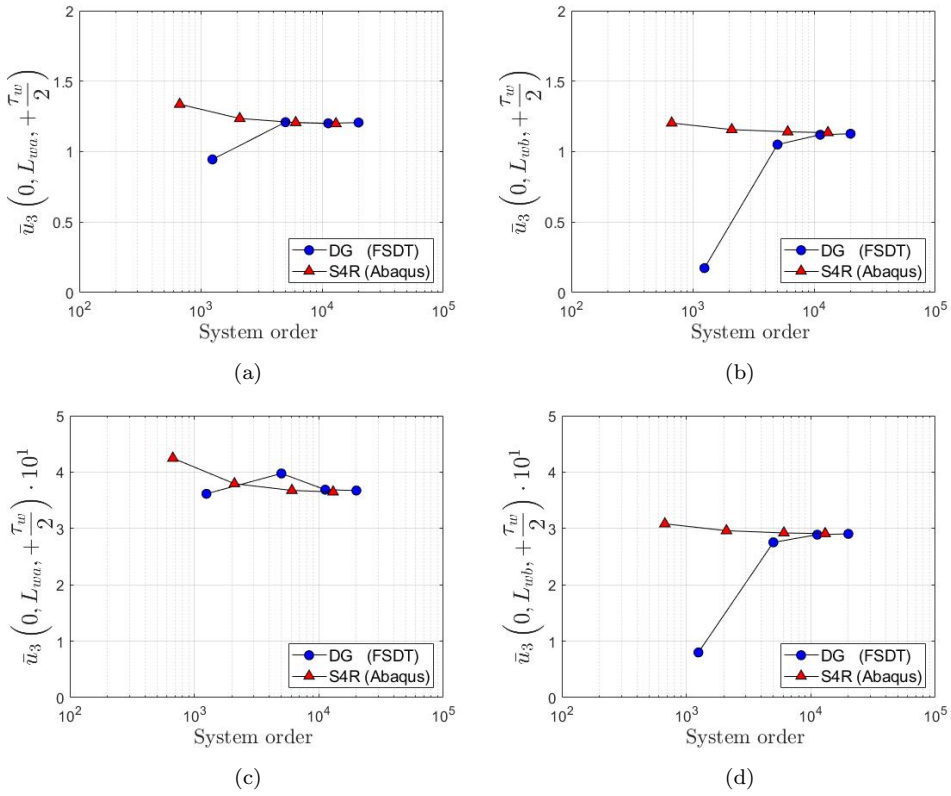

Figure 4.7: Comparison between the FEM solution and the solution obtained by the present formulation for the wing-shaped shell shown in Fig.(4.2d).

versus the number of total degrees of freedom of the algebraic system to be solved; $\overline{u}_3$ is defined as

$$\overline{u}_3 = u_3 \cdot \left(\frac{\tau_w s_w^2 E_2}{L_w^4 q_w} \right), \tag{4.46}$$

where $s_w = 0.475$ m represents the thickness of the wing profile. All numerical tests investigated in this section are performed using the FSDT. Figs.(4.7a) and (4.7c) refer to the case of the short wing, i.e. $L_w = L_{wa}$, and show $\overline{u}_3$ evaluated at $(\xi_1, \xi_2, \xi_3) = (0, L_{wa}, \tau_w/2)$ using the present formulation with polynomial order $p = 4$ and using Abaqus' S4R elements for the shell sections W_1 and W_3, respectively. Similarly, Figs.(4.7b) and (4.7d) refer to the case of the slender wing, i.e. $L_w = L_{wb}$, and show $\overline{u}_3$ evaluated at $(\xi_1, \xi_2, \xi_3) = (0, L_{wb}, \tau_w/2)$ using the present formulation with polynomial order $p = 4$ and using Abaqus' S4R elements for the shell sections W_1 and W_3, respectively. In all cases, it is possible to note that the present formulation reproduces the FEM results.

4.2.4 Planar elasticity using non-orthogonal curvilinear coordinates

To test a case of a geometry described by a set of non-orthogonal curvilinear coordinates, let us consider the planar geometry shown in Fig.(4.2e) and described by the equation

$$\boldsymbol{x} = \begin{bmatrix} 2\xi_1 \cos(\xi_2) \\ \xi_1 \sin(\xi_2) \\ 0 \end{bmatrix}, \tag{4.47}$$

Table 4.6: Numerical values at convergence of Fig.(4.7).

Material	**Lenght**	**Theory**	**Value**
Isotropic	Short	DG (FSDT)	1.2064
		S4R (Abaqus)	1.1982
	Long	DG (FSDT)	1.1270
		S4R (Abaqus)	1.1353
Laminated	Short	DG (FSDT)	3.6726
		S4R (Abaqus)	3.6472
	Long	DG (FSDT)	2.9045
		S4R (Abaqus)	2.9079

where $\xi_1 \in [b_m, b_m + l_m]$, $\xi_2 \in [0, \pi/2]$ and b_m and l_m are reported in the fourth column of Tab.(4.3). For this case, $\boldsymbol{g}_1 \cdot \boldsymbol{g}_2 \neq 0$. Let us also assume that the domain is subjected to a constant strain $\boldsymbol{\gamma}_{\text{ref}} = \{\varepsilon, -\varepsilon, 0, 0, 0, 0\}^\intercal$, with $\varepsilon = 0.01$, generated by a displacement field whose Cartesian components are $\boldsymbol{u}_{\text{ref}} = \varepsilon\{x_1, -x_2, 0\}^\intercal$. The corresponding covariant components of this displacement field are given as

$$\boldsymbol{u}_{\xi,\text{ref}} = \boldsymbol{R}\boldsymbol{u}_{\text{ref}} = \varepsilon \begin{bmatrix} -\xi_1(5\sin^2(\xi_2) - 4) \\ -5\xi_1^2 \sin(2\xi_2)/2 \\ 0 \end{bmatrix}. \tag{4.48}$$

For the problem at hand $\boldsymbol{U}$ contains the zero-th order generalized displacements only, i.e. $\boldsymbol{U} = \{U_{10}, U_{20}, U_{30}\}^\intercal$, since the out-of-plane behavior is disregarded in this case, and the boundary conditions are prescribed as $\boldsymbol{U} = \overline{\boldsymbol{U}} = \boldsymbol{u}_{\xi,\text{ref}}$. The considered shell sections are those denoted by P_2 and P_3 in Tab.(4.2), and, for this case, the angle $\theta^{\langle \ell \rangle}$ is referred to the Cartesian reference system rather than the curvilinear reference system.

The modeling domain $\hat{\Omega}$ of the shell is divided into $n \times n$ elements such that the dimension of each element is $hl_m \times h\pi/2$, being $h = 1/n$ a measure of the element size. The following error measure $e(\boldsymbol{u}_h)$ is introduced

$$e(\boldsymbol{u}_h) = \frac{|\boldsymbol{u}_h - \boldsymbol{u}_{\text{ref}}|_\infty}{|\boldsymbol{u}_{\text{ref}}|_\infty}, \tag{4.49}$$

where $\boldsymbol{u}_h$ collects the Cartesian components of the displacement field computed with the present formulation. Fig.(4.8) shows $e(\boldsymbol{u}_h)$ as a function of the element size h and the polynomial order p for the two considered shell sections. As it can be noted from the figures, the present formulation offers optimal convergence also when a system of non-orthogonal curvilinear coordinates is employed.

4.2.5 Generally-curved shell

In this set of tests, the shell shown in Fig.(4.2f) is considered. The shell consists of a tapered elliptical cylinder swept toward the x_2 axis. Its mid-surface is described by the equation

$$\boldsymbol{x}_0 = \begin{bmatrix} \xi_2 \\ a_g \cos(\xi_1)((f_g - 1)\xi_2/L_g + 1) + \Delta_g \xi_2/L_g \\ b_g \sin(\xi_1)((f_g - 1)\xi_2/L_g + 1) \end{bmatrix} \tag{4.50}$$

where $\xi_1 \in [0, 2\pi]$, $\xi_2 \in [0, L_g]$ and a_g, b_g, f_g, Δ_g and L_g are reported in the fifth column of Tab.(4.3). The considered shell section is the one denoted by G_1 in Tab.(4.2). The

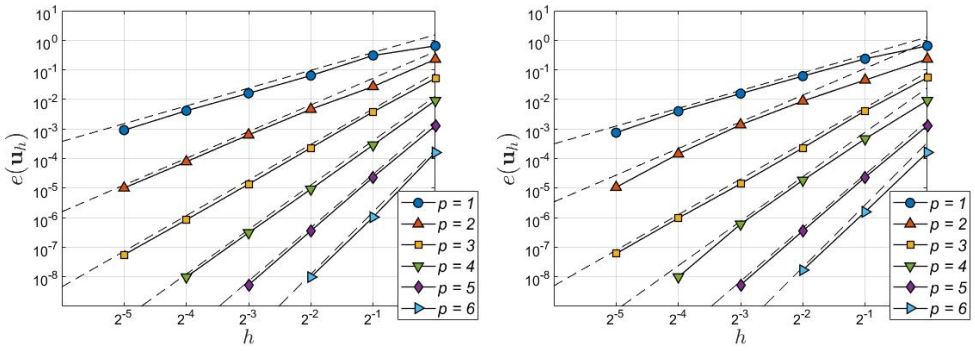

(a) (b)

Figure 4.8: *hp*-convergence analysis for the planar domain shown in Fig.(4.2e).Figure (a) and (b) respectively refer to the shell sections P_2 and P_3 reported in Tab.(4.2). The slope of the dashed lines is $p+1$.

shell is subjected to clamped boundary conditions on the lateral surface identified by $\boldsymbol{x} = \boldsymbol{x}(\xi_1, \xi_2 = 0, \xi_3)$ and to prescribed tractions $\bar{\boldsymbol{t}} = q_g \boldsymbol{e}_3$ on its outer surface, i.e. the surface identified by $\boldsymbol{x} = \boldsymbol{x}(\xi_1, \xi_2, \xi_3 = \tau_g/2)$, being $\boldsymbol{e}_3 = \{0, 0, 1\}^\intercal$, $q_g = 1$ MPa and τ_g the thickness of the shell; the remaining surfaces are traction-free. Moreover, similarly to the case of the wing-shaped shell, the parametrization given by Eq.(4.50) describes a closed surface such that $\boldsymbol{x}(\xi_1 = 0, \xi_2, \xi_3) = \boldsymbol{x}(\xi_1 = 2\pi, \xi_2, \xi_3)$. However, in this case, the geometry is smooth and the present formulation can be employed without the need for adding any additional penalization term provided that the domain $\hat{\Omega}$ is considered periodic in the variable ξ_1.

The results obtained using the present formulation are compared with the results computed using Abaqus®. The comparison is performed in terms of the non-dimensional Cartesian component $\overline{u}_3$, defined as

$$\overline{u}_3 = u_3 \cdot \left(\frac{\tau_g b_g^2 E_2}{L_g^4 q_g} \right), \tag{4.51}$$

versus the number of total degrees of freedom of the algebraic system to be solved.

Fig.(4.9a) shows $\overline{u}_3$ evaluated at $(\xi_1, \xi_2, \xi_3) = (0, L_g, \tau_g/2)$ using the present formulation with the FSDT and a polynomial order $p = 7$ and using Abaqus' S4R elements. Similarly, Fig.(4.9b) show $\overline{u}_3$ evaluated at $(\xi_1, \xi_2, \xi_3) = (0, L_g, \tau_g/2)$ using the present formulation with the ESL theories ED_{222} and ED_{333} and using Abaqus' C3D20R elements. Consistently with the findings related to all the previous tests, the figures show that the present formulation reproduces well the FEM results and offers a significant saving in terms of the total number of degrees of freedom.

For the sake of completeness, Figs.(4.10a) and (4.10b) show the contour plots of the displacement component $\overline{u}_3$ and the stress component $\overline{\sigma}_{11}$, respectively, which have been computed using the present formulation with a 8×8 mesh of the reference domain $\hat{\Omega}$ and a polynomial order $p = 7$. In the figures, $\overline{u}_3$ is given by Eq.(4.51) whereas $\overline{\sigma}_{11} = \sigma_{11} \cdot \left(\frac{\tau_g b_g}{L_g^2 q_g} \right)$.

4.2.6 Fuselage panel with window

The next geometry investigated is a cylindrical shell with a cut-out as shown in Figs.(4.3a), (4.3b) and (4.3c). The dimensions and the level set are chosen in order to resemble a

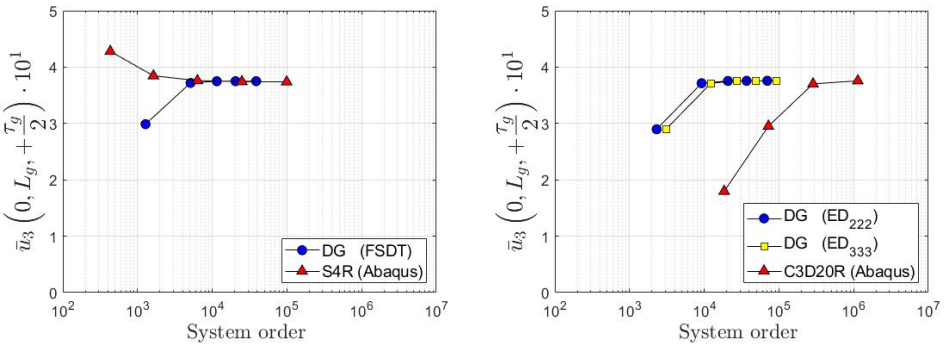

(a) (b)

Figure 4.9: Comparison between the FEM solution and the solution obtained by the present formulation for the shell shown in Fig.(4.2f).

Table 4.7: Numerical values at convergence of Fig.(4.9).

Theory	**Value**
DG (FSDT)	3.7500
DG (ED$_2$22)	3.7567
DG (ED$_3$33)	3.7568
S4R (Abaqus)	3.7375
C3D20R (Abaqus)	3.7563

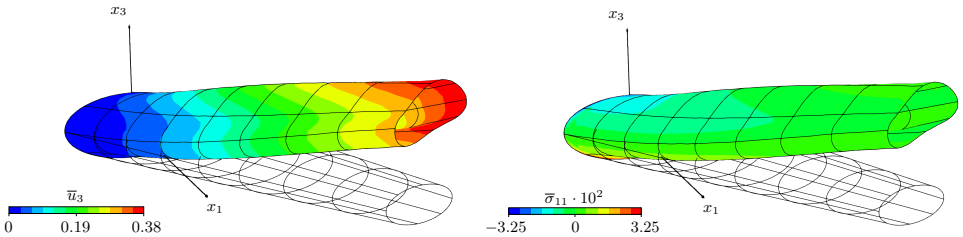

(a) (b)

Figure 4.10: Deformed shaped of the generally-curved shell problem shown in Fig.(4.2f) with superimposed contours of (a) the displacement component $\overline{u}_3$ and (b) the stress component $\overline{\sigma}_{11}$.

fuselage panel with a window. The reference surface is mapped by the equation

$$\boldsymbol{x}_0 = \begin{bmatrix} \xi_1 \\ R_f \sin(\xi_2) \\ R_f \cos(\xi_2) \end{bmatrix}, \tag{4.52}$$

where $\xi_1 \in [-L_f/2, +L_f/2]$ and $\xi_2 \in [-\theta_f, +\theta_f]$ and R_f, L_f and θ_f are reported in Tab.(4.3). The level set function used to define the cut-out is chosen as

$$\phi(\boldsymbol{x}_0) = a_f^{d_f} - |x_{01}|^{d_f} - \left| \frac{x_{02}}{b_f/a_f} \right|^{d_f}, \tag{4.53}$$

where a_f, b_f and d_f are also reported in Tab.(4.3). The shell has clamped external boundaries, traction-free boundary conditions along the cut-out, and is subjected to a uniform pressure on the bottom surface identified by $\boldsymbol{x} = \boldsymbol{x}(\xi_1, \xi_2, -\tau_f/2)$ as

$$\bar{\boldsymbol{t}} = -q_f \boldsymbol{g}^3. \tag{4.54}$$

The four shell sections labelled as F_1 to F_4 in Tab.(4.2) are investigated, and the following non-dimensional magnitude of the displacement is introduced

$$|\overline{u}| \equiv |u| \cdot \left(\frac{\tau_f^3 E_r}{(L_f/2)^4 q_f} \right). \tag{4.55}$$

Consider the point $\boldsymbol{x}^*$ in Fig.(4.3c) corresponding to $\xi_1 = \xi_3 = 0$ and $\xi_2 = \alpha = \arcsin(b_f/R_f)$. The value of $|\overline{u}|$ at $\boldsymbol{x}^*$ is computed using the FSDT and the ED_{444} theory and a DG scheme with polynomial order $p = 4$, and is then compared with the value evaluated at the same location computed using Abaqus S4R shell elements and C3D20R brick elements. Figs.(4.11a), (4.11b), (4.11c) and (4.11d) report the obtained results as functions of the overall number of degrees of freedom of the discrete system for the shell sections F_1, F_2, F_3 and F_4, respectively, and show how the proposed scheme is able to recover the FEM results. Moreover, by looking at Fig.(4.11a), which corresponds to the case of the isotropic shell, one observes no noticeable difference in the values of the displacement magnitude computed with the FSDT, the ED_{444} theory and the 3D FEM model; differently, considering Fig.(4.11b), which corresponds to the case of the orthotropic shell, it is clear how the high-order ED_{444} reproduces more adequately the 3D FEM solution with respect to the low-order FSDT.

The effect of the polynomial order p on the value of the non-dimensional displacement magnitude $|\overline{u}|$ evaluated at the same point $\boldsymbol{x}^* = \boldsymbol{x}(0, \alpha, 0)$ is shown in Fig.(4.12); Fig.(4.12a) is referred to the shell section F_2 modeled with the ED_{444} theory, while Fig.(4.12b) is referred to the shell section F_3 modeled with the FSDT. In both cases, as expected, using $p = 6$ allows obtaining the converged solution with the smallest number of degrees of freedom, whereas using $p = 2$ shows the slowest convergence rate.

Fig.(4.13) shows the value of the non-dimensional displacement magnitude $|\overline{u}|$ as given in Eq.(4.55) along the curve identified by varying ξ_1 and by keeping constant $\xi_2 = \alpha$ and $\xi_3 = 0$; the curve is indicated as r in Fig.(4.3c). Figs.(4.13a), (4.13b), (4.13c) and (4.13d) are referred to the shell sections F_1, F_2, F_3 and F_4, respectively. In all figures, the results referring to the present approach are obtained using the FSDT theory and a DG scheme with polynomial order $p = 4$, whereas the reference solution (the dashed line in the figure) is obtained using Abaqus' S4R shell elements. Also in this case, the obtained results confirm the accuracy of the proposed method.

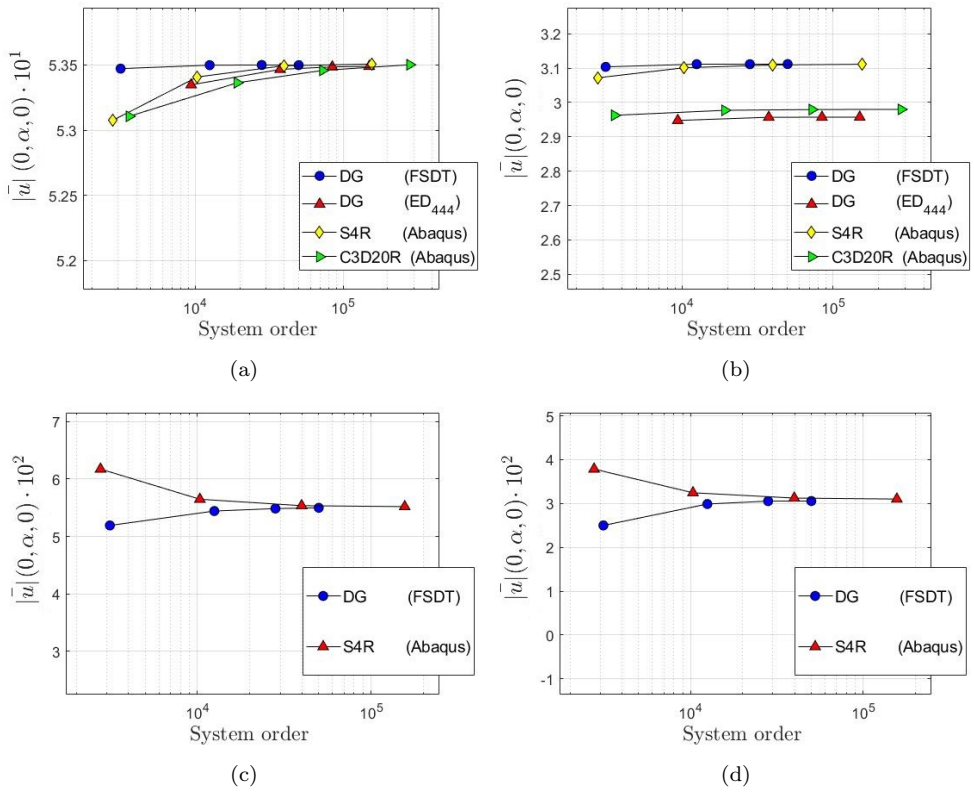

Figure 4.11: Comparison between the convergence of the FEM solution and the convergence of the solution obtained by the present formulation for the fuselage panel.

The effect of the mesh size on the value of $|\overline{u}|$ evaluated along the same curve using the FSDT theory and a DG scheme with polynomial order $p = 2$ is presented in Figs.(4.14a) and (4.14b) for the shell sections F_2 and F_3, respectively. Here, it is interesting to note that the multilayered shell displays a slower convergence rate as a function of the number of cells in the background grid with respect to the case of the homogeneous orthotropic shell.

As a concluding remark for the cylindrical shell test, the contour plots of the non-dimensional displacement magnitude as given in Eq.(4.55) and two selected stress measures are shown in Fig.(4.15), where they are superimposed on the deformed shape of the top surface of the shell. In particular, Fig.(4.15a) shows the contour plot of the non-dimensional displacement magnitude for the shell sections F_1, Fig.(4.15b) shows the contour plot of the non-dimensional displacement magnitude for the shell sections F_3, Fig.(4.15c) shows the contour plot of the non-dimensional Von Mises stress $\overline{\sigma}_m$ for the shell sections F_1, and Fig.(4.15d) shows the contour plot of the non-dimensional stress component $\overline{\sigma}_{11}$ for the shell sections F_3. To compute the stress measures introduced above, the stress components are non-dimensional accordingly to the equation

$$\overline{\sigma}_{ij} \equiv \sigma_{ij} \cdot \left(\frac{\tau_f^2}{(L_f/2)^2 q_f} \right), \tag{4.56}$$

where σ_{ij} is a generic component of $\boldsymbol{\sigma}$.

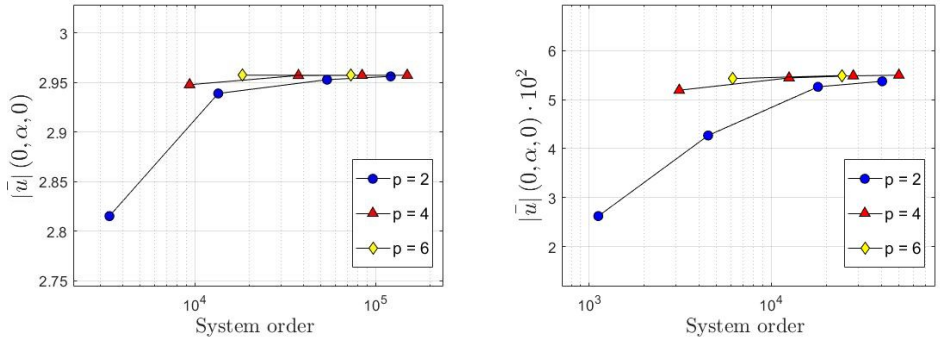

(a) (b)

Figure 4.12: Comparison between the convergence of the solution obtained by the present formulation for different polynomials orders p for the fuselage panel.

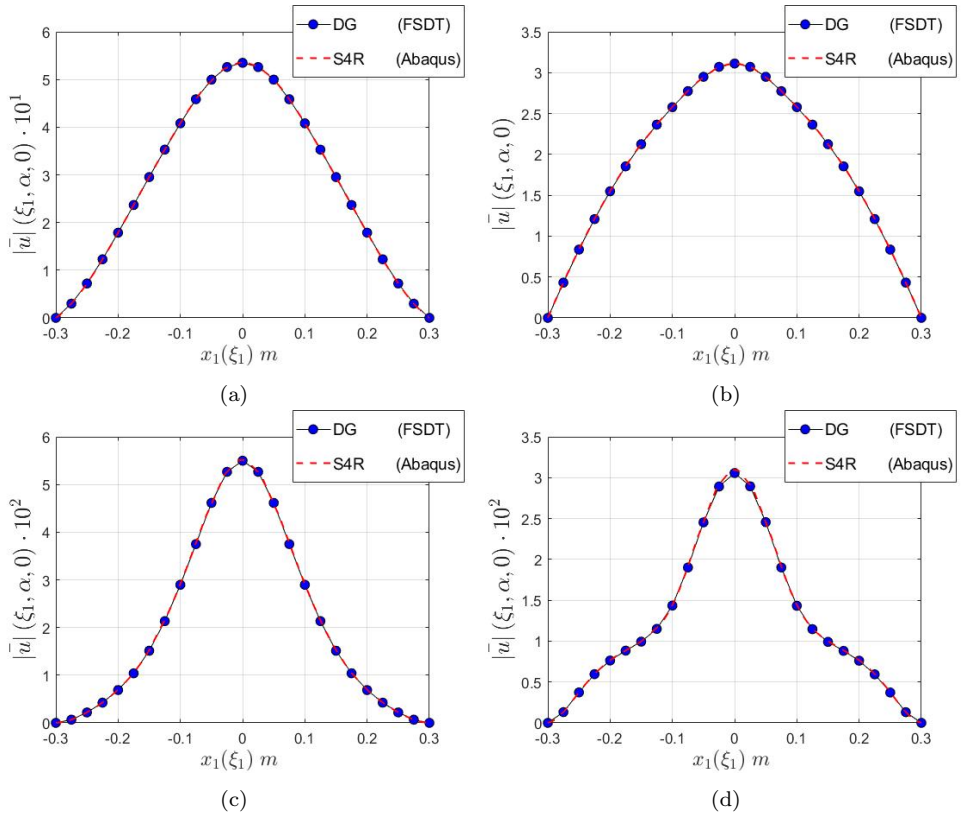

(a) (b) (c) (d)

Figure 4.13: Comparison between the FEM solution and the solution obtained by the present formulation for the fuselage panel.

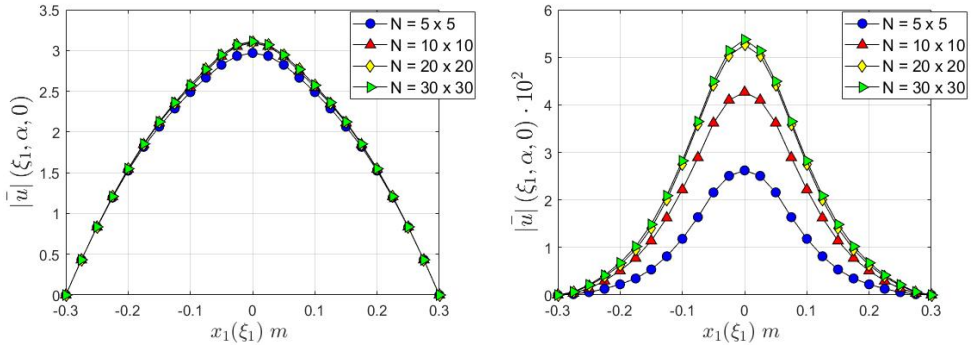

(a) (b)

Figure 4.14: Comparison between the solution obtained by the present formulation for different numbers of mesh elements for the fuselage panel.

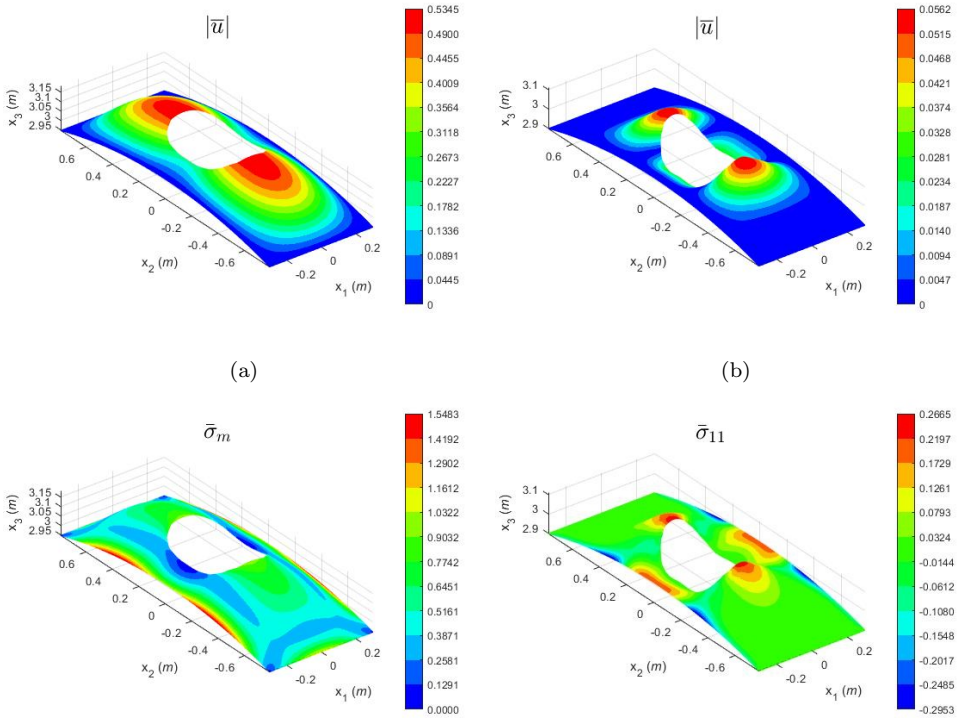

(a) (b)

(c) (d)

Figure 4.15: Deformed shape of the fuselage panel with superimposed contours of (a) the magnitude of the displacement and (c) the Von Mises stress for the section F_1, and (b) the magnitude of the displacement and (d) the stress component $\overline{\sigma}_{11}$ for the section F_3.

4.2.7 Generally-curved NURBS-based shell

The next geometry investigated is defined in terms of NURBS functions as described in the Chapter 5 where $\xi_1 \in [0,1]$ and $\xi_2 \in [0,1]$, the control points $\boldsymbol{P}_{ij}$ and their weights are given in Tab.(4.8), and the open knot vector is $\{0,0,0,0,0,0.2,0.4,0.6,0.8,1,1,1,1,1\}$ for both ξ_1 and ξ_2.

It is worth remarking that in this case the shell is represented by non-orthogonal curvilinear coordinates. The cut-out is obtained through the level set

$$\phi(\boldsymbol{x}_0) = a_n^{d_n} - |x_{01} - x_{1n}|^{d_n} - |x_{02} - x_{2n}|^{d_n}, \tag{4.57}$$

where a_n, d_n, x_{1n} and x_{2n} are reported in Tab.(4.3). The resulting shell geometry is displayed in Figs.(4.3d), (4.3e), and (4.3f). The shell is subjected to clamped boundary conditions on its lateral surfaces and traction free boundary conditions along the cut-out boundary, while a uniform pressure $\boldsymbol{t} = q_n \boldsymbol{g}^3$ is applied on the bottom surface.

The two shell sections labelled as N_1 and N_2 in Tab.(4.2) are investigated. The accuracy of the proposed method is assessed by comparing the solution computed with the present approach using the FSDT theory and a DG scheme with polynomial order $p = 6$ and the solution computed using Abaqus' S3R shell elements. The comparison is shown in Fig.(4.16) in terms of the non-dimensional displacement magnitude defined as

$$|\overline{u}| \equiv |u| \cdot \left(\frac{\tau_n^3 E_r}{(L_n/2)^4 q_n} \right). \tag{4.58}$$

The value of $|\overline{u}|$ is computed along the curve identified by the points $\boldsymbol{x} = \boldsymbol{x}(\beta, \xi_2, 0)$ and along the curve identified by the points $\boldsymbol{x} = \boldsymbol{x}(\xi_1, \alpha, 0)$, where $\beta = 0.43$ and $\alpha = 0.55$. The former curve is indicated as s in Fig.(4.3f), while the latter is indicated as t in Fig.(4.3f). Figures (4.16a) and (4.16c) refer to the shell section N_1, while Figs.(4.16b) and (4.16d) refer to the shell section N_2. The obtained results confirm the accuracy of the proposed method also for a shell described by NURBS functions.

The effect of the mesh size on the value of $|\overline{u}|$ evaluated along the same curves using the FSDT theory and a DG scheme with polynomial order $p = 2$ is presented in Figs.(4.17a) and (4.17c) for the shell section N_1 and in Figs.(4.17b) and (4.17d) for the shell section N_2. The same convergence behavior is observed for the considered shell sections.

To conclude, Fig.(4.18) shows the deformed shape of the top surface of the considered shells with superimposed contour plots of the non-dimensional magnitude as given in Eq.(4.58) and two selected stress measures, which are evaluated using the following non-dimensional stress components

$$\overline{\sigma}_{ij} \equiv \sigma_{ij} \cdot \left(\frac{\tau_n^2}{(L_n/2)^2 q_n} \right). \tag{4.59}$$

The reported figures show the complex stress distribution induced by the interaction between the curvature of the shell and the presence of the cut-out.

4.2.8 Layer-Wise investigation of a cylindrical shell with cut-out

In this section, the proposed LW formulation is assessed through a numerical application to the cylindrical shell shown in Fig.(4.19). The reference surface is defined using a

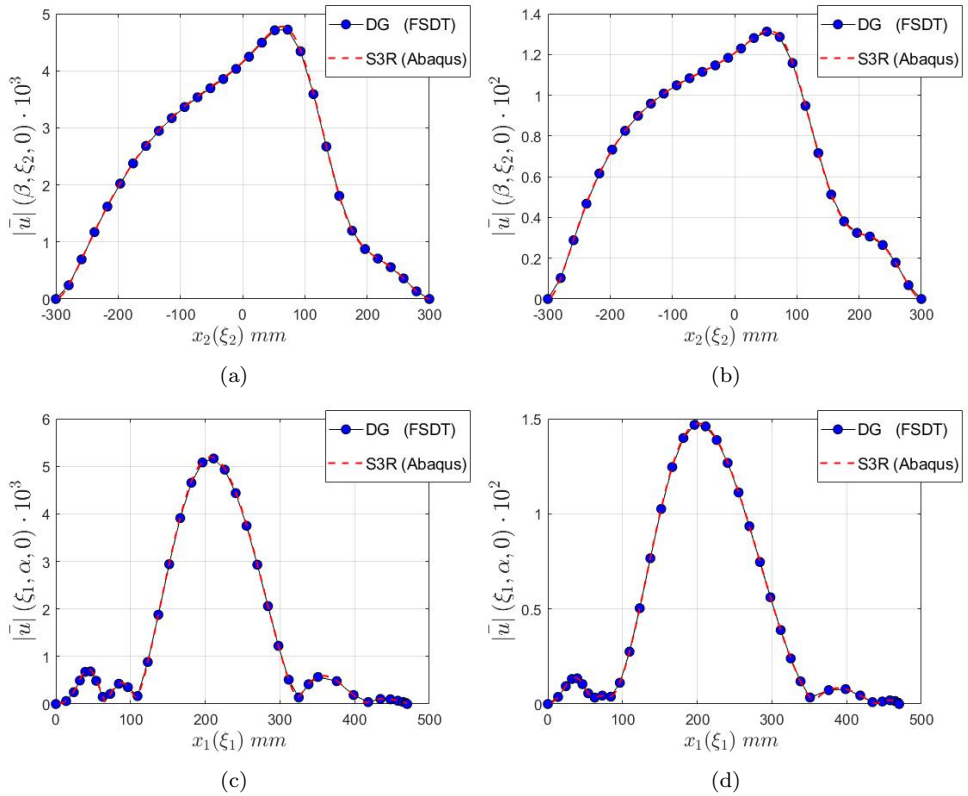

Figure 4.16: Comparison between the FEM solution and the solution obtained by the present formulation for the NURBS-based shell.

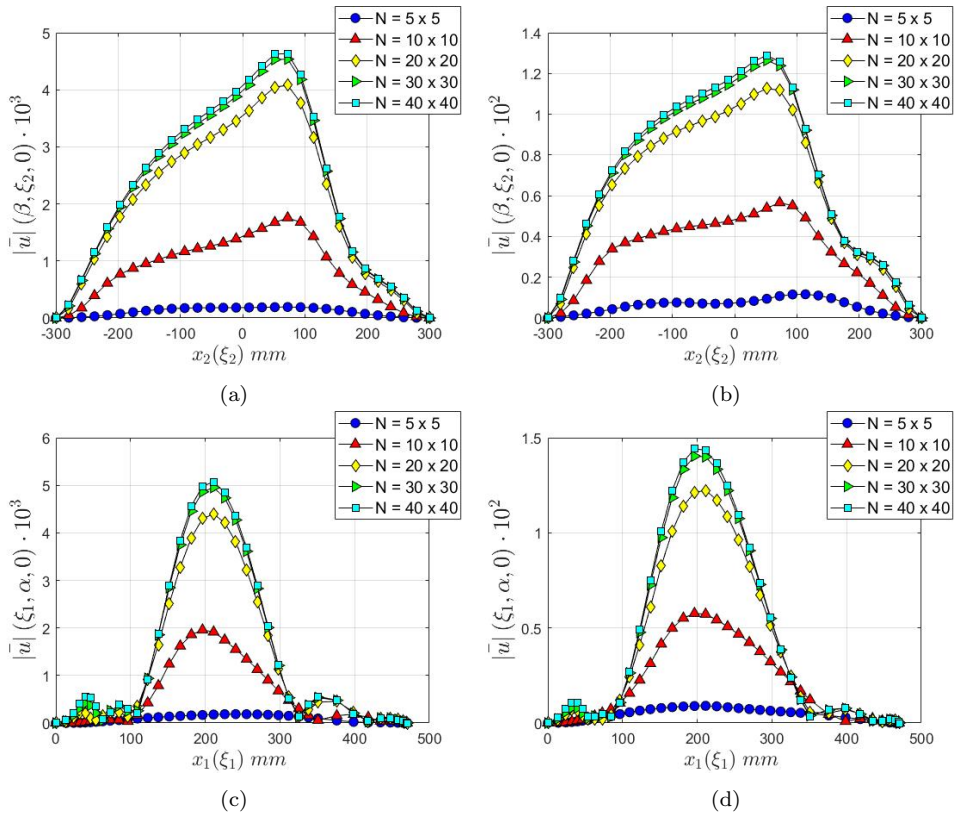

Figure 4.17: Comparison between the solution obtained by the present formulation for different numbers of mesh elements for the NURBS-based shell.

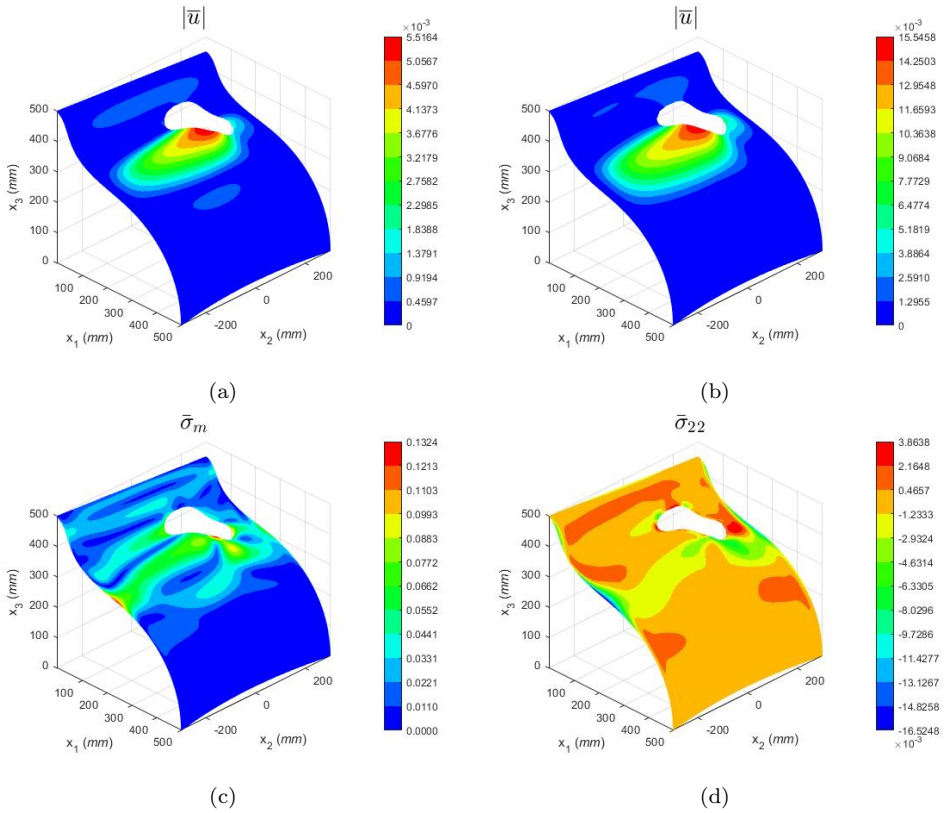

Figure 4.18: Deformed shape of the NURBS-based shell with superimposed contours of (a) the magnitude of the displacement and (c) the Von Mises stress for the section N_1, and (b) the magnitude of the displacement and (d) the stress component $\overline{\sigma}_{22}$ for the section N_2.

Table 4.8: List of control points for the NURBS surface in Fig.(4.3f). For each control point it is reported the correspondent indices i and j, the coordinates x_1, x_2 and x_3 in mm and the weight h_{ij}.

i,j	x_1	x_2	x_3	h_{ij}	i,j	x_1	x_2	x_3	h_{ij}	i,j	x_1	x_2	x_3	h_{ij}
1,1	0.00	−300.00	500.00	1	4,1	153.89	−300.00	328.89	1	7,1	489.97	−300.00	108.82	1
1,2	0.00	−270.00	497.49	1	4,2	152.46	−270.00	327.10	1	7,2	484.12	−270.00	108.82	1
1,3	0.00	−210.00	492.48	1	4,3	150.54	−210.00	323.51	1	7,3	474.05	−210.00	108.83	1
1,4	0.00	−120.00	484.99	1	4,4	149.50	−120.00	318.55	1	7,4	463.69	−120.00	108.84	1
1,5	0.00	0.00	475.01	1	4,5	148.91	0.00	314.01	1	7,5	459.16	0.00	108.85	1
1,6	0.00	120.00	465.04	1	4,6	145.18	120.00	313.29	1	7,6	463.69	120.00	108.83	1
1,7	0.00	210.00	457.53	1	4,7	142.95	210.00	314.32	1	7,7	474.05	210.00	108.82	1
1,8	0.00	270.00	452.51	1	4,8	142.70	270.00	315.27	1	7,8	484.15	270.00	108.81	1
1,9	0.00	300.00	450.00	1	4,9	143.04	300.00	315.74	1	7,9	490.01	300.00	108.80	1
2,1	36.11	−300.00	483.13	1	5,1	304.62	−300.00	309.21	1	8,1	500.01	−300.00	36.28	1
2,2	36.06	−270.00	480.98	1	5,2	301.48	−270.00	308.51	1	8,2	493.99	−270.00	36.28	1
2,3	36.00	−210.00	476.67	1	5,3	296.52	−210.00	307.12	1	8,3	483.58	−210.00	36.28	1
2,4	36.01	−120.00	470.21	1	5,4	292.27	−120.00	305.19	1	8,4	472.81	−120.00	36.27	1
2,5	36.10	0.00	461.57	1	5,5	290.80	0.00	303.39	1	8,5	468.02	0.00	36.27	1
2,6	36.10	120.00	452.86	1	5,6	290.63	120.00	303.04	1	8,6	472.78	120.00	36.28	1
2,7	36.16	210.00	446.27	1	5,7	293.65	210.00	303.37	1	8,7	483.54	210.00	36.28	1
2,8	36.26	270.00	441.86	1	5,8	297.79	270.00	303.69	1	8,8	493.97	270.00	36.28	1
2,9	36.33	300.00	439.65	1	5,9	300.52	300.00	303.85	1	8,9	500.00	300.00	36.28	1
3,1	41.45	−300.00	387.42	1	6,1	441.80	−300.00	213.61	1	9,1	500.00	−300.00	0.00	1
3,2	41.14	−270.00	385.76	1	6,2	436.77	−270.00	213.52	1	9,2	493.98	−270.00	0.00	1
3,3	40.80	−210.00	382.44	1	6,3	428.27	−210.00	213.33	1	9,3	483.57	−210.00	0.00	1
3,4	40.79	−120.00	377.66	1	6,4	419.88	−120.00	213.07	1	9,4	472.80	−120.00	0.00	1
3,5	40.62	0.00	372.26	1	6,5	416.46	0.00	212.86	1	9,5	468.01	0.00	0.00	1
3,6	38.78	120.00	368.63	1	6,6	419.60	120.00	212.87	1	9,6	472.77	120.00	0.00	1
3,7	37.28	210.00	366.62	1	6,7	427.79	210.00	212.98	1	9,7	483.54	210.00	0.00	1
3,8	36.60	270.00	365.41	1	6,8	436.17	270.00	213.06	1	9,8	493.97	270.00	0.00	1
3,9	36.40	300.00	364.80	1	6,9	441.15	300.00	213.10	1	9,9	500.00	300.00	0.00	1

Table 4.9: Control points for the cylindrical shell with cut-outs in Fig.(4.19)

i,j	x_1	x_2	x_3	h_{ij}
1,1	$-l/2$	$-R\sin\theta$	$R\cos\theta$	1
1,2	$-l/2$	0	$R\sqrt{2}$	$\sqrt{2}/2$
1,3	$-l/2$	$R\sin\theta$	$R\cos\theta$	1
2,1	$+l/2$	$-R\sin\theta$	$R\cos\theta$	1
2,2	$+l/2$	0	$R\sqrt{2}$	$\sqrt{2}/2$
2,3	$+l/2$	$R\sin\theta$	$R\cos\theta$	1

NURBS description with control points in Tab.(4.9). The shape functions correspond to a knot vector [0, 0, 1, 1] and a degree of 1 in the ξ_1 direction, as well as a knot vector [0, 0, 0, 1, 1, 1] and a degree of 2 in the ξ_2 direction. Additionally, the following level-set function is used to model the circular cut-out

$$\phi(\boldsymbol{x}_0) = r^2 - |x_{01}|^2 - |x_{02}|^2 \ . \tag{4.60}$$

Regarding the geometrical properties of the shell, the cylinder has a radius of $R = 1$ m, a length of $l = 1$ m, a cut-out radius of $r = 0.25$ m, and the angle of the cylindrical sector is $\theta = \pi/4$ rad. The shell section, denoted as L_1, has a thickness of $\tau = 0.1$ m and consists of three layers, with properties detailed in Tab.(4.2). The shell's boundary is fully clamped, and a uniform pressure q is applied to the external surface. The analysis is performed using a fourth-order LW theory and a grid with 10×10 elements with a polynomial order of $p = 5$. The results are compared with a three-dimensional solution obtained using Abaqus' C3D20R brick elements.

Fig.(4.20a) illustrates the behavior of the first Cartesian component of the non-dimensional displacement vector $\overline{u}_1$ along the thickness at a point with curvilinear coordinates $\xi_1 = \beta = 0.5500$ and $\xi_2 = \gamma = 0.6510$, as indicated in blue in Fig.(4.19c). Fig.(4.20b) displays the behavior along a line obtained by varying ξ_1 for $\xi_2 = \alpha = 0.6534$ and $\xi_3 = \tau/2$, as plotted in red in Fig.(4.19c). In both graphs, $\overline{u}_1$ is computed as

$$\overline{u}_1 = \frac{\tau^2 E_r}{l^3 q} u_1 \ . \tag{4.61}$$

It is evident that the solution is well approximated in the reference domain. Moreover, the use of a fourth-order LW theory enables an accurate reconstruction of the displacement along the thickness, which a common FSDT cannot capture precisely. As a concluding remark, Fig.(4.21) depicts the deformation of the shell and the contour plot of $\overline{u}_1$.

4.2.9 Damaged plate with circular cut-out

In this section, it is tested the versatility of the proposed method in analyzing damaged plate structures, taking as example a plate with a circular central cut-out as illustrated in Fig.(4.22). The square plate has a length of $L = 1$ m, and the internal circular cut-out has a radius of $R = 0.1$ m. The parameterization of the plate surface is based on an identical mapping

$$\boldsymbol{x_0} = \begin{bmatrix} \xi_1 \\ \xi_2 \\ 0 \end{bmatrix} \ , \tag{4.62}$$

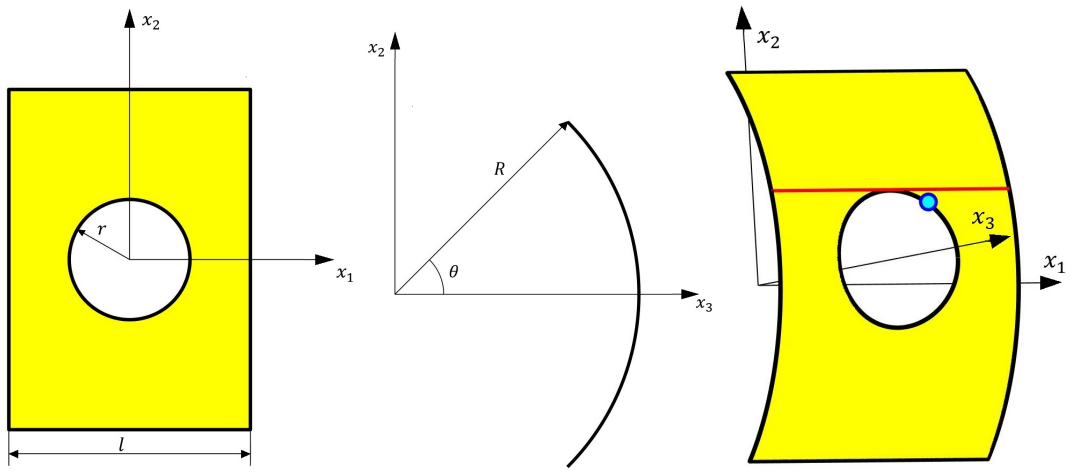

(a) (b) (c)

Figure 4.19: Geometry of the cylindrical shell with cut-out modeled through LW expansion in three different views.

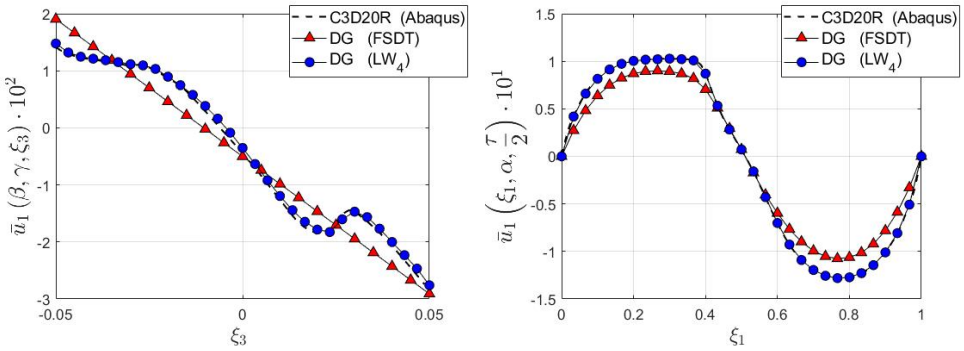

(a) (b)

Figure 4.20: Comparison between the solution obtained to the problem shown in Fig.(4.19) with the present formulation through a LW expansion and the 3D solution to the same problem obtained through Abaqus' C3D20R elements.

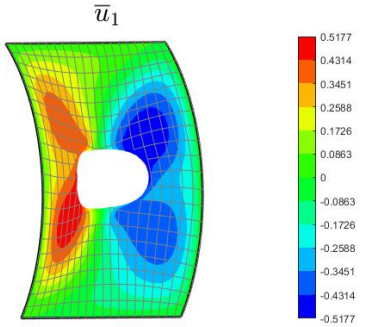

Figure 4.21: Deformation of the shell shown in Fig.(4.19) with superimposed contour of $\overline{u}_1$.

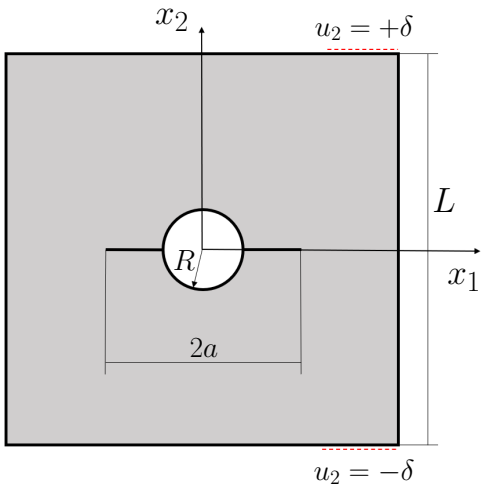

Figure 4.22: Geometry of the damaged plate with cut-out.

where $(\xi_1, \xi_2) \in [-L/2, +L/2] \times [-L/2, +L/2]$. The shell is a laminate denoted as S1, with details provided in Tab.(4.2). The boundaries corresponding to $\xi_1 = \pm L/2$ are left free. At the boundary corresponding to $\xi_2 = +L/2$, a displacement $\overline{\boldsymbol{u}} = 0, +\delta, 0^{\mathrm{T}}$ is imposed, and at the boundary corresponding to $\xi_2 = -L/2$, a displacement $\overline{\boldsymbol{u}} = 0, -\delta, 0^{\mathrm{T}}$ is imposed. It is worth noting that, similar to the case investigated in Sec. 4.2.4, the problem settings result in a purely membrane response, and the theory adopted is ED000, which disregards the along-the-thickness variation of the displacement components. The plate is assumed to be damaged by a fracture with a length of $2a = 0.5$ m, centered within the plate and crossing the cut-out while aligned with x_1.

The internal cut-out is defined using the implicit technique, employing a level-set function defined as

$$\phi(\xi_1, \xi_2) = R^2 - \xi_1^2 - \xi_2^2 \,. \tag{4.63}$$

The domain is discretized using an 8×8 mesh, with elements of order $p = 5$. Leveraging the discontinuous nature of the DG approximation function, the fracture is modeled by deactivating the integration in the internal interfaces that correspond to the the fracture surface. In this way, the continuity among the corresponding elements is not enforced anymore, allowing the fracture surface to open.

In Figs.(4.23a), (4.23b), and (4.23c), the contours of the non-dimensional magnitude of the displacement, the non-dimensional displacement component $\overline{u}_2$, and the non-dimensional stress component $\overline{\sigma}_{22}$ are superimposed on the deformed plate configuration. It can be easily noted how deactivating the integration on the corresponding elements leads to a clear opening of the fracture surface. In Fig.(4.23), the non-dimensional displacement and the non-dimensional stress are computed as

$$\overline{\boldsymbol{u}} = \frac{\boldsymbol{u}}{\delta} \quad \text{and} \quad \overline{\boldsymbol{\sigma}} = \frac{\boldsymbol{\sigma} L}{E_r \delta} \,. \tag{4.64}$$

In Fig.(4.23c) and in the zoom in Fig.(4.23d), a typical stress concentration at the tip of the fracture can be observed. This test demonstrates how the DG method easily lends itself to the study of structures with fractures. However, using such an approach, the interfaces between elements must conform to the fracture geometry, and for complex fracture lines, more refined meshing strategies should be considered.

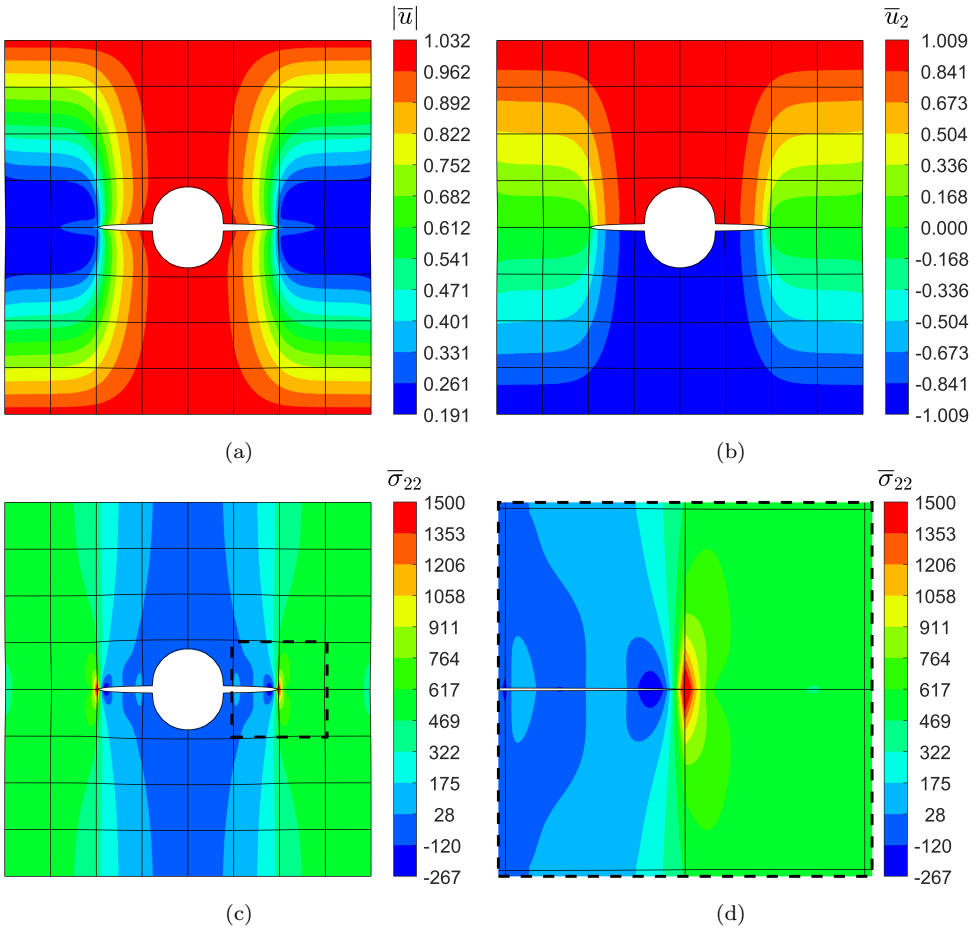

Figure 4.23: Contour of the non-dimensional magnitude of the displacement $|\overline{\boldsymbol{u}}|$ (a), non-dimensional component of the displacement $\overline{u}_2$ (b), and non-dimensional component of the stress tensor $\overline{\sigma}_{22}$ (c), with zoom on the fracture tip (d).

Table 4.10: Properties of the considered materials.

Material ID	Property	Component	Value
M_1	Young's moduli	E_1/E_r	variable
		E_2/E_r, E_3/E_r	1
	Poisson's ratios	ν_{23}, ν_{13}, ν_{12}	0.25
	Shear moduli	G_{23}/E_r	0.5
		G_{13}/E_r, G_{12}/E_r	0.6
M_2	Young's moduli	E_1/E_r	40
		E_2/E_r, E_3/E_r	1
	Poisson's ratios	ν_{23}, ν_{13}, ν_{12}	0.25
	Shear moduli	G_{23}/E_r	0.6
		G_{13}/E_r, G_{12}/E_r	0.5

Table 4.11: Properties of the considered shell sections.

Shell ID	Material	Layup	Layer(s) thickness
P_1	M_1	[0/90/0]	$\tau_0 = \tau/4, \tau_{90} = \tau/2$
P_2	M_1	[0/90/0/90/0/90/0/90/0]	$\tau_0 = \tau/10, \tau_{90} = \tau/8$
C_1	M_2	[0/90/0/90/0]	$\tau/5$
C_2	M_2	[0/90/0]	$\tau_0 = \tau/5, \tau_{90} = 3\tau/5$
H_1	M_1	$[(+30/-30)_2]_s$	$\tau/8$
N_1	M_2	[0/90/90/0]	$\tau/4$

4.3 Numerical results for buckling analysis

In this section the capabilities of the proposed buckling formulation are assessed through several numerical tests. Four composite structures are investigated, namely, a laminated plate, a laminated cylindrical shell, a laminated plate with a circular cutout, and a laminated NURBS-based shell, under various geometrical and material configurations. Various ESL theories are adopted as well as the FSDT as a special case of the ED_{110} theory combined with the plane stress assumption.

The engineering constants of the considered materials are listed in Tab.(4.10), while the lamination sequences of the considered composite structures are reported in Tab.(4.11). Legendre polynomials are employed as thickness functions and as basis functions for the DG formulations.

4.3.1 Laminated plate

The first investigated composite structure is a multilayered square plate with simply-supported edges as illustrated in Fig.(4.24a), i.e. $u_{\xi_1} = u_{\xi_3} = 0$ at $\xi_1 = (0, a)$ and $u_{\xi_2} = u_{\xi_3} = 0$ at $\xi_2 = (0, a)$. The mean surface of the plate is defined through the simple map

$$\boldsymbol{x}_0 = \begin{bmatrix} \xi_1 \\ \xi_2 \\ 0 \end{bmatrix}, \tag{4.65}$$

where $(\xi_1, \xi_2) \in \hat{\Omega} = [0, a] \times [0, a]$. A uniform initial stress state is assumed for each layer and is defined by setting

$$\overline{\sigma}_{11}^{\langle \ell \rangle} = -c_{11}^{\langle \ell \rangle} \varepsilon^0, \quad \text{and} \quad \overline{\sigma}_{22}^{\langle \ell \rangle} = -\chi c_{22}^{\langle \ell \rangle} \varepsilon^0 \tag{4.66}$$

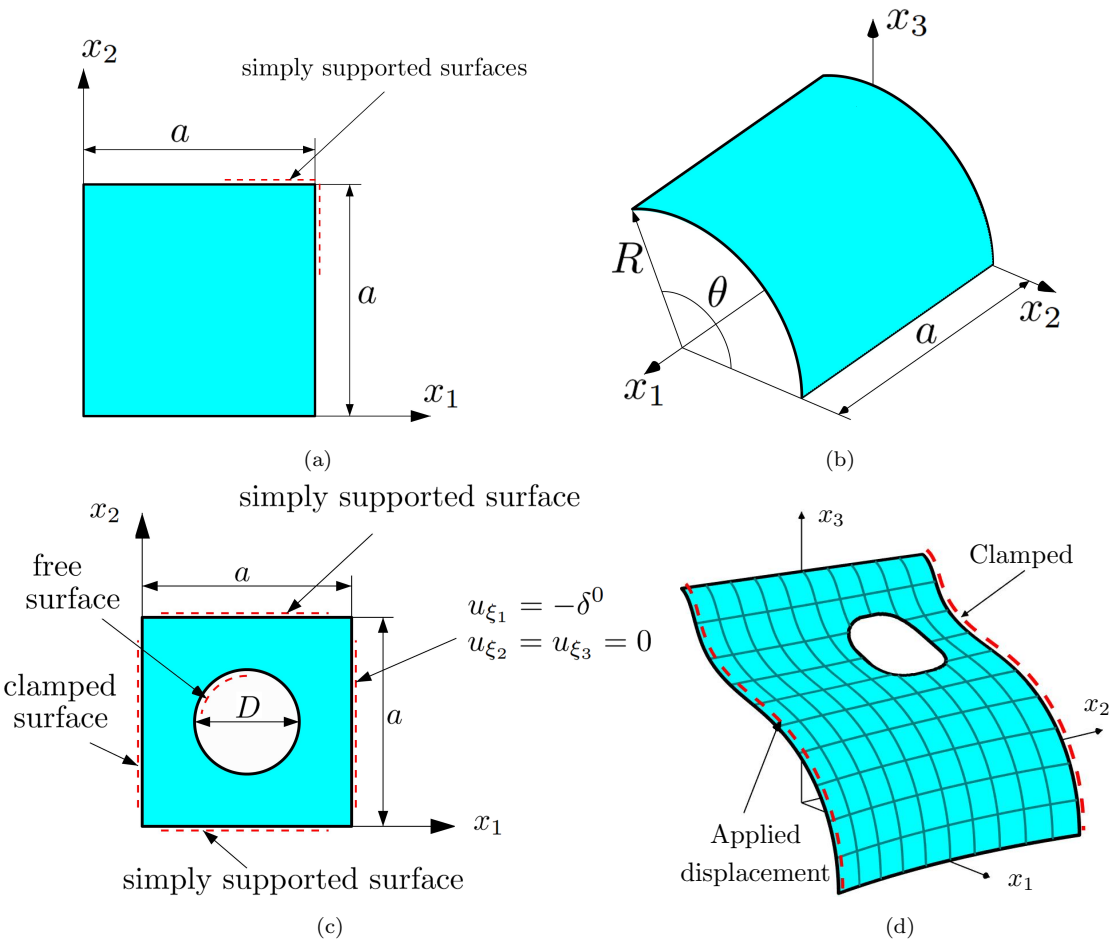

Figure 4.24: Geometry and boundary conditions of the shells investigated in this section. In particular: laminated plate (a), laminated cylindrical shell (b), laminated plate with circular cut-out (c), laminated NURBS-based shell (d).

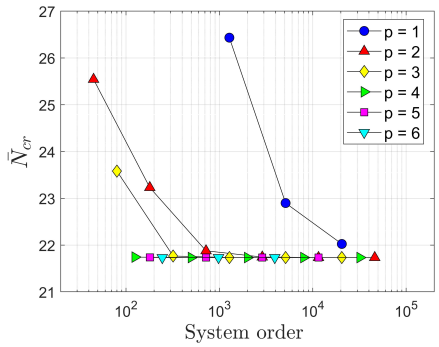

Figure 4.25: Convergence of the non-dimensional buckling load for the multilayered square plate.

and all other components to zero. In Eq.(4.66) ε^0 is a reference strain, $c_{11}^{\langle\ell\rangle}$ and $c_{22}^{\langle\ell\rangle}$ are elements of the stiffness matrix of the ℓ-th layer and χ is a parameter that is equal to 0 for uniaxial compression and 1 for biaxial compression. The non-dimensional critical buckling load is defined as follows

$$\overline{N}_{cr} = \lambda \frac{a^2}{E_r \tau^3} \sum_{\ell=1}^{N_\ell} \int_{\xi_{3b}^{\langle\ell\rangle}}^{\xi_{3t}^{\langle\ell\rangle}} \overline{\sigma}_{11}^{\langle\ell\rangle} \mathrm{d}\xi_3, \tag{4.67}$$

where λ is the smallest eigenvalue obtained by solving the problem in Eq.(4.19).

It is initially considered the stacking sequence denoted by P_1 in Tab.(4.11) with thickness ratio $a/\tau = 20$, orthotropy ratio $E_1/E_r = 25$ and $\chi = 0$, and partition the modeling domain of the plate using a simple structured grid consisting of $N_e = n_e^2$ elements, being n_e the number of elements per side of the modeling domain. The plate is modeled using the FSDT. The value of the non-dimensional critical buckling load $\overline{N}_{cr}$ given in Eq.(4.67) is then computed as a function of the degree p of the basis functions and the number of elements N_e. Figure (4.25) reports the obtained values of $\overline{N}_{cr}$ as a function of the system order defined as $N_e N_p N_U$ where $N_p = (1+p)^2$. As depicted in the figure, higher-order DG formulations show a faster convergence of the critical buckling load and use a smaller number of degrees of freedom to obtain the converged result with respect to lower-order formulations.

The value of $\overline{N}_{cr}$ is then computed using a 4×4 grid and $p = 6$ polynomial basis functions, and the effect of thickness ratio a/τ, the orthotropy ratio E_1/E_r, the biaxial load parameter χ and the selected shell theory is investigated. Table (4.12) reports the values of $\overline{N}_{cr}$ as a function of the ESL theory and the ratio E_1/E_r for the stacking sequences denoted by P_1 and P_2 in Tab.(4.11) with thickness ratio $a/\tau = 10$. The effect of the biaxial load parameter χ on the critical buckling load is reported in Tab.(4.13) for five different values of the thickness ratio a/τ and for two ESL theories upon selecting an orthotropy ratio equal to $E_1/E_r = 25$ and the stacking sequence P_1. In both Tab.(4.12) and (4.13), the results obtained with the present formulation are compared with those obtained in [152] via a 3D model and those obtained in [153] using different ESL theories. In all cases, an excellent agreement between the present DG formulation and the reference models is observed. The largest differences might be noticed in the results obtained using the FSDT and are due the adoption of the von Kármán hypotheses in the referenced work. It is however worth noting that using the full set of non-linear strain components also for the FSDT provides more accurate results if compared with the 3D solution.

Table 4.12: Non-dimensional buckling load for multilayered plate as a function of the ESL theory, the orthotropy ratio E_1/E_r and the stacking sequence. The results obtained in [152] using a 3D model are also reported for comparison purposes. Here, the thickness ratio is $a/\tau = 10$.

	$E_1/E_r = 3$	10	20	30	40
P_1					
3D [152]	5.3044	9.7621	15.0191	19.3040	22.8807
ED_{333} [153]	5.3060	9.7720	15.0551	19.3785	23.0021
ED_{333}	5.3058	9.7713	15.0536	19.3760	22.9986
ED_{222} [153]	5.3556	9.9945	15.6458	20.4027	24.4816
ED_{222}	5.3554	9.9939	15.6441	20.3999	24.4775
$FSDT_{VK}$ [153]	5.3991	9.9653	15.3513	19.7566	23.4529
FSDT	5.2927	9.7578	15.0573	19.4104	23.0734
P_2					
3D [152]	5.3352	10.0417	15.9153	20.9614	25.3436
ED_{333} [153]	5.3385	10.0578	15.9629	21.0501	25.4786
ED_{333}	5.3383	10.0572	15.9613	21.0474	25.4746
ED_{222} [153]	5.3810	10.2301	16.4245	21.8793	26.7207
ED_{222}	5.3809	10.2294	16.4228	21.8763	26.7164
$FSDT_{VK}$ [153]	5.4126	10.1895	16.1459	21.2650	25.7152
FSDT	5.3261	10.0341	15.9295	21.0141	25.4462

Table 4.13: Non-dimensional uniaxial and biaxial buckling load as a function of two shell theories and different thickness ratios a/τ. Here, the orthotropy ratio is $E_1/E_r = 25$ and the stacking sequence is $\mathbf{P_1}$.

	$a/\tau = 10$	20	25	50	100
$\chi = 0$					
ED_{444} [153]	17.3127	21.7304	22.4358	23.4593	23.7316
ED_{444}	17.3106	21.7300	22.4356	23.4593	23.7316
$FSDT_{VK}$ [153]	17.6568	21.8687	22.5307	23.4855	23.7383
FSDT	17.3336	21.7344	22.4382	23.4599	23.7317
$\chi = 1$					
ED_{444} [153]	8.7057	10.8849	11.2314	11.7334	11.8668
ED_{444}	8.7052	10.8848	11.2314	11.7334	11.8668
$FSDT_{VK}$ [153]	8.8284	10.9344	11.2654	11.7428	11.8692
FSDT	8.7324	10.8946	11.2380	11.7352	11.8672

4.3.2 Laminated cylindrical shell

The second set of tests are referred to the cylindrical shell shown in Fig.(4.24b). The shell mean surface is defined as

$$\boldsymbol{x}_0 = \begin{bmatrix} \xi_1 \\ R\cos(\xi_2) \\ R\sin(\xi_2) \end{bmatrix}, \tag{4.68}$$

where $(\xi_1, \xi_2) \in \hat{\Omega} = [0, a] \times [0, \theta]$ and $\theta = a/R$. The shell is simply-supported and subjected to a uniform initial stress state defined by setting

$$\overline{\sigma}_{11}^{\langle \ell \rangle} = -\sigma^0 , \tag{4.69}$$

and zero in all other components. In this case, the following non-dimensional critical buckling load is employed

$$\overline{N}_{cr} = \lambda \frac{\sigma^0 a^2}{E_r \tau^2} . \tag{4.70}$$

The stacking sequence denoted by C_1 in Tab.(4.11) is considered for this set of tests. It is performed a similar convergence analysis to the one presented in Sec.4.3.1 for a cylindrical shell characterized by $a/\tau = 20$ and $a/R = 1$ and modeled using the ED_{333} theory and a cylindrical shell characterized by $a/\tau = 100$ and $a/R = 2$ and modeled using the FSDT theory. Figure (4.26) reports the computed value of the critical buckling load given in Eq.(4.70) as a function of the system order and, similarly to what observed in Fig.(4.25), shows the benefit of using higher-order methods in terms of convergence rate and overall number of degrees of freedom.

The value of $\overline{N}_{cr}$ is then computed using a 4×4 grid and $p = 6$ polynomial basis functions for different ESL theories and different values of the ratios a/τ and a/R. Table (4.14) reports the computed values of $\overline{N}_{cr}$ as a function of various ESL theories and the ratio a/τ for the cylindrical shell with $a/R = 0.05$. A similar parametric analysis is reported in Tab.(4.15), where it is considered the FSDT and the ED_{444} theory and change the ratios a/τ and a/R. Similarly to the plate case, Tab.(4.14) and (4.15) also report the reference critical buckling load $\overline{N}_{cr}$ obtained in [153], and confirm the accuracy of the present formulation. As an example, the first buckling mode of the cylindrical shell characterized by $a/R = 2$ and $a/\tau = 50$ and the cylindrical shell characterized by $a/R = 2$ and $a/\tau = 100$, both modeled by the FSDT theory, are displayed in Fig.(4.27). By looking at Fig.(4.26), it is possible to notice that using high-order polynomials allows achieving convergence of the buckling load with a smaller number of overall degrees of freedom with respect to using low-order polynomials. This is valid for both buckling eigenmodes that involve a small number and a large number of half waves throughout the structure. Eventually, to further illustrate the advantages of using high-order approximations, the error in first buckling load for the shell C_1 with $a/R = 0.05$ and $a/\tau = 50$ is plotted as a function of the computational time for different values of order p of the polynomial basis functions and of number N_e of mesh elements. The obtained results are reported in Figs.(4.28a) and (4.28b) for the FSDT and the ED_{333} theory, respectively, and clearly show the superior performance of higher-order basis functions with respect to low-order basis functions in terms of computational time required to achieve a given level of accuracy. In other words, the results obtained for the considered numerical tests suggest that using higher-order polynomial basis functions in combination with a coarser

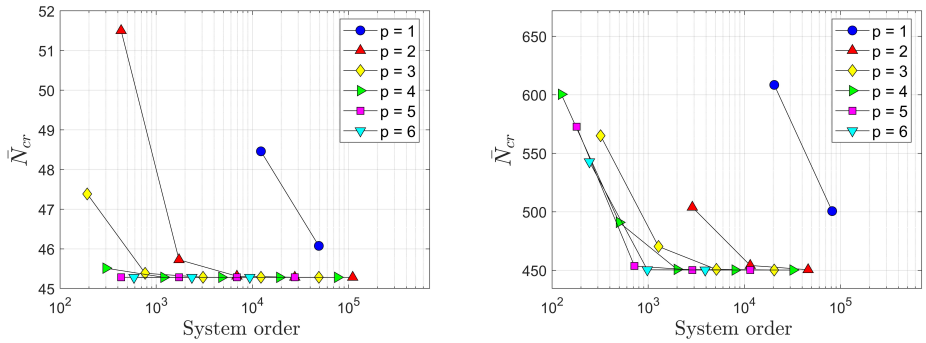

Figure 4.26: Convergence of the non-dimensional buckling load for the multilayered cylindrical shell C_1 with (a) $a/\tau = 20$ and $a/R = 1$ and (b) $a/\tau = 100$ and $a/R = 2$.

Table 4.14: Non-dimensional buckling load for the multilayered cylindrical shell C_1 as a function of the shell theory and the thickness ratio a/τ. Here, $a/R = 0.05$.

	$a/\tau = 10$	20	30	50	100
ED_{444} [153]	24.20	31.94	34.06	35.42	36.85
ED_{444}	24.19	31.94	34.06	35.42	36.85
ED_{333} [153]	24.20	31.94	34.06	35.42	36.85
ED_{333}	24.19	31.94	34.06	35.42	36.85
ED_{222} [153]	25.27	32.37	34.27	35.50	36.87
ED_{222}	25.26	32.37	34.27	35.50	36.87
$FSDT_{VK}$ [153]	24.18	31.90	34.04	35.42	36.85
FSDT	23.95	31.78	33.97	35.39	36.84

mesh is preferable over low-order polynomials combined with a finer mesh, regardless of the chosen through-the-thickness expansion.

As the last test on cylindrical shell structures, the advantage of employing higher-order through-the-thickness approximations is investigated. The cylindrical shell C_2 with $a/R = 0.5$ and variable a/τ is considered. The shell is clamped at the surface corresponding to $\xi_1 = 0$, a pressure $\bar{t}_1 = -q^0$ is applied on the surface corresponding to $\xi_1 = a$, while the other edges are kept free. In this test, the initial stress field $\overline{\sigma}_{ij}^{\langle \ell \rangle}$ is computed as a result of the corresponding linear static analysis. The tests are carried out with a 2×2 structured grid and a polynomial order $p = 6$. For these analyses, the non-dimensional critical buckling load is computed as

$$\overline{N}_{cr} = \lambda \frac{q^0 a^2}{E_r \tau^2} \,. \tag{4.71}$$

Table (4.16) reports the computed values of the buckling load for three different ratios a/τ and different shell theories, namely the FSDT, the ED_{333} and the ED_{444} theories. The table also reports the buckling loads computed with a three-dimensional analysis using the C3D20R elements implemented in Abaqus® [26]. The obtained results show that the buckling load computed with the FSDT matches the three-dimensional result when the shell is relatively thin but differs noticeably for larger values of the thickness. In the latter case, high-order through-the-thickness expansions recover the three-dimensional solutions and their use is recommended.

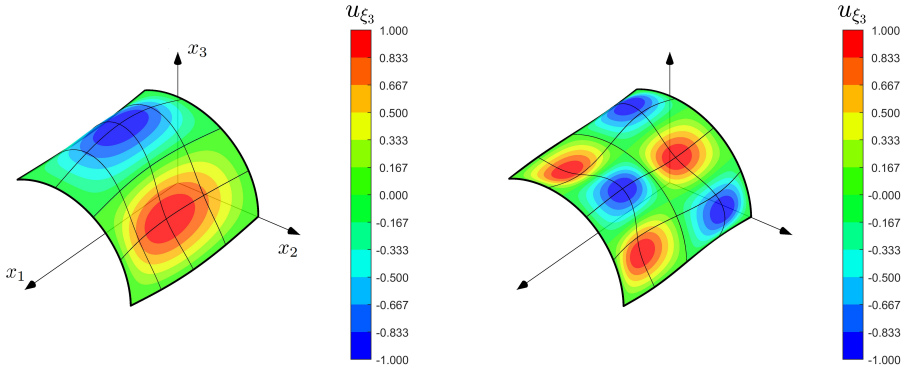

(a) (b)

Figure 4.27: Sample buckling mode for the cylindrical shell C_1 with (a) $a/\tau = 50$ and $a/R = 2$ and (b) $a/\tau = 100$ and $a/R = 2$.

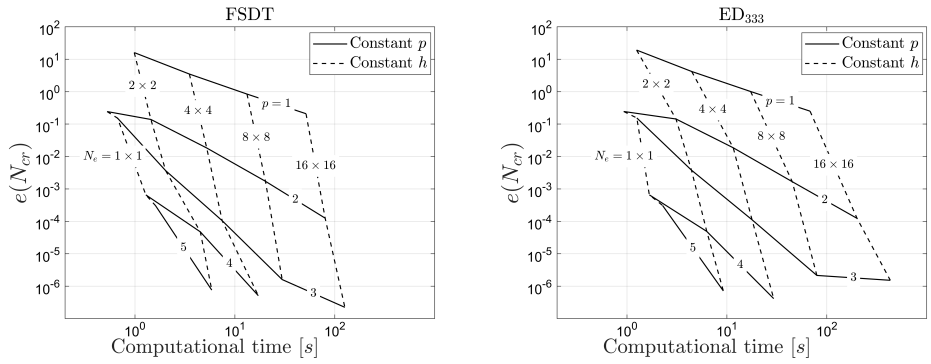

(a) (b)

Figure 4.28: Error in the first buckling load of the cylindrical shell C_1 with $a/R = 0.05$ and $a/\tau = 50$ as function of the computational time for different values of the polynomial order and the number of mesh elements. (a) FSDT and (b) ED_{333} theory.Computational time of the analysis for different numbers of elements and orders of the polynomials.

Table 4.15: Non-dimensional buckling load for the multilayered cylindrical shell C_1 as a function of two shell theories and the ratios a/τ and a/R.

	$a/\tau = 10$	20	50	100
$a/R = 0.1$				
ED_{444} [153]	24.20	32.05	36.29	40.42
ED_{444}	24.20	32.05	36.29	40.42
$FSDT_{VK}$ [153]	24.21	32.04	36.31	40.46
FSDT [153]	23.97	31.90	36.25	40.41
FSDT	23.96	31.90	36.26	40.42
$a/R = 0.2$				
ED_{444} [153]	24.23	32.49	39.74	54.67
ED_{444}	24.24	32.49	39.74	54.67
$FSDT_{VK}$ [153]	24.31	32.57	39.88	54.88
FSDT [153]	24.00	32.33	39.70	54.67
FSDT	24.00	32.34	39.71	54.67
$a/R = 1$				
ED_{444} [153]	25.26	45.28	140.6	253.3
ED_{444}	25.26	45.28	140.6	253.3
$FSDT_{VK}$ [153]	27.63	49.61	154.1	259.4
FSDT [153]	25.03	45.14	140.6	253.2
FSDT	25.11	45.26	140.7	253.4
$a/R = 2$				
ED_{444} [153]	28.23	74.97	220.1	448.2
ED_{444}	28.23	74.97	220.2	448.2
$FSDT_{VK}$ [153]	38.90	103.9	243.7	469.1
FSDT [153]	27.96	74.84	221.3	448.9
FSDT	28.08	75.02	223.1	450.2

Table 4.16: Non-dimensional buckling load for the multilayered cylindrical shell C_2 as a function of the shell theories and the ratio a/τ for $a/R = 0.5$.

	$a/\tau = 20$	10	5
FSDT	3.971	2.350	1.752
ED_{333}	3.957	2.310	1.634
ED_{444}	3.956	2.308	1.631
C3D20R elements [26]	3.965	2.309	1.631

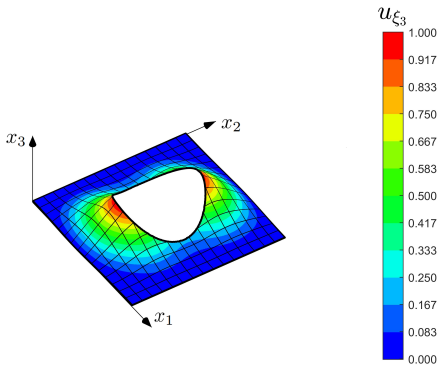

Figure 4.29: Sample buckling mode for the laminated plate with cut-out.

4.3.3 Laminated plate with circular cut-out

In the third set of tests, the critical buckling load is computed for the laminated plate with a circular cut-out shown in Fig.(4.24c). For these tests, the implicit-mesh DG formulation is employed. The shell mean surface is described by the map given in Eq.(4.65) with $(\xi_1, \xi_2) \in \hat{\Omega} = [0, a] \times [0, a]$. The mesh of the domain is constructed starting from a 15×15 background grid, while the space of basis functions uses $p = 3$ polynomials. The modeling domain of the plate is implicitly-defined via the following level-set function

$$\phi(\xi_1, \xi_2) = \frac{D^2}{4} - \left(\xi_1 - \frac{a}{2}\right)^2 - \left(\xi_2 - \frac{a}{2}\right)^2, \tag{4.72}$$

where D is the diameter of the circular cut-out. The stacking sequence denoted by H_1 in Tab.(4.11) is considered for these tests.

Unlike the two previous sets of tests, where the initial stress was prescribed as a constant field, the initial stress distribution for this test case is computed from a linear elastic static analysis. The boundary condition of the static analysis are as follows: the boundaries at $\xi_2 = 0$ and $\xi_2 = a$ are simply supported, i.e. $u_{\xi_2} = u_{\xi_3} = 0$; the boundary at $\xi_1 = 0$ is clamped; and the boundary at $\xi_1 = a$ is subjected to a uniform displacement given by $u_{\xi_1} = -\delta^0$ and $u_{\xi_2} = u_{\xi_3} = 0$. The non-dimensional critical value of the applied displacement for which the buckling occurs is computed as

$$\overline{u}_{cr} = \lambda \frac{\delta^0 a}{\tau^2}. \tag{4.73}$$

Tab.(4.17) reports the computed values of $\overline{u}_{cr}$ as a function of the selected ESL theory, the hole diameter D and the thickness ratio a/τ for the stacking sequence denoted by H_1 in Tab.(4.11). The obtained results and are compared with those obtained with Abaqus® using the S4R elements and demonstrate the accuracy of the present DG formulation combined with the implicitly-defined mesh technique. The first buckling mode for the plate characterized by $a/\tau = 50$ and $D/a = 0.5$ and modeled with the FSDT theory is displayed in Fig.(4.29).

4.3.4 Laminated generally-curved NURBS-based shell

In the final set of tests, the present formulation is employed to perform the buckling analysis of a generally-curved shell with and without a cut-out described as a NURBS surface. The shell investigated is the same as in Sec. 4.2.7 and the associated geometric

Table 4.17: Non-dimensional displacement at buckling for the multilayered plate with the circular cut-out H_1 as a function of different shell theories and the ratios a/τ and D/a.

	$a/\tau = 20$	50	100
$D/a = 0$			
S4R elements [26]	3.231	4.093	4.268
FSDT	3.229	4.080	4.253
ED_{222}	3.367	4.119	4.265
ED_{333}	3.215	4.078	4.253
ED_{444}	3.216	4.078	4.253
$D/a = 0.1$			
S4R elements [26]	3.216	4.035	4.207
FSDT	3.217	4.035	4.208
ED_{222}	3.350	4.074	4.221
ED_{333}	3.203	4.032	4.208
ED_{444}	3.204	4.033	4.209
$D/a = 0.25$			
S4R elements [26]	3.770	4.716	4.914
FSDT	3.759	4.709	4.908
ED_{222}	3.922	4.758	4.924
ED_{333}	3.745	4.709	4.910
ED_{444}	3.747	4.710	4.911
$D/a = 0.5$			
S4R elements [26]	5.670	7.858	8.418
FSDT	5.626	7.850	8.427
ED_{222}	5.977	7.986	8.481
ED_{333}	5.576	7.848	8.435
ED_{444}	5.581	7.850	8.436
$D/a = 0.75$			
S4R elements [26]	9.836	17.318	19.748
FSDT	9.732	17.252	19.734
ED_{222}	10.714	17.783	19.954
ED_{333}	9.493	17.127	19.709
ED_{444}	9.501	17.133	19.713

Table 4.18: Non-dimensional displacement at buckling for the NURBS-based shell N_1 with and without the cut-out.

Shell geometry	1st (DG)	1st (FEM)	2nd (DG)	2nd (FEM)	5th (DG)	5th (FEM)
With cut-out	34.31	34.38	36.02	36.12	58.47	58.51
Without cut-out	61.75	62.09	62.42	62.77	70.35	70.76

properties are not reported here. Fig.(4.24d) shows the shell geometry with its boundary conditions.

The shell is clamped at the surface corresponding to $\xi_2 = 1$, while a uniform displacement $\overline{\boldsymbol{u}} = (0, \delta^0, 0)$ is applied at the surface $\xi_2 = 0$; the other boundaries are kept free. The considered shell section is the one denoted by N_1 in Tab.(4.11), while the selected shell theory is the FSDT. The eigenvalue problem is solved by the present DG formulation using 10×10 grid and a polynomial order $p = 6$. The same problem is solved by the FEM software library Abaqus® using S3 elements and S4R elements for the shell with the cut-out and without the cut-out, respectively.

The comparison between the obtained results is given in Tab.(4.18) in terms of the 1st, 2nd and 5th values of the following non-dimensional critical loading

$$\overline{u}_{cr} = \lambda \frac{\delta^0 H}{\tau^2} \ . \tag{4.74}$$

An excellent agreement is observed for all values of the critical loading for the shell with and without the cut-out. Eventually, the comparison between the eigenmodes obtained with the present formulation and with Abaqus® and corresponding to the 1st, 2nd and 5th eigenvalues is reported in Fig.(4.30) for the shell with the cut-out and in Fig.(4.31) for the shell without the cut-out. An excellent matching is also observed for the eigenmodes of the problem.

4.4 Numerical results for transient and free-vibration analysis

To validate the formulation presented regarding the linear transient and free-vibration analysis, several tests are performed involving different geometries, high-order ESL theories and order of the DG elements. The investigated geometries are a square plate, a cylindrical shell, and a NURBS-based shell. Two different materials are taken into account, namely an isotropic material and an orthotropic material, whose properties are reported in Tab.(4.19).

4.4.1 Square plate

The first investigated geometry is a square plate, whose mid-surface is defined as

$$\boldsymbol{x}_0 = \begin{bmatrix} \xi_1 \\ \xi_2 \\ 0 \end{bmatrix} , \tag{4.75}$$

where $(\xi_1, \xi_2) \in [0, L] \times [0, L]$, being L the length of the sides of the plate. Two plate sections are considered here, an isotropic plate P_1 and a laminated P_2 whose properties

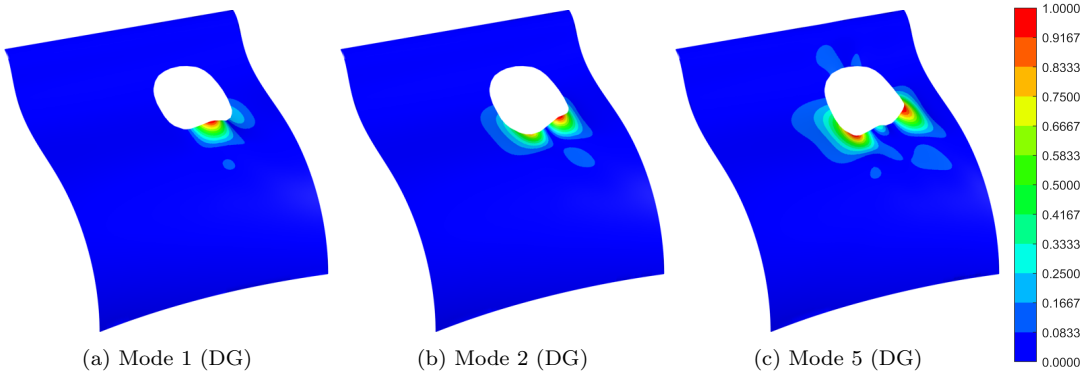

(a) Mode 1 (DG) (b) Mode 2 (DG) (c) Mode 5 (DG)

(d) Mode 1 (Abaqus) (e) Mode 2 (Abaqus) (f) Mode 5 (Abaqus)

Figure 4.30: Buckling modes for the NURBS-based shell N_1 with the cut-out in terms of the magnitude of the displacement.

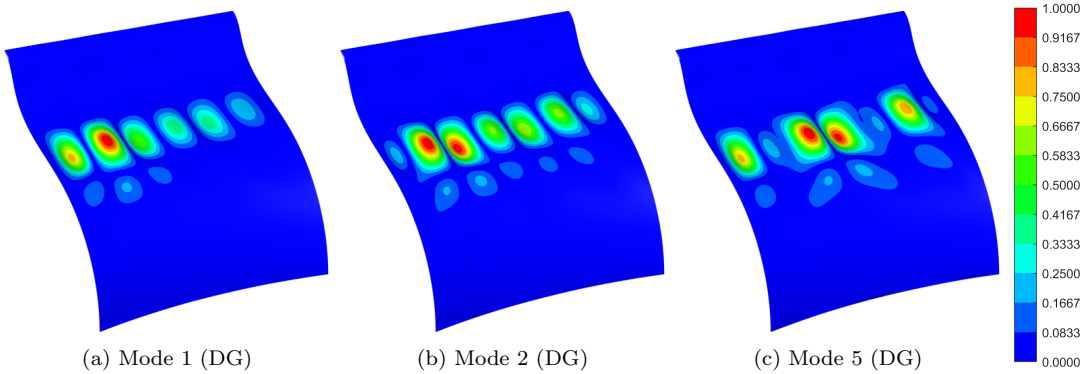

(a) Mode 1 (DG) (b) Mode 2 (DG) (c) Mode 5 (DG)

(d) Mode 1 (Abaqus) (e) Mode 2 (Abaqus) (f) Mode 5 (Abaqus)

Figure 4.31: Buckling modes for the NURBS-based shell N_1 without the cut-out in terms of the magnitude of the displacement.

Table 4.19: Properties of the considered materials.

Material ID	**Property**	**Component**	**Value**
M_1	Young's moduli	E/E_r	1
	Poisson's ratios	ν	0.25
	Density	ρ/ρ_r	1
M_2	Young's moduli	E_1/E_r	25
		E_2/E_r, E_3/E_r	1
	Poisson's ratios	ν_{23}, ν_{13}, ν_{12}	0.25
	Shear moduli	G_{23}/E_r	0.2
		G_{13}/E_r, G_{12}/E_r	0.5
	Density	ρ/ρ_r	1

Table 4.20: Properties of the considered shell sections.

Shell ID	**Material**	**Layup**	**Layer(s) thickness**
P_1	M_1	[0]	τ
P_2	M_2	[0/90/0/90]	$\tau/4$
C_1	M_1	[0]	τ
C_2	M_2	[0/90/0/90]	$\tau/4$
N_1	M_2	[0/90/90/0]	$\tau/4$

are reported in Tab.(4.20). The plate has a thickness ratio of $\frac{\tau}{L} = \frac{1}{100}$ and is subjected to simply-supported boundary conditions. The characteristic dimension of the mesh element h is then given by L_e/L, where L_e is the length of the side of each square elements.

Fig.(4.32) shows the convergence of the error on the first natural frequency and on the first eigenfunction as for a given mesh size h and order p of the DG basis functions using the FSDT. The errors are defined as

$$e(\omega_h) \equiv \frac{\omega_h - \omega_{\text{ref}}}{\omega_{\text{ref}}}, \tag{4.76a}$$

$$e(\boldsymbol{U}_h) \equiv \frac{|\boldsymbol{U}_h - \boldsymbol{U}_{\text{ref}}|_\infty}{|\boldsymbol{U}_{\text{ref}}|_\infty}, \tag{4.76b}$$

where the subscript ref denotes exact solution quantities and the subscript h denotes the quantities computed with the proposed DG formulation.

Four different ESL theories are then taken into account and the corresponding first ten non-dimensional frequencies are computed for the plate P_2 using an order $p = 6$ of the DG basis functions and a 4×4 structured grid. The non-dimensional frequencies are computed as

$$\overline{\omega} \equiv \frac{L^2}{\pi^2}\sqrt{\frac{\rho_r}{E_r\tau^2}}\omega, \tag{4.77}$$

The obtained values are reported in Tab.(4.21) and compared with the analytical solutions, showing excellent matching.

As the last test for this geometry, the transient response of the plate P_2 is investigated. The plate starts from an undeformed configuration and is subjected to simply-supported boundary conditions and to a pressure on the lower surface whose expression is $q_0 \sin(\pi\xi_1/L)\sin(\pi\xi_2/L)H(t)$, where $H(t)$ is the Heaviside step function.

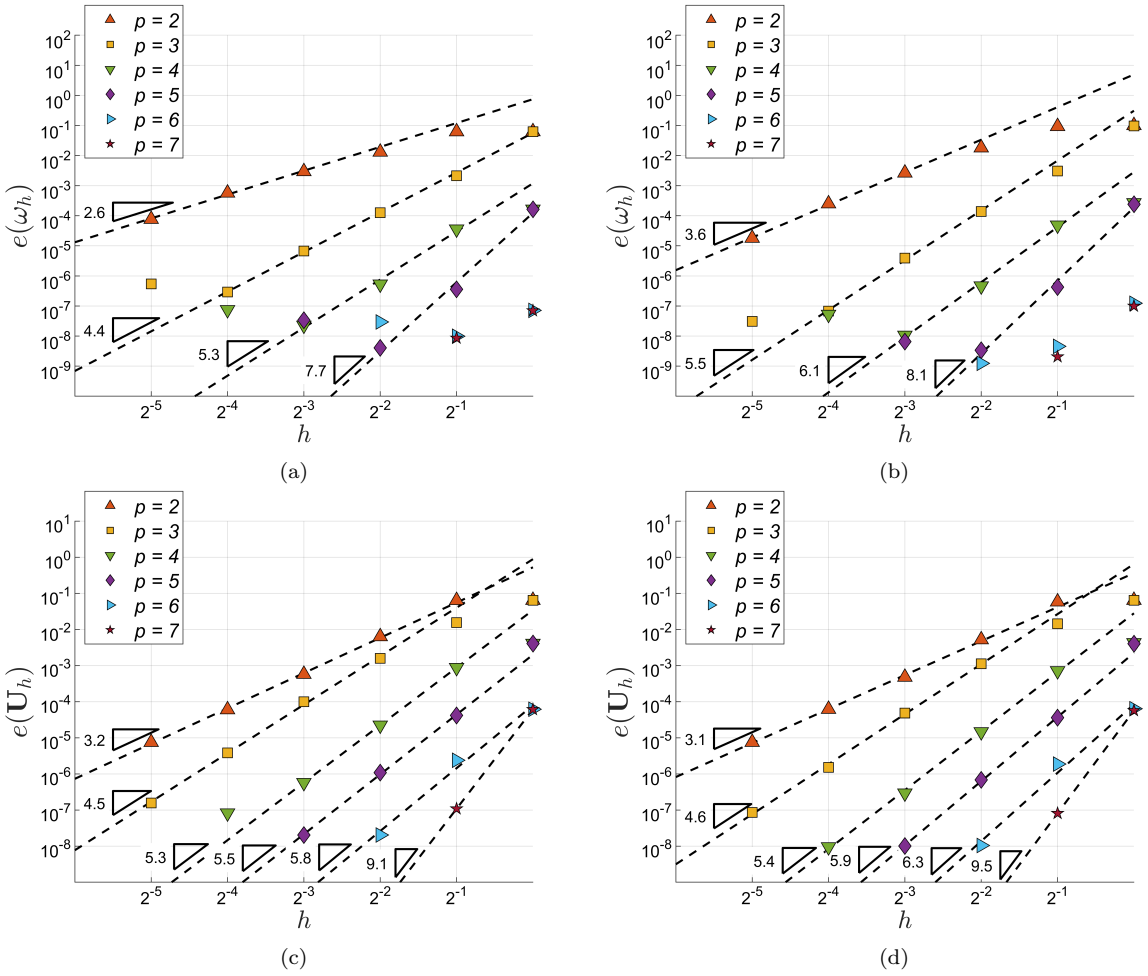

Figure 4.32: *hp*-convergence of the error on the first natural frequency for the plate P_1 (a) and P_2 (b), and on the first eigenfunction for the plate P_1 (c) and P_2 (d)

The transient response of the plate is reported in terms on the third non-dimensional component $\overline{u}_{\xi_3}$ of the displacement vector defined as

$$\overline{u}_{\xi_3} \equiv \frac{\tau^3 E_r}{L^4 q_0} u_{\xi_3}. \tag{4.78}$$

Figure (4.33) shows the computed value of $\overline{u}_{\xi_3}$ at the point of coordinates $(L/2, L/2, 0)$ as a function of time t and order p of the DG basis functions using a 2×2 structured grid; in the figure, T_n is the period of free-vibration of the half-wave bending mode while the dashed line denotes the exact solution, which is accurately recovered for $p > 2$.

4.4.2 Cylindrical shell

The second investigated geometry is a cylindrical shell. The map of the mid-surface is given as

$$\boldsymbol{x}_0 = \begin{bmatrix} R\cos(\xi_1) \\ R\sin(\xi_1) \\ \xi_2 \end{bmatrix}, \tag{4.79}$$

where R denotes the radius of the cylinder. The first curvilinear coordinate for this geometry takes values in $[0, \alpha]$, being $\alpha = 1$ rad, and the second one takes values in $[0, L]$.

Table 4.21: First ten natural frequencies for the plate P_2.

	FSDT (DG)	FSDT $(S.A.)$	ED_{111} (DG)	ED_{111} $(S.A.)$	ED_{222} (DG)	ED_{222} $(S.A.)$	ED_{333} (DG)	ED_{333} $(S.A.)$
$\overline{\omega}_1$	1.4211	1.4211	1.4311	1.4311	1.4214	1.4214	1.4207	1.4207
$\overline{\omega}_2$	4.0147	4.0147	4.0398	4.0398	4.0181	4.0181	4.0108	4.0108
$\overline{\omega}_3$	4.0147	4.0147	4.0398	4.0398	4.0181	4.0181	4.0108	4.0108
$\overline{\omega}_4$	5.6537	5.6537	5.6981	5.6981	5.6593	5.6593	5.6483	5.6483
$\overline{\omega}_5$	8.6321	8.6321	8.6899	8.6899	8.6481	8.6481	8.6125	8.6125
$\overline{\omega}_6$	8.6321	8.6321	8.6899	8.6899	8.6481	8.6481	8.6125	8.6125
$\overline{\omega}_7$	9.6535	9.6535	9.7320	9.7320	9.6710	9.6710	9.6343	9.6343
$\overline{\omega}_8$	9.6535	9.6535	9.7320	9.7320	9.6710	9.6710	9.6343	9.6343
$\overline{\omega}_9$	12.6091	12.6091	12.7243	12.7243	12.6363	12.6363	12.5823	12.5823
$\overline{\omega}_{10}$	15.0412	15.0412	15.1619	15.1619	15.0891	15.0891	14.9808	14.9808

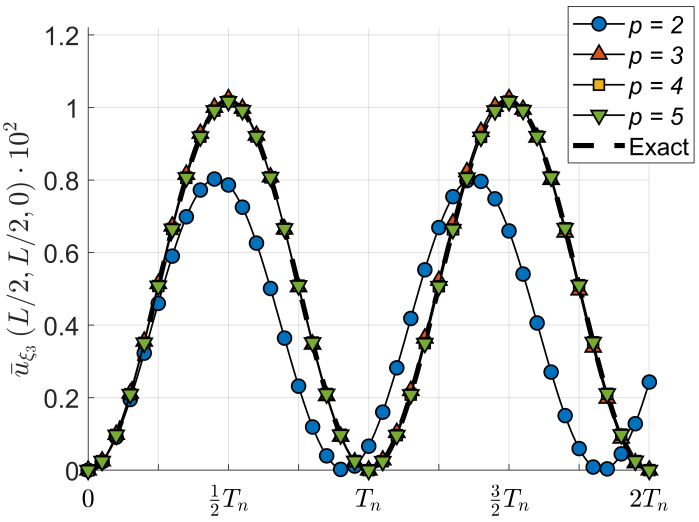

Figure 4.33: Dynamic response of the plate P_2.

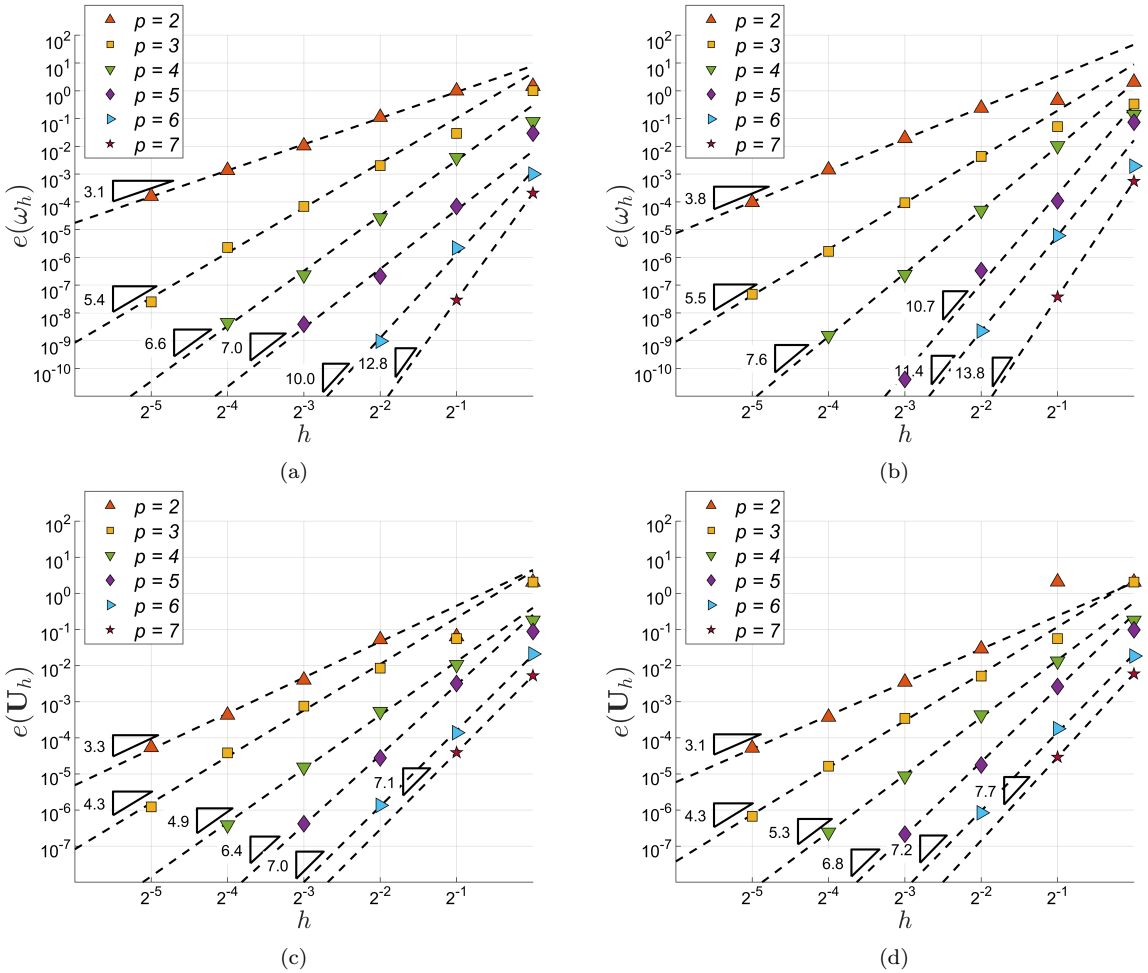

Figure 4.34: *hp*-convergence of the error on the first natural frequency for the shell C_1 (a) and C_2 (b), and on the first eigenfunction for the shell C_1 (c) and C_2 (d).

The considered shell sections are those denoted by C_1 and C_2 in Tab.(4.20) and consist of an isotropic single-layer and a laminated cross-ply section, respectively. The thickness ratio is $\frac{\tau}{L} = \frac{1}{100}$ and the shell is subjected to simply supported boundary conditions. Fig.(4.34) shows the convergence of the error on the first natural frequency and on the first eigenfunction computed using Eq.(4.76) as functions of the order p of the DG basis functions and the mesh size h. The shell theory used in these tests is the FSDT.

In the second set of tests, the values of the first ten non-dimensional natural frequencies for the shell C_2 are computed using an order $p = 6$ of the DG basis functions and a 4×4 structured grid. The values are compared with those obtained analytically in Tab.(4.22) showing excellent matching also in this case. The non-dimensional values of the frequencies are computed as in Eq.(4.77). For the last test, starting from an undeformed configuration, the shell C_2 is subjected to an internal pressure varying as $q_0 \sin(\pi\xi_1/\alpha) \sin(\pi\xi_2/L) H(t)$. The value of the non-dimensional third covariant component of the displacement vector $\overline{u}_{\xi_3}$ is computed as a function of time using different order of the DG basis functions and a 2×2 grid. Fig.(4.35) shows the obtained results, which match very well with the analytical solution for $p > 2$.

Table 4.22: First ten natural frequencies for the shell C_2.

	FSDT (DG)	FSDT $(S.A.)$	ED_{111} (DG)	ED_{111} $(S.A.)$	ED_{222} (DG)	ED_{222} $(S.A.)$	ED_{333} (DG)	ED_{333} $(S.A.)$
$\overline{\omega}_1$	5.1031	5.1031	5.1210	5.1210	5.0987	5.0987	5.0933	5.0933
$\overline{\omega}_2$	6.7424	6.7424	6.7442	6.7442	6.7418	6.7418	6.7417	6.7417
$\overline{\omega}_3$	8.7785	8.7785	8.8269	8.8269	8.7801	8.7801	8.7456	8.7456
$\overline{\omega}_4$	8.7999	8.7999	8.8317	8.8317	8.7999	8.7999	8.7931	8.7931
$\overline{\omega}_5$	10.5801	10.5801	10.6484	10.6484	10.5852	10.5852	10.5522	10.5522
$\overline{\omega}_6$	13.3841	13.3841	13.3911	13.3911	13.3852	13.3852	13.3832	13.3832
$\overline{\omega}_7$	13.8991	13.8991	13.9523	13.9523	13.9102	13.9102	13.8851	13.8851
$\overline{\omega}_8$	14.2770	14.2770	14.3763	14.3763	14.2946	14.2946	14.2474	14.2474
$\overline{\omega}_9$	15.0348	15.0348	15.1503	15.1503	15.0621	15.0621	14.9537	14.9537
$\overline{\omega}_{10}$	16.0497	16.0497	16.1837	16.1837	16.0801	16.0801	15.9738	15.9738

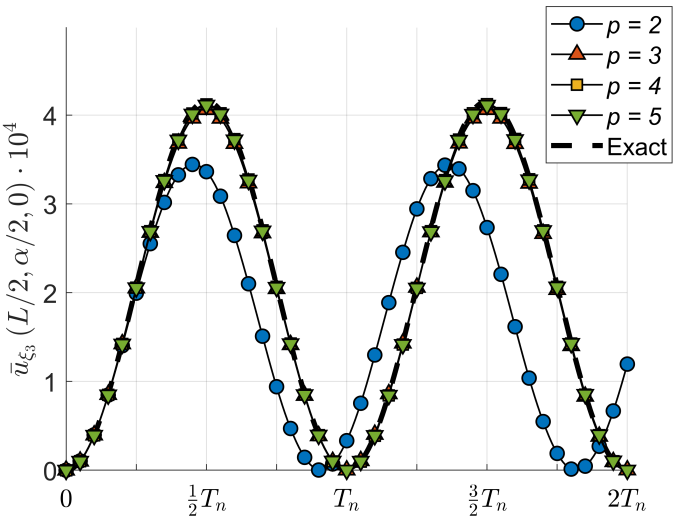

Figure 4.35: Dynamic response of the shell C_2.

4.4.3 NURBS-based shell

The last investigated geometry is a generally-curved NURBS-based shell with a cut-out. The detailed description of the geometry can be found in Sec. 4.2.7, where the information for the definition of the NURBS-surface, such as the coordinates of the control points or the elements of the knot vector, is provided.

The shell is subjected to clamped boundary conditions on the external boundary while the boundary of the cut-out is traction-free. In the first set of tests, the first six free-vibration modes in terms of the magnitude of the displacement are evaluated using a 10×10 background grid and a $p = 6$ for the order of the DG basis functions. The obtained results are compared with those computed using Abaqus' S3 elements; the comparison is reported in Fig.(4.36) showing the accuracy of the present approach.

The last set of tests concerns the transient response of the NURBS-based shell when subjected to a uniform pressure $q_0H(t)$ applied onto the internal surface. In this case, a damped analysis is considered and the damping ratios for the first and sixth free-vibration mode are selected as $\zeta_1 = \zeta_6 = 0.1$. Figure (4.37) shows the non-dimensional magnitude of the displacement for the point with curvilinear coordinates $\xi_1 = \alpha = 0.3922$ and $\xi_2 = \beta = 0.5808$ as a function of time $0 < t < 5T_n$, where T_n is the period of the first free-vibration frequency.

4.5 Numerical results for non-linear static analysis

To validate the proposed method for non-linear static analysis and assess its capabilities, numerical tests are performed considering different plates and shells benchmark problems. The material properties employed in the analyses are given in Table (4.23). The presented results refer to three different theories, namely the $\mathrm{ED}_{N_i,N_i,N_i}$ with $N_i = 1, 2, 3$. For the $\mathrm{ED}_{N_iN_iN_i}$ theory, each covariant component of the displacement vector is expanded using Taylor's polynomials up to the N_i–th order; for the ED_{111} the material stiffness matrix is also modified according to the plane stress state hypothesis and to keep a shear stress factor equal to 5/6.

Four tests are presented: the nonlinear bending of an isotropic plate, the post-buckling analysis of an isotropic slender plate, the snap-back and snap-through of isotropic and laminated cylindrical shells and the nonlinear response of a complex geometry composite shell. The first three of these tests are popular benchmarks and they allow the present results to be compared with solutions available in the literature. The last case is presented to illustrate the method capabilities in dealing with complex, general shell geometries and its solution is compared with finite elements results.

4.5.1 Isotropic plate nonlinear bending

The first validation test regards the nonlinear bending of a constant thickness, isotropic, square plate referred to the $x_1x_2x_3$ orthogonal coordinate system with origin in the mid-plane at a plate corner, the x_1 and x_2 axes directed along the edges and the x_3 axis directed along the plate thickness. The plate is subjected to a uniform surface load q applied on its upper surface and constantly oriented along the x_3 axis during the deformation.

The map of the mid surface of the plate is obtained as $x_{01} = \xi_1$, $x_{02} = \xi_2$ and $x_{03} = 0$, where $(\xi_1, \xi_2) \in [0, L] \times [0, L]$, being $L = 1200$ mm the plate edge length. The plate consists of a single layer with material properties as M_1 in Table (4.23) and

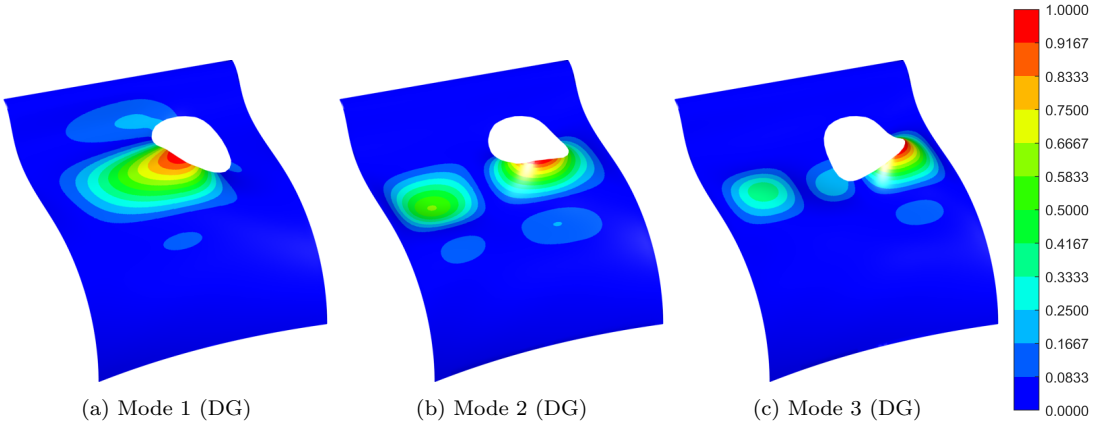

(a) Mode 1 (DG) (b) Mode 2 (DG) (c) Mode 3 (DG)

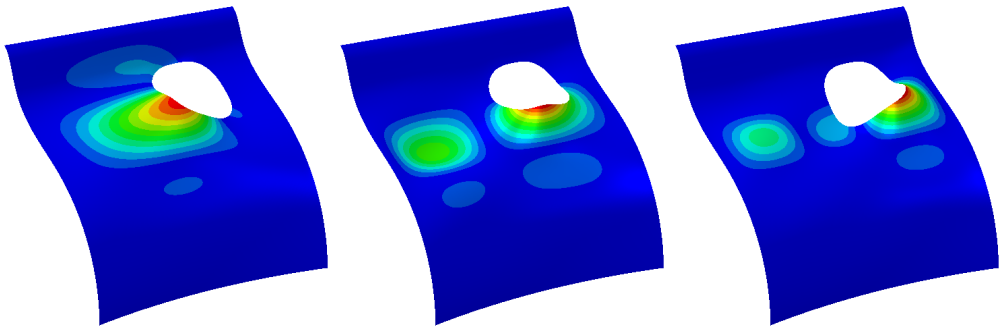

(d) Mode 1 (Abaqus) (e) Mode 2 (Abaqus) (f) Mode 3 (Abaqus)

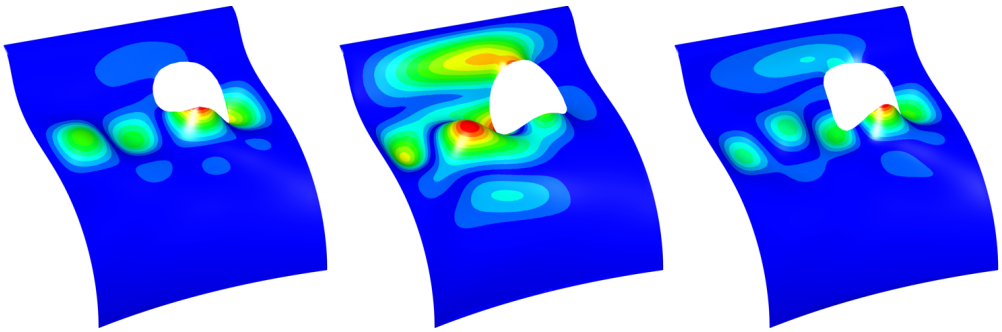

(g) Mode 4 (DG) (h) Mode 5 (DG) (i) Mode 6 (DG)

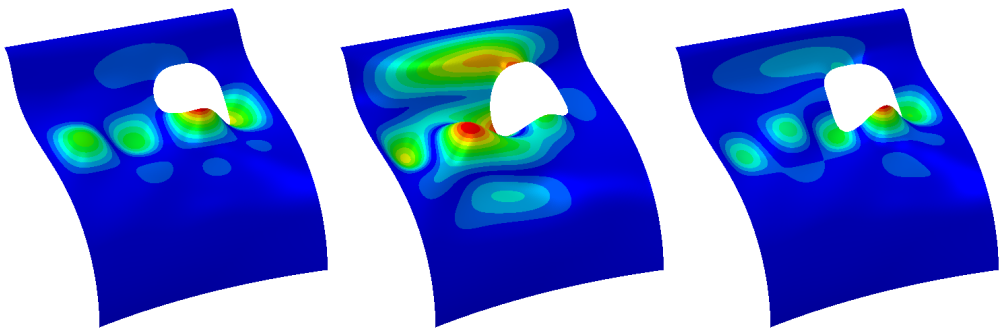

(j) Mode 4 (Abaqus) (k) Mode 5 (Abaqus) (l) Mode 6 (Abaqus)

Figure 4.36: First six free-vibration modes for the shell N_1 computed using DG (a-c and g-i) and Abaqus S3 elements (d-f and j-l).

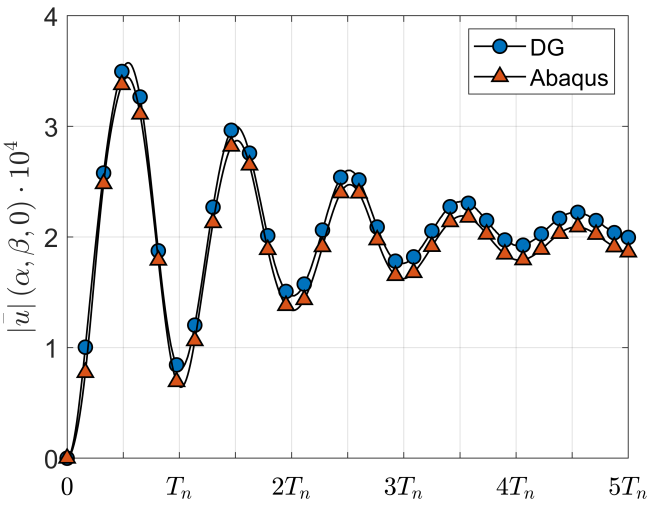

Figure 4.37: Dynamic response of the shell N_1.

Table 4.23: Material properties.

Material ID	**Property**	**Component**	**Value**
M_1	Young's modulus	E	75000 MPa
	Poisson's ratios	ν	0.3
M_2	Young's modulus	E	75000 MPa
	Poisson's ratios	ν	0.316
M_3	Young's modulus	E	3102.75 MPa
	Poisson's ratios	ν	0.3
M_4	Young's moduli	E_1	3300 MPa
		E_2, E_3	1100 MPa
	Poisson's ratios	ν_{23}, ν_{13}, ν_{12}	0.25
	Shear moduli	G_{23}	660 MPa
		G_{13}, G_{12}	660 MPa

thickness τ. Two different values for the thickness have been investigated corresponding to a thin plate having thickness ratio $\tau/L = 0.02$ and a moderately thick plate with $\tau/L = 0.1$. Two sets of boundary conditions are considered: i) all edges clamped, labeled as CCCC, corresponding to $u_{\xi_1} = u_{\xi_2} = u_{\xi_3} = 0$ at the edge points of coordinates $(0, \xi_2, \xi_3)$, (ξ_1, L, ξ_3), (L, ξ_2, ξ_3) and $(\xi_1, 0, \xi_3)$; ii) all edges simply-supported, labeled as SSSS, where $u_{\xi_1} = u_{\xi_2} = u_{\xi_3} = 0$ at the edge points of coordinates $(0, \xi_2, 0)$, $(\xi_1, L, 0)$, $(L, \xi_2, 0)$ and $(\xi_1, 0, 0)$.

To assess the efficiency of the method, the *hp*-convergence for different theories was investigated. The reference solution $\boldsymbol{U}_{\text{ref}}$ employed for the convergence studies has been obtained by the present method with a 4×4 grid of elements with polynomial trial function of order $p = 7$, which can be considered as converged. For the simply-supported panel with $\tau/L = 0.1$ and the ED_{111} and ED_{333} theories, Figs.(4.38a) and (4.38b) show the solution error versus the element size measure $h = 1/\sqrt{N_e}$ for different approximation polynomial order p; the error is computed at the step corresponding to a non-dimensional surface load $\overline{q} = qL^4/(E\tau^4) = 400$ as

$$e(\boldsymbol{U}_h) = \frac{|\boldsymbol{U}_h - \boldsymbol{U}_{\text{ref}}|_\infty}{|\boldsymbol{U}_h|_\infty} \tag{4.80}$$

where $|\cdot|_\infty$ is the ∞-norm defined over $\hat{\Omega}$. It is worth to note that the number of degrees of freedom associated with the theory $\text{ED}_{k_1k_2k_3}$ is equal to $(k_1+k_2+k_3+3)(p+1)^2N_e$. The data of Figs.(4.38a) and (4.38b) evidences that higher polynomial orders are characterized by higher convergence rates and lower errors.

These findings are confirmed by similar studies carried out for different cases whose results are not reported here for the sake of brevity. To complement the illustration of the method convergence characteristics, Figs.(4.38c) and (4.38d) show the plate equilibrium paths in terms of the non-dimensional surface load $\overline{q} = p_0L^4/E\tau^4$ and the transverse displacement at the central point of the plate $\overline{u}_3 = u_3/\tau$.

They refer to the case of $\tau/L = 0.1$ and simply-supported edges, analysed by the ED_{111} theory. In particular, Fig.(4.38c) shows solutions for different polynomials orders and fixed spatial discretisation, whereas Fig.(4.38d) reports the solutions for fixed approximating polynomials order and different number of elements N_e arranged in an $m \times m$ regular grid.

For the considered boundary conditions and thickness ratios, Fig.(4.39) shows the plate equilibrium paths in terms of the non-dimensional surface load $\overline{q} = p_0L^4/E\tau^4$ and transverse displacement at the central point of the plate $\overline{u}_3 = u_3/\tau$. The presented results are computed through a 2×2 mesh grid of quadrilateral elements with polynomial trial functions of order $p = 5$ and they refer to the solution of the ED_{111} and ED_{333} models, which consists of 864 and 1728 degrees of freedom, respectively. The results are compared with those reported in Ref.[154], in which the FSDT with von Kármán geometrical non-linearities is employed, and in Ref.[155] whose solution is based on a second order theory. It is noticed that in general there is good agreement between the present and reference results. In particular, for thick plates there is an excellent agreement for the high-order theory whereas contained differences are observed for the FSDT case (Fig.(4.39b)). As regard the case of thin plates (Fig.(4.39a)) excellent agreement is remarked for the simply-supported boundary conditions whereas for the clamped plate the DG solution appears less stiff.

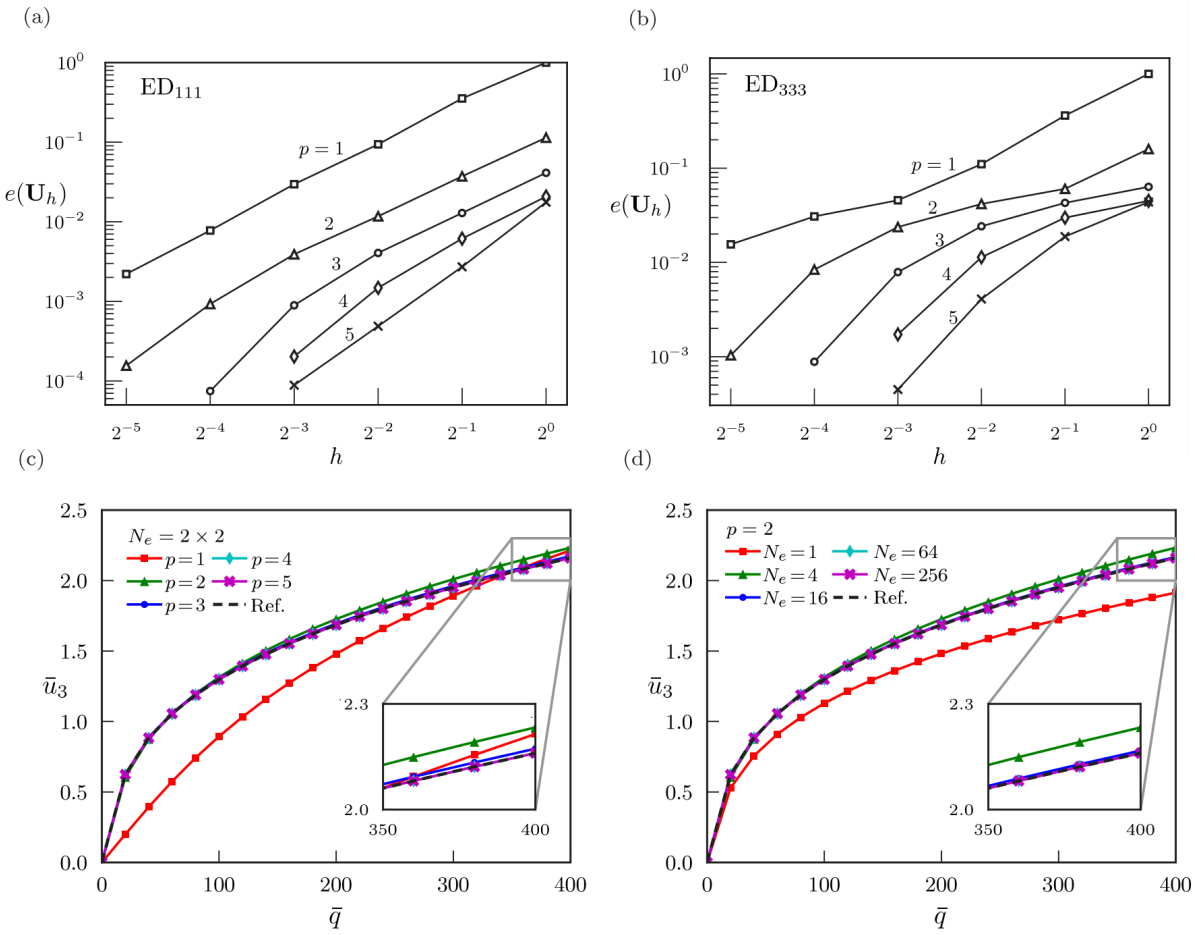

Figure 4.38: Convergence study for the simply-supported, isotropic, square plate. Convergence is assessed with respect a reference solution (labeled as Ref. in the figures). (a) and (b) show the curves of the solution error $e(\boldsymbol{U}_h)$ versus the element size h for the ED_{111} and the ED_{333} theories, respectively. Curves correspond to different approximation polynomial order p. (c) and (d) show the convergence of the ED_{111} equilibrium path of the non-dimensional transverse displacement $\overline{u}_3 = u_3/\tau$ at the plate central point for different polynomial orders p and constant number of elements N_e and for different number of elements N_e and fixed approximation polynomial order p, respectively.

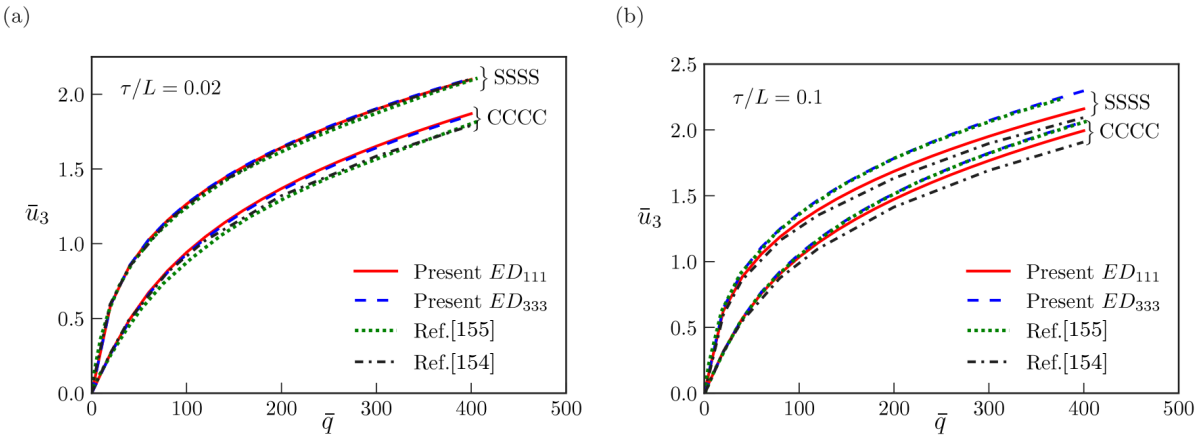

Figure 4.39: Nonlinear bending equilibrium paths of the isotropic square plate with different thickness ratio τ/L and different boundary conditions, namely simply-supported (SSSS) and clamped (CCCC) edges. The curves show the non-dimensional transverse displacement at the central point of the plate versus the non-dimensional surface load. Present results are computed through a 2×2 mesh grid of quadrilateral elements with order $p = 5$, and compared with literature solutions. (a) Thin plate case with $\tau/L = 0.02$. (b) Thick plate case with $\tau/L = 0.1$.

4.5.2 Post-buckling of isotropic plate

The second test regards the post-buckling behaviour of an isotropic, slender, rectangular plate with edge lengths $a = 300$ mm and $b = 60$ mm and thickness ratio $\tau/b = 0.1$, see Fig.(4.40a).

The material properties employed correspond to those of material M_2 in Table (4.23). The reference system $x_1x_2x_3$ and the map of the plate are the same as in the previous case with $\xi_1 \in [0, a]$ and $\xi_2 \in [0, b]$. The plate is clamped on one edge, meaning $u_{\xi_1} = u_{\xi_2} = u_{\xi_3} = 0$ at $\xi_1 = 0$, while the other edges are free. A compression point load $\boldsymbol{F}$ is applied at the coordinates $(\xi_1 = a, \xi_2 = b/2, \xi_3 = 0)$, being constantly directed along the direction of x_1. Additionally, in order to enforce post-buckling behaviour, a perturbation consisting of a small concentrated load $\boldsymbol{P}$ directed along x_3 is applied at the point of coordinates $\xi_1 = a, \xi_2 = b/2, \xi_3 = \tau/2$. The results presented in the following have been obtained through the ED_{222} theory solved by a 2×2 mesh grid of elements with polynomial trial function order $p = 5$, which provides a resolving system with 1296 degrees of freedom. These results are reported and discussed as representative; indeed, similar accuracy can be achieved with different combination of polynomials order and number of elements as illustrated in the previous section. Fig.(4.40b) shows the equilibrium path of the plate in terms of the non-dimensional load amplitude $\overline{F} = F(48a^2)/(\pi^2 E b \tau^3)$ versus the non-dimensional transverse displacement $\overline{u}_3 = u_3/a$ evaluated at the load application point. The comparison of the present results with those of Ref.[155] evidences good agreement with small differences noticeable for higher load levels, being the DG solution less stiff. However, for both curves buckling starts in correspondence of very close load levels and the agreement is very good for the first part of the post-buckling behaviour. To show the evolution of the cantilever, slender plate kinematics with the applied load, some post-buckling configurations are shown in Fig.(4.40c) for different equilibrium states, which correspond to the load levels $\overline{F} = 0.0, 1.1, 1.72, 2.27, 2.75$; the color map represents the normalized displacement magnitude $|\boldsymbol{u}|/a$.

Eventually, computation of stresses has been carried out and to complete the illustra-

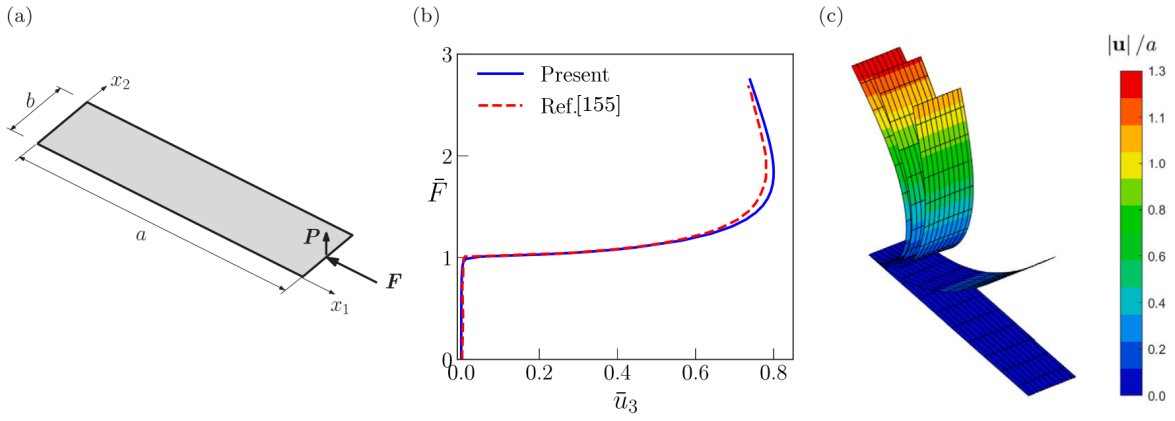

Figure 4.40: Post-buckling response of the cantilevered, isotropic, slender, rectangular plate with edge lengths $a = 300$ mm and $b = 60$ mm and thickness ratio $\tau/b = 0.1$ under the compression load $\boldsymbol{F}$ and the perturbation load $\boldsymbol{P}$. (a) Plate geometry, loads and boundary conditions. (b) Equilibrium path in terms of non-dimensional transverse displacement $\overline{u}_3 = u_3/a$ at the compression load application point versus the non-dimensional load amplitude $\overline{F} = F(48a^2)/(\pi^2 Eb\tau^3)$. Results refer to the ED_{222} theory solved by a 2×2 mesh grid of elements with polynomial trial function order $p = 5$. (c) Post-buckling configurations of the plate for different equilibrium states corresponding to the following compression loads $\overline{F} = 0.0, 1.1, 1.72, 2.27, 2.75$. The color map represents the normalized displacement magnitude $|\boldsymbol{u}|/a$.

tion of the method capabilities, and representative results are presented. They refer to the cantilevered slender plate modeled by the ED_{333} theory solved with the same discretization described above, resulting in 1728 degrees of freedom. Figs.(4.41a) and (4.41b) show the normal stress σ_{11} and the transverse shear stress σ_{13} through-the-thickness distributions at different load amplitudes $\overline{F}$. The through-the-thickness stress distributions are plotted at the plate reference domain points of coordinates $\xi_2 = b/2$ and $\xi_1 = a/3, a/2$. It is worth to note the characteristic of a third-order model to inherently describe the quadratic distributions of the transverse shear stress.

4.5.3 Snap-back and snap-through of cylindrical shells

The third test focuses on the study of a cylindrical shell under loads and boundary conditions that result in a snap-back or snap-through behaviour of the structure. Fig.(4.42a) shows the geometry, boundary conditions and loads of the cylindrical shell along with the orthogonal reference system $x_1x_2x_3$. Only a quarter of the structure is modeled for symmetry conditions.

The mean surface of the shell is mapped as $x_{01} = R\sin(\xi_1)$, $x_{02} = \xi_2$ and $x_{03} = R\cos(\xi_1)$ where $\xi_1 \in [-\theta, 0]$, $\xi_2 \in [0, L]$, $L = 254$ mm, $R = 2540$ mm and $\theta = 0.1$ rad. Three different shell sections have been considered: i) a single-layer section of material M_3 (see Table (4.23)) and thickness $\tau = 6.35$mm, which is labeled as C_1 case (thin shell); ii) a single-layer section of material M_3 (see Table (4.23)) and thickness $\tau = 12.7$mm, which is labeled as C_2 case (moderately thick shell); iii) a three-layer section with [0/90/0] layup of 4.233 mm thick plies having properties as M_4 material in Table (4.23)), which is labeled as C_3 case. The boundary conditions of the first edge correspond to simply-supported, that is $u_{\xi_1} = u_{\xi_2} = u_{\xi_3} = 0$ at the points of coordinates $(-\theta,\ \xi_2,\ 0)$; the edge corresponding to $\xi_2 = 0$ is free, while the boundary conditions on the other two edges are used to enforce symmetry restraints, meaning $u_{\xi_1} = 0$ at the points of coordinates

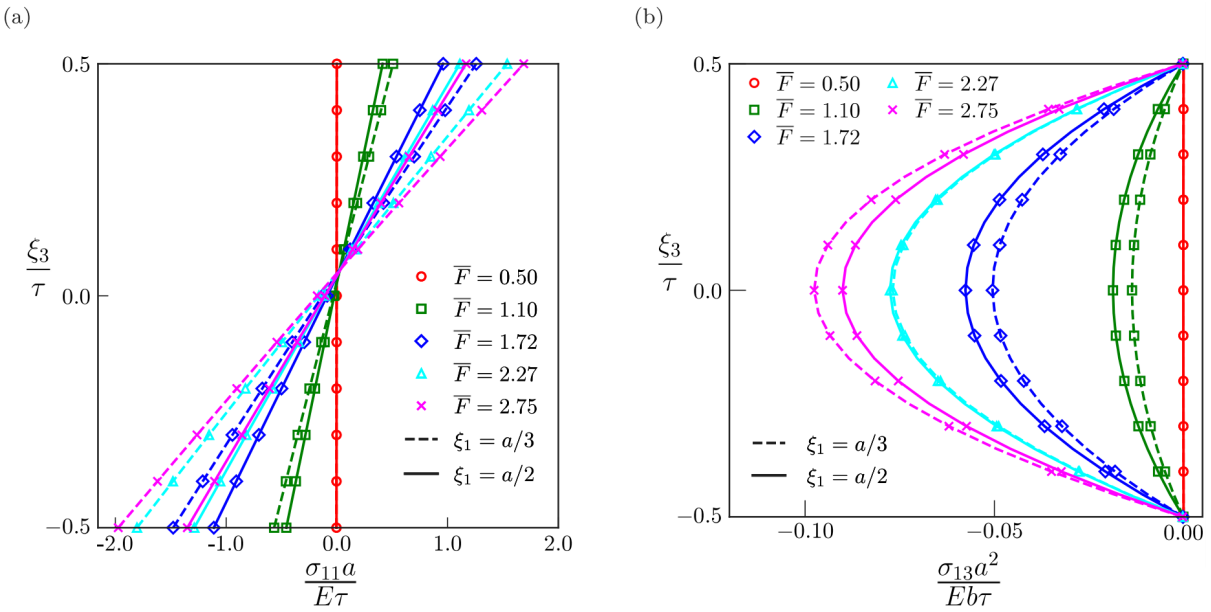

Figure 4.41: Through-the-thickness stress distributions at the reference domain points of coordinates $\xi_1 = a/3, a/2$ and $\xi_2 = b/2$ for the cantilevered slender plate with edge lengths $a = 300$ mm and $b = 60$ mm and thickness ratio $\tau/b = 0.01$. Stress distributions computed by the ED_{333} theory are plotted for different equilibrium states corresponding to the following compression loads $\overline{F} = 0.0, 1.1, 1.72, 2.27, 2.75$. (a) non-dimensional normal stress $\sigma_{11}a/E\tau$; (b) non-dimensional transverse shear stress $\sigma_{13}a^2/Eb\tau$.

$(0,\ \xi_2,\ 0)$ and $u_{\xi_2} = 0$ at the points of coordinates $(\xi_1,\ L,\ 0)$. A transverse point load with amplitude F is applied at the coordinates $\xi_1 = 0, \xi_2 = L, \xi_3 = \tau/2$.

Fig. (4.42b) shows the response of the analysed shells computed using the ED_{222} theory and a 2×2 mesh grid of elements with polynomial trial function order $p = 5$ resulting in 1296 degrees of freedom. Once again, it is remarked that the results obtained by this discretisation are representative and the same accuracy has been achieved with different combinations of mesh and elements approximation order. The curves of Fig.(4.42b) plots the value of the load amplitude F as a function of the transverse displacement u_3 at the load application point. Figs. from (4.42c) to (4.42l) show the shell configurations for selected equilibrium states. In particular, for the C_1 section shell, Figs. from (4.42c) to (4.42g) show the shell deformed shape at the load levels $F = 0.283,\ -0.315,\ 0.185,\ 1.576,\ 3.0$ [kN], whereas Figs. from (4.42h) to (4.42l) illustrate the behaviour of the C_3 section shell showing its configurations at $F = 1.043,\ 1.661,\ 0.861,\ 1.803,\ 3.045,$ [kN]. The shell configurations of Figs. from (4.42c) to (4.42l) are supplemented by the displacement magnitude $|\boldsymbol{u}|$ maps. Clearly, snap-back or snap-through behaviour occurs depending on the shell thickness ratio and the comparison of the present results with those available from Refs.[156], [157] and [158] shows good agreement for both isotropic and multilayered cases.

Fig.(4.43) illustrate the through-the-thickness distribution of representative stress components computed for the C_3 section shell at the point $\xi_1 = \theta/4$ and $\xi_2 = L/4$. These are computed for the equilibrium states corresponding to $F = 1.043,\ 1.661,\ 0.861,\ 1.803,\ 3.045,$ [kN] by using both the ED_{222} and ED_{333} models with the same domain discretization described above. As expected, the results shows that both the employed models are able to capture the in-plane stress distribution with the same accuracy level as illustrated by Fig.(4.43a) where the σ_{11} curves are almost coincident for the two shell

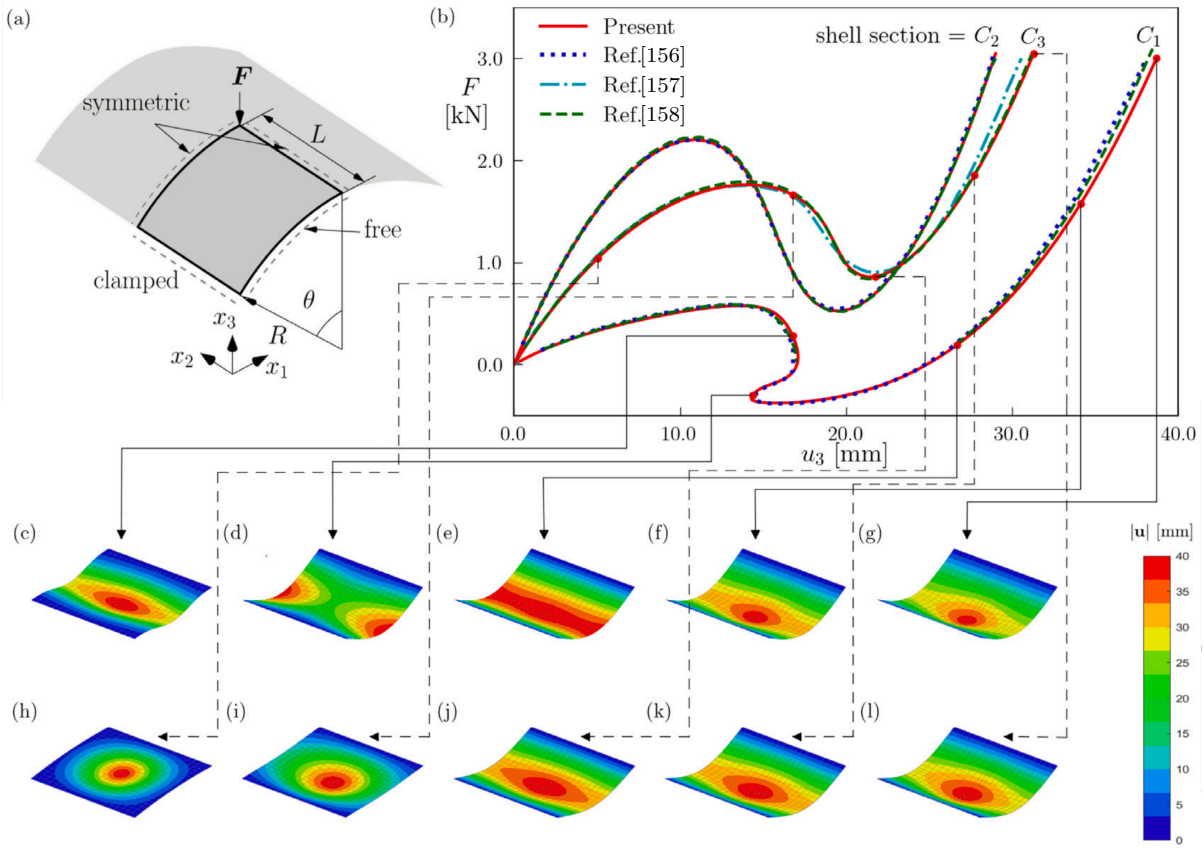

Figure 4.42: Cylindrical shells with snap-back and snap-through behaviour. (a) Geometry, boundary conditions and applied load: $L = 254$ mm, $R = 2540$ mm and $\theta = 0.1$ rad. (b) Nonlinear equilibrium path in terms of load amplitude F versus the transverse displacement u_3 at the load application point for the three examined shell sections: i) a 6.35mm thin homogeneous section of material M_3, labeled as C_1, ii) a 12.7mm moderately thick homogeneous section of material M_3, labeled as C_2, and iii) a 12.7mm thick layered section with [0/90/0] layup of M_4 material, equal thickness plies, labeled as C_3. M_3 and M_4 material properties are given in Table (4.23). Results are obtained using the ED_{222} theory solved by a 2×2 mesh grid of elements with polynomial trial function order $p = 5$. (c-g) show the C_1 section shell configurations for different equilibrium states corresponding to $F = 0.283, -0.315, 0.185, 1.576, 3.0$ [kN]. (h-l) show the C_3 section shell configurations for different equilibrium states corresponding to $F = 1.043, 1.661, 0.861\, 1.803, 3.045$ [kN]. The color maps represent the displacement magnitude $|\boldsymbol{u}|$.

theories employed. As regard the transverse shear stresses, Fig.(4.43b) shows the σ_{13} stress results. These indicate that the ED_{222} model is not able to provide reliable shear stress distributions as the traction-free boundary condition is not ensured; on the other hand the ED_{333} theory generally give physically reliable and sound distributions. These results illustrate the capabilities of the proposed method to deal with complex nonlinear behaviour of shells.

4.5.4 NURBS-based laminated shell

In the last test, a generally-curved shell is considered, whose geometry is shown in Fig.(4.44) being $L = 600$ mm, $H = 500$ mm and $D = 50$ mm.

The shell geometry is described via NURBS functions and for its data, including the coordinates of the control points, the degree of the basis functions and the knot vectors, the reader is referred to Sec. 4.2.7. The shell section is a four layers laminate with

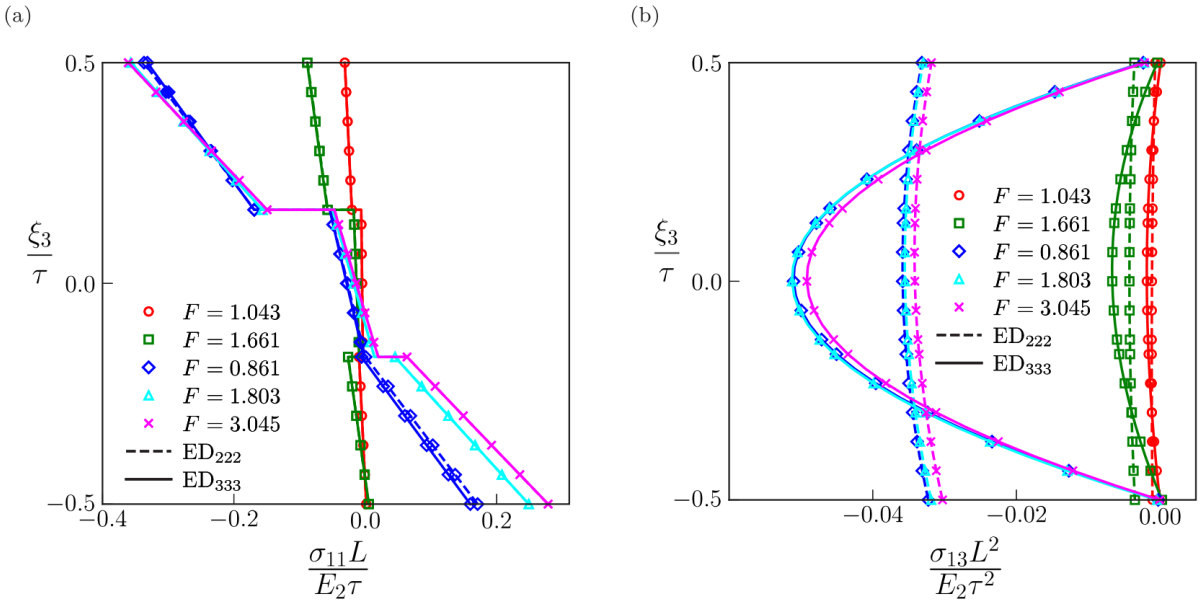

Figure 4.43: Through-the-thickness stress distributions for the pinched cylindrical shell with radius $R = 2540$ mm, central half-angle $\theta = 0.1$ rad, half-length $L = 254$ mm and [0/90/0] layup with 4.233 mm thick plies of M_4 material (see Table (4.23)). Stress distributions at the reference domain points of coordinates $\xi_1 = \theta/4$ and $\xi_2 = L/4$ are plotted for different equilibrium states corresponding to the load amplitudes $F = 1.043, 1.661, 0.861, 1.803, 3.045$ [kN]. (a) non-dimensional normal stress $\sigma_{11}L/E_2\tau$; (b) non-dimensional transverse shear stress $\sigma_{13}L^2/E_2\tau^2$, being E_2 the M_4 material transverse Young's module and τ the shell thickness.

1 mm thick plies of material M_4 (see Table (4.23)) and $[0, 30, 60, 90]$ layup. The shell is clamped on the edge corresponding to $\xi_2 = 1$ and it is subjected on the opposite edge to an uniform, compression displacement u_2 directed along x_2. The shell is modeled with the ED_{222} theory and the simulation has been carried out using a 10×10 grid of elements with polynomial order $p = 4$ resulting in 22500 degrees of freedom.

Fig. (4.45a) shows the shell load-end displacement curve in terms of the average x_2-directed edge force resultant per unit length, namely N_{22}^{av}, versus the applied edge displacement u_2. The curve is compared with that obtained by finite elements using the Abaqus® software [26] evidencing very good agreement.

Additionally, Figs. from (4.45b) to (4.45g) show the contour maps of the displacement vector magnitude $|\boldsymbol{u}|$ of the reference surface points at the loading steps corresponding to 1%, 20%, 40%, 60%, 80% and 100% of the maximum applied compression displacement $u_{2_{max}}$. It is evidenced the complex behaviour of the investigated shell which experiences coupling effects related to its geometry and layup. It is worth to note that a thin shell has been used in this test. This allows to consider accurate the finite element solution obtained with the first order shear deformation theory whereas a second order theory has been employed in the DG modelization, so as to validate the proposed refined approach in the framework of such a complex shell geometry.

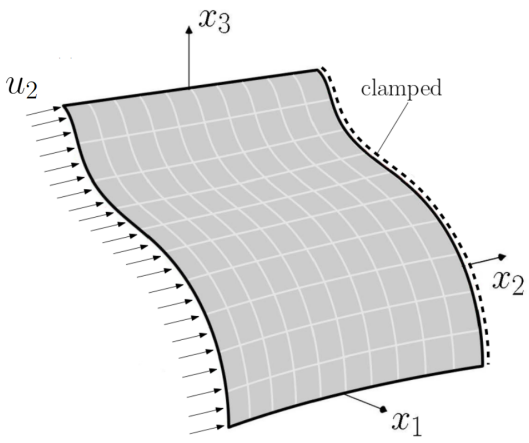

Figure 4.44: Geometry and loading conditions of NURBS-based shell undergoing compression loading.

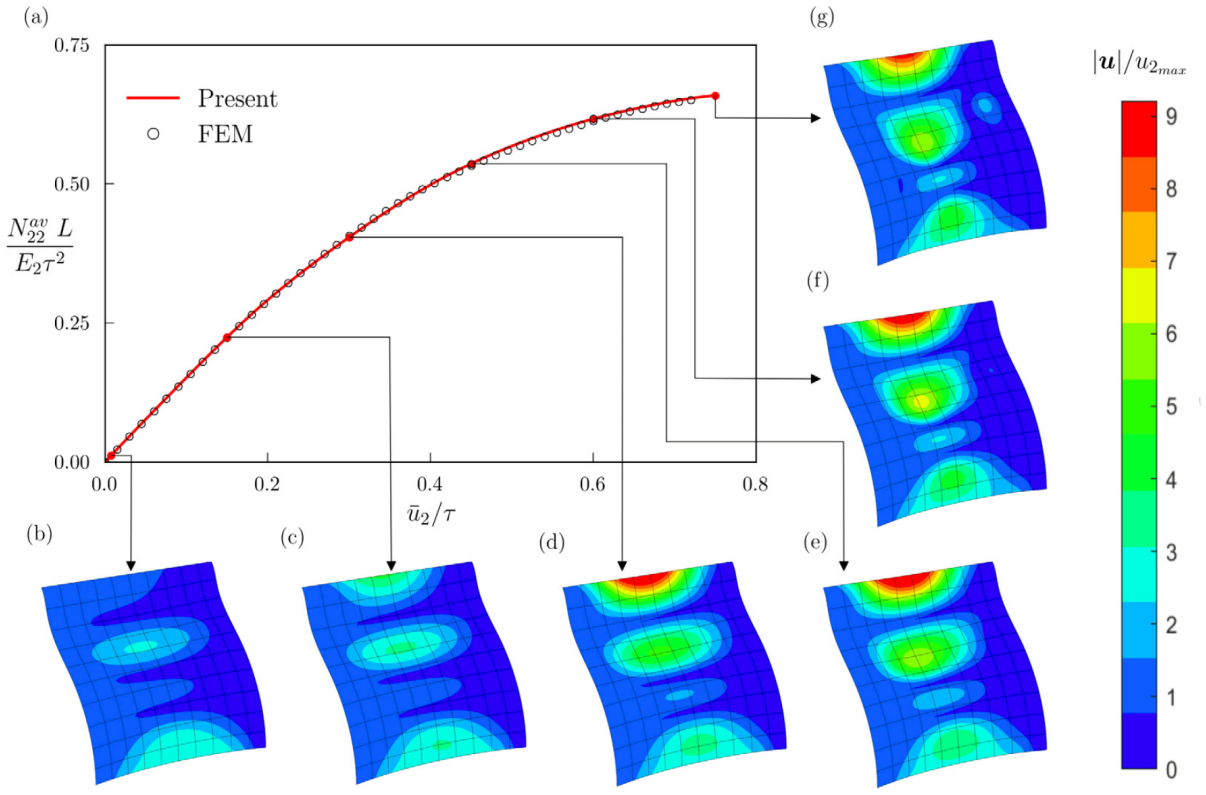

Figure 4.45: NURBS-based shell undergoing compression loading. (a) Equilibrium path in terms of the average x_2-directed edge force resultant per unit length N_{22}^{av} versus the applied edge displacement u_2. Color maps of the non-dimensional displacement vector magnitude $|\boldsymbol{u}|/u_{2_{max}}$ at the reference surface points are also shown at the following percentage levels of the loading: (b) 1%, (c) 20%, (d) 40%, (e) 60%, (f) 80%, (g) 100%; they refer to the colorbar where $u_{2_{max}}$ is the maximum loading amplitude.

Chapter 5

The Isogeometric Analysis method

5.1 The basis functions for Isogeometric Analysis

In this section, an overview of B-splines and NURBS functions is given. In the context of IGA methods, they are utilized to construct both surfaces of shells and to discretize their displacement field. In this thesis, shell surfaces are eventually represented using a trimming approach. This approach begins with a simple background surface that follows a tensor product structure. The surface is then trimmed by defining its boundary through some additional curves. The details of this trimming operations are provided in the following sections.

5.1.1 The B-splines functions

Univariate B-splines are created based on a polynomial order p and a knot vector, which is a sequence of non-decreasing knot values $\Xi = \{\xi^1, \xi^2, ..., \xi^{n+p+1}\}$. These parameters are used to construct n basis functions $N_i^p(\xi)$, where $\xi \in [\xi_1, \xi_2]$ is the curvilinear coordinate and $i = 1, 2, ..., n$. The Cox-de Boor recursion formula is employed to generate these basis functions [127]. A B-spline curve embedded in $\mathbb{R}^3$ can be constructed by multiplying the basis functions by some control points $\boldsymbol{P}_i \in \mathbb{R}^3$ and summing up as

$$\boldsymbol{\mathcal{F}}(\xi) = \sum_{i=1}^{n} N_i^p(\xi) \boldsymbol{P}_i \, . \tag{5.1}$$

It is important to highlight the following aspects of B-splines:

i) From the knot vector Ξ, the vector $\Theta = [\eta^1, \eta^2, \ldots, \eta^r]$ is constructed taking only the consecutive, non-repeating values η^i in such a way that in the intervals $[\eta^i, \eta^{i+1}]$ the partition of unity property of the spline basis functions is satisfied. It is worth noting that the number of elements of Θ, here denoted by r, depends on the specificity of Ξ. The B-spline function is therefore defined piece-wise in the intervals $[\eta^i, \eta^{i+1}]$.

ii) Within each interval, the B-spline function is infinitely differentiable (C^∞). However, at the knots, the continuity is at most C^{p-1} and is reduced of one unity for every repetition of the knot value.

iii) The piece-wise nature of the B-spline naturally leads to a mesh-like structure, where each element corresponds to a different interval.

From univariate B-splines basis functions, their bivariate counterparts are constructed using a tensor product approach as

$$B_{ij}(\xi_1, \xi_2) = N_i^p(\xi_1) N_j^p(\xi_2) \ , \tag{5.2}$$

where, for the sake of simplicity, it is assumed the same polynomial degree in both curvilinear direction ξ_1 and ξ_2. Additionally, $N_i^p(\xi_1)$ and $N_j^p(\xi_2)$ are univariate basis functions constructed from the knot vectors $\Xi^1 = \{\xi_1^1, \xi_1^2, ..., \xi_1^{n+p+1}\}$ and $\Xi^2 = \{\xi_2^1, \xi_2^2, ..., \xi_2^{m+p+1}\}$, respectively. Therefore, a B-spline surface is constructed as

$$\boldsymbol{\mathcal{F}}(\xi_1, \xi_2) = \sum_{i=1}^{n} \sum_{j=1}^{m} B_{ij}(\xi_1, \xi_2) \boldsymbol{P}_{ij} \ , \tag{5.3}$$

where $\boldsymbol{P}_{ij} \in \mathbb{R}^3$ is a generic control point. The knot vectors in a B-spline identify the parametric domain. When open knot vectors are adopted, the parametric domain before trimming is defined as $\hat{\Pi}_0 = [\xi_1^1, \xi_1^{n+p+1}] \times [\xi_2^1, \xi_2^{m+p+1}]$, meaning that $(\xi_1, \xi_2) \in \hat{\Pi}_0$. The bivariate splines inherit the piece-wise definition property from univariate ones through the tensor product structure. Therefore, a rectangular Bezier grid is identified in $\hat{\Pi}_0$ and the domain of a generic cell is denoted as $\hat{\Pi}^e = [\eta_1^i, \eta_1^{i+1}] \times [\eta_2^j, \eta_2^{j+1}]$, where $[\eta_\alpha^i, \eta_\alpha^{i+1}]$ denotes the i-th interval of definition of the univariate basis functions corresponding to ξ_α.

For more details on 1D and 2D B-splines, together with the extension to NURBS curves and surfaces, that is not reported here for the sake of conciseness, the interest reader is referred to [127, 128].

5.1.2 Space of trimmed splines

When adopting an immersed boundary representation to describe a complex geometry, the surface of the shell, as well as its corresponding parametric domain, are divided into an active and a non-active region. In particular, it is reminded that the active part of the domain is denoted by $\hat{\Omega} \subset \hat{\Pi}_0$. If, after the trimming of the domain, some of the B-splines have a support that does not intersect the parametric domain anymore, they are excluded from the basis of the function space used for approximating the variable problems. The space of bivariate B-splines used for the displacement approximation becomes

$$\mathcal{S}_h = \text{span}\{B_{ij} \circ \boldsymbol{\mathcal{F}}^{-1} : i \in \{1, ..., n\}, \ j \in \{1, ..., m\}, \ \text{supp}\{B_{ij}\} \cap \hat{\Omega} \neq 0\} \tag{5.4}$$

It is worth mentioning that as long as the trimming process does not result in empty elements, $\mathcal{S}_h$ is equal to $\text{span}\{B_{ij}\}$. Additionally, depending on the degree selected for the elements of the analysis, the support of the bivariate B-spline may extend to multiple elements. Therefore, even if some of the elements are empty, $\mathcal{S}_h$ might still coincide with $\text{span}\{B_{ij}\}$. The space of vector field used to approximate displacement vector is then defined as

$$\mathcal{V}_h = {\mathcal{S}_h}^3 \ . \tag{5.5}$$

5.2 The interior penalty coupling for Kirchhoff-Love shells

In this section, the Kirchhoff-Love shell problem, presented in a continuous framework in Chapter 3, is discretized by selecting appropriate spaces $\mathcal{V}^u$ and $\mathcal{V}^v$ for a single patch

problem and $\boldsymbol{\mathcal{V}}^u$ and $\boldsymbol{\mathcal{V}}^v$ for a multi-patch problem. In an IGA approach, these spaces are constructed starting from the trimmed B-spline space introduced in Sec. 5.1.2. In this thesis, Dirichlet boundary conditions for KL shells are applied in either a weak or a strong sense, depending on the specific problem being investigated.

For a single patch shell, in order to impose Dirichlet boundary conditions in a strong sense, it is necessary to ensure that the test and trial functions $\boldsymbol{u}_h$ and $\boldsymbol{v}_h$ of $\mathcal{V}_h^u$ and $\mathcal{V}_h^v$, respectively, satisfy $\boldsymbol{u}_h = \tilde{\boldsymbol{u}}$ and $\boldsymbol{v}_h = \boldsymbol{0}$ on $\partial\Omega_{D_1}^h$ and $\theta_n(\boldsymbol{u}_h) = \tilde{\theta}_n$ and $\theta(\boldsymbol{v}_h) = 0$ on $\partial\Omega_{D_2}^h$. Displacement boundary conditions can be imposed strongly only on conforming edges. However, if Dirichlet boundary conditions are enforced in a weak sense, these requirements no longer need to be satisfied. The same principles apply when considering shell structures composed of multiple patches. More specifically, regarding the coupling conditions, this work adopts exclusively a weak imposition, as explained in the following sections. Additionally, similarly to other fourth-order equations, in the Kirchhoff-Love one there is a continuity requirement on the trial functions of at least C^1 [115, 159].

Different methods are available in literature to apply boundary conditions and coupling conditions in a weak sense. In this work, the symmetric stabilized Nitsche method [115], also known as the interior penalty method [28] in the context of coupling conditions, is employed. This method requires the computation of the fluxes of the formulation obtained as explained in Sec. 5.2.1.

5.2.1 The fluxes for the Kirchhoff-Love problem

Due to the complexity of the Kirchhoff-Love shell equations, the computation of the fluxes is not a trivial task. In fact, the initially proposed expression for the fluxes by Koiter [114] was found to be incorrect, as discussed in [115]. For a complete derivation of their expression, interested readers are referred to this source. However, the correct definition is also provided here for the sake of completeness.

Recalling the outer-facing unit normal $\boldsymbol{n}$ introduced in Chapter 3, in this direction, the fluxes associated with the problem are of two types: those corresponding to the ersatz force and those corresponding to the bending moment. Respectively, their definitions are

$$\boldsymbol{T}(\boldsymbol{u}) = T^\alpha \boldsymbol{a}_\alpha + T^3 \boldsymbol{a}_3 \,, \tag{5.6a}$$

$$M_{nn}(\boldsymbol{u}) = M^{\alpha\beta} n_\alpha n_\beta \,, \tag{5.6b}$$

where n_α is the component of $\boldsymbol{n}$ referred to $\boldsymbol{a}^\alpha$, and the components of the vector $\boldsymbol{T}$ are defined as

$$T^\alpha = N^{\alpha\beta} n_\beta - b_\gamma^\alpha M^{\gamma\beta} n_\beta - M_{nt} b_\gamma^\alpha t^\gamma \,, \tag{5.7a}$$

$$T^3 = M_{|\beta}^{\alpha\beta} n_\alpha + (M^{\alpha\beta} n_\alpha t_\beta)_{,t} \,, \tag{5.7b}$$

where with the notation $(\bullet)_{,t}$ it is denoted the arc-lenght derivative along the curve that identified $\boldsymbol{t}$.

Details on the computation of the fluxes

The covariant and contravariant component of the vector $\boldsymbol{t}$ are obtained as $t_\alpha = \boldsymbol{t} \cdot \boldsymbol{a}_\alpha$ and $t^\alpha = \boldsymbol{t} \cdot \boldsymbol{a}^\alpha$, respectively. The same applies to the vector $\boldsymbol{n}$. The bending and twisting

moments are derived from $M_{nn} = M^{\alpha\beta} n_\alpha n_\beta$ and $M_{nt} = M^{\alpha\beta} n_\alpha t_\beta$, respectively. The covariant derivative of the moment tensor is obtained as

$$M^{\alpha\beta}_{|\gamma} = M^{\alpha\beta}_{,\gamma} + \Gamma^{\alpha}_{\lambda\gamma} M^{\lambda\beta} + \Gamma^{\beta}_{\lambda\gamma} M^{\alpha\lambda} \ , \tag{5.8}$$

where $\Gamma^{\gamma}_{\alpha\beta}$ represents the Christoffel symbols of the second kind which are defined as

$$\Gamma^{\gamma}_{\alpha\beta} = \boldsymbol{a}^{\gamma} \cdot \boldsymbol{a}_{\alpha,\beta} \ . \tag{5.9}$$

Recalling the generalized constitutive relationship for a KL shell, the coordinate derivative of the moment tensor is computed as

$$M^{\alpha\beta}_{,\rho} = \mathbb{C}^{\alpha\beta\gamma\delta}_{,\rho} \ \varepsilon_{\gamma\delta} + \mathbb{C}^{\alpha\beta\gamma\delta} \ \varepsilon_{\alpha\beta,\rho} + \mathbb{D}^{\alpha\beta\gamma\delta}_{,\rho} \ \kappa_{\gamma\delta} + \mathbb{D}^{\alpha\beta\gamma\delta} \ \kappa_{\alpha\beta,\rho} \ . \tag{5.10}$$

The derivatives appearing in Eq.(5.10) are not reported here for the sake of conciseness. However, their computation through the chain rule is straightforward, albeit somewhat laborious. To what regards the second term in Eq.(5.7b), the following relationship holds:

$$(M^{\alpha\beta} n_\alpha t_\beta)_{,t} = (M^{\alpha\beta})_{,t} n_\alpha t_\beta + M^{\alpha\beta} (n_\alpha)_{,t} t_\beta + M^{\alpha\beta} n_\alpha (t_\beta)_{,t} \ , \tag{5.11}$$

Let us suppose that this curve is known in the Euclidean space through a map $\boldsymbol{y} = \boldsymbol{y}(\tau)$, being τ an auxiliary curvilinear direction. Then, the tangent unit vector is computed as $\boldsymbol{t} = \frac{\boldsymbol{y}_{,\tau}}{|\boldsymbol{y}_{,\tau}|}$, while its derivative with respect to τ is

$$\boldsymbol{t}_{,\tau} = \frac{(\boldsymbol{I} - \boldsymbol{t}\boldsymbol{t}^{\intercal})}{|\boldsymbol{y}_{,\tau}|} \boldsymbol{y}_{,\tau\tau} \ , \tag{5.12}$$

where $\boldsymbol{I}$ is the identity 3×3 tensor. The arc-length derivative of $\boldsymbol{t}$ is further obtained as

$$(\boldsymbol{t})_{,t} = \frac{\boldsymbol{t}_{,\tau}}{|\boldsymbol{y}_{,\tau}|} \ . \tag{5.13}$$

To what regards the normal vector $\boldsymbol{n} = \boldsymbol{t} \times \boldsymbol{a}_3$, its arc-length derivative is computed as

$$(\boldsymbol{n})_{,t} = (\boldsymbol{t})_{,t} \times \boldsymbol{a}_3 + \boldsymbol{t} \times (\boldsymbol{a}_3)_{,t} \ . \tag{5.14}$$

However, it is worth noting that when dealing with shells coupling, the relative orientation of $\boldsymbol{t}$, $\boldsymbol{n}$ and $\boldsymbol{a}_3$ may be such that $\boldsymbol{n} = \boldsymbol{a}_3 \times \boldsymbol{t}$, which implies a straightfoward adaptation of Eq.(5.14). The arc-length derivative of $\boldsymbol{a}_3$ is computed as $(\boldsymbol{a}_3)_{,t} = \boldsymbol{a}_{3,\gamma} t^{\gamma}$, where, introducing the vector $\boldsymbol{p} = \boldsymbol{a}_1 \times \boldsymbol{a}_2$, $\boldsymbol{a}_{3,\gamma}$ is obtained as

$$\boldsymbol{a}_{3,\gamma} = \frac{(\boldsymbol{I} - \boldsymbol{a}_3 \boldsymbol{a}_3^{\intercal})}{\lambda} \boldsymbol{p}_{,\gamma} \ , \tag{5.15}$$

and $\boldsymbol{p}_{,\gamma}$ is computed through the chain rule. The arc-length derivatives of the covariant components of $\boldsymbol{t}$ and $\boldsymbol{n}$ are obtained as $(t_\alpha)_{,t} = (\boldsymbol{t})_{,t} \cdot \boldsymbol{a}_\alpha$ and $(n_\alpha)_{,t} = (\boldsymbol{n})_{,t} \cdot \boldsymbol{a}_\alpha$. Finally, the arc-length derivative of $M^{\alpha\beta}$ is obtained as $(M^{\alpha\beta})_{,t} = M^{\alpha\beta}_{|\gamma} t^{\gamma}$.

5.2.2 The Nitsche's method for Dirichlet boundary conditions

When a strong imposition of Dirichlet boundary conditions is not possible, the symmetric stabilized Nitsche's method [115] is employed. For a single-patch shell, the discretized Kirchhoff-Love variational statement is formulated as follows: find $\boldsymbol{u}_h \in \mathcal{V}_h^u$ such that

$$a_h(\boldsymbol{u}_h, \boldsymbol{v}_h) + a_n(\boldsymbol{u}_h, \boldsymbol{v}_h) + a_s(\boldsymbol{u}_h, \boldsymbol{v}_h) = f_h(\boldsymbol{v}_h) + f_n(\boldsymbol{v}_h) + f_s(\boldsymbol{v}_h) \quad \forall \boldsymbol{v} \in \mathcal{V}_h^v \,. \tag{5.16}$$

Where $\mathcal{V}_h^u$, and $\mathcal{V}_h^v$ are constructed from the space of B-splines defined over $\hat{\Omega}$ and their exact definition depends on whether the boundary conditions are imposed strongly in a portion of the boundary. In the equations presented in this section, it is assumed that essential boundary conditions are applied in a weak sense in the entire $\partial\Omega_{D_1}^h$ and $\partial\Omega_{D_2}^h$, whereas in the results presented in Sec. 5.3 it is preferred, when possible, to enforce them in a strong sense. Both the bilinear form on the left-hand side and the linear form on the right-hand side of Eq.(5.16) are constructed by summing three contributions. As for the terms with a subscript h, they are defined as follows:

$$a_h(\boldsymbol{u}_h, \boldsymbol{v}_h) = \int_{\Omega^h} \boldsymbol{\varepsilon}(\boldsymbol{v}_h) : \boldsymbol{N}(\boldsymbol{u}_h) \mathrm{d}\Omega + \int_{\Omega^h} \boldsymbol{\kappa}(\boldsymbol{v}_h) : \boldsymbol{M}(\boldsymbol{u}_h) \mathrm{d}\Omega \,, \tag{5.17a}$$

$$f_h(\boldsymbol{v}_h) = \int_{\Omega^h} \boldsymbol{v} \cdot \tilde{\boldsymbol{F}} \mathrm{d}\Omega + \int_{\partial\Omega_{N_1}^h} \boldsymbol{v}_h \cdot \tilde{\boldsymbol{T}} \mathrm{d}\partial\Omega + \int_{\partial\Omega_{N_2}^h} \theta_n(\boldsymbol{v}_h) \tilde{M}_{nn} \mathrm{d}\partial\Omega + \sum_{C \in \chi_N^h} \left(v_{3h} \tilde{R} \right) \Big|_C \,, \tag{5.17b}$$

and constitute the discretized version of the KL shell equations. As such, Ω^h, $\partial\Omega_{N_1}^h$, $\partial\Omega_{N_2}^h$, and χ_N^h are the approximated versions after discretization of $\partial\Omega_{N_1}$, $\partial\Omega_{N_2}$, and χ_N, respectively. The terms with a subscript n are the symmetric Nitsche terms, which include the fluxes described in Sec. 5.2.1. These terms are defined as

$$\begin{aligned} a_n(\boldsymbol{v}_h, \boldsymbol{u}_h) = &- \int_{\partial\Omega_{D_1}^h} \left(\boldsymbol{T}(\boldsymbol{v}_h) \cdot \boldsymbol{u}_h + \boldsymbol{v}_h \cdot \boldsymbol{T}(\boldsymbol{u}_h) \right) \mathrm{d}\partial\Omega \\ &- \int_{\partial\Omega_{D_2}^h} \left(M_{nn}(\boldsymbol{v}_h) \theta_n(\boldsymbol{u}_h) + \theta_n(\boldsymbol{v}_h) M_{nn}(\boldsymbol{u}_h) \right) \mathrm{d}\partial\Omega - \sum_{C \in \chi_D^h} \left(R(\boldsymbol{v}_h) u_{3h} + v_{3h} R(\boldsymbol{u}_h) \right) \big|_C \,, \end{aligned} \tag{5.18a}$$

$$f_n(\boldsymbol{v}_h) = - \int_{\partial\Omega_{D_1}^h} \boldsymbol{T}(\boldsymbol{v}_h) \cdot \tilde{\boldsymbol{u}} \mathrm{d}\partial\Omega - \int_{\partial\Omega_{D_2}^h} M_{nn}(\boldsymbol{v}_h) \tilde{\theta}_n \mathrm{d}\partial\Omega - \sum_{C \in \chi_D^h} \left(R(\boldsymbol{v}_h) \tilde{u}_3 \right) \big|_C \,, \tag{5.18b}$$

where $\tilde{\boldsymbol{u}}$ and $\tilde{\theta}_n$ are the applied displacement and normal rotation, respectively and $\partial\Omega_{D_1}^h$, $\partial\Omega_{D_2}^h$, and χ_D^h are the approximated versions of $\partial\Omega_{D_1}$, $\partial\Omega_{D_2}$, and χ_D, respectively. The subscript 3 in u_{3h} and v_{3h} denotes the component of the respective vector relative to $\boldsymbol{a}^3 = \boldsymbol{a}_3$. Additionally, the following definition has been employed:

$$R = \lim_{\epsilon \to 0} \left(M_{nt}(\boldsymbol{x} + \epsilon \boldsymbol{t}) - M_{nt}(\boldsymbol{x} - \epsilon \boldsymbol{t}) \right) \,, \tag{5.19}$$

where $M_{nt} = M^{\alpha\beta} n_\alpha t_\beta$ and t_β is the component of $\boldsymbol{t}$ along $\boldsymbol{a}^\beta$. Both $a_n(\boldsymbol{v}_h, \boldsymbol{u}_h)$ and $f_n(\boldsymbol{v}_h)$ are composed of three terms. The first and second terms correspond to the displacements and rotation boundary conditions, respectively. The third term, which involves the displacements at the corners, is introduced to ensure optimal convergence, as discussed in [115]. Each of the three contributes are constructed from a consistency

term (e.g., $\boldsymbol{v}_h \cdot \boldsymbol{T}(\boldsymbol{u}_h)$) and a symmetry term (e.g., $\boldsymbol{T}(\boldsymbol{v}_h) \cdot \boldsymbol{u}_h$ and $\boldsymbol{T}(\boldsymbol{v}_h) \cdot \tilde{\boldsymbol{u}}$). Finally, the stabilization terms in Eq.(5.16), denoted by a subscript s, are defined as

$$\begin{aligned} a_s(\boldsymbol{v}_h, \boldsymbol{u}_h) = &\int_{\partial\Omega^h_{D_1}} \mu^b_D \boldsymbol{v}_h \cdot \boldsymbol{u}_h \mathrm{d}\partial\Omega + \int_{\partial\Omega^h_{D_2}} \mu^b_R \theta_n(\boldsymbol{v}_h)\theta_n(\boldsymbol{u}_h)\mathrm{d}\partial\Omega + \\ &+ \int_{\partial\Omega^h_{D_1}} \mu^b_3 v_{3h} u_{3h} \mathrm{d}\partial\Omega + \sum_{C\in\chi^h_D} \left(\mu^b_C v_{3h} u_{3h}\right)\big|_C \,, \end{aligned} \tag{5.20a}$$

$$\begin{aligned} f_s(\boldsymbol{v}_h) = &\int_{\partial\Omega^h_{D_1}} \mu^b_D \boldsymbol{v}_h \cdot \tilde{\boldsymbol{u}} \mathrm{d}\partial\Omega + \int_{\partial\Omega^h_{D_2}} \mu^b_R \theta_n(\boldsymbol{v}_h)\tilde{\theta}_n \mathrm{d}\partial\Omega + \\ &+ \int_{\partial\Omega^h_{D_1}} \mu^b_3 v_{3h} \tilde{u}_3 \mathrm{d}\partial\Omega + \sum_{C\in\chi^h_D} \left(\mu^b_C v_{3h} \tilde{u}_3\right)\big|_C \,, \end{aligned} \tag{5.20b}$$

where μ^b_D, μ^b_R, μ^b_3, and μ^b_C are the so-called penalty parameters, which play a crucial role in the weak imposition of boundary and coupling conditions, since they provide stability to the method. The choice of these parameters is still an open question and depends on the specific problem at hand. A discussion on the importance of these parameters, some guidelines on how to choose them, and the approach adopted in this thesis is presented in Sec. 5.2.4.

5.2.3 The interior penalty method for coupling IGA patches

The framework presented in Sec. 5.2.2 focuses on a single-patch shell. However, when dealing with structures composed of multiple shells that intersect at common interfaces, the formulation needs to be extended to address the coupling conditions. To achieve this, the terms in Eq.(5.16) are enriched with a superscript p to indicate that they belong to the p-th patch. Then, the following forms are defined:

$$a^p(\boldsymbol{u}_h, \boldsymbol{v}_h) = a^p_h(\boldsymbol{u}_h, \boldsymbol{v}_h) + a^p_n(\boldsymbol{u}_h, \boldsymbol{v}_h) + a^p_s(\boldsymbol{u}_h, \boldsymbol{v}_h) \,, \tag{5.21a}$$

$$f^p(\boldsymbol{v}_h) = f^p_h(\boldsymbol{v}_h) + f^p_n(\boldsymbol{v}_h) + f^p_s(\boldsymbol{v}_h) \,. \tag{5.21b}$$

The discretized version of the Kirchhoff-Love shell equation for multi-patch structures becomes: find $\boldsymbol{u}_h$ in $\boldsymbol{\mathcal{V}}^u_h$ such that

$$\sum_{p=1}^{N_P} a^p(\boldsymbol{u}_h, \boldsymbol{v}_h) + \sum_{i=1}^{N_I} b^i(\boldsymbol{u}_h, \boldsymbol{v}_h) = \sum_{p=1}^{N_P} f^p(\boldsymbol{v}_h) \quad \forall \boldsymbol{v}_h \in \boldsymbol{\mathcal{V}}^v_h \,, \tag{5.22}$$

where $\boldsymbol{\mathcal{V}}^u_h$ and $\boldsymbol{\mathcal{V}}^v_h$ are the discretized spaces correspondent to $\boldsymbol{\mathcal{V}}^u$ and $\boldsymbol{\mathcal{V}}^v$, respectively, and $b^i(\boldsymbol{u}_h, \boldsymbol{v}_h)$ is the contribute to the variational statement ensuring the coupling between the patches intersecting at the i-th interface. These terms are obtained as

$$b^i(\boldsymbol{u}_h, \boldsymbol{v}_h) = b^i_n(\boldsymbol{u}_h, \boldsymbol{v}_h) + b^i_s(\boldsymbol{u}_h, \boldsymbol{v}_h) \,. \tag{5.23}$$

Once again, Nitsche and stabilization terms have been introduced, denoted by the subscripts n and s, respectively. The definitions of these terms are

$$b_n^i(\boldsymbol{u}_h, \boldsymbol{v}_h) = \int_{\Gamma_i^h} (\{\boldsymbol{T}(\boldsymbol{v}_h)\} \cdot [\boldsymbol{u}_h] + \{M_{nn}(\boldsymbol{v}_h)\}[\theta_n(\boldsymbol{u}_h)]) \, \mathrm{d}\Gamma + \\ + \gamma_1 \int_{\Gamma_i^h} ([\boldsymbol{v}_h] \cdot \{\boldsymbol{T}(\boldsymbol{u}_h)\} + [\theta_n(\boldsymbol{v}_h)]\{M_{nn}(\boldsymbol{u}_h)\}) \, \mathrm{d}\Gamma \, , \tag{5.24a}$$

$$b_s^i(\boldsymbol{u}_h, \boldsymbol{v}_h) = \int_{\Gamma_i^h} (\mu_D^c [\boldsymbol{v}_h] \cdot [\boldsymbol{u}_h]) \, \mathrm{d}\Gamma + \int_{\Gamma_i^h} (\mu_R^c [\theta_n(\boldsymbol{v}_h)][\theta_n(\boldsymbol{u}_h)]) \, \mathrm{d}\Gamma \, . \tag{5.24b}$$

Where Γ_i^h denotes the approximation of the i-th interface Γ_i. The penalty terms μ_D^c and μ_R^c, associated to the displacement and the rotation coupling conditions, respectively, have been introduced. Their choice is discussed together with their counterparts for boundary conditions in Sec. 5.2.4. $\{\bullet\}$ and $[\bullet]$ are the average and jump operators, defined as

$$\{\bullet\} = \gamma_2 \, \bullet^+ + (1 - \gamma_2) \, \bullet^- \, , \tag{5.25a}$$

$$[\bullet] = \bullet^+ - \bullet^- \, , \tag{5.25b}$$

where $\bullet$ denotes a generic quantity defined over both patches at the same point on the interface Γ_i. The superscript $+$ and $-$ are used to distinguish between the two patches. The parameters γ_1 and γ_2 are used to differentiate amongst the Nitsche type methods. Their meaning and effect on the stabilization of the method is discussed in Sec. 5.2.4. In this contribute, these are chosen as $\gamma_1 = 1$ and $\gamma_2 = 0.5$ that leads to a symmetric interior penalty formulation.

In this formulation, it is assumed that the curves in the Euclidean space describing the i-th interface are known explicitly. Consequently, the unit vector $\boldsymbol{t}$ tangent to the interface is also assumed to be known. $\boldsymbol{t}$ denotes the tangent vector to both the external boundaries of the patch and the interface between two patches. Moreover, since an interface is common to both the intersecting patches that generate it, the unit vector $\boldsymbol{t}$ is also the same for both patches. The context always makes it clear which condition is being referred to, whether a boundary or a coupling one. However, in the case of the coupling condition, the requirement of $\boldsymbol{t}$ to be oriented in a counter-clockwise direction is discarded, and whether the orientation is clockwise or counter-clockwise depends on the relative position between $\boldsymbol{t}$, $\boldsymbol{a}_3$, and $\boldsymbol{n}$ for each specific patch, being $\boldsymbol{n}$ the outer unit vector normal to the interface, lying on the plane locally tangent to the patch surface.

As a result, $\boldsymbol{n}^+$ and $\boldsymbol{n}^-$ can be different. In the simplest case, they lie in the same direction, either coinciding or being opposite. But, if the patches meet at an angle, their directions differ. The formulation presented in this thesis is capable of handling every possible case. However, in order to properly compute the average, the fluxes for the second patch (in contrast to the first patch) are obtained with respect to a normal vector entering the surface domain.

5.2.4 Choice of the parameters of the methods

In order to weakly enforce essential boundary and coupling conditions, various methods have been investigated in literature. In particular, different penalty and Nitsche's methods can be constructed based on the presence of Nitsche and/or stabilization terms, the

presence and the sign of the symmetry terms, and the definition of the average operator. The unified formulation proposed in [160] introduces the parameters γ_1 and γ_2, which allow for the construction of different Nitsche type methods. When no Nitsche terms are present in the formulation, the resulting method is the pure penalty [161, 96, 97, 98, 99, 101]. The symmetric interior penalty method [105, 106, 107, 111] is constructed adopting $\gamma_1 = 1$ and $\gamma_2 = 0.5$, requiring the introduction of penalty terms to ensure stability. The skew Nitsche's method [108] is obtained with $\gamma_1 = -1$ and $\gamma_2 = 0.5$ without adding stabilization terms. This choice leads to a skew-symmetric solving linear system and has the advantage of being parameter-free. Taking $\gamma_1 = -1$ and $\gamma_2 \neq 0.5$ leads to the weighted non-symmetric Nitsche's method [162, 163, 109, 110]. This method provides increased stability compared to other Nitsche's methods but at the expense of losing any symmetry of the linear system.

In pure penalty methods, which rely solely on penalty integrals, the choice of the penalty parameter can significantly impact the accuracy of the method, setting a lower bound on the achievable error corresponding to that particular value of the penalty parameter [101]. If the value is too low, it results in a weak enforcement of the boundary/coupling condition. Conversely, if the value is too high, it leads to ill-conditioning of the linear system and can induce spurious locking. When employing a Nitsche's method that includes the flux terms, the penalty terms are used solely for stabilization purposes. In this case, the minimum value of the penalty parameter required to achieve optimal convergence is lower than that needed for pure penalty methods, allowing for more flexibility in its selection.

In this work, the symmetric Nitsche terms defined in Eq.(5.18) and Eq.(5.24a) offer the advantage, compared to other Nitsche's methods, of resulting in symmetric positive-defined linear systems. This property can be beneficial in terms of computational efficiency, allowing the use of efficient algorithms for hermitian positive-defined matrices such as the one based on a Cholesky decomposition implemented in the MATLAB internal solver. For this method, the values of the penalty parameters can be bounded by solving an eigenvalue problem [164, 104, 165, 108]. However, this approach can significantly increase computational time and lead to high penalty parameters in some critical scenarios such as coupling of patches with different constitutive properties or when dealing with trimmed domains. In these cases, choosing a different value of γ_2 to compute the average of the fluxes can lead to a more stable formulation, as shown in [120], with the drawbacks of loosing symmetry of the linear system. Fortunately, for the symmetric Nitsche's method, penalty parameters that ensure optimal convergence while preserving a reasonable condition number of the system matrix span a wide range. In this thesis, the chosen approach takes advantage of this property and follows the recommendations already available in the literature for the choice of the penalty parameters. More sophisticated techniques to achieve stability follow out of the scope of this contribution.

To properly scale the penalty terms with respect to the problem parameters, a typical construction involves multiplying a problem-independent constant, a problem-dependent term, and a mesh-size-dependent term, that might be raised to a mesh-order-dependent power, accordingly to the problem at hand and the method adopted. Following [115], and extending the construction of the penalty parameters to interface coupling, the penalty

parameters are chosen as:

$$\mu_D^b = \mu_D^c = \beta E_l \tau / h \ , \tag{5.26a}$$
$$\mu_R^b = \mu_R^c = \beta E_l \tau^3 / h \ , \tag{5.26b}$$
$$\mu_3^b = \beta E_l \tau^3 / h^3 \ , \tag{5.26c}$$
$$\mu_C^b = \beta E_l \tau^2 / h^2 \ , \tag{5.26d}$$

where μ_D^b and μ_D^c are employed for displacement boundary and coupling conditions, respectively. Similarly, μ_R^b and μ_R^c are employed for rotation boundary and coupling conditions, respectively. The parameters μ_3^b and μ_C^b relate the component of the displacement vector along $\boldsymbol{a}_3$ at the boundaries and at the corners, respectively. The corresponding integrals to these last two penalty terms in Eq.(5.20) are proven to be necessary for achieving optimal convergence in [115]. In Eq.(5.26), E_l represents the maximum Young modulus of the laminate, and h is a measure of the mesh size. The problem-independent parameter β is taken here as either 10, 10^2, or 10^3 for all the penalty terms, as specified in the tests of Sec. 5.3. This choice helps balance the enforcement of the boundary/coupling conditions while maintaining a well-conditioned system.

5.3 Numerical Results for IGA coupling

In this section, the performances of the proposed method are evaluated through various numerical experiments on benchmark problems involving isotropic and laminated plates and shells. The structures in the proposed tests are loaded by domain forces and subjected to various boundary conditions, including homogeneous and non-homogeneous Dirichlet conditions. The application of these boundary conditions varies depending on the cases, with some being enforced in a strong manner, while others are applied weakly. When available, the numerical solution are compared with analytical ones. These are manufactured computing the applied domain force from the desired distribution of the displacement field by using the strong form of the Kirchhoff-Love shell equations, as presented in [115].

To what concerns software, the open-source MATLAB® library GeoPDEs [166, 167] is utilized, with additional functions implemented for the coupling. High-order integration over trimmed elements and their boundaries is achieved using the algorithm presented in [129, 121], which is based on a reparameterization of the trimmed elements.

As typical for immersed boundary approaches, a huge difference in element size can appear in certain refinement level of the discretization. If not treated properly, this problem could cause a severe ill-conditioning of the solving linear systems. To mitigate this issue, the approach used in this work is the utilization of a Jacobi preconditioner [168] that, despite its simplicity, has demonstrated remarkable efficacy. Additionally, it is worth mentioning that the proposed interior penalty formulation may lead to stability issues when using a fixed penalty parameter with small cut elements. As a possible solution the minimal stabilization method was proposed in [169] for trimmed IGA patches, however, no extension to KL equations is available in the literature. For KL shells, a more stable formulation would include skew-symmetric Nitsche coupling terms and non-symmetric average operator [162], resulting in non-symmetric linear systems, which is rather avoided in this work. However, no evident stability issues arose in the examples presented here.

The coupling strategy is tested on multi-patch geometries connected at non-conforming trimming interfaces with problems having an analytical solution. The convergence of the

proposed coupling strategy in the L^2 norm and H^1 seminorm is assessed by comparison with those obtained from single patch discretizations, which are considered as reference solutions. Furthermore, results involving a complex geometry of multiple intersecting laminated cylindrical shells showcase the method's potential for industrial problems.

5.3.1 Square Kirchhoff plate

In this test, the mechanical response of an isotropic plate structure is modeled using two trimmed planar patches coupled along a non-conforming interface. The main geometrical features of the structure are depicted in Fig.(5.1a) and the two patches for a specific refinement level are illustrated in Fig.(5.1b). The map of the shell is constructed to ensure that the lines of constant curvilinear coordinates are curved in the physical space, making in such way this example more significant.

To create a non-conforming interface, an additional knot is inserted in each patch, specifically $(0.5, 0.5)$ for the first patch and $(0.45, 0.53)$ for the second patch. After trimming both patches using the same trimming curve, which is also constructed to be curved in the physical domain, they are joined together. This configuration ensures that subsequent dyadic refinements of the discretization maintain the non-conforming nature of the coupling interface.

As a reference for efficiency comparison, Fig.(5.1c) displays the same structure modeled with a single patch, which corresponds to the untrimmed left patch of the multi-patch configuration. The material used for the analysis is characterized by a Young modulus $E = 70$ GPa and a Poisson ratio $\nu = 0.3$. The plate has a square mid-surface with an edge length $L = 1$ m and three values of the thickness are considered, namely $\tau = 0.1$ m, $\tau = 0.01$ m, and $\tau = 0.001$ m. Simply-supported boundary conditions are applied, with homogeneous displacements Dirichlet boundary conditions enforced in a strong manner along the entire external boundaries. A distributed surface force is applied in the direction $\boldsymbol{e}_3$ to reproduce the manufactured smooth solution:

$$\boldsymbol{u}_{\text{ref}} = U_0 \sin\left(\frac{2\pi x}{L}\right) \sin\left(\frac{2\pi y}{L}\right) \boldsymbol{e}_3 \,, \tag{5.27}$$

where $U_0 = 0.1$ m is the maximum absolute value of the displacement. Regarding the choice of the penalty parameters, the arbitrary coefficient in Eq.(5.26) is selected as $\beta = 10^2$.

In Fig.(5.2), the convergence behavior of L^2 norm and H^1 seminorm of the error for different polynomial values, plate thickness, and discretization approaches in the presented test case is illustrated. The dashed lines represent the convergence curves for the single-patch case, serving as a reference for optimal convergence relative to that specific polynomial order. The solid lines correspond to the interior penalty method discussed in Sec. 5.2.3, showing how accurately they follow the reference convergence curves. On the other hand, the dotted lines depict the convergence results for the pure penalty method, where only the stabilization terms in Eq.(5.24) are considered.

Consistently with the findings in [101], the pure penalty method fails to ensure optimal convergence due to the choice of the penalty parameters. Achieving optimal convergence with the pure penalty method would require super-penalization, where the penalty parameters scales with powers of the mesh size that depends on the order of the polynomials [103]. However, such high penalty values typically lead to ill-conditioning of the linear system, especially for high-order polynomials. This underscores the advantage of

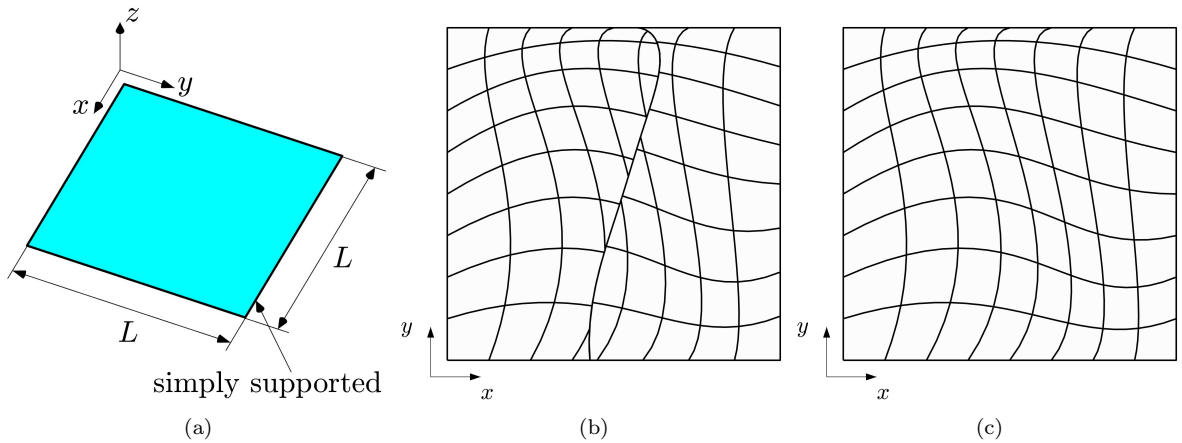

(a) (b) (c)

Figure 5.1: Geometry of the Kirchhoff plate described in Sec. 5.3.1 (a). Discretization of the plate employing two non-conforming IGA patches (b) and a single IGA patch (c).

the interior penalty method, which achieves accurate convergence without facing severe ill-conditioning issues and therefore ensuring accurate results without compromising numerical stability, although some locking phenomena can still be observed in the curves for $p = 2$ and $p = 3$ when $\tau = 0.001$ m. The triangles in the graphs show the optimal convergence rates expected for the Kirchhoff-Love theory [115]. It is worth noting that, consistently with the expected theoretical prediction [115, 159], in our results the optimal convergence rate in L^2 norm for $p = 2$ is equal to p and not $p + 1$.

As a final observation, Fig.(5.3) depicts the plate's bent structure. The mesh lines and the contour of the displacement vector's magnitude are presented superimposed on the deformed surface of the plate. It is important to note that some of the lines in the image are merely used to visualise trimmed elements and do not actually delimit any actual elements.

The geometry depicted in Fig.(5.1a) is also utilized for conducting a laminate test, with its multi-patch and single-patch configurations presented in Fig.(5.4). In the multi-patch discretization, a knot is inserted in the position $(0.5, 0.5)$ for the left patch and $(0.45, 0.53)$ for the right one. The laminate is constructed using orthotropic laminae with the following properties: longitudinal Young's modulus $E_1^{\langle \ell \rangle} = 25$ GPa, transversal Young's modulus $E_2^{\langle \ell \rangle} = 1$ GPa, Poisson's ratio $\nu_{12}^{\langle \ell \rangle} = 0.25$, shear modulus $G_{12}^{\langle \ell \rangle} = 0.4$ GPa and thickness $\tau^{\langle \ell \rangle} = 0.0025$ m. The lamination sequence employed is $[0, 90]_s$. The boundary conditions are identical to those of the isotropic case, while the force applied to the shell surface is modified in order to manufacture the distribution of the displacement in Eq.(5.27) with the different material properties. The L^2 and H^1 convergence curves for this laminated test are depicted in Fig.(5.5). Similar to the isotropic case, the observations regarding the convergence properties of the methods investigated hold true also in this scenario.

5.3.2 Hyperbolic paraboloid Kirchhoff-Love shell

The second set of numerical experiments focuses on a curved isotropic shell with a mid-surface represented by a hyperbolic paraboloid. This example is derived from the shell obstacle course introduced in [115], which offers a collection of tests having analytical solutions. These tests serve as an appropriate benchmark to assess the performance of the proposed coupling method by evaluating the convergence curve based on the L^2

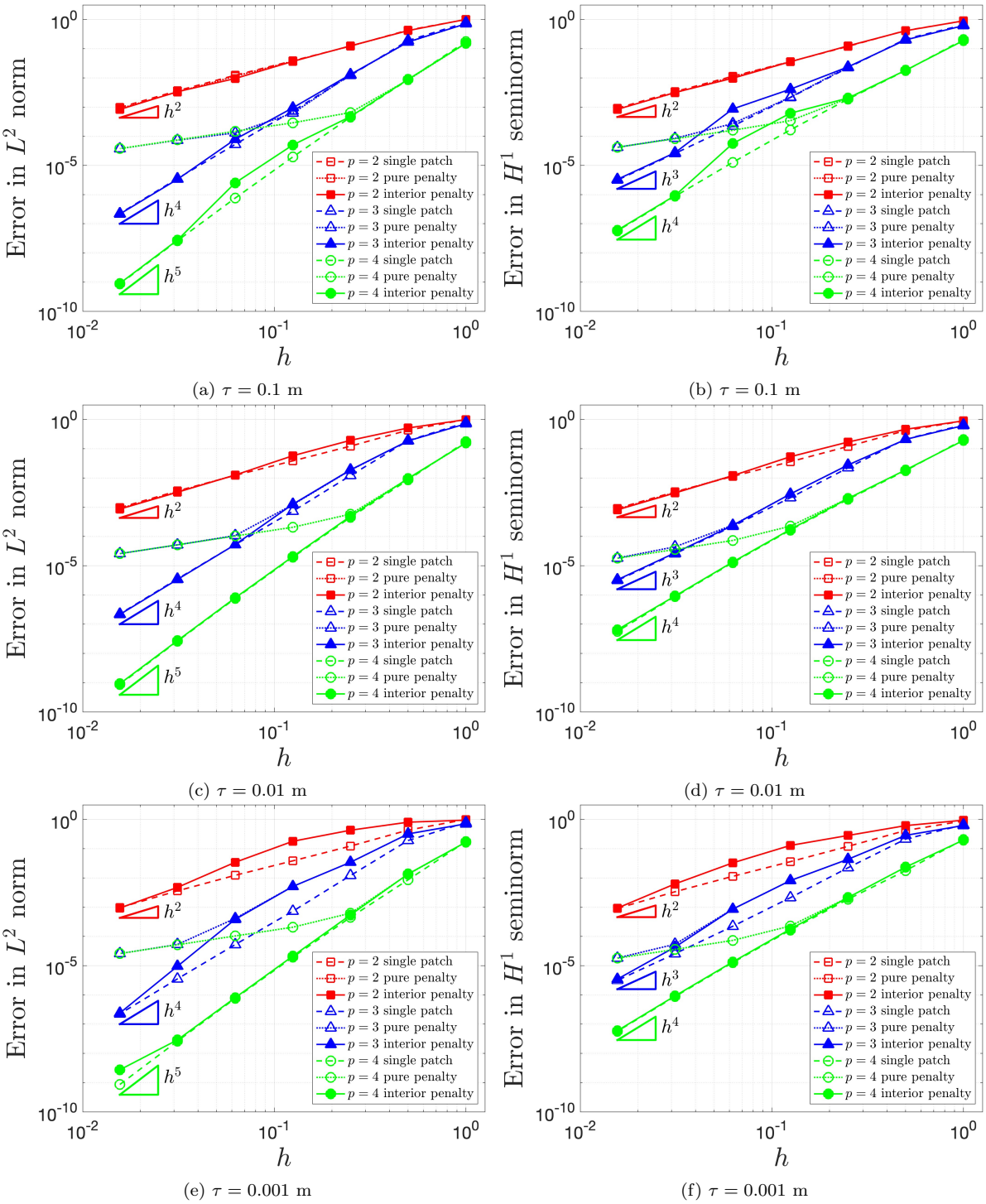

(a) $\tau = 0.1$ m (b) $\tau = 0.1$ m

(c) $\tau = 0.01$ m (d) $\tau = 0.01$ m

(e) $\tau = 0.001$ m (f) $\tau = 0.001$ m

Figure 5.2: L^2 convergence (a), (c) and (e), and H^1 convergence (b), (d), and (f) associated with the Kirchhoff plate shown in Sec. 5.3.1, for different values of the thickness τ.

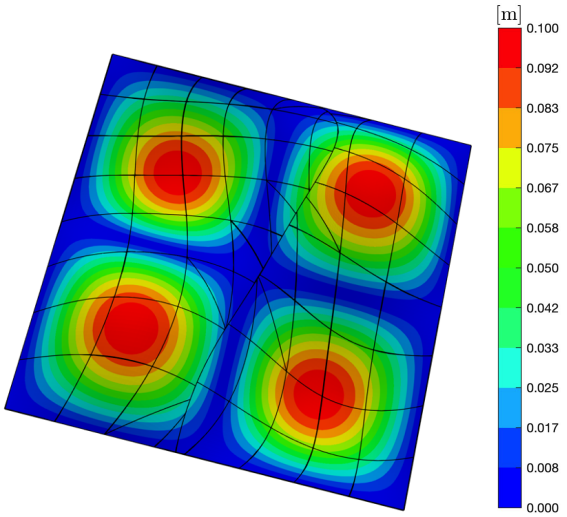

Figure 5.3: Deformed configuration for the plate in in Fig.(5.1a) with superimposed contour of the magnitude of the displacements and mesh elements.

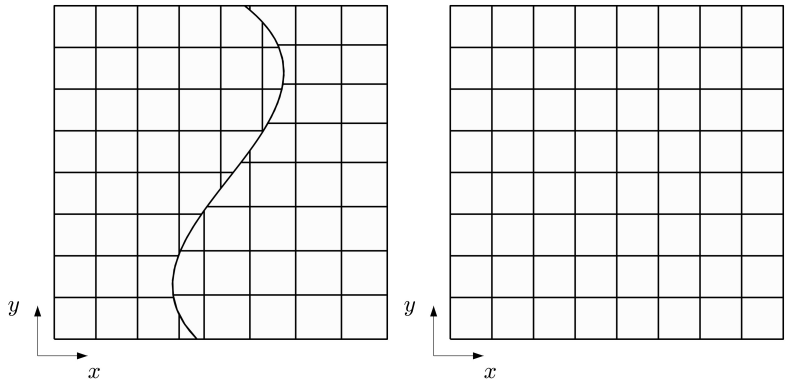

(a) (b)

Figure 5.4: Discretization of the Kirchhoff laminate in a non-conforming multi-patch (a) and a single-patch (b) setting.

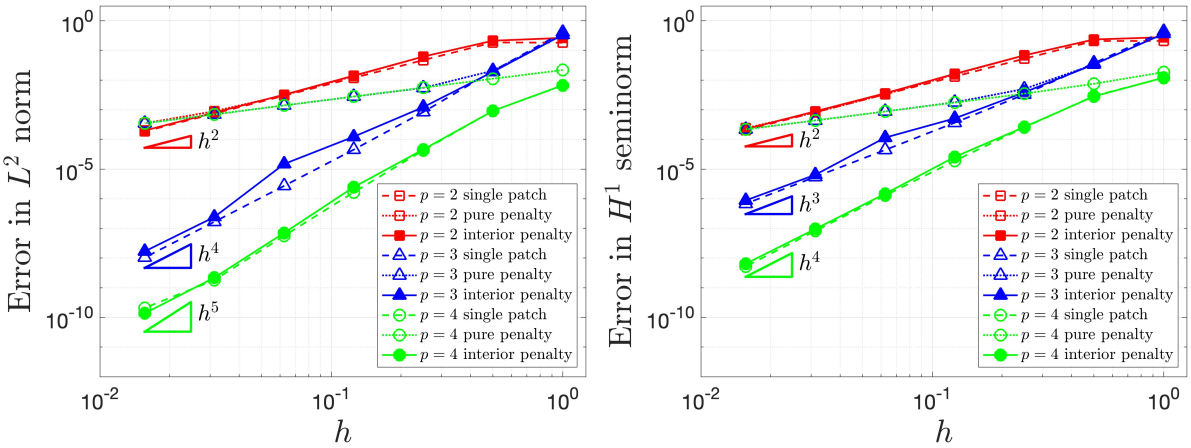

(a) $\tau = 0.01$ m (b) $\tau = 0.01$ m

Figure 5.5: L^2 norm convergence (a) and H^1 seminorm convergence (b) correspondent to the Kirchhoff laminate.

norm of the solution error. This allows for a rigorous evaluation of the accuracy and convergence properties of the coupling approach.

In this test, three values of the shell thickness are taken into account $\tau = 0.1$ m, $\tau = 0.01$ m, and $\tau = 0.001$ m, and the complete definition of the mid-surface can be found in [115]. However, for a better understanding, the geometry of the shell and the coordinates of the vertices are illustrated in Fig.(5.6a). The material is isotropic with a Young's modulus of $E = 70$ GPa and a Poisson ratio of $\nu = 0.3$. The shell is subjected to non-homogeneous Dirichlet boundary conditions that for the displacement are enforced strongly assigning values directly to the degrees of freedom after the L^2 projection of the displacement field in the spline space of the corresponding edges. Conversely, the bending rotation corresponding to the reference displacement field is weakly imposed at the boundary using the interior penalty method described in Sec. 5.2.3, using in Eq.(5.24) only the terms corresponding to the bending rotation. The boundary conditions and the domain force are chosen to manufacture the reference displacement field:

$$\boldsymbol{u}_{\text{ref}} = U_0 \xi_2 \sin\left(\frac{\pi}{2}\xi_2\right)\boldsymbol{e}_1 + U_0 \xi_2 \sin\left(\frac{\pi}{2}\xi_2\right)\boldsymbol{e}_2, \tag{5.28}$$

where $U_0 = 1$ m. Similarly to the previous test, the shell is modeled using a two-patch configuration (see Fig.(5.6b)) as well as a single patch configuration (see Fig.(5.6c)) which serves as a reference for the convergence curves. To make the two patches in the multi-patch configuration non-conforming at the interface, a knot is inserted in each patch at the curvilinear coordinates $(0.5, 0.5)$ and $(0.54, 0.43)$, respectively. In such way, even after subsequent dyadic refinements of the discretization, the non-conforming nature of the interface is maintained.

Fig.(5.7) shows the L^2 convergence for the proposed test, considering different values of the shell thickness, the parameter β that appears in the penalty terms in Eq.(5.26), the polynomial order, and the approximation approach. Three different approaches are compared: a single-patch, a two-patch configuration coupled through a pure penalty method, and a two-patch configuration coupled through the interior penalty method. It can be observed that the curves corresponding to the interior penalty approach closely follow the convergence of the reference curve for the single patch. In contrast, the pure penalty method exhibits poor performance when the penalty value is small and not properly scaled with the mesh size. Once again, it is important to note that the scaling required for the pure penalty approach to achieve optimal convergence leads to premature ill-conditioning of the linear system for high-order polynomial values. However, due to the combination of trimming and high-degree polynomials also in the case of the interior penalty coupling a too high condition number of the linear system is obtained for the last refinement level of the curves corresponding to $p = 4$ and, as a result, convergence is lost. Constructing a preconditioner more efficient than the simple Jacobi one would be beneficial to solve this issue. Despite this would constitute an interesting direction for further research, it falls outside the scope of this work.

Another noteworthy observation is that higher values of β result in increased errors for the interior penalty method. This effect is expected since the non-conforming nature of the coupling interface leads to a locking effect due to the stabilization terms in the integrals in Eq.(5.24b). In fact, the discrete approximation spaces of the displacement fields for the two patches are unable to perfectly match at the interface for non-trivial distribution, causing spurious locking phenomena. Further increasing the penalty exacerbates this issue.

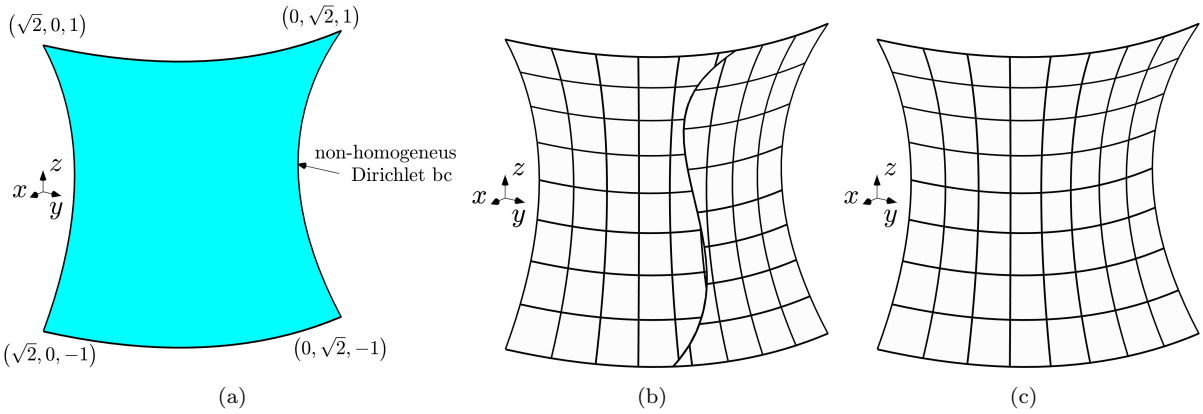

Figure 5.6: Geometry of the hyperbolic paraboloid described in Sec. 5.3.2 (a). Discretization of the shell employing two non-conforming IGA patches (b) and a single IGA patch (c), shown for a certain refinement level.

It is worth noting that the proposed method still achieves optimal convergence rates for a wide range of thickness values. However, it is important to highlight that the Kirchhoff-Love shell equation may not be suitable for thickness ratios that are too high. In such cases, higher-order theories should be employed to accurately capture the behavior of the shells.

Lastly, for the sake of completeness, in Fig.(5.8) it is shown the contour of the magnitude of the displacement vector superimposed to the shell mid-surface, together with the mesh edges. However, it should be noted that some of the lines are only utilised for visualization purposes of reparameterized trimmed elements but do not correspond to actual edges.

5.3.3 Coupling of intersecting cylindrical shells

The final test aims to demonstrate the efficiency and robustness of the proposed method, as well as the effectiveness of the trimming and coupling algorithms. This test involves a geometry with a complexity level comparable to that encountered in real-world industrial applications, consisting of multiple patches intersecting at variable angles. The structure under investigation consists of five intersecting cylinders, as depicted in Fig.(5.9a). The main cylinder has a length of $L = 8$ m and a radius of $R = 1$ m, while the remaining cylinders have an untrimmed length of $L = 4$ m and a radius of $R = 0.8$. The complete geometrical description of the structure is not provided here for the sake of conciseness.

Figs.(5.9b) to (5.9f) illustrate the trimmed parametric domains of the corresponding cylindrical patches in Fig.(5.9a). It is noteworthy that the intersecting curves, both in the physical and parametric domains, consist of multiple segments connected in general with C^0 continuity. For such geometric configurations, the robustness of the algorithm for identifying quadrature points with high-order precision becomes crucial.

The cylinders in the structure are simply-supported at the external edges, and the structure is subjected to a uniformly applied domain traction given by $\tilde{\boldsymbol{F}} = \{10^5, 10^5, 10^5\}^T$ Pa. The material used is a laminate with layers made of the same orthotropic material as described in Sec. 5.3.1, with a thickness of $\tau^{\langle \ell \rangle} = 0.0025$ m, and lamination sequence $[90, 0, 0, 90]$;

In each patch, the continuity along the circumferential directions between the edges corresponding to the first and last values of the knot vector is enforced here using periodic

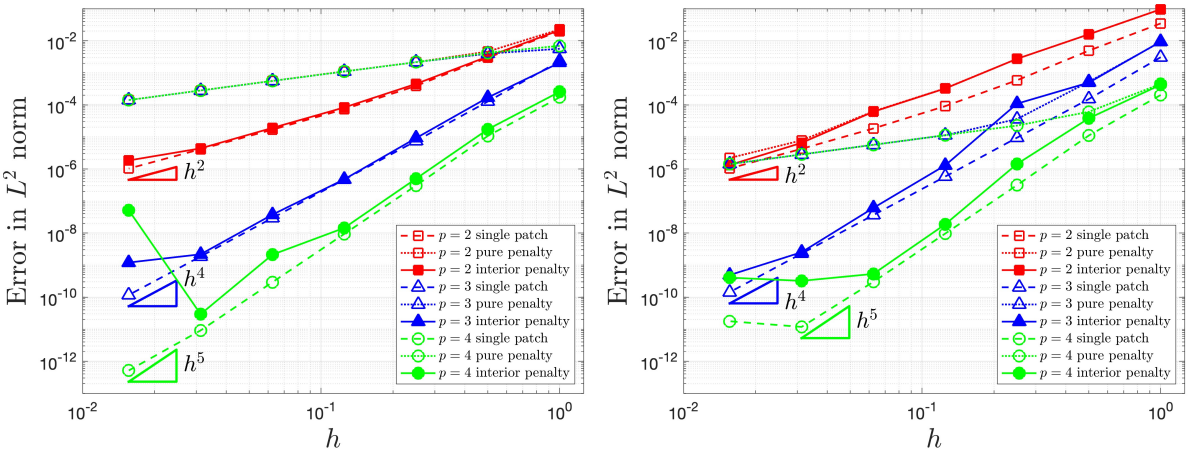

(a) $\beta = 10$, $\tau = 0.1$ m

(b) $\beta = 10^3$, $\tau = 0.1$ m

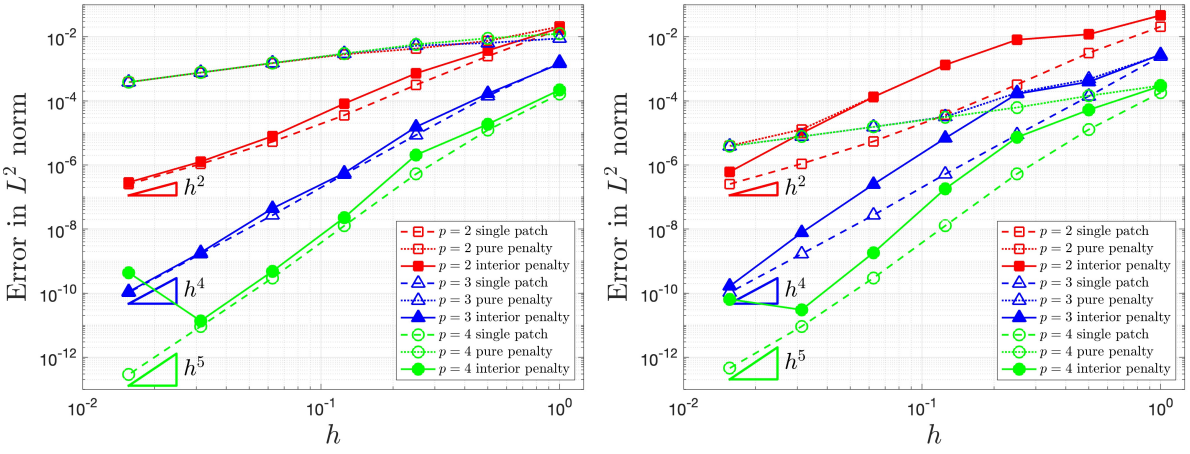

(c) $\beta = 10$, $\tau = 0.01$ m

(d) $\beta = 10^3$, $\tau = 0.01$ m

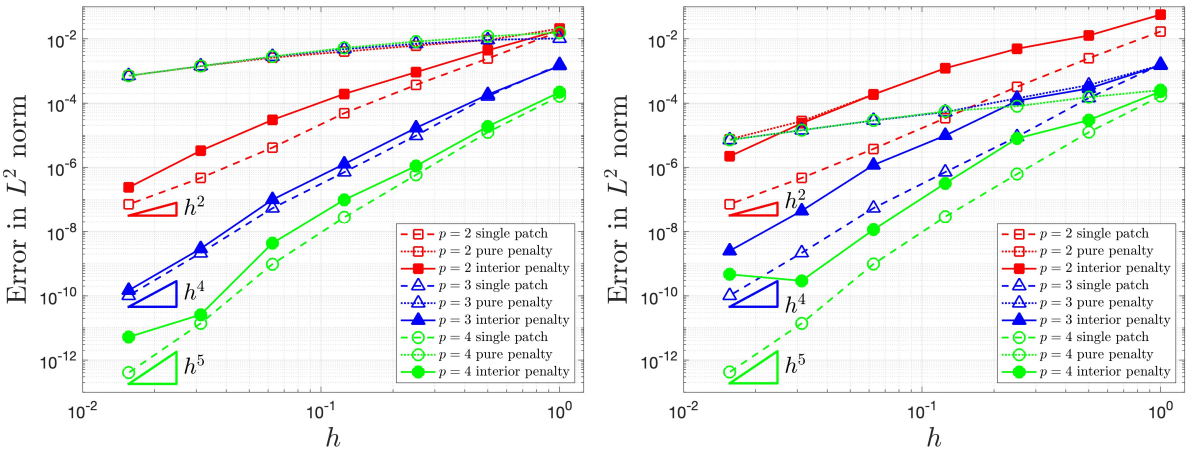

(e) $\beta = 10$, $\tau = 0.001$ m

(f) $\beta = 10^3$, $\tau = 0.001$ m

Figure 5.7: L^2 convergence associated with the shell shown in Fig.(5.6a), for different values of the thickness τ and arbitrary parameter β.

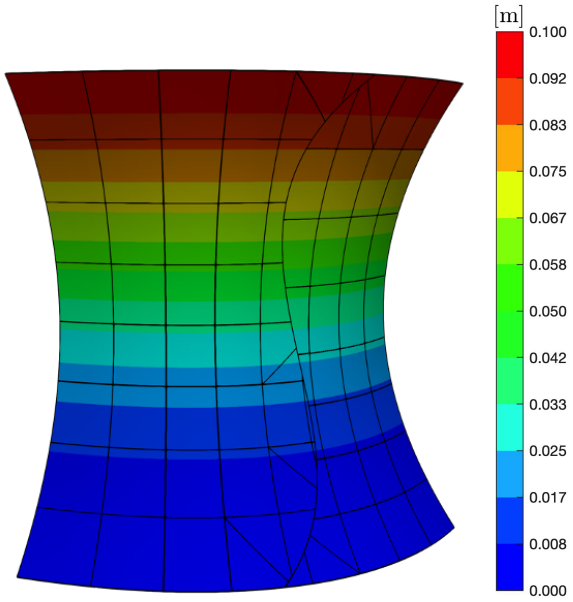

Figure 5.8: Undeformed configuration for the shell in in Fig.(5.6a) with superimposed contour of the magnitude of the displacements and mesh elements.

boundary conditions obtained adopting periodic spline spaces [127]. It is worth noting that along these edges, a weak imposition of the coupling condition could also be applied by considering an interface with both edges coming from the same patch. However, using periodic boundary conditions allows for a reduction in the overall number of degrees of freedom in the analysis. The cylindrical patches meet at interfaces with non-zero angles, and the proposed formulation can easily manage this, as it is not limited to G^1 surfaces. The polynomial degree used for each patch in each direction is $p = 6$, that can be easily adopted thanks to the straightforward construction of B-spline basis functions. It is worth mentioning that to properly integrate in the trimmed elements and their respective boundaries nine Gaussian points were adopted in each direction.

Fig.(5.10) presents the contour plot of the magnitude of the displacement from two different views. The results obtained using the formulation described in this thesis (a) and (b) are compared with those obtained using triangular elements (STRI3) in the Abaqus® software [26], (c) and (d). The close agreement between the two approaches highlights the competitiveness of the proposed method with the available finite element software, affirming its accuracy and reliability even for complex geometries consisting of patches intersecting at a variable angle.

5.4 The immersed boundary conformal method for IGA shells

The method presented so far allows one to study trimmed surfaces, which increases the flexibility in defining the shell surface while retaining the simplicity of an embedded approach. However, two main issues arise when dealing with trimmed boundaries:

i) Dirichlet boundary conditions can only be applied in a weak sense on the trimmed boundaries.

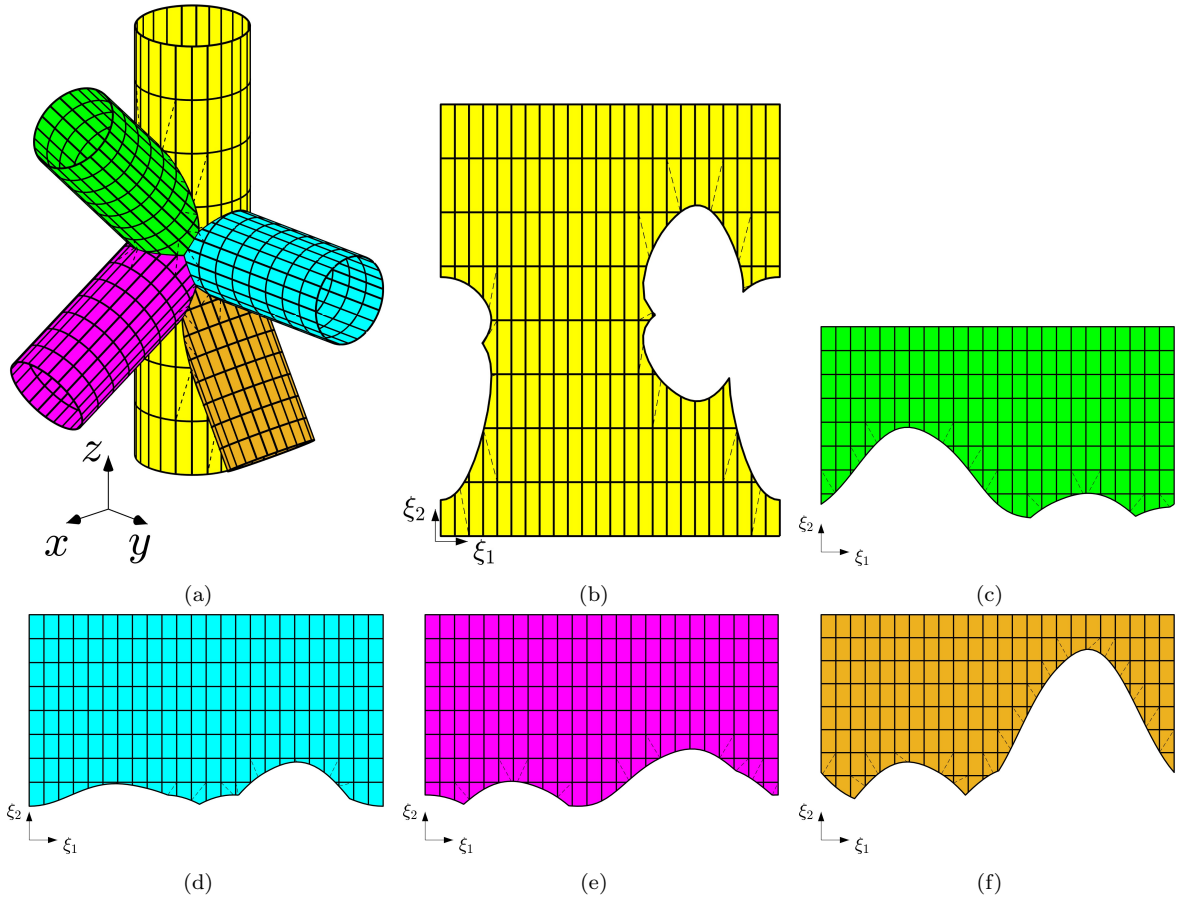

Figure 5.9: Geometry of the test described in Sec. 5.3.3 with superimposed mesh (a). Parametric domain of each of the trimmed patches (b) to (f).

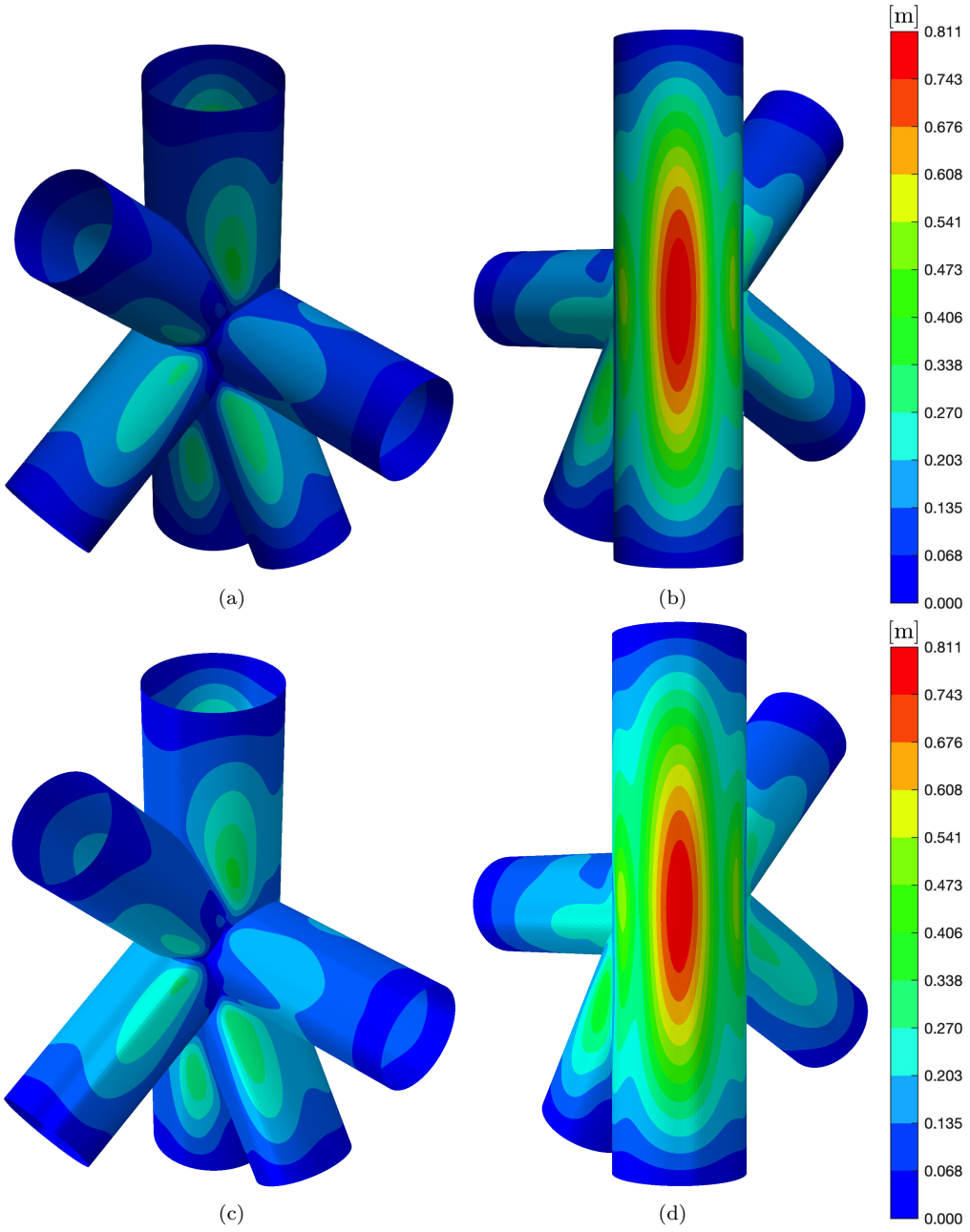

Figure 5.10: Two different views of the contour of the magnitude of the displacement for the structure described in Sec. 5.3.3 obtained with the method presented here (a) and (b), and with the elements STRI3 in Abaqus® (c) and (d).

ii) Increasing the resolution at the surface boundary, where localized phenomena tend to occur, is not straightforward.

To model localized behavior, such as stress concentration, one possible strategy involves using H-splines [170]. This approach, however, still requires a weak imposition of essential boundary conditions. An alternative approach is the Immersed Boundary Conformal Method (IBCM), which was recently proposed in the context of IGA in [121], where it is applied to Poisson's problems and two-dimensional linear elasticity problems. This approach involves creating auxiliary boundary conforming layers with the advantages of a strong enforcing of Dirichlet boundary conditions, and a natural refinement strategy near the boundaries. These boundary layers are then coupled in a weak way with the main patch in a region further inside the domain where localized phenomena are less likely to occur. Here, the IBCM is extended for the first time to the KL shell equations. In the following section, the details on how to create these boundary layers are provided together with some preliminary applications to demonstrate the efficiency of this approach.

5.4.1 Construction of boundary conforming patches

It is reminded that the parametric domain and its boundary are denoted as $\hat{\Omega}$ and $\partial\hat{\Omega}$, respectively. It is assumed that a trimming approach is used in the definition of shell surface, and therefore $\partial\hat{\Omega}$ is constructed as

$$\partial\hat{\Omega} = \bigcup_{i=1}^{N_\Gamma} \hat{\Gamma}^{[i]'} \ . \tag{5.29}$$

Here, N_Γ represents the number of curves involved in defining $\partial\hat{\Omega}$. It is assumed here, without loss of generality, that each of the curves $\hat{\Gamma}^{[i]'}$ is described as a closed univariate B-splines in $\mathbb{R}^2$ using the auxiliary coordinate $\tau^{[i]} \in [0,1]$, meaning that $\hat{\Gamma}^{[i]'} = \hat{\Gamma}^{[i]'}(\tau^{[i]})$. Then, for each $\hat{\Gamma}^{[i]'}$, an offset curve $\hat{\Gamma}^{[i]}$ is constructed in a region more internal to the parametric domain using the same curvilinear coordinates $\tau^{[i]}$. Although a detailed description of the offset curve's construction is not provided here, various approaches can be adopted. For example, one can create a curve that approximates a uniform distance condition from the main one or opt for a simpler curve with an easier definition that does not necessarily follow the geometrical features of the boundary. However, as demonstrated in [121], this choice does not significantly affect the accuracy of the method.

The boundary layers are created as ruled domains $\hat{\Omega}^{[i]} \in \mathbb{R}^2$ using the algorithm described in [127], taking as generating curves $\hat{\Gamma}^{[i]}(\tau^{[i]})$ and $\hat{\Gamma}^{[i]'}(\tau^{[i]})$. Accordingly, two auxiliary coordinates are introduced: $\eta_1^{[i]} = \tau^{[i]}$ that follows the boundary curve direction, and $\eta_2^{[i]} \in [0,1]$ that goes along the offset direction. The map of the i-th boundary layer from $\tilde{\Omega}^{[i]}$ to $\hat{\Omega}^{[i]}$ is

$$\boldsymbol{\xi} = \boldsymbol{\xi}^{[i]}\left(\eta_1^{[i]}, \eta_2^{[i]}\right) \tag{5.30}$$

where $\boldsymbol{\xi} = \{\xi_1, \xi_1\}^\intercal$ are the curvilinear coordinates of the main patch, and $\tilde{\Omega}^{[i]} = [0,1] \times [0,1]$. Figs.(5.11a), (5.11c), and (5.11e) show the step-by-step construction of the boundary layers in the parametric domain. The untrimmed reference domain $\hat{\Pi}_0$ is shown in Fig.(5.11a), which is then trimmed into $\hat{\Omega}$ in Fig.(5.11b) by defining the external boundary and introducing an internal cut-out. Finally, following the procedure described above, two boundary layers are introduced in Fig.(5.11c).

The parametric domain of the main patch (restricted by the contruction of the boundary layers) and its boundary are finally redefined as

$$\hat{\Omega}^{[0]} = \hat{\Omega} \setminus \bigcup_{i=1}^{N_\Gamma} \hat{\Omega}^{[i]} \,, \tag{5.31}$$

$$\partial\hat{\Omega}^{[0]} = \bigcup_{i=1}^{N_\Gamma} \hat{\Gamma}^{[i]} \,. \tag{5.32}$$

5.4.2 Composition of maps

To describe the boundary layers in Euclidean space, the maps in Eq.(5.30) need to be composed with the map of the main patch. Therefore, for the i-th boundary layer the mapping from $\tilde{\Omega}^{[i]}$ to $\Omega^{[i]}$ is obtained as

$$\boldsymbol{x}_0\left(\eta_1^{[i]}, \eta_2^{[i]}\right) = \boldsymbol{x}_0(\xi_1, \xi_2) \circ \boldsymbol{\xi}^{[i]}\left(\eta_1^{[i]}, \eta_2^{[i]}\right) \,. \tag{5.33}$$

Figs.(5.11b), (5.11d), and (5.11f) show the different steps in the construction of the boundary layers in the Euclidean space. It is worth mentioning that, for the construction adopted here, the curves $\hat{\Gamma}^{[i]}$ that constitute the boundaries of $\partial\hat{\Omega}^{[0]}$ are mapped into the interfaces Γ_i between the main patch $\Omega^{[0]}$ and the boundary layers $\Omega^{[i]}$ in Euclidean space.

The KL formulation adopted in this work requires the derivatives of the map up to the third order. As such, for the sake of completeness, these derivatives are reported here

$$\frac{\partial \boldsymbol{x}_0}{\partial \eta_\alpha} = \frac{\partial \boldsymbol{x}_0}{\partial \xi_\lambda}\frac{\partial \xi_\lambda}{\partial \eta_\alpha} \,, \tag{5.34a}$$

$$\frac{\partial^2 \boldsymbol{x}_0}{\partial \eta_\alpha \partial \eta_\beta} = \frac{\partial^2 \boldsymbol{x}_0}{\partial \xi_\lambda \partial \xi_\mu}\frac{\partial \xi_\lambda}{\partial \eta_\alpha}\frac{\partial \xi_\mu}{\partial \eta_\beta} + \frac{\partial \boldsymbol{x}_0}{\partial \xi_\lambda}\frac{\partial^2 \xi_\lambda}{\partial \eta_\alpha \partial \eta_\beta} \,, \tag{5.34b}$$

$$\begin{aligned}\frac{\partial^3 \boldsymbol{x}_0}{\partial \eta_\alpha \partial \eta_\beta \partial \eta_\gamma} = &\frac{\partial^3 \boldsymbol{x}_0}{\partial \xi_\lambda \partial \xi_\mu \partial \xi_\nu}\frac{\partial \xi_\lambda}{\partial \eta_\alpha}\frac{\partial \xi_\mu}{\partial \eta_\beta}\frac{\partial \xi_\nu}{\partial \eta_\gamma} + \frac{\partial^2 \boldsymbol{x}_0}{\partial \xi_\lambda \partial \xi_\mu}\frac{\partial^2 \xi_\lambda}{\partial \eta_\alpha \partial \eta_\gamma}\frac{\partial \xi_\mu}{\partial \eta_\beta} + \frac{\partial^2 \boldsymbol{x}_0}{\partial \xi_\lambda \partial \xi_\mu}\frac{\partial \xi_\lambda}{\partial \eta_\alpha}\frac{\partial^2 \xi_\mu}{\partial \eta_\beta \eta_\gamma} + \\ &+ \frac{\partial^2 \boldsymbol{x}_0}{\partial \xi_\lambda}\frac{\partial^2 \xi_\lambda}{\partial \eta_\alpha \partial \eta_\beta}\frac{\partial \xi_\mu}{\partial \eta_\gamma} + \frac{\partial \boldsymbol{x}_0}{\partial \xi_\lambda}\frac{\partial^3 \xi_\lambda}{\partial \eta_\alpha \partial \eta_\beta \partial \eta_\mu} \,,\end{aligned} \tag{5.34c}$$

where the superscript $[i]$ of the auxiliary curvilinear variables $\eta_1^{[1]}$ and $\eta_1^{[2]}$ has been discarded to enhance readability. It is important to mention that for the boundary layers, the definition of the space for the trial and test functions remains the same as presented in Eq.(5.4), except that in this case, the map $\boldsymbol{\mathcal{F}}$ is now obtained as a composition of two maps, and the bivariate B-splines are defined as function of $\eta_1^{[1]}$ and $\eta_1^{[2]}$ in the domain $\tilde{\Omega}^{[i]}$. Therefore, for these auxiliary patches, the isoparametric concept of using the same spline space for both geometry description and trial function definition is discarded. One might argue that this approach deviates from the principles of IGA. The author acknowledges this concern. However, he believes that the advantages offered by the creation of arbitrarily refinable conforming boundary layers outweigh this drawback and deserves further investigation.

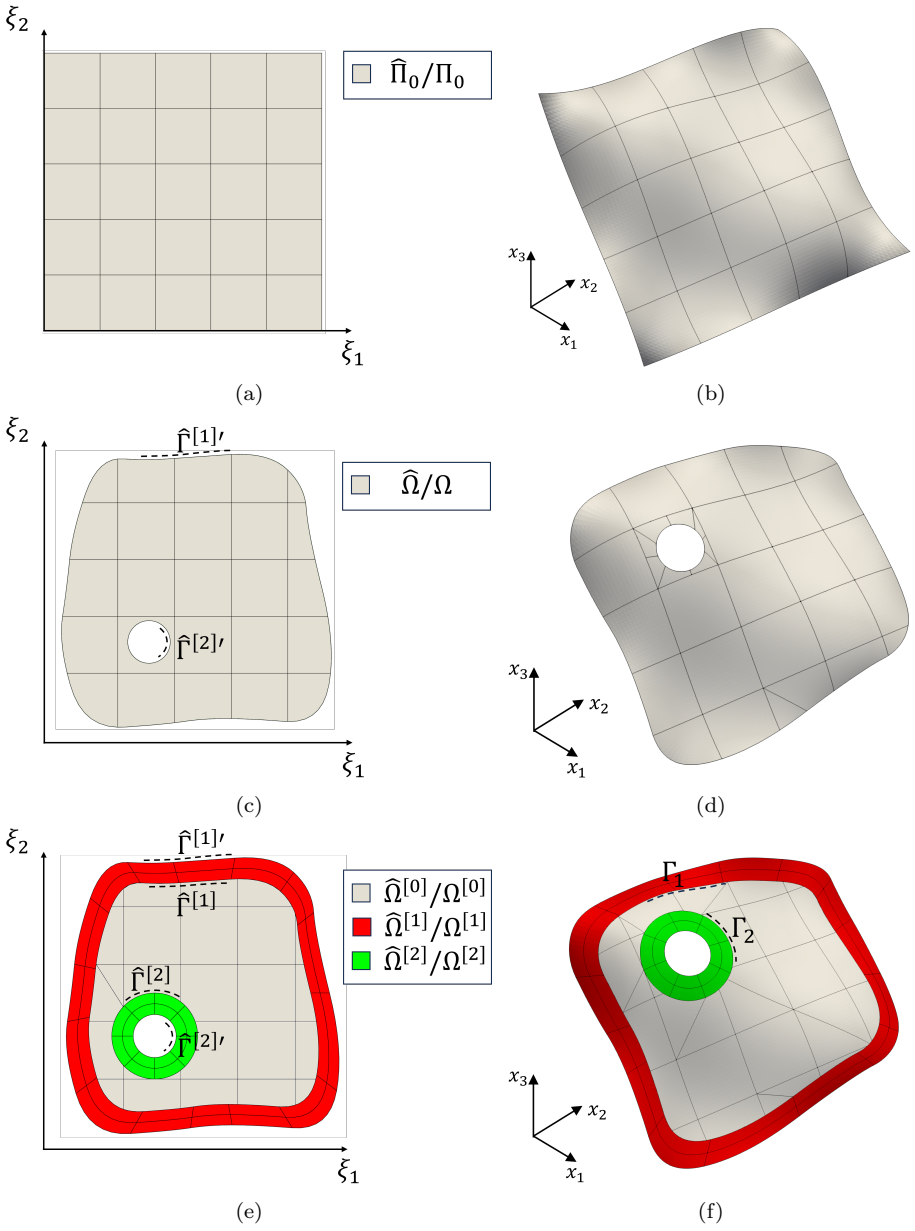

Figure 5.11: Step-by-step construction of the boundary layers in the parametric domain $\hat{\Omega}$ (a), (c), and (e), and correspondent mapping in the Euclidean space (b), (d), and (f). Untrimmed reference domain $\hat{\Pi}_0$ (a) and correspondent untrimmed surface Π_0 (b). Parametric domain $\hat{\Omega}$ (c) and shell surface Ω (d), obtained trimming the reference domain Π_0 with the curves $\hat{\Gamma}^{[1]\prime}$ and $\hat{\Gamma}^{[2]\prime}$. New parametric domain of the main patch $\hat{\Omega}^{[0]}$ and boundary layers $\hat{\Omega}^{[1]}$ and $\hat{\Omega}^{[2]}$ obtained as ruled domains from $\hat{\Gamma}^{[1]\prime}$ and $\hat{\Gamma}^{[1]}$, and $\hat{\Gamma}^{[2]\prime}$ and $\hat{\Gamma}^{[2]}$ (e). Corresponding patches $\Omega^{[0]}$, $\Omega^{[1]}$, and $\Omega^{[2]}$ in the Euclidean space with interfaces between patches denoted as Γ_1 and Γ_2 (e).

5.5 Numerical results for the IBCM

In this section, various applications of the IBCM are conducted to showcase the method's efficiency. These tests can be divided into three sets: i) a set involving a plate with a pseudo cut-out, constructed in such a way to retain an analytical solution to rigorously assess the convergence of the error; ii) a set involving structures with multiple cut-outs where displacement boundary conditions can imposed strongly through the construction of boundary layers; iii) a case involving two intersecting cylindrical shells that are coupled through boundary layers conforming at the interface.

5.5.1 Square Kirchhoff plate with pseudo cut-outs

The first series of tests for the IBCM involves a square Kirchhoff plate as shown in Fig.(5.12). The geometry, loads, and boundary conditions for these tests are the same as those described in Sec. 5.3.1. In particular, the applied distributed force is tailored to replicate the analytical solution presented in Eq.(5.27). However, homogeneous displacement boundary conditions to model a simply-supported scenario are applied here in a weak sense. The plate's mapping is achieved using a bivariate B-spline through the following steps: i) a simple identity map is initially created with a spline of degree $p = 3$; ii) a knot is inserted at the position (0.29, 0.31); iii) the positions of the internal control points are changed. In such way, the parametric domain in Fig.(5.12a) is mapped into the plate surface in Fig.(5.12b). This description of the plate doesn't alter the surface Ω but introduces two lines $\xi_1 = 0.29$ and $\xi_2 = 0.31$ with reduced continuity C^2 on its map.

Two pseudo cut-outs are created. These cut-outs are referred to as pseudo because they are filled with auxiliary patches, eliminating the need to impose essential boundary conditions within the internal boundaries and easily retrieving the analytical solution. For each of them two patches are created in the parametric domain: a ring-shaped one having center in (ξ_{1C}, ξ_{2C}) that extend from an internal radius R_{int} to an external one R_{ext}, and a second patch internal to the pseudo cut-out and trimmed in a circular shape thought the internal circle that delimits the correspondent ring-shaped patch. Tab.(5.1) reports the values for the construction of the additional patches for the analysis. Fig.(5.12b) shows how the shape of the patches is modified by the composition with the map of the main patch.

The contour plot in Fig.(5.12c) shows the magnitude of the non-dimensional displacement $|\overline{u}_3| = |u_3/U_0|$, with superimposed mesh grid from the discretization in Fig.(5.12b). Fig.(5.12d) displays the same contour with the shell's deformed configuration. Both images demonstrate the smoothness of the solution at the interfaces between patches, with no artifacts introduced by the discretization.

To demonstrate that this discretization does not affect the analysis's convergence properties, Fig.(5.13) illustrates the convergence of the error in L^2 norm and H^1 seminorm. The curves are plotted for different values of the penalty parameter and for varying degrees of the spline, p. The value of h is computed as $1/2^s$, where $s = 0, 1, 2, \ldots$ denotes the dyadic refinement level, and is used as a measure of the mesh size. For reference, each curve also includes the convergence for a discretization involving only the primary patch. It is worth noting that the convergence curves for the single patches are still influenced by the penalty parameter due to the weak imposition of boundary conditions. The results indicate that the convergence curves for the chosen discretization closely follow the reference one.

Table 5.1: Values for defining the auxiliary cut-out patches in the parametric domain of the main patch as described in Sec. 5.5.1.

ξ_{1C}	ξ_{2C}	R_{int}	R_{ext}
0.25	0.250	0.08	0.20
0.75	0.750	0.08	0.20

It is wort saying that the map due to the composition of $\boldsymbol{x}_0(\xi_1, \xi_2)$ and $\boldsymbol{\xi}^{[i]}\left(\eta_1^{[i]}, \eta_2^{[i]}\right)$, lines with reduced continuity appear across the domain of some elements of the auxiliary patches. For this reason, the error in L^2 norm is expected in the asymptotic regime to converge with rates associated with the maximum continuity of the map, meaning $p = 2$ in this case, even for higher degree of the elements. However, the convergence analysis results demonstrate that, in the pre-asymptotic regime, the rate of convergence is comparable to the reference one achieved with a single patch with the same polynomial degree.

5.5.2 Plate and shell with multiple cut-outs

The next geometry investigated is a plate, as shown in Fig.(5.14a), characterized by a parametric space consisting of a main patch and five additional boundary ring-shaped layers. Their respective center coordinates, internal, and external radii are provided in Tab.(5.2).

The mapping is constructed using a bivariate B-spline that reproduces the equations: $x_{10} = \xi_1 L$, $x_{20} = 2\xi_2 L$, and $x_{30} = 0$, where $L = 1$ m resulting in the plate shown in Fig.(5.14b). The shell section has a thickness of $\tau = 10$ cm and is made of an isotropic material with a Poisson's ratio of $\nu = 0.3$ and a Young modulus of 100 GPa;

The external boundaries of the main patch are subjected to simply-supported boundary conditions, $\overline{\boldsymbol{u}} = \boldsymbol{0}$. On the internal boundary of the cut-outs, a uniform displacement in the x_3 direction is applied. The values of the applied displacement for each patch are reported in the last column of Tab.(5.2). It is important to note that, thanks to the construction of the boundary conforming patches, the displacement boundary conditions can be applied in a strong sense in this test. Figs.(5.15a) and (5.15b) display the plate's undeformed configuration with superimposed discretization and the deformed configuration with superimposed contour of the magnitude of the displacement, respectively. It is evident that the solution is smooth, and no artifacts are introduced by the boundary layers.

In Fig.(5.15c), the geometry is obtained by randomly moving the control points of the surface shown in Fig.(5.15a) along the x_3 axis. In this test, the internal boundaries of the cut-outs are left free, and a surface force $\boldsymbol{\tau} = \{1, 1, 1\}^\intercal$ kPa is applied on the shell. Here too, a smooth coupling between the main patch and the boundary patches is evident in the contour of the displacement's magnitude displayed in Fig.(5.15d).

5.5.3 Conforming coupling of cylindrical patches

In the next test, an approach based on the IBCM is employed to create conforming interfaces between two intersecting cylindrical patches. In this case, the cylindrical shells

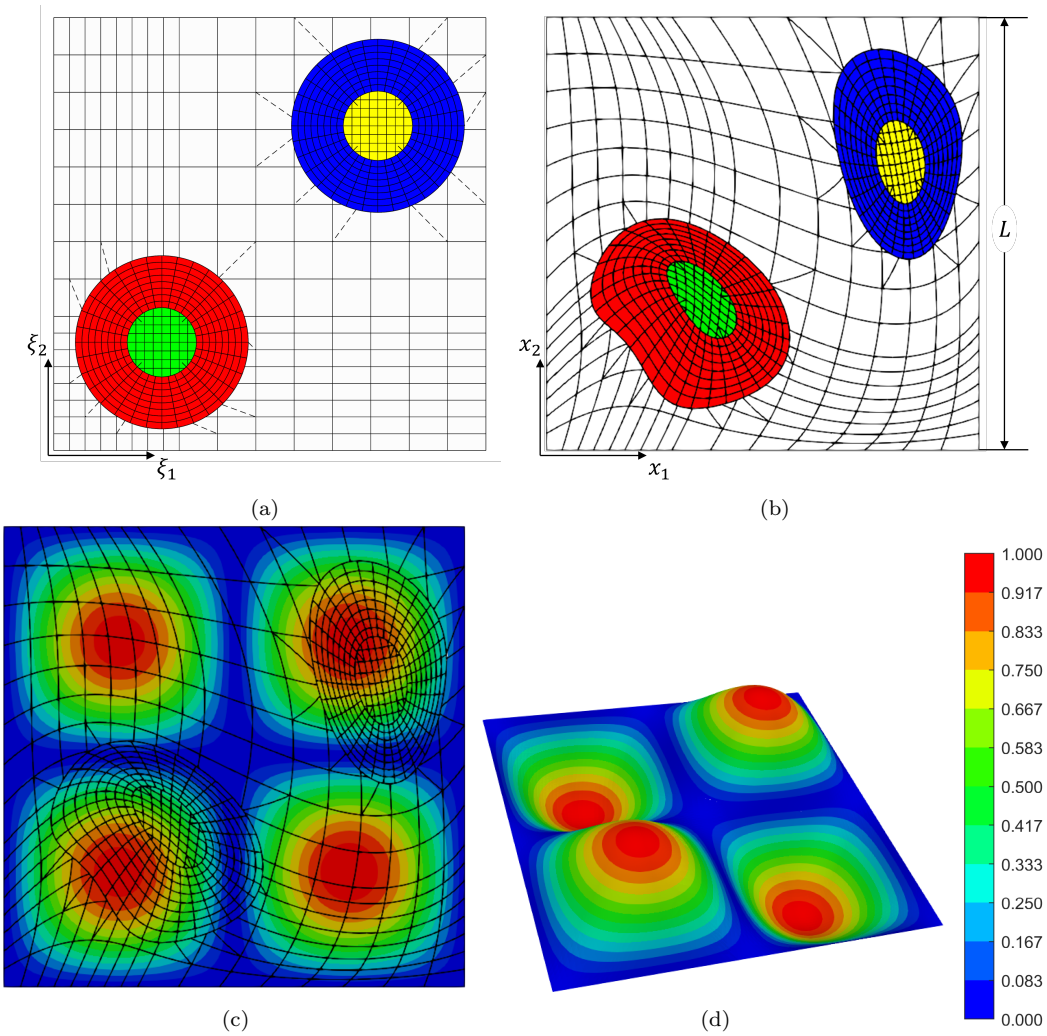

Figure 5.12: Mesh discretization for the Kirchhoff plate described in Sec. 5.5.1 in the parametric domain of the main patch (a) and in the Euclidean space (b). Contour of the magnitude of the displacement with superimposed mesh (c), and deformed configuration of the plate with superimposed contour of the magnitude of the displacement.

Table 5.2: Values for defining the auxiliary cut-out layers in the parametric domain of the main patch as described in Sec. 5.5.2 and corresponding applied displacement.

ξ_{1C}	ξ_{2C}	R_{int}	R_{ext}	$\overline{u}_3$
0.25	0.750	0.10	0.20	0.1
0.75	0.750	0.08	0.14	0.2
0.60	0.500	0.04	0.09	0.3
0.25	0.250	0.05	0.10	0.4
0.75	0.255	0.01	0.05	0.5

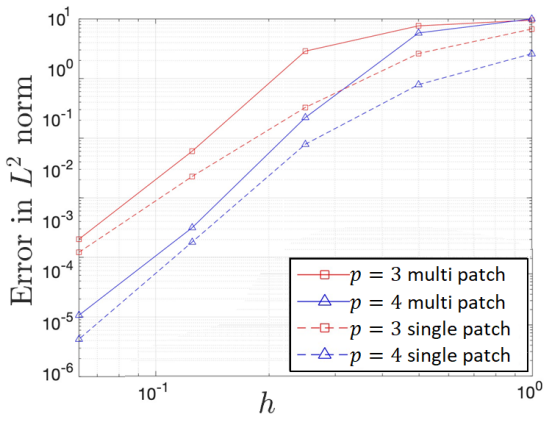

(a) $\beta = 10$

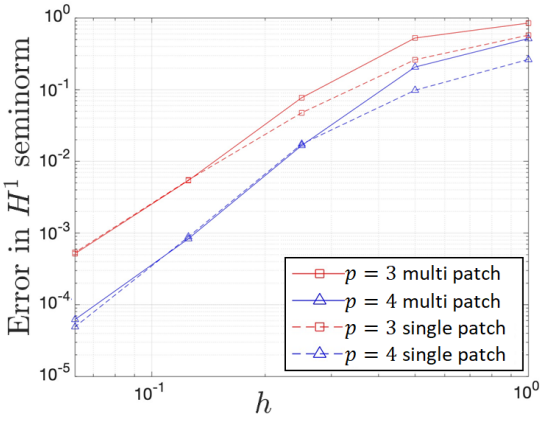

(b) $\beta = 10$

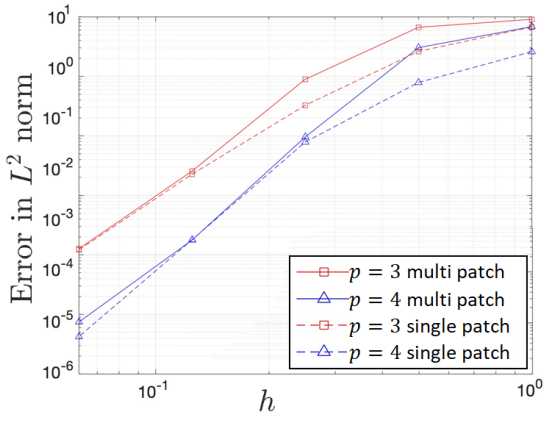

(c) $\beta = 10^2$

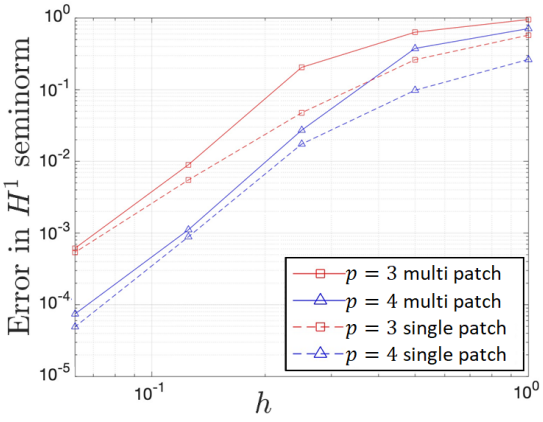

(d) $\beta = 10^2$

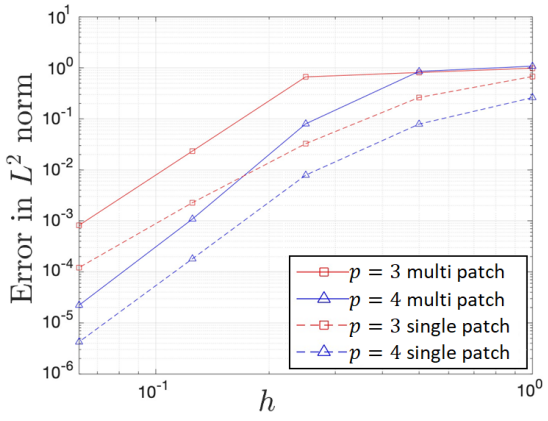

(e) $\beta = 10^3$

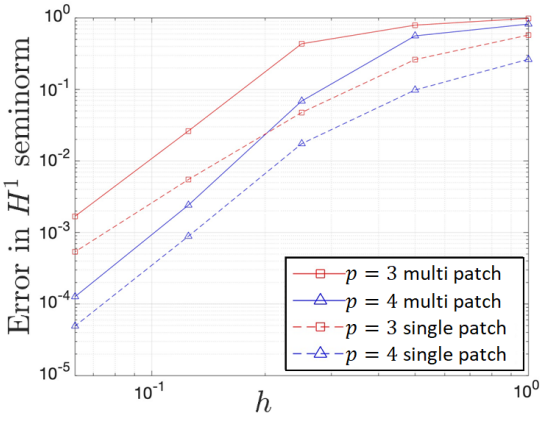

(f) $\beta = 10^3$

Figure 5.13: L^2 convergence (a), (c) and (e), and H^1 convergence (b), (d), and (f) associated with the Kirchhoff plate shown in Sec. 5.5.1, for different values of the penalty parameter and for different polynomial degrees.

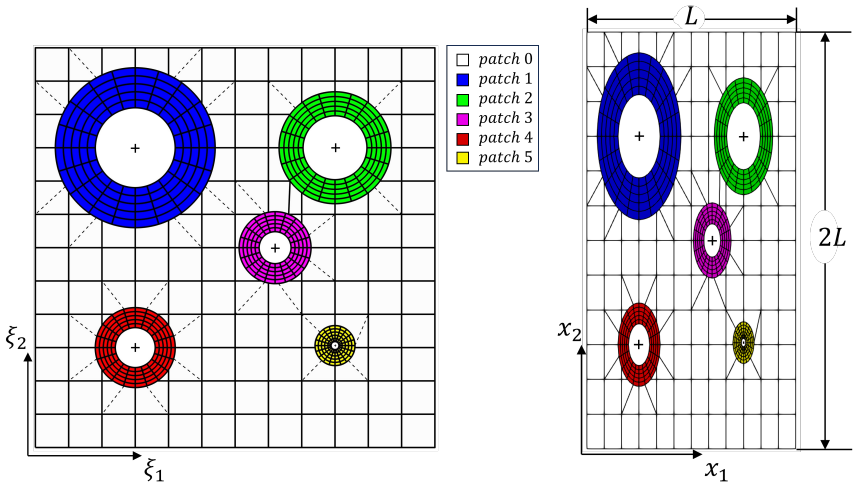

(a) (b)

Figure 5.14: Mesh discretization for the Kirchhoff plate described in Sec. 5.5.2 in the parametric domain of the main patch (a) and in the Euclidean space (b).

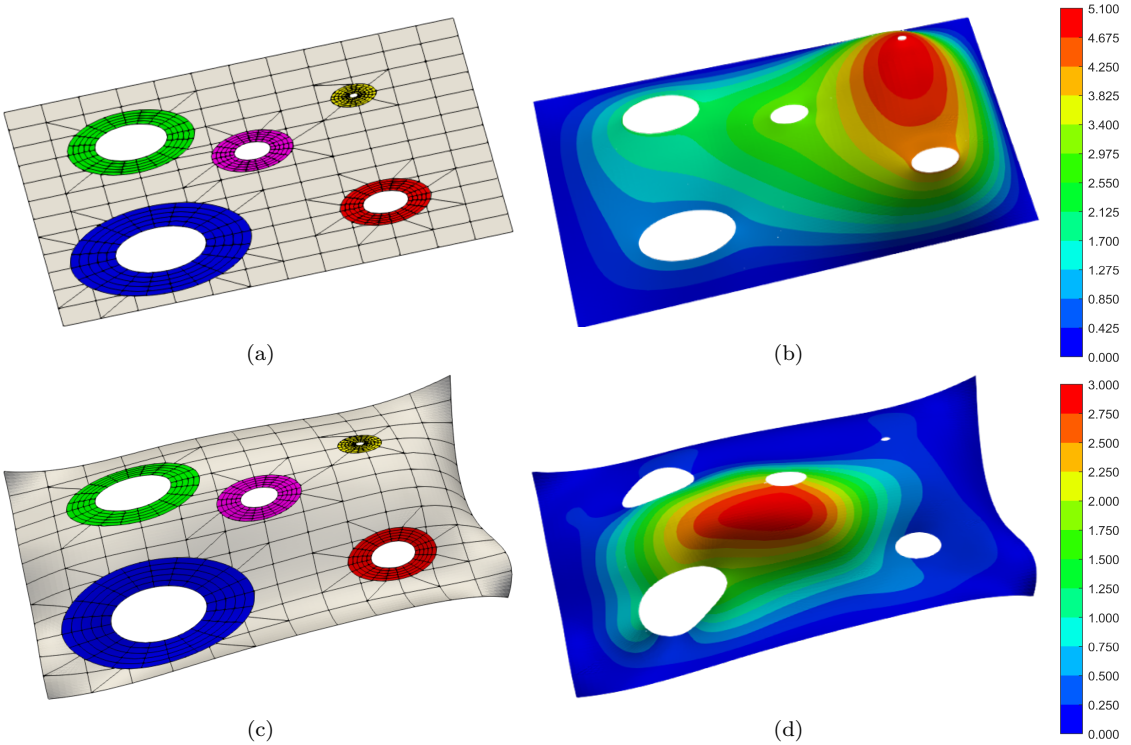

(a) (b)

(c) (d)

Figure 5.15: Geometry of the plate (a) and the shell (c) structures with cut-outs as described in Sec. 5.5.2 with superimposed discretization. Deformed configuration of the plate (b) and the shell (d) with superimposed contour of the displacement magnitude.

are described using analytical functions. In particular the map of first shell is

$$\boldsymbol{x}_0^a = \begin{bmatrix} -R_a \cos \xi_1^a \\ -R_a \sin \xi_1^a \\ \xi_2 \end{bmatrix} , \tag{5.35}$$

where $(\xi_1^a, \xi_2^a) \in \hat{\Omega}^a = [0, 2\pi] \times [-L, L]$, and the map of the second one is

$$\boldsymbol{x}_0^b = \begin{bmatrix} \cos\theta & 0 & -\sin\theta \\ 0 & 1 & 0 \\ \sin\theta & 0 & \cos\theta \end{bmatrix} \begin{bmatrix} -R_b \cos \xi_1^b \\ -R_b \sin \xi_1^b \\ \xi_2^b \end{bmatrix} , \tag{5.36}$$

where $(\xi_1^b, \xi_2^b) \in \hat{\Omega}^b = [0, 2\pi] \times [0, L]$. The parameters for the geometry are set as follows: $L = 4$ m, $R_a = 1$ m, $R_b = 0.6$ m, and $\theta = -\pi/3$ rad. Fig.(5.16) displays the geometry of the structure from two different views, highlighting the intersection between the two cylinders, which creates an interface Γ_0.

The shell section has a thickness $\tau = 10$ cm and is composed of a single isotropic layer with a Young's modulus of $E = 100$ GPa and a Poisson's ratio of $\nu = 0.3$. A uniform surface force of $\boldsymbol{\tau} = \{10, 10, 10\}^\intercal$ Pa is applied on the surfaces of the shells, while the external boundaries are simply-supported ($\boldsymbol{u} = 0$ at $\xi_2^a = \pm L/2$ and $\xi_2^b = L$). To create the conforming interface layers, the following steps are carried out:

i) A cloud of points is created in the Euclidean space at the intersection of the two cylinders. This is achieved by finding the intersection of lines from the second cylinder corresponding to uniform values of ξ_2^b with the surface of the first cylinder. This operation can be easily solved analytically.

ii) The cloud of points is projected onto the parametric domains of the two cylinders. This is also straightforward since the curvilinear coordinates correspond to the cylindrical ones.

iii) An auxiliary chord-length coordinate τ, approximating the true arc-length at the interface, is defined, and a value of this coordinate is associated with each point of the cloud.

iv) The curves in the parametric domains of the two cylinders are obtained with an L^2 projection into the same univariate spline space. This ensures that each value of the auxiliary interface coordinate τ corresponds (ξ_1^a, ξ_2^a) and (ξ_1^b, ξ_2^b) that when composed with the correspondent maps lead to an approximation of the same point in Euclidean space.

v) The curves in each parametric space are used to define its trimmed boundary.

vi) The boundary layers are then created for each main cylindrical patch following the procedure described above in this section. It is worth noting that, by refining the auxiliary layers with the same number of elements along the interface's curvilinear direction, the interface remains conforming.

Fig.(5.17) illustrates the parametric domains of the cylindrical patches each constituted by a main patch and a boundary layer. The boundary layer $\hat{\Omega}^{[2]}$ is constructed as a ruled domain between the projection of the interface in the parametric domain of the first

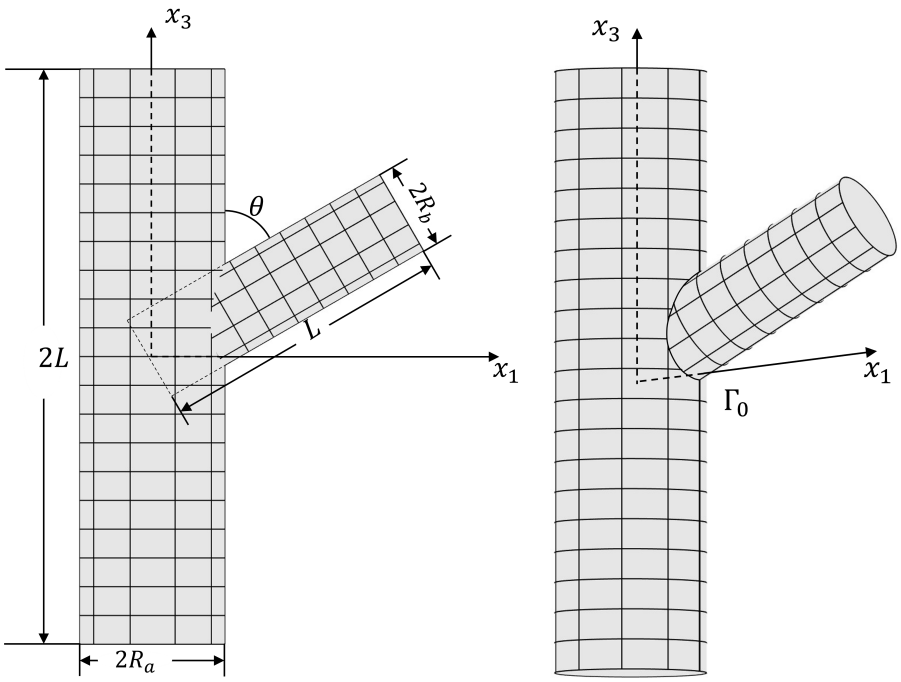

(a) (b)

Figure 5.16: Geometry of the test described in Sec. 5.5.3 in two different views. The intersection of the two cylinders generates the interface denoted as Γ_0.

cylinder $\hat{\Gamma}^{[1]'}$ and the offset curve $\hat{\Gamma}^{[1]}$. Similarly, the boundary layer $\hat{\Omega}^{[4]}$ is constructed as a ruled domain between the the projection of the interface in the parametric domain of the second cylinder $\hat{\Gamma}^{[2]'}$ and the offset curve $\hat{\Gamma}^{[2]}$. Furthermore, the patch $\hat{\Omega}^{[1]}$ is obtained from the parametric domain $\hat{\Omega}^a$ subtracting the domain of the corresponding boundary layer $\hat{\Omega}^{[2]}$, the patch $\hat{\Omega}^{[3]}$ is obtained from the parametric domain $\hat{\Omega}^b$ subtracting the domain of the corresponding boundary layer $\hat{\Omega}^{[4]}$.

Fig.(5.18a) shows the mapping in Euclidean space, highlighting the conforming nature of the interface layers, allowing the displacement interface continuity condition to be imposed in a strong sense. However, rotational continuity still needs to be imposed in a weak manner through the interior penalty formulation. Fig.(5.18b) displays the deformed configuration of the structure with a superimposed map of the magnitude of the displacement. It can be observed the smoothness of the contour map at the intersection between the cylinders.

5.6 A mixed IGA-DG local refinement strategy

As a concluding remark, the mixed IGA-DG refinement strategy is presented. This innovative approach combines IGA to model the majority of the domain, while leveraging a novel DG-based refinement strategy in areas where local phenomena are expected. Elements in proximity to the local feature are disconnected from the rest of the domain. This disconnection allows to replace these areas with elements having discontinuous shape functions that are more flexible when it comes to local mesh refinement. The proposed approach is based on a hierarchical dyadic subdivision of DG elements. Each rectangular element in the parametric domain is divided into four smaller, geometrically similar rectangular elements that are connected to each other and to neighboring elements through

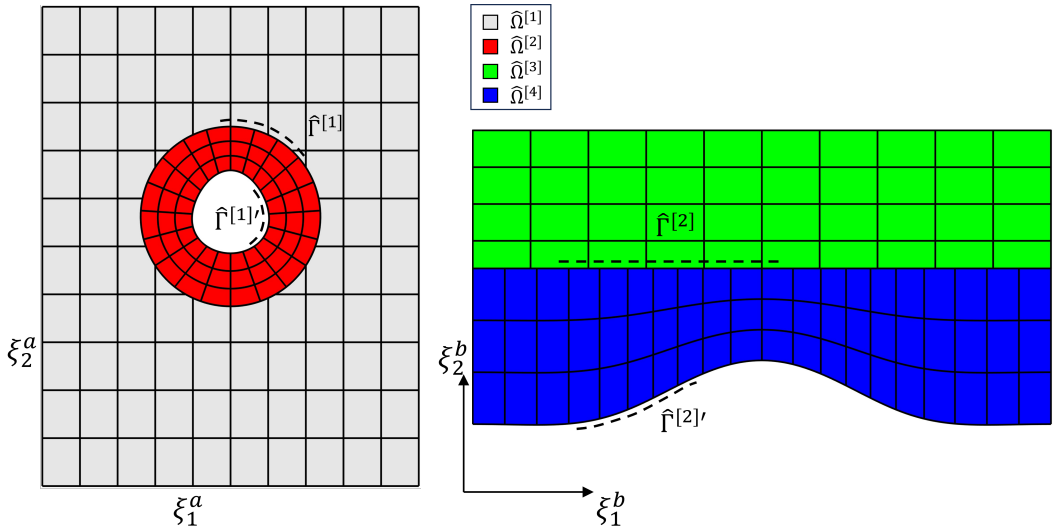

(a) (b)

Figure 5.17: Parametric domain of the two cylinders of the test in Sec. 5.5.3. Each parametric domain consists of a trimmed main patch ($\hat{\Omega}^{[1]}$ and $\hat{\Omega}^{[3]}$) and a boundary layer ($\hat{\Omega}^{[2]}$ and $\hat{\Omega}^{[4]}$). In (a) there are also shown the projections of the interface in the parametric domain of the first cylinder $\hat{\Gamma}^{[1]\prime}$, and the offset curve $\hat{\Gamma}^{[1]}$ that defines $\hat{\Omega}^{[1]}$. Similarly, in (b) there are shown the projections of the interface in the parametric domain of the second cylinder $\hat{\Gamma}^{[2]\prime}$, and the offset curve $\hat{\Gamma}^{[2]}$ that trims the domain $\hat{\Omega}^{[2]}$.

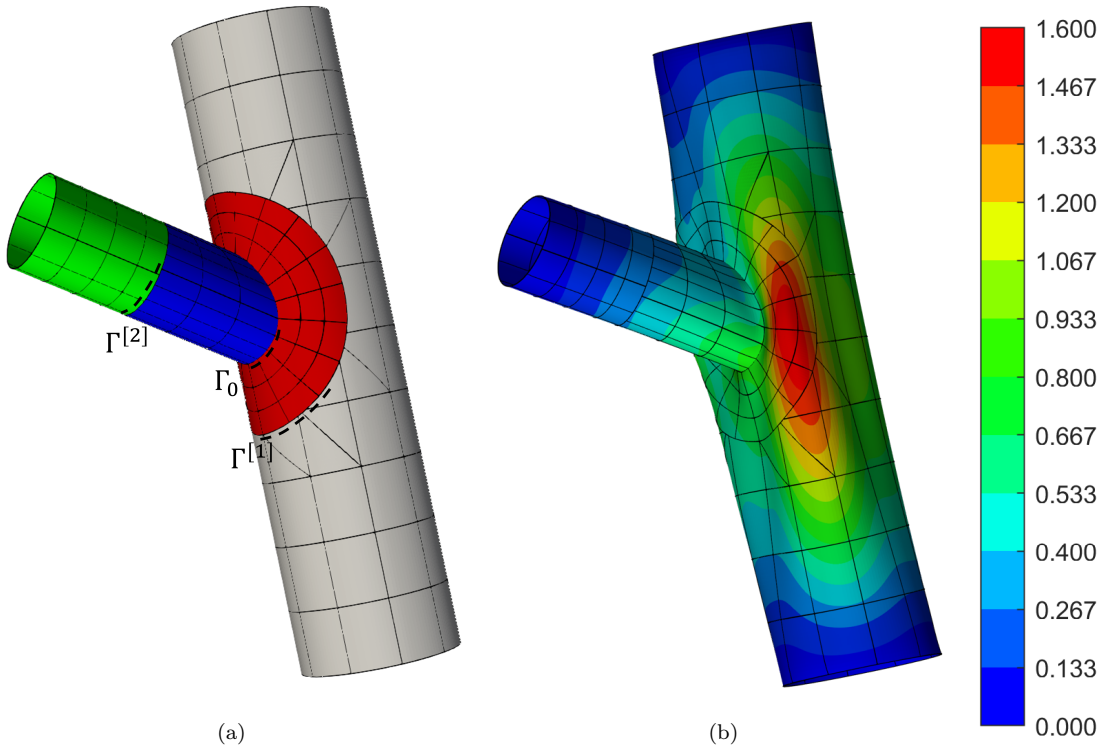

(a) (b)

Figure 5.18: Discretization of the cylinders in the Euclidean space (a), with interfaces between patches Γ_0, $\Gamma^{[1]}$, and $\Gamma^{[2]}$. Deformed configuration with superimposed contour of the magnitude of the displacement and mesh (b).

the interior penalty strategy introduced in Sec. 5.2. The polynomial degree of the elements is kept unchanged throughout this process. However, in the area approximated using DG elements, implementing a p refinement would be straightforward.

5.6.1 Isotropic Kirchhoff plate with internal damage

The feasibility of the mixed IGA-DG local refinement strategy is tested on a square isotropic Kirchhoff plate with an internal damage. The geometry for this test is shown in Fig.(5.19). The mid-plate surface is described using a B-spline, and the curvilinear coordinates take values in $\hat{\Pi} = [0,1] \times [0,1]$. The length of the plate is denoted as L, and the through-the-thickness crack is characterized by the dimensions: $2a/L = 0.375$ and $a/b = 60$. The material for this test is characterized by a Poisson's ratio of $\nu = 0.3$. It is important to note that in the linear elasticity theory for the given problem settings, the results are not dependent on Young's modulus. The plate thickness ratio is $L/\tau = 1600$. The boundaries corresponding to $\xi_1 = 0$ and and $\xi_1 = 1$ are kept free, while an external displacement is applied to the boundary at $\xi_2 = 0$ with a value of $\overline{u}_2 = -\delta$, and to the boundary at $\xi_2 = 1$ with a value of $\overline{u}_2 = +\delta$.

The initial discretization is achieved using an original background grid consisting of 4×4 IGA elements with a polynomial degree of $p = 3$. Subsequent refinements are performed exclusively on the elements directly adjacent to the cut-out. These refinements involve disconnecting the element from the main patch and dividing it into four smaller elements. Fig.(5.20) displays the grids obtained for three different levels of local refinement and the corresponding contours of the non-dimensional displacement magnitude, denoted as $|\overline{\boldsymbol{u}}| = |\boldsymbol{u}|/\delta$.

It is important to note that, due to the embedded approach and the fact that the local feature is smaller than the characteristic size of the mesh elements, the continuity of the underlying spline space is not modified in the first refinement level. As such the space of trial functions is not capable of reproducing the typical deformation that characterizes a through-the-thickness crack under tensile stress. This issue is sometimes addressed in the literature by introducing additional discontinuous shape functions within each element where damage is present. In the context of FEM, this is known as Extended Finite Element Method (XFEM) [171]. In the method proposed here, a discontinuity in the approximation space is only allowed after local refinement through DG elements, leading to more accurate results.

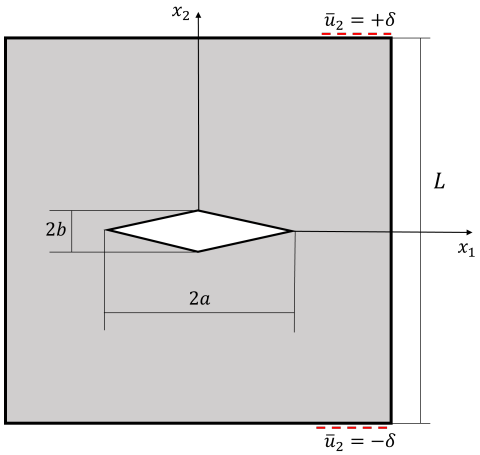

Figure 5.19: The geometry and boundary conditions of the Kirchhoff plate in Sec. 5.6.1 are presented. It is worth noting that the dimensions of the damage have been enlarged for visualization purposes.

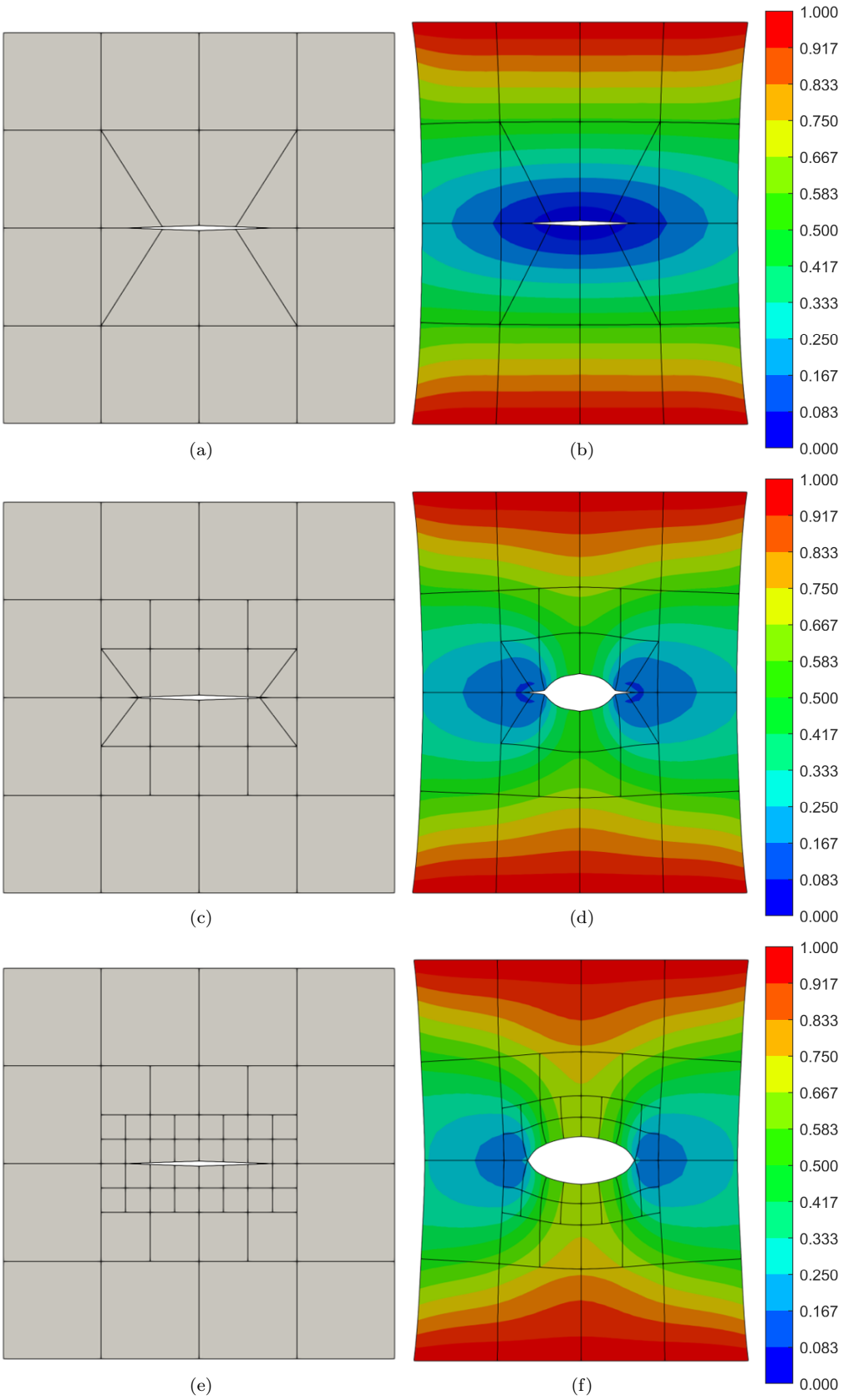

Figure 5.20: The test in Sec. 5.6.1 utilizes three hierarchically refined grid levels denoted as (a), (b), and (c). For each refinement level, the contour of the non-dimensional magnitude of the displacement is superimposed onto the deformed configuration. It is worth mentioning that the diagonal lines in the grid do not correspond to actual interfaces but are included solely for visualization purposes, a result of the integration algorithm adopted.

Chapter 6

Concluding remarks

6.1 Scientific contributions

The scientific contributions in this thesis are based on the articles [64, 122, 65, 67] that have already been published, and the articles [123, 124] that are still under preparation. In this section, the main results obtained in this thesis are highlighted.

6.1.1 Contributions to the DG method for shells

In this work, the study of laminated shells was first conducted using the discontinuous Galerkin (DG) method and the main features are reported as follows:

- The DG approach was employed in combination with higher-order shell theories. Starting from the three-dimensional variational statement for the problem of interest, the shell equation in weak form was obtained replacing the kinematic assumptions, and integrating through the thickness of the shell.

- Within the Equivalent Single Layer (ESL) approach, the covariant components of the displacement field were expressed as a series of generalized displacements throughout the shell's thickness, leading to the definition of a layer of equivalent properties for the entire laminate. This approach allowed the development of multiple theories with different through-the-thickness resolutions, including the First-Order Shear Deformation Theory (FSDT) as a special case.

- The DG method was also utilized in combination with Layer-Wise (LW) theories based on a discontinuous expansion of the displacement field components through the thickness. The continuity condition of the displacement is then used to connect the generalized stiffness matrices of each individual layer allowing to treat the theory as two-dimensional.

- To handle generally-curved shells, the mid-surface was described using both analytically defined surfaces and Non-Uniform Rational B-Spline (NURBS) surfaces. Analytical descriptions were useful for testing on simple shapes, while NURBS surfaces, commonly used in CAD design, allowed for the description of complex geometries. The formulation proposed handles non-orthogonal curvilinear coordinate systems.

- To account for the presence of cut-outs, such as in a fuselage panels with a window, the DG scheme was implemented in conjunction with the implicitly-defined mesh technique, whereby the shell modeling domain is implicitly represented via a level set function and the mesh elements are constructed by intersecting an easy-to-generate background grid and the implicitly-defined domain, increasing the range of geometries that can be treated.

- To handle small cut elements and prevent ill-conditioning, the merging technique was adopted, were small elements degrees of freedom are discarded and their domain is merged with nearby non-small elements referred to as extended.

- The two-dimensional variational formulation was developed for different mechanical problems, including linear and geometrically non-linear static analysis, linear free-vibration analysis, linear transient analysis, and linear buckling analysis.

- The two-dimensional equations were solved with the DG method that is based on a discontinuous representation of the approximated solution throughout the mesh elements and on the use of suitably defined interface and boundary integrals to enforce the inter-element solution continuity and the boundary conditions.

- The interior penalty DG method was used for all the linear analyses. This method allowed for the weak enforcement of continuity and boundary conditions through appropriate interface and boundary integrals. The high flexibility of the interior penalty in the choice of the penalty parameter makes the method more robust then the pure penalty one.

- For the non-linear static analysis, the pure penalty method was preferred, motivated by the possibility to compute the penalty integrals only at the beginning of the analysis and not at each iteration. The resulting nonlinear algebraic system is solved with a Newton-Raphson arc-length scheme.

- Extensive testing was conducted on various shell geometries, including singly curved, doubly curved, and generally-curved shapes, both with and without cut-outs. Different types of shell sections, such as homogeneous isotropic shells, homogeneous orthotropic shells, and laminated composite shells, were tested. The structures were subjected to a variety of loads and boundary conditions, including surface and boundary loads and simply-supported, clamped, applied displacement, and mixed boundary conditions.

- In cases where analytical solutions were available, they were used as a reference to compute convergence curves. Various numerical tests were conducted to investigate the effect of the material, geometry, mesh size, and polynomial order on the computed solutions. The method proved to provide optimal convergence with respect to the number of degrees of freedom in the linear static analysis and showed good convergence in all other cases. Convergence tests regarding the analysis time were also conducted for buckling analysis; similar behavior was observed for other analyses and is not reported here.

- Results were compared with those from the literature and with simulations using the Finite Element Method (FEM) software Abaqus®. Comparisons were made between FSDT and FEM shell elements, as well as higher-order theories and FEM 3D elements to highlight the differences in resolution between the approaches.

6.1.2 Contributions to the IGA method for shells

A different approach used here for the linear elastic static analysis for isotropic and laminated plates and shells relied on the Isogeometric Analysis (IGA) to solve the Kirchhoff-Love (KL) shell theory. The main feature of the method are reported as follows:

- Differently form other two-dimensional shell theories the KL equations imposes a C^1 continuity requirement on the solution space to which the IGA offered seamless solution by simply using high-degree splines.
- The proposed method is capable of handling structures formed by multiple IGA patches meeting at interfaces that may not necessarily be conforming and might even intersect at an angle.
- The software adopted was capable of importing directly STEP files, making it a powerful tool for mechanical analysis.
- To address the ill-conditioning issue, a simple Jacobi preconditioning was adopted.
- It was employed the symmetric interior penalty method to weakly impose the coupling conditions and the Dirichlet conditions on cut boundaries.
- A variationally consistent expression for the fluxes used to apply coupling conditions and essential boundary conditions was adopted. The method proved optimal convergence, although for high refinement level and for high polynomials some ill-conditioning of the linear system appeared.
- In the numerical results, various multi-patch discretization with non conforming interfaces were tested. Isotropic and laminated shell sections with uniform thickness were considered.
- The error norms showed optimal convergence in the asymptotic regime, in agreement with expected theoretical rates, and proved to be competitive respect to single patch discretizations.
- Comparisons with solution obtained with FEM proved the efficiency of the method also for more complex geometries.
- To enforce displacement Dirichlet boundary and interface conditions on cut edges, the Immersed Boundary Conformal (IBCM) was adopted. This method relies on the construction of additional conformal boundary patches.
- A mixed IGA-DG refinement strategy was introduced and tested on a damaged Kirchhoff plate. The domain was modeled mainly through a IGA discretization, while hierarchically refined DG elements were employed for local enrichment of the approximation space nearby the geometrical discontinuity.

6.1.3 Benefits and drawbacks of the investigated approaches

The two approaches presented here are somehow similar but differs in many aspects. To summarize, the pros and cons are listed here as:

- Utilizing higher-order polynomial approximations for partial differential equations leads to faster convergence rates, compensating for increased degrees of freedom.

- Higher-order theories can offer more accurate solutions through the shell thickness, making them a valid alternative to full three-dimensional analysis and leading to significant computational savings. However, for small thickness and single-layer shell sections the use of higher-order theories is not motivated since the accuracy of KL and FSDT is acceptable.

- IGA is particularly effective in achieving higher-degree elements due to the higher continuity properties of spline basis functions. This results in a significant reduction in the number of degrees of freedom when compared to DG. However, the DG method lands itself to intuitive refinement strategy and easiness to construct non conforming meshes.

- The use of NURBS basis functions for shell geometries allows for high-fidelity representation of complex structures encountered in practical industrial applications. The use of NURBS ensures that the elements built are geometrically exact, as they precisely matches the output of the CAD.

- All kinematic theories presented (KL, ESL, and LW), supported generally-curved curvilinear coordinates, enabling the use of various mappings, even with non-orthogonal curvilinear coordinates.

- The higher-order kinematics theories started from the components of displacement in covariant coordinates, while KL theory was based on Cartesian coordinates. Using a through-the-thickness expansion that starts from a local basis has the advantage to deduce the FSDT as a special case of the ESL. On the opposite, the use of Cartesian components simplifies significantly the differential geometry involved.

- The embedded domain approach allows for modeling internal and external cuts while maintaining a simple description of the underlying surface. Among the strategies presented, the implicit domain is limited to geometries described through a level-set function, but leads to faster algorithms, the trimmed boundary has virtually no limits in terms of boundaries representation, but the involved routines are generally slower.

- The proposed strategies for applying boundary conditions and enforcing continuity conditions relied on weak enforcement using the interior penalty formulation. This approach provided flexibility in choosing the penalty parameter and ensured optimal convergence, even with low penalty values. The pure penalty leads to a less stable formulation, but for non-linear analysis allows for the penalty integrals to be computed only once. Both formulation lead to symmetric linear systems.

- Imposing boundary and continuity conditions weakly eliminates the necessity to embed them in the solution space, facilitating the use of trimmed geometries. However, with the IBCM method strong imposition of displacement conditions can be still achieved.

- Two approaches were suggested to handle small cut elements. The merging technique is very effective to make the linear system well conditioned, but involves more complex algorithms. A simpler alternative that also demonstrates to be efficient involves applying a diagonal Jacobi preconditioner.

- The software used was capable of directly importing STEP files, making it a powerful tool for the mechanical analysis of complex shell structures.

- The combined IGA-DG approach seamlessly integrates the advantages of a high-order globally IGA model with the flexibility of the DG method when used for local refinement of critical areas of the domain.

6.2 Future research directions

This work represents merely a glimpse into the potential of higher-order methods for modeling shell structures. Nonetheless, it offers a foundation for potential research directions. These directions can be categorized into two distinct groups: those related to the physical model and those associated with the numerical model.

6.2.1 Extension to more complex physical model

A compelling direction for further exploration lies in extending the proposed formulations to address various mechanical problems. Specifically, for the DG approach, addressing into the nonlinear dynamic response of shells presents an intriguing challange.

Regarding the IGA approach, the analysis was limited to linear static scenarios. Consequently, the formulation could be extended to linear buckling, linear transient dynamics, free-vibration analysis, as well as non-linear static and transient analysis. Additionally, further investigation is needed regarding the application of IGA to high-order kinematic shells.

On the material front, exploring laminates with variable thickness and lamination angles holds substantial research potential. Another interesting direction would involve the incorporation of a hyper-elastic model, facilitating the study of shell structures with relevance in various sectors, such as biomechanical tissues.

Another realm of mechanical challenges pertains to the analysis of damaged structures. While two examples were presented in the context of linear static analysis, the DG method offers a unique opportunity to further investigate through-the-thickness cracks by disconnecting certain elements and discarding the corresponding integrals. Further prospects also include the utilization of additional shape functions to model discontinuities for intra-element cracks.

Furthermore, addressing delamination could be accomplished through a combination of a Layer-Wise formulation and a through-the-thickness DG approach, wherein DG would be used for continuity between both layers and elements.

Finally, utilizing the methods presented here for modeling thin-walled structural components would confer considerable advantages in computational efficiency in multi-physics problems where analysis time is a primary concern, e.g. fluid-structure interaction.

6.2.2 Development of the numerical modeling techniques

From the method perspective, an intriguing path involves further explore the integration of the IGA method with the DG method. The DG, in particular, serves as a valuable tool for localized hp refinement, as well as for modeling regions of the domain that require extended shape functions or the introduction of local solution discontinuities.

Expanding the IGA approach presented here to encompass Reissner-Mindlin theory and higher-order theories presents another promising avenue for further research.

Exploring the limitations of the interior penalty method and devising efficient strategies to address potential stability issues and ill-conditioning problems, particularly in the context of trimmed patches, should also be a priority.

An additional compelling direction would be the development of an efficient strategy for modeling the connection of patches employing higher-order kinematics that meet at a kink. Such an approach might involve the creation of a three-dimensional object along the interface, serving as a higher-order connection between patches

For geometrically continuous patches, it would be valuable to develop an efficient strategy for connecting patches modeled with different through-the-thickness resolutions. This could be achieved by penalizing jumps in the relevant components of generalized displacements.

Bibliography

[1] Jones, R. *Mechanics Of Composite Materials*. Materials Science and Engineering Series. Taylor & Francis, 1998.

[2] Reddy, J. N. *Mechanics of laminated composite plates and shells: theory and analysis*. CRC press, 2003. doi: https://doi.org/10.1201/b12409.

[3] Reddy, J. *Theory and Analysis of Elastic Plates and Shells*. CRC Press, 2006.

[4] Ren, J. Analysis of simply-supported laminated circular cylindrical shell roofs. *Composite Structures*, 11(4):277–292, 1989. doi: https://doi.org/10.1016/0263-8223(89)90092-5.

[5] Varadan, T. and Bhaskar, K. Bending of laminated orthotropic cylindrical shells—an elasticity approach. *Composite Structures*, 17(2):141–156, 1991. doi: https://doi.org/10.1016/0263-8223(91)90067-9.

[6] Brischetto, S. Exact three-dimensional static analysis of single-and multi-layered plates and shells. *Composites Part B: Engineering*, 119:230–252, 2017. doi: https://doi.org/10.1016/j.compositesb.2017.03.010.

[7] Kirchhoff, V. G. Über das gleichgewicht und die bewegung einer elastischen scheibe. *Journal fur die reine und angewandte Mathematik*, 40:51–88, 1850.

[8] Love, A. E. H. The small free vibrations and deformation of a thin elastic shell. *Philosophical Transactions of the Royal Society of London*, 179:491–546, 1888. doi: https://doi.org/10.1098/rsta.1888.0016.

[9] Stravsky, Y. Bending and stretching of laminated aeolotropic plates. *Journal of the Engineering Mechanics Division*, 87(6):31–56, 1961. doi: https://doi.org/10.1061/JMCEA3.0000267.

[10] Dong, S. B., Pister, K. S., and Taylor, R. L. On the theory of laminated anisotropic shells and plates. *Journal of the Aerospace Sciences*, 29(8):969–975, 1962. doi: https://doi.org/10.2514/8.9668.

[11] Reissner, E. The Effect of Transverse Shear Deformation on the Bending of Elastic Plates. *Journal of Applied Mechanics*, 12(2):A69–A77, 1945. doi: https://doi.org/doi.org/10.1115/1.4009435.

[12] Mindlin, R. D. Influence of Rotatory Inertia and Shear on Flexural Motions of Isotropic, Elastic Plates. *Journal of Applied Mechanics*, 18(1):31–38, 1951. doi: https://doi.org/10.1115/1.4010217.

[13] Von Kármán, T. Festigkeitsprobleme im maschinenbau. In *Mechanik*, pages 311–385. Springer, 1907. doi: https://doi.org/10.1007/978-3-663-16028-1_5.

[14] Chia, C.-Y. *Nonlinear analysis of plates*. McGraw-Hill International Book Company, 1980.

[15] Reddy, J. and Liu, C. A higher-order shear deformation theory of laminated elastic shells. *International journal of engineering science*, 23(3):319–330, 1985. doi: https://doi.org/10.1016/0020-7225(85)90051-5.

[16] Cho, M., Kim, K.-O., and Kim, M.-H. Efficient higher-order shell theory for laminated composites. *Composite Structures*, 34(2):197–212, 1996. doi: https://doi.org/10.1016/0263-8223(95)00145-X.

[17] Arciniega, R. A. and Reddy, J. Consistent third-order shell theory with application to composite cylindrical cylinders. *AIAA journal*, 43(9):2024–2038, 2005. doi: https://doi.org/10.2514/1.6593.

[18] Carrera, E. Mixed Layer-Wise models for multilayered plates analysis. *Composite Structures*, 43(1):57–70, 1998. doi: https://doi.org/10.1016/S0263-8223(98)00097-X.

[19] Reddy, J. N. and Savoia, M. Layer-Wise shell theory for postbuckling of laminated circular cylindrical shells. *AIAA Journal*, 30(8):2148–2154, 1992. doi: https://doi.org/10.2514/3.11193.

[20] Epstein, M. and Huttelmaier, H.-P. A finite element formulation for multilayered and thick plates. *Computers & Structures*, 16(5):645–650, 1983. doi: https://doi.org/10.1016/0045-7949(83)90113-X.

[21] Carrera, E. Theories and finite elements for multilayered, anisotropic, composite plates and shells. *Archives of Computational Methods in Engineering*, 9(2):87–140, 2002. doi: https://doi.org/10.1007/BF02736649.

[22] Carrera, E. Theories and finite elements for multilayered plates and shells: a unified compact formulation with numerical assessment and benchmarking. *Archives of Computational Methods in Engineering*, 10(3):215–296, 2003. doi: https://doi.org/10.1007/BF02736224.

[23] Carrera, E. *Introduction to the Unified Formulation*, chapter 5, pages 51–69. Wiley, 2014.

[24] Petrolo, M. and Carrera, E. Methods and guidelines for the choice of shell theories. *Acta Mechanica*, pages 1–40, 2020. doi: https://doi.org/10.1007/s00707-019-02601-w.

[25] Bathe, K. *Finite Element Procedures*. Prentice Hall, 2006.

[26] Smith, M. *ABAQUS 6.14 Documentation*. Dassault Systèmes, 2014. Providence, RI, USA.

[27] Reed, W. H. and Hill, T. Triangular mesh methods for the neutron transport equation. Technical report, Los Alamos Scientific Lab., N. Mex.(USA), 1973.

[28] Arnold, D. N., Brezzi, F., Cockburn, B., and Marini, L. D. Unified analysis of discontinuous Galerkin methods for elliptic problems. *SIAM journal on numerical analysis*, 39(5):1749–1779, 2002. doi: https://doi.org/10.1137/S0036142901384162.

[29] Rivière, B., Shaw, S., Wheeler, M. F., and Whiteman, J. Discontinuous Galerkin finite element methods for linear elasticity and quasistatic linear viscoelasticity. *Numerische Mathematik*, 95:347–376, 2003. doi: https://doi.org/10.1007/s002110200394.

[30] Ten Eyck, A. and Lew, A. Discontinuous Galerkin methods for non-linear elasticity. *International Journal for Numerical Methods in Engineering*, 67(9):1204–1243, 2006. doi: https://doi.org/10.1002/nme.1667.

[31] An, R. and Huang, X. A compact C^0 discontinuous Galerkin method for Kirchhoff plates. *Numerical Methods for Partial Differential Equations*, 31(4):1265–1287, 2015. doi: https://doi.org/10.1002/num.21946.

[32] Huang, X. and Huang, J. A superconvergent C^0 discontinuous Galerkin method for Kirchhoff plates: Error estimates, hybridization and postprocessing. *Journal of Scientific Computing*, 69(3):1251–1278, 2016. doi: https://doi.org/10.1007/s10915-016-0232-7.

[33] Cui, J. and Zhang, Y. A new analysis of discontinuous Galerkin methods for a fourth order variational inequality. *Computer Methods in Applied Mechanics and Engineering*, 351:531–547, 2019. doi: https://doi.org/10.1016/j.cma.2019.04.005.

[34] Bösing, P. and Carstensen, C. Weakly over-penalized discontinuous Galerkin schemes for Reissner–Mindlin plates without the shear variable. *Numerische Mathematik*, 130(3):395–423, 2015. doi: https://doi.org/10.1007/s00211-014-0672-7.

[35] Bösing, P. and Carstensen, C. Discontinuous Galerkin with weakly over-penalized techniques for Reissner–Mindlin plates. *Journal of Scientific Computing*, 64(2):401–424, 2015. doi: https://doi.org/10.1007/s10915-014-9936-8.

[36] Mu, L., Wang, J., and Ye, X. A weak Galerkin method for the Reissner–Mindlin plate in primary form. *Journal of Scientific Computing*, 75(2):782 – 802, 2018. doi: https://doi.org/10.1007/s10915-017-0564-y.

[37] Noels, L. and Radovitzky, R. A new discontinuous Galerkin method for Kirchhoff-Love shells. *Computer Methods in Applied Mechanics and Engineering*, 197(33-40):2901–2929, 2008. doi: https://doi.org/10.1016/j.cma.2008.01.018.

[38] Zhang, S. Analysis of a discontinuous Galerkin method for the bending problem of Koiter shell. *Numerische Mathematik*, 133(2):333 – 370, 2016. doi: https://doi.org/10.1007/s00211-015-0747-0.

[39] Xia, Y., Wang, H., Zheng, G., Shen, G., and Hu, P. Discontinuous Galerkin isogeometric analysis with peridynamic model for crack simulation of shell structure. *Computer Methods in Applied Mechanics and Engineering*, 398, 2022. doi: https://doi.org/10.1016/j.cma.2022.115193.

[40] Bonito, A., Nochetto, R. H., and Ntogkas, D. Discontinuous Galerkin approach to large bending deformation of a bilayer plate with isometry constraint. *Journal of Computational Physics*, 423:109785, 2020. doi: https://doi.org/10.1016/j.jcp.2020.109785.

[41] Bonito, A., Nochetto, R., and Ntogkas, D. DG approach to large bending plate deformations with isometry constraint. *Mathematical Models and Methods in Applied Sciences*, 31(1):133–175, 2021. doi: https://doi.org/10.1142/S0218202521500044.

[42] Bartels, S., Bonito, A., and Hornung, P. Modeling and simulation of thin sheet folding. *Interfaces and Free Boundaries*, 24(4):459–485, 2022. doi: https://doi.org/10.4171/IFB/478.

[43] Noels, L. A discontinuous Galerkin formulation of non-linear Kirchhoff-Love shells. *International journal for numerical methods in engineering*, 78(3):296–323, 2009. doi: https://doi.org/10.1002/nme.2489.

[44] Noels, L. A one-field discontinuous Galerkin formulation of non-linear Kirchhoff-Love shells. *International Journal of Material Forming*, 2(SUPPL. 1):877 – 880, 2009. doi: https://doi.org/10.1007/s12289-009-0448-2.

[45] Becker, G. and Noels, L. A full-discontinuous Galerkin formulation of nonlinear Kirchhoff-Love shells: Elasto-plastic finite deformations, parallel computation, and fracture applications. *International Journal for Numerical Methods in Engineering*, 93(1):80–117, 2013. doi: https://doi.org/10.1002/nme.4381.

[46] Talamini, B. L. and Radovitzky, R. A discontinuous Galerkin method for nonlinear shear-flexible shells. *Computer methods in applied mechanics and engineering*, 303:128–162, 2016. doi: https://doi.org/10.1016/j.cma.2016.01.001.

[47] Talamini, B. L. and Radovitzky, R. A parallel discontinuous Galerkin/cohesive-zone computational framework for the simulation of fracture in shear-flexible shells. *Computer Methods in Applied Mechanics and Engineering*, 317:480 – 506, 2017. doi: https://doi.org/10.1016/j.cma.2016.12.018.

[48] Versino, D., Mourad, H. M., and Williams, T. O. A global-local discontinuous Galerkin shell finite element for small-deformation analysis of multi-layered composites. *Computer Methods in Applied Mechanics and Engineering*, 271:269 – 295, 2014. doi: https://doi.org/10.1016/j.cma.2013.12.007.

[49] Versino, D., Mourad, H. M., Williams, T. O., and Addessio, F. L. A global-local discontinuous Galerkin finite element for finite-deformation analysis of multilayered shells. *Computer Methods in Applied Mechanics and Engineering*, 283:1401–1424, 2015. doi: https://doi.org/10.1016/j.cma.2014.10.017.

[50] Antonietti, P. F., Buffa, A., and Perugia, I. Discontinuous Galerkin approximation of the Laplace eigenproblem. *Computer methods in applied mechanics and engineering*, 195(25-28):3483–3503, 2006. doi: https://doi.org/10.1016/j.cma.2005.06.023.

[51] Giani, S. and Hall, E. J. An a posteriori error estimator for hp-adaptive discontinuous Galerkin methods for elliptic eigenvalue problems. *Mathematical Models and Methods in Applied Sciences*, 22(10):1250030, 2012. doi: https://doi.org/10.1142/S0218202512500303.

[52] Buffa, A. and Perugia, I. Discontinuous Galerkin approximation of the maxwell eigenproblem. *SIAM Journal on Numerical Analysis*, 44(5):2198–2226, 2006. doi: https://doi.org/10.1137/050636887.

[53] Buffa, A., Houston, P., and Perugia, I. Discontinuous Galerkin computation of the Maxwell eigenvalues on simplicial meshes. *Journal of computational and applied mathematics*, 204(2):317–333, 2007. doi: https://doi.org/10.1016/j.cam.2006.01.042.

[54] Hesthaven, J. S. and Warburton, T. High-order nodal discontinuous Galerkin methods for the Maxwell eigenvalue problem. *Philosophical Transactions of the Royal Society of London. Series A: Mathematical, Physical and Engineering Sciences*, 362 (1816):493–524, 2004. doi: https://doi.org/10.1098/rsta.2003.1332.

[55] Cliffe, K. A., Hall, E. J., and Houston, P. Adaptive discontinuous Galerkin methods for eigenvalue problems arising in incompressible fluid flows. *SIAM Journal on Scientific Computing*, 31(6):4607–4632, 2010. doi: https://doi.org/10.1137/080731918.

[56] Meng, J. and Mei, L. Discontinuous Galerkin methods of the non-selfadjoint Steklov eigenvalue problem in inverse scattering. *Applied Mathematics and Computation*, 381:125307, 2020. doi: https://doi.org/10.1016/j.amc.2020.125307.

[57] Hansbo, P. and Larson, M. G. A posteriori error estimates for continuous/discontinuous Galerkin approximations of the Kirchhoff-Love buckling problem. *Computational Mechanics*, 56(5):815–827, sep 2015. doi: https://doi.org/10.1007/s00466-015-1204-8.

[58] Wells, G. N. and Dung, N. T. A C^0 discontinuous Galerkin formulation for Kirchhoff plates. *Computer Methods in Applied Mechanics and Engineering*, 196(35):3370–3380, 2007. doi: https://doi.org/10.1016/j.cma.2007.03.008.

[59] Shen, Y. and Lew, A. An optimally convergent discontinuous galerkin-based extended finite element method for fracture mechanics. *International Journal for Numerical Methods in Engineering*, 82(6):716–755, 2010. doi: https://doi.org/10.1002/nme.2781.

[60] Becker, G., Geuzaine, C., and Noels, L. A one field full discontinuous galerkin method for kirchhoff–love shells applied to fracture mechanics. *Computer Methods in Applied Mechanics and Engineering*, 200(45):3223–3241, 2011. doi: https://doi.org/10.1016/j.cma.2011.07.008.

[61] Gulizzi, V., Benedetti, I., and Milazzo, A. An implicit mesh discontinuous Valerkin formulation for higher-order plate theories. *Mechanics of Advanced Materials and Structures*, 27(17):1494–1508, 2020. doi: https://doi.org/10.1080/15376494.2018.1516258.

[62] Gulizzi, V., Benedetti, I., and Milazzo, A. A high-resolution Layer-Wise discontinuous Galerkin formulation for multilayered composite plates. *Composite Structures*, page 112137, 2020. doi: https://doi.org/10.1016/j.compstruct.2020.112137.

[63] Benedetti, I., Gulizzi, V., and Milazzo, A. Layer-Wise discontinuous Galerkin methods for piezoelectric laminates. *Modelling*, 1(2):198–214, 2020. doi: https://doi.org/10.3390/modelling1020012.

[64] Guarino, G., Milazzo, A., and Gulizzi, V. Equivalent-Single-Layer discontinuous Galerkin methods for static analysis of multilayered shells. *Applied Mathematical Modelling*, 98:701–721, 2021. doi: https://doi.org/10.1016/j.apm.2021.05.024.

[65] Guarino, G., Gulizzi, V., and Milazzo, A. Accurate multilayered shell buckling analysis via the implicit-mesh discontinuous Galerkin method. *AIAA Journal*, 60 (12):6854–6868, 2022. doi: https://doi.org/10.2514/1.J061933.

[66] Guarino, G., Gulizzi, V., Milazzo, A., et al. Transient and free-vibration analysis of laminated shells through the discontinuous Galerkin method. In *ICAS PROCEEDINGS 33th Congress of the International Council of the Aeronautical Sciences Stockholm, Sweden*, 2022.

[67] Guarino, G. and Milazzo, A. A discontinuous Galerkin formulation for nonlinear analysis of multilayered shells refined theories. *International Journal of Mechanical Sciences*, 255:108426, 2023. doi: https://doi.org/10.1016/j.ijmecsci.2023.108426.

[68] Cottrell, J. A., Hughes, T. J. R., and Bazilevs, Y. *Isogeometric Analysis: Toward Integration of CAD and FEA*. Wiley Publishing, 2009.

[69] Babuska, I., Szabo, B. A., and Katz, I. N. The p-version of the finite element method. *SIAM Journal on Numerical Analysis*, 18(3):515–545, 1981. doi: https://doi.org/10.1137/0718033.

[70] Rank, E., Krause, R., and Preusch, K. On the accuracy of p-version elements for the reissner–mindlin plate problem. *International Journal for Numerical Methods in Engineering*, 43(1):51–67, 1998. doi: https://doi.org/10.1002/(SICI)1097-0207(19980915)43:1⟨51::AID-NME382⟩3.0.CO;2-T.

[71] Düster, A., Bröker, H., and Rank, E. The p-version of the finite element method for three-dimensional curved thin walled structures. *International Journal for Numerical Methods in Engineering*, 52(7):673–703, 2001. doi: https://doi.org/10.1002/nme.222.

[72] Rank, E., Düster, A., Nübel, V., Preusch, K., and Bruhns, O. High order finite elements for shells. *Computer Methods in Applied Mechanics and Engineering*, 194 (21):2494–2512, 2005. doi: https://doi.org/10.1016/j.cma.2004.07.042. Computational Methods for Shells.

[73] Yan, C. A. and Vescovini, R. Application of the ps-version of the finite element method to the analysis of laminated shells. *Materials*, 16(4):1395, 2023. doi: https://doi.org/10.3390/ma16041395.

[74] Hughes, T., Cottrell, J., and Bazilevs, Y. Isogeometric analysis: CAD, finite elements, NURBS, exact geometry and mesh refinement. *Computer Methods in Applied Mechanics and Engineering*, 194(39):4135–4195, 2005. doi: https://doi.org/10.1016/j.cma.2004.10.008.

[75] Kiendl, J., Bletzinger, K.-U., Linhard, J., and Wüchner, R. Isogeometric shell analysis with Kirchhoff–Love elements. *Computer Methods in Applied Mechanics and Engineering*, 198(49):3902–3914, 2009. doi: https://doi.org/10.1016/j.cma.2009.08.013.

[76] Schöllhammer, D. and Fries, T. P. Kirchhoff–Love shell theory based on tangential differential calculus. *Computational Mechanics*, 64(1):113–131, 2019. doi: https://doi.org/10.1007/s00466-018-1659-5.

[77] Benson, D., Bazilevs, Y., Hsu, M., and Hughes, T. Isogeometric shell analysis: The Reissner–Mindlin shell. *Computer Methods in Applied Mechanics and Engineering*, 199(5):276–289, 2010. doi: https://doi.org/10.1016/j.cma.2009.05.011.

[78] Dornisch, W., Klinkel, S., and Simeon, B. Isogeometric Reissner–Mindlin shell analysis with exactly calculated director vectors. *Computer Methods in Applied Mechanics and Engineering*, 253:491–504, 2013. doi: https://doi.org/10.1016/j.cma.2012.09.010.

[79] Schöllhammer, D. and Fries, T. Reissner–Mindlin shell theory based on tangential differential calculus. *Computer Methods in Applied Mechanics and Engineering*, 352:172–188, 2019. doi: https://doi.org/10.1016/j.cma.2019.04.018.

[80] Patton, A., Antolín, P., Kiendl, J., and Reali, A. Efficient equilibrium-based stress recovery for isogeometric laminated curved structures. *Composite Structures*, 272: 113975, 2021. doi: https://doi.org/10.1016/j.compstruct.2021.113975.

[81] Li, W., Nguyen-Thanh, N., and Zhou, K. Geometrically nonlinear analysis of thin-shell structures based on an isogeometric-meshfree coupling approach. *Computer Methods in Applied Mechanics and Engineering*, 336:111–134, 2018. doi: https://doi.org/10.1016/j.cma.2018.02.018.

[82] Kiendl, J., Bazilevs, Y., Hsu, M.-C., Wüchner, R., and Bletzinger, K.-U. The bending strip method for isogeometric analysis of Kirchhoff–Love shell structures comprised of multiple patches. *Computer Methods in Applied Mechanics and Engineering*, 199(37):2403–2416, 2010. doi: https://doi.org/10.1016/j.cma.2010.03.029.

[83] Duong, T. X., Roohbakhshan, F., and Sauer, R. A. A new rotation-free isogeometric thin shell formulation and a corresponding continuity constraint for patch boundaries. *Computer Methods in Applied Mechanics and Engineering*, 316:43–83, 2017. doi: https://doi.org/10.1016/j.cma.2016.04.008.

[84] Dornisch, W. and Klinkel, S. Treatment of Reissner–Mindlin shells with kinks without the need for drilling rotation stabilization in an isogeometric framework. *Computer Methods in Applied Mechanics and Engineering*, 276:35–66, 2014. doi: https://doi.org/10.1016/j.cma.2014.03.017.

[85] Kapl, M., Sangalli, G., and Takacs, T. An isogeometric C^1 subspace on unstructured multi-patch planar domains. *Computer Aided Geometric Design*, 69:55–75, 2019. doi: https://doi.org/10.1016/j.cagd.2019.01.002.

[86] Farahat, A., Jüttler, B., Kapl, M., and Takacs, T. Isogeometric analysis with C^1-smooth functions over multi-patch surfaces. *Computer Methods in Applied Mechanics and Engineering*, 403:115706, 2023. doi: https://doi.org/10.1016/j.cma.2022.115706.

[87] Farahat, A., Verhelst, H. M., Kiendl, J., and Kapl, M. Isogeometric analysis for multi-patch structured Kirchhoff–Love shells. *Computer Methods in Applied Mechanics and Engineering*, 411:116060, 2023. doi: https://doi.org/10.1016/j.cma.2023.116060.

[88] Reichle, M., Arf, J., Simeon, B., and Klinkel, S. Smooth multi-patch scaled boundary isogeometric analysis for Kirchhoff-Love shells, 2023.

[89] Horger, T., Reali, A., Wohlmuth, B., and Wunderlich, L. A hybrid isogeometric approach on multi-patches with applications to Kirchhoff plates and eigenvalue problems. *Computer Methods in Applied Mechanics and Engineering*, 348:396–408, 2019. doi: https://doi.org/10.1016/j.cma.2018.12.038.

[90] Hirschler, T., Bouclier, R., Dureisseix, D., Duval, A., Elguedj, T., and Morlier, J. A dual domain decomposition algorithm for the analysis of non-conforming isogeometric Kirchhoff–Love shells. *Computer Methods in Applied Mechanics and Engineering*, 357:112578, 2019. doi: https://doi.org/10.1016/j.cma.2019.112578.

[91] Dittmann, M., Schuß, S., Wohlmuth, B., and Hesch, C. Weak C^n coupling for multipatch isogeometric analysis in solid mechanics. *International Journal for Numerical Methods in Engineering*, 118(11):678–699, 2019. doi: https://doi.org/10.1002/nme.6032.

[92] Brivadis, E., Buffa, A., Wohlmuth, B., and Wunderlich, L. Isogeometric mortar methods. *Computer Methods in Applied Mechanics and Engineering*, 284:292–319, 2015. doi: https://doi.org/10.1016/j.cma.2014.09.012. Isogeometric Analysis Special Issue.

[93] Schuß, S., Dittmann, M., Wohlmuth, B., Klinkel, S., and Hesch, C. Multi-patch isogeometric analysis for Kirchhoff–Love shell elements. *Computer Methods in Applied Mechanics and Engineering*, 349:91–116, 2019. doi: https://doi.org/10.1016/j.cma.2019.02.015.

[94] Chasapi, M., Dornisch, W., and Klinkel, S. Patch coupling in isogeometric analysis of solids in boundary representation using a mortar approach. *International Journal for Numerical Methods in Engineering*, 121(14):3206–3226, 2020. doi: https://doi.org/10.1002/nme.6354.

[95] Benvenuti, A., Loli, G., Sangalli, G., and Takacs, T. Isogeometric multi-patch C^1-mortar coupling for the biharmonic equation, 2023.

[96] Herrema, A. J., Johnson, E. L., Proserpio, D., Wu, M. C., Kiendl, J., and Hsu, M.-C. Penalty coupling of non-matching isogeometric Kirchhoff–Love shell patches with application to composite wind turbine blades. *Computer Methods in Applied Mechanics and Engineering*, 346:810–840, 2019. doi: https://doi.org/10.1016/j.cma.2018.08.038.

[97] Leonetti, L., Liguori, F. S., Magisano, D., Kiendl, J., Reali, A., and Garcea, G. A robust penalty coupling of non-matching isogeometric Kirchhoff–Love shell patches in large deformations. *Computer Methods in Applied Mechanics and Engineering*, 371:113289, 2020. doi: https://doi.org/10.1016/j.cma.2020.113289.

[98] Zhao, H., Liu, X., Fletcher, A. H., Xiang, R., Hwang, J. T., and Kamensky, D. An open-source framework for coupling non-matching isogeometric shells with application to aerospace structures. *Computers & Mathematics with Applications*, 111: 109–123, 2022. doi: https://doi.org/10.1016/j.camwa.2022.02.007.

[99] Breitenberger, M., Apostolatos, A., Philipp, B., Wüchner, R., and Bletzinger, K.-U. Analysis in computer aided design: Nonlinear isogeometric B-rep analysis of shell structures. *Computer Methods in Applied Mechanics and Engineering*, 284:401–457, 2015. doi: https://doi.org/10.1016/j.cma.2014.09.033. Isogeometric Analysis Special Issue.

[100] Proserpio, D. and Kiendl, J. Penalty coupling of trimmed isogeometric Kirchhoff–Love shell patches. *Journal of Mechanics*, 38:156–165, 04 2022. doi: https://doi.org/10.1093/jom/ufac008.

[101] Pasch, T., Leidinger, L., Apostolatos, A., Wüchner, R., Bletzinger, K.-U., and Duddeck, F. A priori penalty factor determination for (trimmed) NURBS-based shells with dirichlet and coupling constraints in isogeometric analysis. *Computer Methods in Applied Mechanics and Engineering*, 377:113688, 2021. doi: https://doi.org/10.1016/j.cma.2021.113688.

[102] Coradello, L., Kiendl, J., and Buffa, A. Coupling of non-conforming trimmed isogeometric Kirchhoff–Love shells via a projected super-penalty approach. *Computer Methods in Applied Mechanics and Engineering*, 387:114187, 2021. doi: https://doi.org/10.1016/j.cma.2021.114187.

[103] Coradello, L. and ans Annalisa Buffa, G. L. A projected super-penalty method for the C^1-coupling of multi-patch isogeometric Kirchhoff plates. *Computational Mechanics*, 67:1133–1153, 2021. doi: https://doi.org/10.1007/s00466-021-01983-w.

[104] Ruess, M., Schillinger, D., Özcan, A. I., and Rank, E. Weak coupling for isogeometric analysis of non-matching and trimmed multi-patch geometries. *Computer Methods in Applied Mechanics and Engineering*, 269:46–71, 2014. doi: https://doi.org/10.1016/j.cma.2013.10.009.

[105] Guo, Y. and Ruess, M. Nitsche's method for a coupling of isogeometric thin shells and blended shell structures. *Computer Methods in Applied Mechanics and Engineering*, 284:881–905, 2015. doi: https://doi.org/10.1016/j.cma.2014.11.014.

[106] Guo, Y., Heller, J., Hughes, T. J., Ruess, M., and Schillinger, D. Variationally consistent isogeometric analysis of trimmed thin shells at finite deformations, based on the STEP exchange format. *Computer Methods in Applied Mechanics and Engineering*, 336:39–79, 2018. doi: https://doi.org/10.1016/j.cma.2018.02.027.

[107] Guo, Y., Zou, Z., and Ruess, M. Isogeometric multi-patch analyses for mixed thin shells in the framework of non-linear elasticity. *Computer Methods in Applied Mechanics and Engineering*, 380:113771, 2021. doi: https://doi.org/10.1016/j.cma.2021.113771.

[108] Guo, Y., Ruess, M., and Schillinger, D. A parameter-free variational coupling approach for trimmed isogeometric thin shells. *Computational Mechanics*, 59:693–715, 2017. doi: https://doi.org/10.1007/s00466-016-1368-x.

[109] Wang, Y., Yu, Y., and Lin, Y. Isogeometric analysis with embedded stiffened shells for the hull structural mechanical analysis. *Journal of Marine Science and Technology*, 27(1):786–805, 2022. doi: https://doi.org/10.1007/s00773-021-00868-0.

[110] Yu, Y., Wang, Y., and Lin, Y. Isogeometric analysis with non-conforming multi-patches for the hull structural mechanical analysis. *Thin-Walled Structures*, 187: 110757, 2023. doi: https://doi.org/10.1016/j.tws.2023.110757.

[111] Nguyen-Thanh, N., Zhou, K., Zhuang, X., Areias, P., Nguyen-Xuan, H., Bazilevs, Y., and Rabczuk, T. Isogeometric analysis of large-deformation thin shells using RHT-splines for multiple-patch coupling. *Computer Methods in Applied Mechanics and Engineering*, 316:1157–1178, 2017. doi: https://doi.org/10.1016/j.cma.2016.12.002. Special Issue on Isogeometric Analysis: Progress and Challenges.

[112] Chasapi, M., Antolin, P., and Buffa, A. Fast parametric analysis of trimmed multi-patch isogeometric Kirchhoff-Love shells using a local reduced basis method, 2023.

[113] Ciarlet, P. G. An introduction to differential geometry with applications to elasticity. *Journal of Elasticity*, 78(1-3):1–215, 2005. doi: https://doi.org/10.1007/s10659-005-4738-8.

[114] Koiter, W. On the mathematical foundation of shell theory. In *Actes du Congrès International des Mathématiciens*, volume 3, pages 123–130, 1970.

[115] Benzaken, J., Evans, J. A., McCormick, S. F., and Tamstorf, R. Nitsche's method for linear Kirchhoff–Love shells: Formulation, error analysis, and verification. *Computer Methods in Applied Mechanics and Engineering*, 374:113544, 2021. doi: https://doi.org/10.1016/j.cma.2020.113544.

[116] Saye, R. I. High-order quadrature methods for implicitly defined surfaces and volumes in hyperrectangles. *SIAM Journal on Scientific Computing*, 37(2):A993–A1019, 2015. doi: https://doi.org/10.1137/140966290.

[117] Saye, R. I. High-order quadrature on multi-component domains implicitly defined by multivariate polynomials. *Journal of Computational Physics*, 448:110720, 2022. doi: https://doi.org/10.1016/j.jcp.2021.110720.

[118] Kudela, L., Zander, N., Bog, T., Kollmannsberger, S., and Rank, E. Efficient and accurate numerical quadrature for immersed boundary methods. *Advanced Modeling and Simulation in Engineering Sciences*, 2(1), 2015. doi: https://doi.org/10.1186/s40323-015-0031-y.

[119] Antolin, P., Wei, X., and Buffa, A. Robust numerical integration on curved polyhedra based on folded decompositions. *Computer Methods in Applied Mechanics and Engineering*, 395:114948, 2022. doi: https://doi.org/10.1016/j.cma.2022.114948.

[120] Antolin, P., Buffa, A., Puppi, R., and Wei, X. Overlapping multipatch isogeometric method with minimal stabilization. *SIAM Journal on Scientific Computing*, 43(1): A330–A354, 2021. doi: https://doi.org/10.1137/19M1306750.

[121] Wei, X., Marussig, B., Antolin, P., and Buffa, A. Immersed boundary-conformal isogeometric method for linear elliptic problems. *Computational Mechanics*, 68(6): 1385–1405, 2021. doi: https://doi.org/10.1007/s00466-021-02074-6.

[122] Guarino, G., Gulizzi, V., and Milazzo, A. High-fidelity analysis of multilayered shells with cut-outs via the discontinuous Galerkin method. *Composite Structures*, 276:114499, 2021. doi: https://doi.org/10.1016/j.compstruct.2021.114499.

[123] Guarino, G., Buffa, A., Milazzo, A., and Antolin, P. An interior penalty coupling strategy for isogeometric non-conformal Kirchhoff-Love shell patches, . In preparation.

[124] Guarino, G., Buffa, A., Milazzo, A., and Antolin, P. An immersed boundary conformal method for Kirchhoff-Love shells, . In preparation.

[125] Schenk, O. and Gärtner, K. Solving unsymmetric sparse systems of linear equations with pardiso. *Future Generation Computer Systems*, 20(3):475–487, 2004. doi: https://doi.org/10.1016/j.future.2003.07.011. Selected numerical algorithms.

[126] Hernandez, V., Roman, J. E., and Vidal, V. Slepc: A scalable and flexible toolkit for the solution of eigenvalue problems. *ACM Transactions on Mathematical Software (TOMS)*, 31(3):351–362, 2005. doi: https://doi.org/10.1145/1089014.1089019.

[127] Piegl, L. and Tiller, W. *The NURBS Book (monographs in visual communication)*. Springer, 1997.

[128] Rogers, D. F. *An Introduction to NURBS: With Historical Perspective*. Morgan Kaufmann Publishers Inc., 2001.

[129] Antolin, P., Buffa, A., and Martinelli, M. Isogeometric Analysis on V-reps: First results. *Computer Methods in Applied Mechanics and Engineering*, 355:976–1002, 2019. doi: https://doi.org/10.1016/j.cma.2019.07.015.

[130] Quarteroni, A., Sacco, R., and Saleri, F. *Numerical mathematics*, volume 37. Springer, 2006. doi: https://doi.org/10.1007/b98885.

[131] Pagani, A., Azzara, R., Wu, B., and Carrera, E. Effect of different geometrically nonlinear strain measures on the static nonlinear response of isotropic and composite shells with constant curvature. *International Journal of Mechanical Sciences*, 209:106713, 2021. ISSN 0020-7403. doi: https://doi.org/10.1016/j.ijmecsci.2021.106713.

[132] Ting, T. *Anisotropic Elasticity: Theory and Applications*. Oxford Engineering Science Series. Oxford University Press, 1996. URL `https://books.google.it/books?id=RxBoH9GyPkEC`.

[133] Bracco, C., Giannelli, C., Kapl, M., and Vázquez, R. Isogeometric analysis with C^1 hierarchical functions on planar two-patch geometries. *Computers & Mathematics with Applications*, 80(11):2538–2562, 2020. doi: https://doi.org/10.1016/j.camwa.2020.03.018.

[134] Washizu, K. *Variational Methods in Elasticity and Plasticity*. Pergamon, 1975.

[135] Carrera, E. Historical review of Zig-Zag theories for multilayered plates and shells . *Applied Mechanics Reviews*, 56(3):287–308, 2003. ISSN 0003-6900. doi: https://doi.org/10.1115/1.1557614.

[136] Pagani, A., Carrera, E., Augello, R., and Scano, D. Use of Lagrange polynomials to build refined theories for laminated beams, plates and shells. *Composite Structures*, 276:114505, 2021. doi: https://doi.org/10.1016/j.compstruct.2021.114505.

[137] Patton, A., Carraturo, M., Auricchio, F., and Reali, A. Cost-effective and accurate interlaminar stress modeling of composite Kirchhoff plates via immersed isogeometric analysis and equilibrium. *Journal of Mechanics*, 38:32–43, 03 2022. doi: https://doi.org/10.1093/jom/ufac005.

[138] Douglas, J. and Dupont, T. Interior penalty procedures for elliptic and parabolic Galerkin methods. In Glowinski, R. and Lions, J. L., editors, *Computing Methods in Applied Sciences*, pages 207–216, 1976. doi: https://doi.org/10.1007/BFb0120591.

[139] Bösing, P. R., Madureira, A. L., and Mozolevski, I. A new interior penalty discontinuous Galerkin method for the Reissner-Mindlin model. *Mathematical Models and Methods in Applied Sciences*, 20(08):1343–1361, 2010. doi: https://doi.org/10.1142/S0218202510004623.

[140] Babuška, I. The finite element method with penalty. *Mathematics of computation*, 27(122):221–228, 1973. doi: https://doi.org/10.1090/S0025-5718-1973-0351118-5.

[141] Babuška, I. and Zlámal, M. Nonconforming elements in the Finite Element Method with penalty. *SIAM Journal on Numerical Analysis*, 10(5):863–875, 1973. doi: https://doi.org/10.1137/071007.

[142] Castillo, P. Performance of discontinuous Galerkin methods for elliptic PDEs. *SIAM Journal on Scientific Computing*, 24(2):524–547, 2002. doi: https://doi.org/10.1137/S1064827501388339.

[143] Liu, M. and Gorman, D. Formulation of Rayleigh damping and its extensions. *Computers & Structures*, 57(2):277–285, 1995. doi: https://doi.org/10.1016/0045-7949(94)00611-6.

[144] Crisfield, M. A. A fast incremental/iterative solution procedure that handles "snap-through". In *Computational methods in nonlinear structural and solid mechanics*, pages 55–62. Elsevier, 1981. doi: https://doi.org/10.1016/0045-7949(81)90108-5.

[145] Crisfield, M. An arc-length method including line searches and accelerations. *International Journal for Numerical Methods in Engineering*, 19(9):1269–1289, 1983. doi: https://doi.org/10.1002/nme.1620190902.

[146] Zheng, X., Sun, Y., Huang, M., An, D., Li, P., Wang, B., and Li, R. Symplectic superposition method-based new analytic bending solutions of cylindrical shell panels. *International Journal of Mechanical Sciences*, 152:432–442, 2019. doi: https://doi.org/10.1016/j.ijmecsci.2019.01.012.

[147] An, D., Xu, D., Ni, Z., Su, Y., Wang, B., and Li, R. Finite integral transform method for analytical solutions of static problems of cylindrical shell panels. *European Journal of Mechanics - A/Solids*, 83:104033, 2020. doi: https://doi.org/10.1016/j.euromechsol.2020.104033.

[148] Ruban, A. and Gajjar, J. *Fluid Dynamics: Classical fluid dynamics*. Fluid Dynamics. Oxford University Press, 2014.

[149] Oliveri, V., Milazzo, A., and Weaver, P. M. Thermo-mechanical post-buckling analysis of variable angle tow composite plate assemblies. *Composite Structures*, 183:620–635, 2018. doi: https://doi.org/10.1016/j.compstruct.2017.07.050.

[150] Gulizzi, V., Oliveri, V., and Milazzo, A. Buckling and post-buckling analysis of cracked stiffened panels via an X-Ritz method. *Aerospace Science and Technology*, 86:268–282, 2019. doi: https://doi.org/10.1016/j.ast.2019.01.019.

[151] Sciascia, G., Oliveri, V., Milazzo, A., and Weaver, P. M. Ritz solution for transient analysis of variable-stiffness shell structures. *AIAA Journal*, 58(4):1796–1810, 2020. doi: https://doi.org/10.2514/1.J058686.

[152] Noor, A. K. Stability of multilayered composite plates. *Fibre Science and Technology*, 8(2):81–89, 1975. doi: https://doi.org/10.1016/0015-0568(75)90005-6.

[153] D'Ottavio, M. and Carrera, E. Variable-kinematics approach for linearized buckling analysis of laminated plates and shells. *AIAA journal*, 48(9):1987–1996, 2010. doi: https://doi.org/10.2514/1.J050203.

[154] Turvey, G. and Osman, M. Elastic large deflection analysis of isotropic rectangular Mindlin plates. *International Journal of Mechanical Sciences*, 32(4):315–328, 1990. doi: https://doi.org/10.1016/0020-7403(90)90096-2.

[155] Wu, B., Pagani, A., Filippi, M., Chen, W., and Carrera, E. Large-deflection and post-buckling analyses of isotropic rectangular plates by Carrera Unified Formulation. *International Journal of Non-Linear Mechanics*, 116:18–31, 2019. doi: https://doi.org/10.1016/j.ijnonlinmec.2019.05.004.

[156] Wu, B., Pagani, A., Chen, W., and Carrera, E. Geometrically nonlinear refined shell theories by Carrera Unified Formulation. *Mechanics of Advanced Materials and Structures*, 28(16):1721–1741, 2021. doi: https://doi.org/10.1080/15376494.2019.1702237.

[157] Carrera, E., Pagani, A., Azzara, R., and Augello, R. Vibration of metallic and composite shells in geometrical nonlinear equilibrium states. *Thin-Walled Structures*, 157:107131, 2020. doi: https://doi.org/10.1016/j.tws.2020.107131.

[158] Sze, K., Liu, X., and Lo, S. Popular benchmark problems for geometric nonlinear analysis of shells. *Finite Elements in Analysis and Design*, 40(11):1551–1569, 2004. doi: https://doi.org/10.1016/j.finel.2003.11.001.

[159] Sande, E., Manni, C., and Speleers, H. Explicit error estimates for spline approximation of arbitrary smoothness in Isogeometric Analysis. *Numerische Mathematik*, 144:889–929, 2020. doi: https://doi.org/10.1007/s00211-019-01097-9.

[160] Hu, Q., Chouly, F., Hu, P., Cheng, G., and Bordas, S. P. Skew-symmetric Nitsche's formulation in isogeometric analysis: Dirichlet and symmetry conditions, patch coupling and frictionless contact. *Computer Methods in Applied Mechanics and Engineering*, 341:188–220, 2018. doi: https://doi.org/10.1016/j.cma.2018.05.024.

[161] Babuška, I. The finite element method with penalty. *Mathematics of Computation*, 27:221–228, 1973. doi: https://doi.org/10.1090/S0025-5718-1973-0351118-5.

[162] Annavarapu, C., Hautefeuille, M., and Dolbow, J. E. A robust Nitsche's formulation for interface problems. *Computer Methods in Applied Mechanics and Engineering*, 225-228:44–54, 2012. doi: https://doi.org/10.1016/j.cma.2012.03.008.

[163] Jiang, W., Annavarapu, C., Dolbow, J. E., and Harari, I. A robust Nitsche's formulation for interface problems with spline-based finite elements. *International Journal for Numerical Methods in Engineering*, 104(7):676–696, 2015. doi: https://doi.org/10.1002/nme.4766.

[164] Griebel, M. and Schweitzer, M. A. *A Particle-Partition of Unity Method Part V: Boundary Conditions*, pages 519–542. Springer Berlin Heidelberg, 2003.

[165] Apostolatos, A., Schmidt, R., Wüchner, R., and Bletzinger, K.-U. A Nitsche-type formulation and comparison of the most common domain decomposition methods in isogeometric analysis. *International Journal for Numerical Methods in Engineering*, 97(7):473–504, 2014. doi: https://doi.org/10.1002/nme.4568.

[166] Falco, C. D., Reali, A., and Vázquez, R. GeoPDEs: A research tool for isogeometric analysis of PDEs. *Advances in Engineering Software*, 42(12):1020–1034, 2011. doi: https://doi.org/10.1016/j.advengsoft.2011.06.010.

[167] Vázquez, R. A new design for the implementation of isogeometric analysis in octave and matlab: GeoPDEs 3.0. *Computers & Mathematics with Applications*, 72(3): 523–554, 2016. doi: https://doi.org/10.1016/j.camwa.2016.05.010.

[168] de Prenter, F., Verhoosel, C. V., van Brummelen, E. H., Larson, M. G., and Badia, S. Stability and conditioning of immersed finite element methods: Analysis and remedies. *Archives of Computational Methods in Engineering*, 30(6):3617–3656, 2023. doi: https://doi.org/10.1007/s11831-023-09913-0.

[169] Buffa, A., Puppi, R., and Vázquez, R. A minimal stabilization procedure for isogeometric methods on trimmed geometries. *SIAM Journal on Numerical Analysis*, 58(5):2711–2735, 2020. doi: https://doi.org/10.1137/19M1244718.

[170] Coradello, L., D'Angella, D., Carraturo, M., Kiendl, J., Kollmannsberger, S., Rank, E., and Reali, A. Hierarchically refined isogeometric analysis of trimmed shells. *Computational Mechanics*, 66(2):431–447, 2020. doi: https://doi.org/10.1007/s00466-020-01858-6.

[171] Belytschko, T. and Black, T. Elastic crack growth in finite elements with minimal remeshing. *International Journal for Numerical Methods in Engineering*, 45(5): 601–620, 1999. doi: https://doi.org/10.1002/(SICI)1097-0207(19990620)45:5⟨601::AID-NME598⟩3.0.CO;2-S.